

Decadal and long-term sea-level changes in the tropical Indo-Pacific Ocean

A Thesis submitted to Goa University
for the Award of the Degree of

DOCTOR OF PHILOSOPHY
in
Marine Sciences

By
Nidheesh A. G.

Research Guide
A. S. Unnikrishnan

Goa University
Taleigao, Goa
2017



577.77

NID/Dec

F- 780 780

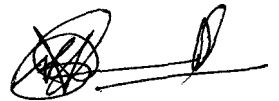
to

my father

Statement

As required under the University ordinance OB-9.9 (v-vi), I state that this thesis entitled *Decadal and long-term sea-level changes in the tropical Indo-Pacific Ocean* is my original contribution and it has not been submitted on any previous occasion.

The literature related to the problem investigated has been cited. Due acknowledgements have been made wherever facilities and suggestions have been availed of.

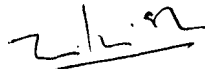


NIDHEESH A. G.

CSIR-National Institute of Oceanography, Goa.

Certificate

This is to certify that the thesis entitled *Decadal and long-term sea-level changes in the tropical Indo-Pacific Ocean*, submitted by Nidheesh A. G. to the Goa University for the degree of Doctor of Philosophy, is based on his original studies carried out under my supervision. The thesis or any part thereof has not been previously submitted for any other degree or diploma in any university or institution.


A. S. UNNIKRISHNAN

CSIR-National Institute of Oceanography, Goa.

All the corrections suggested by the referees have been incorporated.
 22/06/17




22/6/17
C.H. B. Menon

Acknowledgements

This is time to recall many people, events and experiences in CSIR-NIO where I lived nearly seven years. It is difficult to write life compared to science; however, my heart is filled with gratitude at this moment.

I was a man of excuses when I joined CSIR-NIO as a project assistant with Dr. A. S. Unnikrishnan in July 2009. He guided me from that phase to a man of pursuit that I am today. Being a simple and silent person, it is completely beyond words how Dr. Unni moulded me to work hard without any diversions. He rarely answered my questions directly but always reminded me *how to listen* to the problem to figure out the possible ways to the solution. Gradually, I attained a habit of listening to everything rather than being satisfied with any given answer. Dr. Unni is, therefore, my true mentor.

The most remarkable thing Dr. Unni did in the beginning of my research was to introduce me to two visiting scientists at CSIR-NIO: Dr. Jerome Vialard and Dr. Matthieu Lengaigne. Today, after five years of research with Jerome and Matt, they are like my two elder brothers born in France. In the early summer of 2012, when I was working at LOCEAN, Paris, on deputation, Jerome asked me in the presence of Matt: "What do you think is the ultimate aim of your PhD?" After my answering session he said: "Well, these are fine, but the ultimate aim is *to become independent*." In the following years, during the hour-long discussions in the visiting scientist's cabin at NIO, both Matt and Jerome asked me questions, assigned me weighted tasks and subsequently let me plan, perform and present the analysis in front of them with confidence. I was closely associated with Matt and worked on his advices as Jerome left for France in 2010. The elegant way of Matt for reaching a consensus in our discussions with Jerome taught me how to do research in (as) a group. Thank you Matt and Jerome for paving a wonderful path for me towards this end. Let me also thank Dr. Takeshi Izumo for his invaluable involvement in this thesis. He is philosophical yet simple. Once he said: "Remember Nidheesh, perfect is the enemy of good." Thank you Kenshi for making my path much easier.

I express my gratitude to CSIR-NIO and the Director for providing all the necessary infrastructure and facilities to carry out this study. I duly acknowledge with much gratefulness the research fellowship awarded by CSIR. I wish to express my sincere thanks to HOD and other staffs at the Department of Marine Sciences for helping with office formalities in Goa University. I also wish to acknowledge the financial support provided by IRD-France, which enabled me to work at LOCEAN, Paris, for 5 months. I acknowledge AVISO and PSMSL for

making observational sea-level data available through web, which were extensively used in this research. I must thank all the reanalysis and reconstruction groups, NEMO system team and CMIP community for providing various oceanographic data; without the huge efforts behind these datasets this thesis would not have been possible. I express my special thanks to Dr. Meyssignac for providing reconstructed sea-level data through personal communication.

I remember H2-08, my working lab situated at the far end of POD wing at NIO, and many people who worked in this lab during the last seven years. It is in this lab I learned the science of oceans. Nearly everything was new to me when I came to this lab for the first time. It was from my lab-mates that I learned many things like Unix, Ferret, GMT, etc. I should mention some names like Manoj, Vijith, Amol, Mahalingam, Nandu, Subeesh, Abhishek, Arnab, Sarvesh, Remya, Charles, Vineet, Somu, Vipin, Anil and Sreekanth among a lot of others from whom I learned a lot. The oceanography classes and discussions conducted in the lab were always fruitful. Let me also express my gratitude to Dr. D. Shankar for delivering numerous GFD lectures that often sowed seeds for thoughts and discussions in the lab.

I am grateful to Dr. S. G. Aparna who evaluated the progress of my research in time and had a friendly approach all the time. I thank all other members of the Faculty Research Committee and staff at the Department of Marine Sciences, Goa University. I am grateful to Drs. S. Prasana Kumar, M.R. Ramesh Kumar and P. Vethamony for their support and encouragement. I thank HRM, ITG, accounts, administration and all other departments and staff at CSIR-NIO for the invaluable services they provided. I thank Dr. Haris K. for his valuable advice for shaping this thesis in the present form. Thank you Michael Sir, Yathishettan and Vidyechi for your affection and support.

Let me express my gratitude towards Ms. Sandhya Jayakumar and Ms. Ambili Sudarshan who taught me the basic lessons of Carnatic music during my stay at Goa. I am grateful to Gokul and Chitturamma who showed me how to find the meaning of life in both joy and suffering. I thank all my NIO friends who made this mission much easier and indelible. No words are enough to thank my grandma, parents, Giri and Kunji; I know you wished me to be near but I was always away. Let me come home like a castaway, with full of love and gratitude in my heart. Thank you Goa, you allowed me to find myself on your beaches, hills and waterfalls. I am leaving for a new coast with you in my heart.

Nidheesh

CSIR-NIO, Goa

Abstract

The present thesis investigates the decadal and long-term sea-level variability and associated processes in the tropical Indo-Pacific Ocean. As the observational sea-level data (altimeter and tide gauge) are not enough to study the large-scale decadal variability, this thesis attempts to improve our understanding of the tropical Indo-Pacific decadal sea-level variability through a holistic approach that combines a large set of sea-level data, encompassing available observations, reconstructions/reanalyses and long-term simulations from forced and coupled general circulation models. All the observationally-derived sea-level products display a consistent pattern of decadal sea-level variability in the Pacific, associated with two leading climate modes in this basin - decadal ENSO and Modoki. However these products do not show any robust pattern of Pacific-related Indian Ocean (IO) decadal sea-level variability, most likely because of sparse observational coverage of the IO. The various sea-level and wind products analysed show that IO decadal sea-level variability is to a large extent independent of the Pacific. However, the disparity in the IO decadal sea-level variations depicted by observational datasets does not allow to draw definitive conclusions on the dominant pattern of IO decadal sea-level variability and its relationship with the Pacific.

On the other hand, CMIP simulations display two consistent modes of IO decadal sea-level variability, which explain more than 50% of the total decadal sea-level variance in this basin. The first mode consists of a basin-scale sea-level pattern (referred as *Indian Ocean Basin-Scale Mode - IOBSM*), with negative SLA in the eastern IO largely centered off the west coast of Java/Sumatra which extend to the northern BoB and positive SLA in the western part of the basin (centered off the northeast of Madagascar). The IOBSM is found to be largely driven by the wind variations over the IO related to the decadal Indian Ocean Dipole which is partly modulated by the decadal climate variability in the tropical Pacific (ENSO and Modoki). The second mode of IO decadal sea-level variability depicted by CMIP models is largely independent from the Pacific, and consists of a broad sea-level signature in the SWIO (hence named *Southwest Indian Ocean Mode - SWIOM*). This mode is most likely excited by decadal wind variations in the subtropical IO, probably driven by the Mascarene High variability. The two modes of Indian Ocean decadal sea level identified in CMIP models are broadly consistent with those deduced from the relatively short altimeter data or from the longer ORA-S4 dataset. The present thesis hence suggests that CMIP outputs can provide some guidance for identifying robust modes of decadal sea-level variability in regions that are not well sampled in observations.

Contents

Statement	iii
Certificate	iv
Acknowledgements	v
Abstract	vii
Contents	viii
Acronyms	xii
List of Figures	xiv
List of Tables	xvii
1. Introduction	1
1.1. Global climate Change.....	1
1.2. Climate change and natural variability.....	3
1.3. Natural sea-level variations in the Indo-Pacific.....	3
1.4. Sea-level observation and caveats.....	4
1.5. Thesis outline.....	5
2. State of the art	7
2.1. Global mean sea-level change.....	8
2.1.1. Observations.....	8
2.1.2. Coupled Model Intercomparison project.....	9
2.2. Regional sea-level changes.....	11
2.3. Theoretical considerations.....	13
2.4. Tropical Indo-Pacific annual mean state.....	16
2.5. Indo-Pacific interannual climate and sea level	20
2.5.1. The El Niño Southern Oscillation.....	20
2.5.2. The Indian Ocean Dipole.....	24
2.5.3. Imprint of interannual climate variability on sea level.....	25
2.5.4. Representation of interannual variability in CMIP.....	28
2.6. Indo-Pacific decadal climate and sea-level variability.....	30
2.6.1. Pacific decadal climate variability.....	30

2.6.2. Indian Ocean decadal climate variability.....	35
2.6.3. Imprint of decadal climate variability on sea level.....	36
2.6.4. Representation in CMIP models.....	39
2.7. Aliasing of long-term sea-level trend by decadal variability.....	40
3. Decadal and long-term sea-level variability in an OGCM	44
3.1. Data.....	46
3.1.1. Ocean model experiment.....	46
3.1.2. Observational datasets.....	47
3.2. Methods.....	48
3.2.1. Model steric sea level.....	48
3.2.2. Time scale definition.....	49
3.2.3. Definition of climate indices.....	50
3.3. Observed and modelled variability.....	52
3.4. Decadal sea-level variations and related mechanisms.....	58
3.4.1. Basin scale pattern of sea-level.....	59
3.4.2. Mechanisms of regional decadal variability.....	61
3.5. Robustness of the decadal wind forcing.....	65
3.6. Long-term trends.....	68
3.6.1. Pattern of steric sea-level long-term trend.....	68
3.6.2. Robustness of the wind forcing trends.....	69
3.7. Summary.....	71
3.8. Discussion.....	73
4. Robustness of Indo-Pacific decadal sea-level variability	76
4.1. Data.....	78
4.1.1. Satellite altimeter.....	78
4.1.2. Tide gauge sea level.....	78
4.1.3. Reanalysis/Reconstructed sea level.....	82
4.1.4. SST and wind.....	84
4.1.5. The LCS model.....	84
4.2. Method.....	85
4.2.1. Time scale definition.....	85
4.2.2. Definition of climate indices.....	86
4.3. Sea-level products evaluation.....	87
4.4. Indo-Pacific sea-level signature of Pacific decadal climate.....	89

4.4.1. Pacific sea-level variability and related climate modes.....	89
4.4.2. Indian Ocean sea level related to Pacific variability.....	93
4.4.3. A destructive interference between ENSO atmospheric.....	96
4.4.4. Interannual vs decadal SLA signature of ENSO.....	98
4.5. Modes of IO decadal sea-level variability.....	101
4.6. Summary and discussion.....	105
4.6.1. Pacific decadal sea-level variability.....	106
4.6.2. Indian Ocean decadal sea-level variability.....	107
5. Influence of ENSO forcing on the Indo-Pacific decadal variability in CMIP models	109
5.1. Data.....	111
5.1.1. Observational data.....	111
5.1.2. CMIP models.....	112
5.2. Method.....	113
5.2.1. Climate indices definition.....	113
5.2.2. Statistical analysis.....	113
5.3. ENSO-PDO relationship in CMIP models.....	115
5.4. Explaining the diversity of ENSO-PDO relationship.....	122
5.5. ENSO teleconnection in the Indian Ocean.....	127
5.6. Summary.....	131
5.7. Discussion.....	132
6. Natural decadal sea-level variability in the Indo-Pacific in CMIP models	135
6.1. Data and method.....	136
6.2. Amplitude of decadal sea-level variability.....	137
6.3. Decadal ENSO and Modoki in CMIP models.....	138
6.4. Sea-level fingerprint of Pacific climate modes.....	140
6.4.1. ENSO SLA fingerprint.....	140
6.4.2. Modoki SLA fingerprint.....	142
6.5. Main modes of Indian Ocean decadal sea-level variability.....	144
6.6. Summary and discussion.....	149
6.6.1. Summary.....	149
6.6.2. Discussion.....	149

7. Summary and Perspective	153
7.1. Summary.....	153
7.1.1. Decadal sea-level variations in the Pacific.....	153
7.1.2. Pacific influence on IO decadal sea level.....	154
7.1.3. Independent IO decadal variability.....	154
7.1.4. Representation of decadal ENSO variations in CMIP..	155
7.1.5. IO decadal sea-level variability in CMIP models.....	155
7.2. Perspectives.....	156
7.2.1. Improving the observational sea-level products.....	156
7.2.2. Improve understanding of IO decadal sea-level variability	157
7.2.3. Accounting for natural decadal variability in the estimation of mean sea-level change induced by climate change.....	158
Bibliography	161

Acronyms

AVISO	Archiving Validation and Interpretation of Satellite Oceanographic
BoB	Bay of Bengal
C&W	Church and White
CCAR	Colorado Centre for Astrodynamics Research
CMIP	Coupled Model Intercomparison Project
DMI	Dipole Mode Index
EEIO	Eastern Equatorial Indian Ocean
EIO	Equatorial Indian Ocean
ENH	Expanded Null Hypothesis
ENSO	El Niño Southern Oscillation
EOF	Empirical Orthogonal Function
ERA	ECMWF Re-Analysis
ERSST	Extended Reconstructed Sea Surface Temperature
GMSL	Global Mean Sea Level
HadISST	Hadley Centre Sea Ice and Sea Surface Temperature
IO	Indian Ocean
IOBSM	Indian Ocean Basin-scale Mode
IOD	Indian Ocean Dipole
IPO	Interdecadal Pacific Oscillation
ITCZ	Inter-tropical Convergence Zone
ITF	Indonesian Throughflow
MESSIs	Meyssignac's sea-level products
MME	Multi-Model Ensemble
MOE	Multi-Observational Ensemble
NCEP	National Centers for Environmental Prediction
NEMO	Nucleus for European Modeling of the Ocean
NIO	North Indian Ocean

NWP	Northwest Pacific
OGCM	Ocean General Circulation Model
ORA	Ocean Reanalysis System
PDO	Pacific Decadal Oscillation
PSMSL	Permanent Service for Mean Sea Level
SEIO	Southeast Indian Ocean
SIO	South Indian Ocean
SLA	Sea-level Anomaly
SLP	Sea-level Pressure
SODA	Simple Ocean Data Assimilation
SSLA	Steric Sea-level Anomaly
SST	Sea Surface Temperature
STL	Seasonal Trend decomposition procedure based on Loess
SWIO	Southwest Indian Ocean
SWIOM	Southwest Indian Ocean Mode
SWP	Southwest Pacific
TP/J	TOPEX/Poseidon and Jason
20CR	20 th Century Reanalysis
WAC	West Australian Coast
WASWind	Wave and Anemometer-based Sea surface Wind
WEP	West Equatorial Pacific
WOD	World Ocean Data

List of Figures

1.1	Global warming in observation.....	2
1.2	Global mean sea-level rise (Satellite).....	2
2.1	Global mean sea-level rise (Tide gauge).....	8
2.2	Sea-level rise projection in CMIP.....	10
2.3	Regional variability in sea-level rise.....	11
2.4	Spatial map of sea-level rise projection.....	12
2.5	Annual mean state of tropical Indo-Pacific.....	16
2.6	Walker circulation and ITF.....	17
2.7	Seasonal movement of ITCZ.....	18
2.8	Annual cycle of sea level and wind in the NIO.....	19
2.9	ENSO and Modoki: Spatial maps.....	21
2.10	IOBM and IOD: Spatial maps.....	24
2.11	Pacific sea level related to interannual ENSO.....	26
2.12	IO sea-level response to El Niño.....	27
2.13	IO response to IOD and El Niño.....	27
2.14	Interannual ENSO and IOD in CMIP models.....	28
2.15	Spatial and temporal features of ENSO and PDO.....	30
2.16	Annual cycle of cross-correlation between ENSO and PDO.....	34
2.17	Decadal SST variability in the IO and Pacific.....	35
2.18	IPO sea-level pattern in the Pacific.....	36
2.19	Decadal sea-level variability at Christmas and Fremantle.....	37
2.20	Decadal sea-level changes in altimeter SLA.....	38
2.21	Modoki sea-level pattern in altimeter SLA.....	39
2.22	PDO SST pattern in CMIP models.....	40
2.23	Sea-level trend aliasing by climate variability.....	42
3.1	Satellite sea-level maps.....	45
3.2	Time series filtering using STL.....	49
3.3	Major climate modes in the tropical Pacific.....	51

3.4	Spatial maps of sea level standard deviation.....	53
3.5	Model SSLA validation.....	54
3.6	Thermosteric and halosteric SLA.....	58
3.7	Main modes of Indo-Pacific decadal sea-level variability.....	59
3.8	Regional variability of SSLA in the Indo-Pacific.....	62
3.9	Main modes of decadal wind variability.....	65
3.10	Time evolution of decadal wind over key regions.....	66
3.11	Long-term trend in SSLA and wind	68
3.12	Long-term changes in wind over key regions in different products..	69
3.13	Dependence of trend estimation on estimation period.....	70
4.1	Map of sea-level trend and tide gauge locations.....	78
4.2	Selection procedure of tide gauge records	80
4.3	Time series of selected tide gauge sea level.....	81
4.4	GMSL time series from gridded sea-level products.....	85
4.5	Standard deviation of interannual and decadal SLA	87
4.6	Agreement between SLA from tide gauges and gridded products...	88
4.7	EOF1 of Pacific decadal SLA.....	90
4.8	EOF2 of Pacific decadal SLA.....	92
4.9	Decadal ENSO-driven IO SLA.....	94
4.10	Decadal Modoki-driven IO SLA	95
4.11	IO wind pattern related to decadal ENSO and Modoki.....	96
4.12	IO SLA response to ENSO and Modoki: LCS experiment.....	97
4.13	Interannual Vs decadal SLA signature of ENSO.....	98
4.14	Model EOF pattern of IO decadal SLA.....	101
4.15	Ensemble EOF1 pattern of IO decadal SLA.....	102
4.16	Mode2 EOF pattern of IO decadal SLA.....	103
4.17	EOF1 and EOF2 SLA pattern from TP/J and NEMO.....	104
4.18	Contribution of ENSO and Modoki to IO decadal SLA.....	105
4.19	Influence of ENSO on decadal SLA as seen in tide gauges.....	107
5.1	Maximum lag-correlation between ENSO and PDO.....	116
5.2	Skill of Newman's model and ENSO influence on PDO.....	117
5.3	Power spectrum of PDO time series.....	118
5.4	ENSO and IPO pattern in the Pacific in CMIP models.....	120
5.5	Relationship between ENSO and IPO pattern.....	122

5.6	ENSO teleconnection to north Pacific: Mechanisms in CMIP...	123
5.7	Correlation map of SLP anomalies to the ENSO index.....	124
5.8	Scatter of ENSO/PDO correlation against ENSO/NP-SLP.....	125
5.9	Controlling factors of ENSO/PDO relationship.....	126
5.10	Scatter of ENSO amplitude Vs PDO amplitude.....	127
5.11	Scatter of ENSO amplitude Vs IO SST amplitude.....	128
5.12	IO SST pattern related to ENSO in CMIP models.....	129
5.13	Agreement between CMIP and observation on IO decadal SST...	131
6.1	MME and MOE maps of SLA standard deviation	137
6.2	Decadal ENSO and Modoki related SST: MME and Observation..	138
6.3	ENSO sea-level fingerprint in CMIP and observations.....	140
6.4	ENSO and Modoki sea-level fingerprint: Details.....	141
6.5	Modoki sea-level fingerprint in CMIP and observations.....	142
6.6	EOF1 pattern of IO decadal SLA in CMIP and observation....	144
6.7	Correlation between IOBSM time series and decadal DMI	146
6.8	EOF2 pattern of IO decadal SLA in CMIP and observation.....	147
6.9	Contribution of ENSO and Modoki on IOBSM and SWIOM....	148
6.10	ENSO, Modoki and DMI patterns of decadal IO SLA.....	150
7.1	Spatial map of sea-level trend from various sea-level products....	159

List of Tables

3.1	Correlation coefficient between box-averaged SSLA and SSLA at tide gauge location.....	53
3.2	Maximum lag-correlation of SLA between different regions in the Indo-Pacific for model and observations.....	55
3.3	Correlation coefficient of model SSLA between selected regions in the Indo-Pacific at interannual and decadal time scales.....	56
3.4	Linear trend of observed and model sea level at tide gauge locations.....	57
3.5	Maximum lag-correlation between decadal SSLA with ENSO and Modoki indices in the selected regions in the Indo-Pacific.....	63
3.6	Maximum lag-correlation between decadal zonal wind stress PC1 and PC2 with ENSO and Modoki indices.....	67
3.7	Cross-correlation between decadal wind stress variations in selected regions of the Indo-Pacific sector.....	68
4.1	Details of tide-gauge data.....	82
4.2	Brief summary of gridded sea-level products.....	83
5.1	List of CMIP models.....	112
5.2	List of models that display a peak at decadal time scales which is not explained by the AR-1 model.....	119

Introduction

“A problem clearly stated is a problem half solved”

Brande

1.1 Global climate change

There is strong consensus amongst climate scientists that the world ocean has warmed during the past fifty years (Bindoff et al. 2007, Levitus et al. 2000, 2012). During 1960-2010, the global mean sea surface temperature has raised by about 0.3 to 0.5°C (fig. 1.1b). The warming of our globe has been largely attributed to the emission of greenhouse gases into the atmosphere mainly from combustion of fossil fuels (Church et al. 2013, Christensen et al. 2014). The observation of atmospheric CO₂ concentrations since 1958 at the Mauna Loa observatory (see description of “Keeling curve” in fig. 1.1a) indeed shows a clear increasing trend that is consistent with the warming of the Earth observed during the last fifty years. In the climate system, the ocean acts as a “buffer” for the atmospheric temperature by storing a large amount of heat from the atmosphere and transporting it at depth via the ocean conveyor belt. Observations suggest that ~84% of the total heating of the Earth system over the last 40 years has gone into the ocean owing its large heat capacity compared to the atmosphere (Levitus et al 2005). Over the 1961-2003 period, the 0-700 m average global ocean temperature has risen by about 0.1°C. Consequently, the global ocean heat content has increased during the same period, equivalent to absorbing energy at a rate of 0.21 Wm⁻² globally averaged over the Earth’s surface. The excess heat in the ocean (an increased ocean heat content) directly translates into a rise in mean sea level through thermal expansion. Satellite observations show that the global mean sea level is rising at a rate of ~3.2 mm yr⁻¹ during the last two decades (fig. 1.2a), which further underlines the ocean response to current global warming scenario.

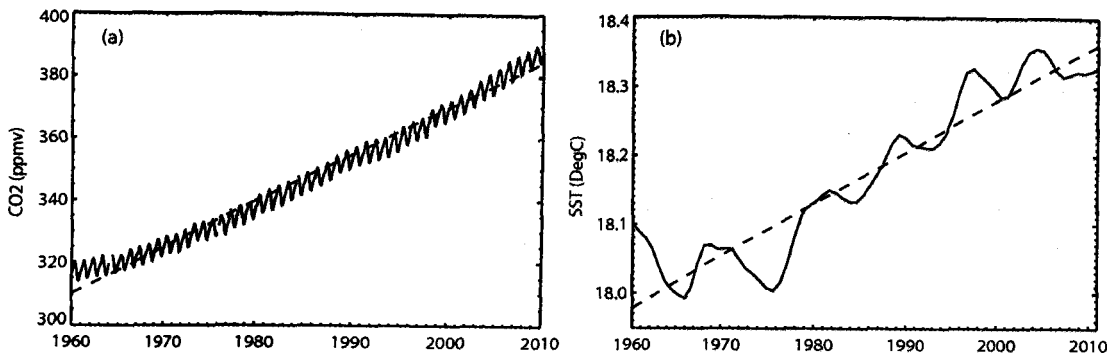


Fig. 1.1: (a) Atmospheric CO₂ concentration measured at Mauna Loa observatory (black curve) located at the island of Hawaii in the central tropical Pacific Ocean (155W, 19N). This curve is popularly known as “Keeling curve” in tribute to Charles David Keeling¹ who started this observation which is one of the most remarkable geophysical records ever made. Measurements are adjusted to account for local out-gassing of CO₂ from the volcano. (b) Evolution of global mean sea surface temperature during 1960-2010. The linear trend of the time series is shown by red dashed line in both panel (a) and (b). Source of data is NOAA [<http://www.esrl.noaa.gov/gmd/ccgg/trends/data.html> and <https://www.ncdc.noaa.gov/data-access/marineocean-data>].

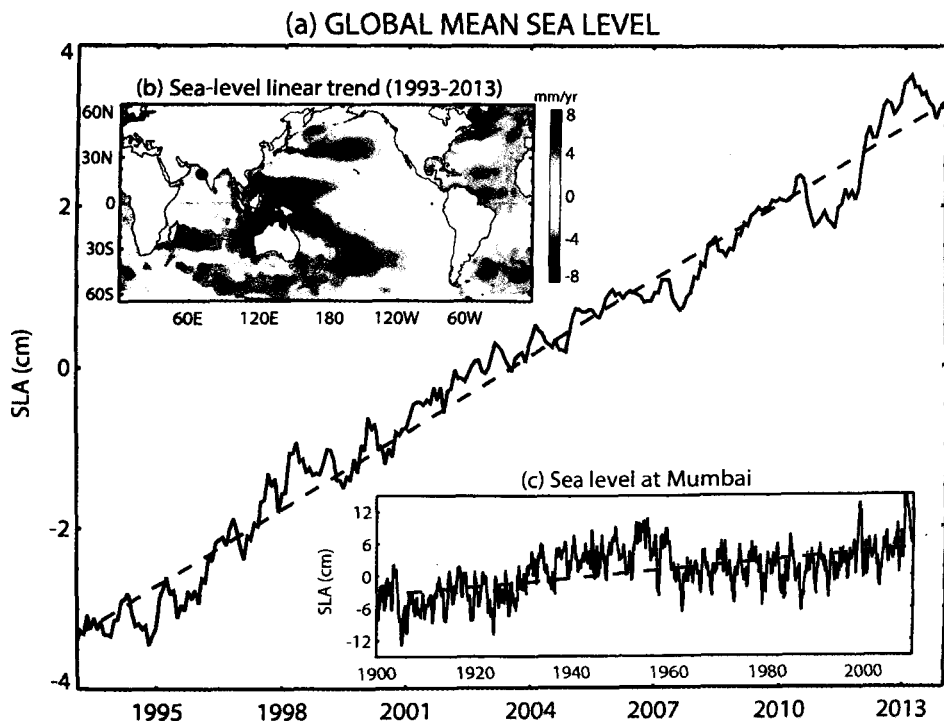


Fig. 1.2: (a) Global mean sea-level time series from satellite altimeter data. (b) Spatial map of sea-level trend from altimeter data for the period 1993-2013. (c) Tide gauge Sea-level record at Mumbai, west coast of India (location shown by a green dot in (b)). Linear trend of sea level is shown by red dashed line in panels (a) and (c).

¹ Charles David Keeling (1928-2005) was a post doctoral student at CIT during 1953 - 1956. In 1958, Keeling began to measure CO₂ from Hawaii’s Mauna Loa volcano. After one year of observation, Keeling discovered a seasonal rhythm in CO₂ evolution in such a way that CO₂ builds up after winter decay of plants and decreases with plants regrowth after summer. Over the years, Keeling noticed a long-term change in the mean CO₂ level in this record. This rising graph of CO₂ (fig. 1.1a) has been later referred to as the *Keeling curve*. The strong seasonal cycle seen in the curve is a good example of “*natural variability*”- a term that is widely used in this thesis. But the long-term trend (a rise in the mean CO₂ level) shows the added CO₂ mainly through burning of fossil fuels (anthropogenic change).

1.2 Climate change and natural variability

Fig. 1.1a, b and 1.2a are evidences of global long-term trends (highlighted by red dashed-lines in these panels) of climate variables (here CO₂, sea surface temperature (SST) and sea level) induced by anthropogenic forcing during the last few decades. These changes in our global climate have drawn a considerable attention amongst the world nations. The curves on Fig. 1.1a, b and 1.2a however also illustrate that the long-term trends induced by climate change are embedded within natural oscillations of the climate system over a wide range of timescales. A clear understanding of these natural variations of the climate system and their driving mechanisms are hence crucial for the detection of human-induced changes. This thesis primarily addresses this issue. We have a reasonably good understanding of some of these natural oscillations: for example, the strong annual variations found in the CO₂ record are the result of global photosynthetic activity which has a strong dependence on the migration of sun between the two hemispheres of the Earth in an year. On the other hand, some of these natural variations that occur over much lower frequencies are more difficult to detect as well as to understand. For example, fig. 1.1b and 1.2c show such decadal/multi-decadal low frequency oscillations in global mean SST time series and sea level measured at Mumbai along the west coast of India (which is the longest sea-level record in the Indian Ocean). The aliasing of climate change signals by natural low-frequency climate variations are even more prominent at regional scales: the sea-level trends (fig. 1.2b) are indeed not globally uniform mainly because the secular change in any region is largely affected by natural variability, especially those occurring over time scales comparable to the length of the record itself (i.e. decadal to multi-decadal periods). There is hence a potentially large aliasing of long-term trends by natural variability at lower frequencies (decadal and multi-decadal).

This led Meehl et al. (2009) to state that understanding of natural low-frequency variability is crucial for the detection and attribution of any secular change found in the climate system. The problem seems to be clear but the solution is not as simple because:

- we do not always have a sufficient amount of observational data both spatially and temporally to accurately describe natural variability.
- we do not fully understand the physics of low-frequency climate variability and the complex feedback mechanisms among its various components (land-atmosphere-ocean).

1.3 Natural sea-level variations in the Indo-Pacific Ocean

This thesis is a synthesis of my research on the decadal and multi-decadal sea-level variability in the Indo-Pacific Ocean. In a recent review paper, Han et al. (2014) noted that our understanding of Indian Ocean decadal variability is “primitive” compared to that in the Pacific and Atlantic Oceans. This lack of knowledge was a strong motivation for this research which I initiated in early 2012. Sea-level variations largely reflect low-frequency oceanic variability since

sea level “integrates” subsurface changes across a wide range of spatio-temporal scales, generally driven by or coupled to overlying atmospheric variability. The tropical Indo-Pacific interannual variability is well documented and is dominated by important climate modes rooted in each of these basins: the El Niño Southern Oscillation (ENSO, McPhaden et al. 2006) and the Indian Ocean Dipole (IOD, Saji et al. 1999). The variability associated with these climate modes has been extensively studied over the last couple of decades. As a result, we have a rather good description and understanding of interannual sea-level variations in this region (e.g. Landerer et al. 2008, Clarke and Liu 1994). On the other hand, less is known about Indo-Pacific decadal oceanic variations (Han et al. 2014), primarily because of the lack of reliable, basin-wide sea-level data for sufficiently long periods.

The globally-averaged sea-level rise over the last 50 years can largely be attributed to anthropogenic climate change (Levitus et al. 2000, 2005, Church et al. 2013). At the regional scale, however, there is a much larger influence of natural low-frequency variability on sea-level decadal changes. In the Pacific, for example, the Inter-decadal Pacific Oscillation (IPO) is the main driver of natural decadal sea-level variations and a major contributor to the intensified sea-level rise over the western Pacific during the last two decades (e.g. Merrifield et al. 2012). In contrast, the Indian Ocean still remains as a largely uncharted territory in terms of decadal sea-level variability. Identifying the main patterns of decadal sea-level variability in the Indian Ocean is hence a prerequisite for climate change attribution purposes. This is however a very challenging task because of the temporal and/or spatial limits of sea-level observations in the Indian Ocean. In addition, existing studies indicate that it is difficult to study the Indian Ocean decadal sea-level variability in isolation from that in the Pacific (e.g. Lee and McPhaden 2008, Zhuang et al. 2013). Previous studies have indeed illustrated that Pacific decadal variability can influence the sea level in the Indian Ocean either through the “oceanic bridge” (the Indonesian throughflow that connects these two oceans) or the “atmospheric bridge” (e.g. the influence of equatorial Pacific variability on the Walker circulation which is a common feature of the tropical Indo-Pacific basin).

1.4 Sea-level observation and caveats

Description of observed low-frequency sea-level variability often relies on analysis of sea level from tide gauges and satellite altimetry, which are the most directly available sea-level measurements. Even though some of the tide gauges provide data spanning the entire 20th century, they are located either on islands or in coastal regions and hence do not allow describing open-ocean sea-level variability. Besides, many of the tide gauge records suffer from data gaps (missing data) and the tide gauge measurements are vulnerable to be affected by non-climatic signals like local vertical land movements. Some of these tide-gauges have however been used to describe both coastal and basin-scale decadal sea-level variations (see for example Feng et al. 2004, 2010; Shankar and Shetye 1999).

The modern satellite altimetry offers sea-level measurements with a near-global coverage, which provides insights on the decadal sea-level phase changes in the recent decades (e.g. Lee and McPhaden 2008). The satellite period however only spans twenty years and does not allow a robust description of decadal and multi-decadal sea-level variability. This thesis hence attempts to improve our understanding of the tropical Indo-Pacific low-frequency sea-level variability by a “*holistic*” approach that combines a large set of sea-level data, including available observations, reconstructions/reanalyses and long-term simulations from forced and coupled general circulation models.

1.5 Thesis outline

The main objective of this thesis is to describe and understand tropical Indo-Pacific decadal and long-term sea-level variability.

Chapter 2 is a detailed review of the scientific literature discussing the decadal and multi-decadal Indo-Pacific variability. This chapter is intended to provide a thorough description of the platform on which we stand while considering the research problem taken up in this thesis.

As the duration of satellite sea-level data is too short to have a robust description of the natural decadal sea-level variations, **Chapter 3** will provide a basic description and understanding of the decadal sea-level variability in the tropical Indo-Pacific Ocean using simulations from an ocean general circulation model, which reproduces the observed decadal sea-level variations reasonably well. The results described in this chapter are published in Nidheesh et al. (2013).

In **Chapter 4**, I extended the study described in Chapter 3 by considering an extensive set of observationally-derived sea-level products. The lack of “long” observational data to study the long-term sea-level changes indeed prompted the sea-level science community to reconstruct past sea level from a combination of various ocean data, ocean models and sophisticated statistical techniques. This eventually led to the development of a number of different sea-level reconstructions and reanalysis products that provide global sea-level estimates for at least the past fifty years. Chapter 4 will hence assess the robust features of Indo-Pacific decadal variability among these various products and highlight regions where these products either converge or disagree.

The observational uncertainties in the Indian Ocean inferred from Chapter 3 and Chapter 4 led me to analyse sea-level signals in CMIP (Coupled Model Intercomparison Project) coupled models to see if they can provide some guidance for identifying robust modes of decadal sea-level variability in this region. A prerequisite for this attempt is to evaluate whether the known modes of Pacific decadal climate variability are reasonably reproduced in CMIP models. **Chapter 5** hence assesses the ability of CMIP models to capture the main characteristics of the Interdecadal Pacific Oscillation (IPO) and its signature over the Indian Ocean. Results discussed in this Chapter are in revision in *Climate Dynamics*.

The robustness of Indo-Pacific decadal sea-level variability across CMIP models is discussed in **Chapter 6**. In combination with observational analyses, this Chapter allows to provide an improved description of Indo-Pacific decadal sea-level variability, particularly in the Indian Ocean which is not well sampled in observations. It is worth to note that the fifth phase of the CMIP project (CMIP5) has put a special emphasis on decadal hindcasts and prediction experiments (see Taylor et al. 2012), hence justifying the thorough evaluation of these models undertaken in the current thesis.

Chapter 7 summarises the thesis and states its main perspectives.

State of the art

“Men argue. Nature acts.”

Voltaire

Global warming due to anthropogenic (man-induced) activities is unique in the history of the Earth and humankind and the warming is being accelerated after the industrial revolution. A direct consequence of it is a gradual warming of the world oceans. Thermal expansion of seawater and melting of the continental ice-storage caused by global warming directly translates into a global mean sea-level rise. Satellite-based sea-level measurements since 1992 monitored a global mean sea-level rise by about 6-7 cm during the last two decades (Masters et al. 2012). This sea-level rise is of great concern, as about half of the global population lives within 100km of the sea and most of the large cities in the world are on or near the shore. In brief, mean sea-level rise is a direct consequence of recent global warming that potentially affects a large population living on coasts and islands.

As we have seen in Fig. 1.2, the spatial pattern of sea-level trend is not globally uniform. Sea level rises much faster in certain regions (e.g. western tropical Pacific) than in others (e.g. eastern tropical Pacific). This regional disparity in sea-level trends raises a complex research problem. Regional sea-level trends are indeed a combined response of the ocean and its circulation to both natural climate variability (especially at the longer [decadal and multidecadal] timescales) and anthropogenic climate change. A proper description and understanding of long-term regional sea-level changes hence requires a precise knowledge of sea-level variations induced by natural climate variability over decadal to multi-decadal time scales. Even though a number of climate modes have been extensively described in the literature at interannual timescales during the last few decades, climate variations at decadal timescales and their impact on low-frequency sea-level evolution are not yet properly understood. This is particularly true for the IO, which has for long been one of the least-sampled

oceanic regions in the world. Besides, climate science has largely focussed on the Pacific Ocean over the past few decades owing to the global impacts of ENSO. The present thesis therefore focuses on IO natural decadal climate variability and its connection with the Pacific variability, with a specific focus on sea level. I will start with a brief summary of the key features of the Indo-Pacific climate and sea-level variability over a wide range of time scales.

2.1 Global mean sea-level change

2.1.1 Observations

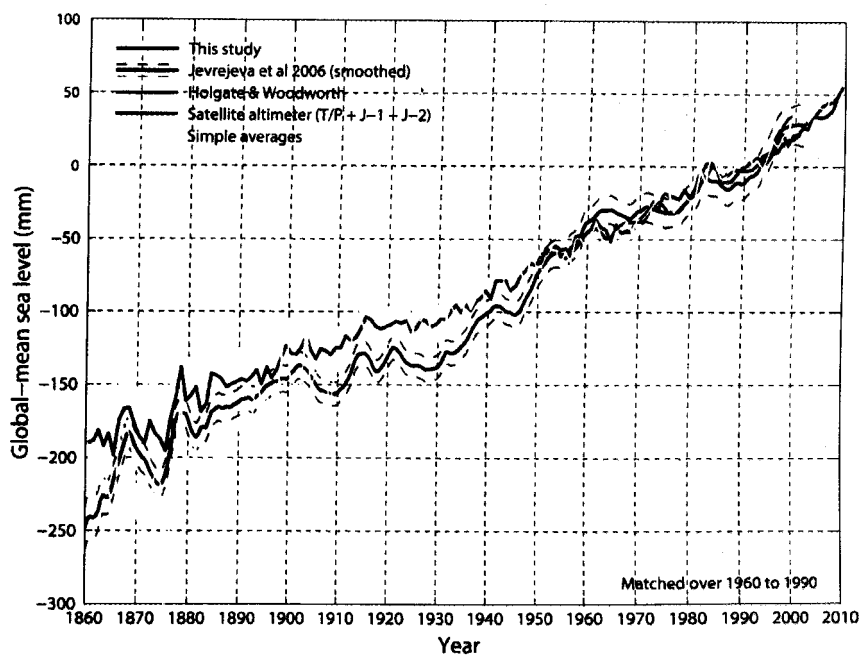


Fig. 2.1: Global average sea level from 1860 to 2009 as estimated from the coastal and island sea-level data (blue) compared with estimates of Jevrejeva et al. (2006, brown), Holgate and Woodworth (2004, red) and from a simple average of the gauges (yellow). The satellite altimeter data since 1993 is also shown in black. These curves clearly show the global mean sea-level rise during the past century. Adapted from Church and White (2011).

The ocean warming induced by climate change directly translates into a sea-level rise by thermal expansion of the water column. In addition, the melting of continental glaciers and ice sheets, further enhances this global mean sea level rise (this process indeed contributes to nearly 40% of the total sea-level rise). This global mean sea-level rise is clearly captured by the estimates made from altimeter measurements (Fig. 2.1), reaching a rate of $\sim 3.2 \text{ mm}\cdot\text{yr}^{-1}$ during the last two decades (1993-2013). After removing the effect of vertical land motion due to global isostatic adjustment, a number of studies also used various strategies to compile and correct the tide gauge data and provided consistent and reliable estimates of the global mean sea-level rise (Fig. 2.1), with a mean sea-level rise trend of $1.7 \pm 0.2 \text{ mm}\cdot\text{yr}^{-1}$ over the 20th century (Church et al. 2013). This rate of sea-level rise over the past century is significantly lower than the rate estimated

oceanic regions in the world. Besides, climate science has largely focussed on the Pacific Ocean over the past few decades owing to the global impacts of ENSO. The present thesis therefore focuses on IO natural decadal climate variability and its connection with the Pacific variability, with a specific focus on sea level. I will start with a brief summary of the key features of the Indo-Pacific climate and sea-level variability over a wide range of time scales.

2.1 Global mean sea-level change

2.1.1 Observations

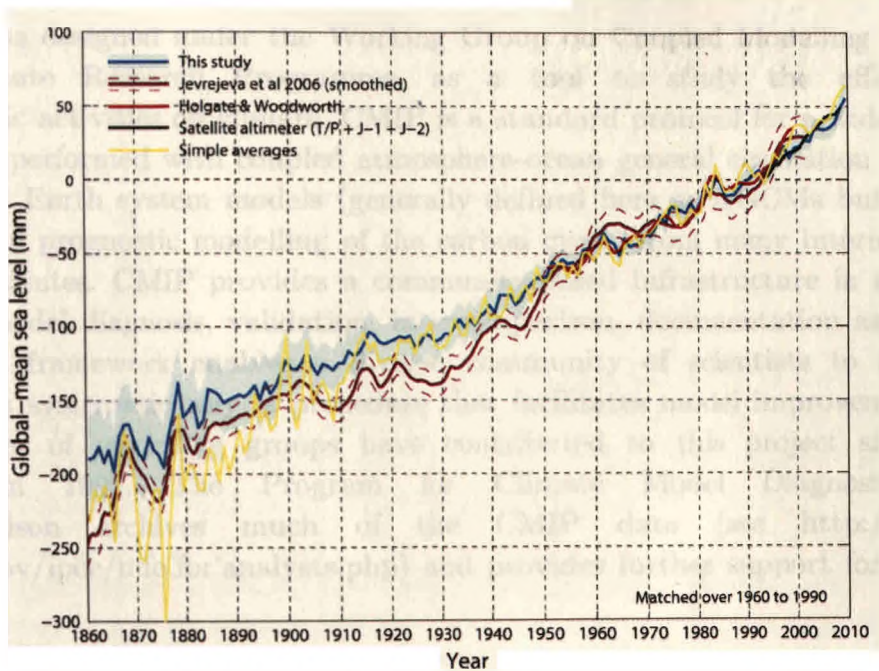


Fig. 2.1: Global average sea level from 1860 to 2009 as estimated from the coastal and island sea-level data (blue) compared with estimates of Jevrejeva et al. (2006, brown), Holgate and Woodworth (2004, red) and from a simple average of the gauges (yellow). The satellite altimeter data since 1993 is also shown in black. These curves clearly show the global mean sea-level rise during the past century. Adapted from Church and White (2011).

The ocean warming induced by climate change directly translates into a sea-level rise by thermal expansion of the water column. In addition, the melting of continental glaciers and ice sheets, further enhances this global mean sea level rise (this process indeed contributes to nearly 40% of the total sea-level rise). This global mean sea-level rise is clearly captured by the estimates made from altimeter measurements (Fig. 2.1), reaching a rate of $\sim 3.2 \text{ mm}\cdot\text{yr}^{-1}$ during the last two decades (1993-2013). After removing the effect of vertical land motion due to global isostatic adjustment, a number of studies also used various strategies to compile and correct the tide gauge data and provided consistent and reliable estimates of the global mean sea-level rise (Fig. 2.1), with a mean sea-level rise trend of $1.7 \pm 0.2 \text{ mm}\cdot\text{yr}^{-1}$ over the 20th century (Church et al. 2013). This rate of sea-level rise over the past century is significantly lower than the rate estimated

over the past two decades (Fig. 2.1). The enhanced rate during recent decades likely results from an accelerated warming of the Earth but could also partly be a signature of natural low-frequency climate variations (Gornitz et al. 1982, Douglas 1991, Miller et al. 2004, Church and White 2006, 2011, Church et al. 2013). The main features of this sea-level rise and its major consequences are well described in the literature (Douglas et al. 2001). The available observational network is hence able to provide an accurate description of the past mean sea-level change but the use of numerical simulations are required to project future sea level rise. These models are further described in the next section.

2.1.2 The Coupled Model Intercomparison Project (CMIP)

CMIP was designed under the Working Group on Coupled Modelling by the World Climate Research Programme, as a tool to study the effects of anthropogenic activities on climate. CMIP is a standard protocol for a wide set of experiments performed with coupled atmosphere-ocean general circulation models (CGCMs) or Earth system models (generally defined here as CGCMs but which also include a prognostic modelling of the carbon cycle) from many international research institutes. CMIP provides a community-based infrastructure in support of climate model diagnosis, validation, intercomparison, documentation and data access. This framework enables a diverse community of scientists to analyse CGCMs in a systematic way, a procedure that facilitates model improvement. A large number of modelling groups have contributed to this project since its inception in 1995. The Program for Climate Model Diagnosis and Intercomparison archives much of the CMIP data (see http://www-pcmdi.llnl.gov/ipcc/info_for_analysts.php) and provides further support for CMIP mission.

CMIP began in 1995 by collecting output from “control simulations” in which climate forcing (i.e. the solar constant and globally-averaged concentration of greenhouse gases and aerosols in the atmosphere) is held constant. Phase 2 of CMIP have collected output from an idealized scenario of global warming, with atmospheric CO₂ increasing at the rate of 1% per year until it doubles after 70 years of simulation. Phase three of CMIP (CMIP3) included a “realistic” scenario for past climate forcing as well as several possible future scenarios for the evolution of climate forcing over the 21st century. In the late 2000’s, the World Climate Research Programme agreed to promote a new set of coordinated climate model experiments similar to CMIP3 but specifically intended to provide a multi-model context for examining climate “predictability” and exploring the ability of models to predict climate on decadal time scales and to determine more generally why similarly forced models produce a range of responses. These new set of coordinated experiments were designed under the fifth phase of the CMIP (CMIP5). More details of CMIP models can be found at [<http://cmip-pcmdi.llnl.gov/>].

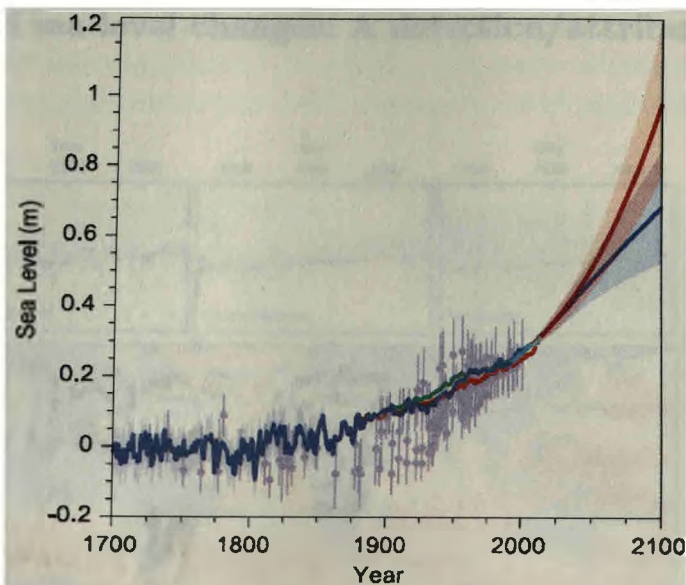


Fig. 2.2: Compilation of paleo sea-level data (purple), tide gauge data (blue), altimeter data (green), and central estimates and likely ranges for projections of global mean sea-level rise for RCP2.6 (very low emissions - blue) and RCP8.5 (very high emissions - red) scenarios, all relative to pre-industrial values. Adapted from Fig. 13.27 of IPCC AR5.

As seen in section 2.1.1, the observed global mean sea level is rising mainly due to thermal expansion and the melting of land-based ice. The observed global mean sea-level rise is within the range of hindcasts by CMIP models over the historical period, giving confidence in future projections from those models. Fig. 2.2 provides the projected evolution of global mean sea level for the 21st century for two emission scenarios (RCP8.5 corresponding to high emission scenario and RCP2.6 corresponding to a very low emission scenario). For the high emission scenario, CMIP5 models predict a global mean sea-level rise by 52-98 cm by the year 2100, which would threaten the survival of coastal cities and entire island nations. Even with a highly optimistic emission scenario, this rise would be about 28-61 cm, with serious impacts on many coastal areas, including coastal erosion and a greatly increased risk of flooding.

As the present thesis focuses on natural low-frequency variability in the Indo-Pacific Ocean, I analysed pre-industrial *control simulations* from the CMIP3 and CMIP5 databases in this thesis. This allows me to assess the *natural* low-frequency (decadal to multi-decadal) climate and sea-level variability which is discussed in the final part of this thesis. As we will see, natural decadal climate variability in the Indian Ocean (and western Pacific) has a much larger amplitude than global sea-level rise due to anthropogenic effects over the past decades, and it is hence very important to improve its description for properly detecting anthropogenic regional sea level rise in the observational record.

2.2 Regional sea-level changes: A detection/attribution problem

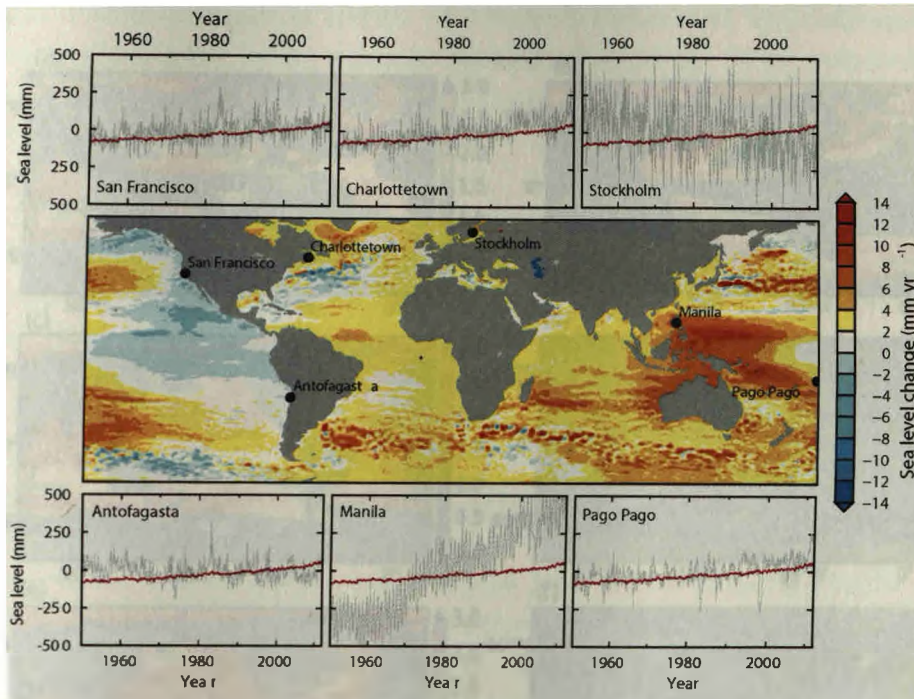


Fig. 2.3: Spatial map of rate of sea level change for the 1993-2012 period from satellite altimetry. Also shown are relative sea-level changes (grey lines) from selected tide gauges for the period 1950-2012. For comparison, an estimate of global mean sea-level change is also shown (red line) with each tide gauge time series. The relatively large, short-term oscillations in local sea level (grey lines) are due to the natural climate variability. For example, the large, regular deviations at Pago Pago (a tide gauge station situated in the central Pacific) are associated with the El Niño-Southern Oscillation. Adapted from the IPCC-AR5 chapter on sea level (Church et al. 2013).

While the global mean sea-level rise has strong societal implications, we will now see that regional sea-level changes can be considerably larger. As shown in Fig. 2.3, the observed sea-level rise over the altimeter period is indeed not uniform over the world oceans. While sea level rises at a faster rate in some oceanic regions, such as the western Pacific and along the west coast of Australia (3-4 times larger than global mean sea-level rise), sea level remains unaltered or even falls in some places, as in the eastern Pacific.

Most of the contrasted regional patterns of the sea-level rise observed in altimetry or reconstructed from tide gauges for the past decades appear to be steric, i.e. due to non-uniform changes/redistribution in temperature and salinity (Levitus et al. 2005, 2009; Ishii and Kimoto 2009). Indeed, changes in the water cycle can result into additional freshwater over the world ocean, but this additional height will spread very quickly uniformly over the globe (at the speed of barotropic waves, i.e. ~ 200 m/s over the deep ocean) and will hence contribute to *global* rather than *regional* sea-level variations. On the other hand, air-sea momentum and heat fluxes variations are associated with spatially variable sea-level changes. For example, the excess surface latent heat flux associated with

global warming penetrates differentially into the ocean depending on, for example, the mixed layer depth and circulation. Similarly, climate change induces changes in surface winds, which will further cause sea-level regional changes.

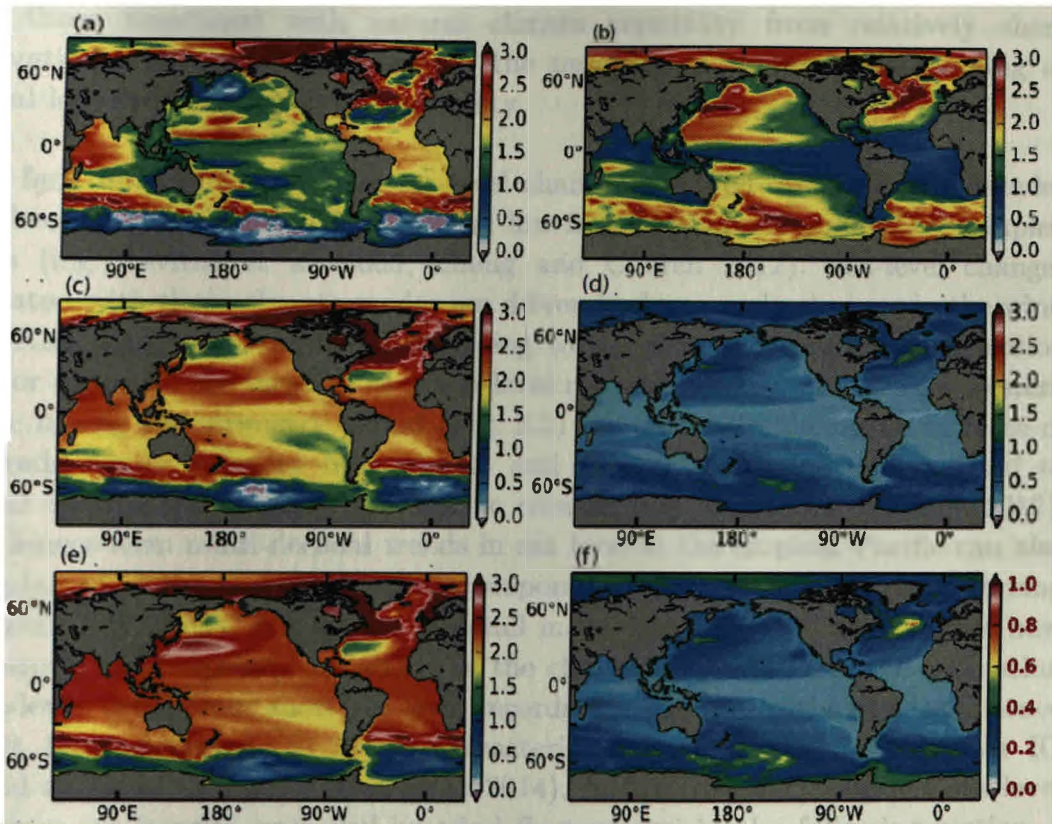


Fig. 2.4: Projected RCP4.5 for 20-yr SLA trend (global thermosteric + dynamic) from the CMIP5 ensemble mean over (a) 20-yr period (2006-2025), (c) 50-yr period (2006-2055) and (e) 100-yr period (2006-2105). Trend uncertainty from control runs: ensemble RMS of individual models' standard deviations of (b) 20-yr trend (d) 50-yr trends and (f) 100-yr trend. Reproduced from Carson et al. (2015).

The left panels in Fig. 2.4 display the ensemble sea-level trends from 21 CMIP5 models (see Carson et al. 2015 for more details) estimated over a 20-yr, 50-yr and 100-yr periods. These projections reveal a clear regional pattern in sea-level changes, with complex ridge-and-trough patterns superimposed on a generally rising sea level. For instance, the reduced sea-level rise in the South Pacific has been attributed to wind-induced redistributions of upper-ocean water, which plays a key role in establishing the spatial characteristics of projected regional sea-level rise (Timmerman et al. 2010). The much slowly occurring sea-level changes associated with anthropogenic forcing superimpose themselves on much faster regional patterns associated with natural climate variability. The right panels of Fig. 2.4 provide an estimate of the amplitude of these naturally driven sea-level (i.e. the “noise”) relative to that of the sea-level patterns induced by anthropogenic forcing (left panels of Fig. 2.4, i.e. the “signal”). This figure clearly illustrates that the signal is considerably larger than the noise everywhere when considering the entire 21st century but the internal variability largely dominates the anthropogenic signal on shorter time scales (~20 yr). Although the

mean trend (mean sea-level change) is generally larger than the natural variability in most of the places at 50 yr period, the internal variability can still significantly contribute to the trend. This is an illustration of the difficulty to distinguish precisely regional trends in sea level associated with climate change from those associated with natural climate variability from relatively short observational records, and underlines the necessity of proper understanding of natural low-frequency sea-level variability.

In fact, most of the regional sea-level changes observed during recent decades have been largely attributed to natural low-frequency ocean-atmosphere coupled modes (e.g. Levitus et al. 2005, Zhang and Church 2012). Sea-level changes associated with those climate modes are driven by large-scale changes in the wind field (Kohl and Stammer 2008), according to the principles presented in section 2.3. For example, the large rates of sea-level rise observed in the tropical western Pacific during the altimetry period (Fig. 2.3) are partly driven by an increase of the trade winds intensity over central and eastern tropical Pacific related to natural decadal variations of the Pacific climate (e.g. Zhang and Church 2012). Even longer-term multi-decadal trends in sea level in the tropical Pacific can also be explained as the ocean's dynamical response to variations in the wind forcing (Qiu and Chen 2006). We will see in detail in the last section of this chapter how the natural low-frequency variability of the climate system aliases the estimation of sea-level trend from short sea-level records like satellite altimetry, and hence why it is so necessary to better characterize the so-far largely unknown IO decadal sea-level variability (Han et al. 2014). As low-frequency regional sea-level variations are largely controlled by wind fluctuations, in the following section, I briefly summarise some of the fundamental concepts that allows to understand the observed regional low-frequency sea-level variability.

2.3 Regional sea-level variability: Theoretical considerations

The variability seen in an instrumental record of sea level (either for coastal or open ocean) actually reflects interactions of many components including the ocean, atmosphere and land (coasts and islands). As a result, describing sea-level variability for a given region often relates to the dynamics and thermodynamics of ocean and atmosphere.

The nature and underlying processes that cause sea-level change is not homogeneous in time and geographically. Sea surface undergoes continuous deformations from tropics to higher-latitudes and from daily to decadal time scales¹. For example, Fukumori et al. (1998) described the large-scale sea-level variability in a modelling framework and showed that, while mid-latitude sea-level variability is primarily associated with density variations of the oceanic upper layer by the seasonal heating (i.e. steric sea-level changes associated with

¹ In a theoretical point of view, sea level varies at "all" time and space scales. However, this thesis focuses those changes occur over Earth's climatic time scales i.e. above annual time scales to a first approximation.

the thermodynamics of the mid-latitude air-sea interactions), sea-level variability is mainly wind-driven in the tropics. This wind-driven natural low-frequency sea-level variability in the tropical Indo-Pacific is the main focus of this thesis. In fact, wind-driven sea-level variability has a strong dependence on latitude: this variability is largely baroclinic (i.e. sea-level changes mostly associated with ocean density changes) in the tropics but barotropic (i.e. sea-level changes mostly associated with mass convergence/divergence over the entire depth) at higher latitudes (refer to Fig. 12 of Fukumori et al 1998). I provide some basic dynamical formulations below, which depict the low-frequency sea-level variations associated with wind changes in both equatorial and extra-equatorial regions.

In extra-equatorial regions, the open ocean low-frequency sea-level variability can be largely explained by westward propagating Rossby waves (either radiated from the eastern boundary of the basin and/or induced by wind-driven Ekman pumping in the interior part of the ocean). Considering the long-wave approximation², these processes can be quantified through a 1.5-layer reduced gravity model (i.e. a model in which the deep ocean is assumed to be at rest and the upper ocean in motion which stands for the layer above the thermocline in the real ocean; e.g. Qiu, 2002, Qui and Chen 2006), which is governed by the linear vorticity equation:

$$\frac{\partial h}{\partial t} - C_r \frac{\partial h}{\partial x} = -g' \nabla \times \frac{\tau}{\rho_0 g f} - \Gamma h \quad (1)$$

where,

$$g' = g(\rho_2 - \rho_1)/\rho_0 \quad (\text{reduced gravity}) \quad (2) \quad \text{and,}$$

ρ_1, ρ_2 are the density of the upper and lower layers respectively, h is the baroclinic component of sea level (perturbations on the *undisturbed* sea surface), C_r is the zonal phase speed of the long baroclinic Rossby wave, τ is the anomalous wind-stress vector, ρ_0 is the ocean reference density, f is the Coriolis parameter and Γ is the Newtonian damping coefficient. Integrating (1) westward from the eastern boundary (x_e) gives the following solution:

$$h(x, y, t) = h\left(x_e, y, t + \frac{x - x_e}{C_r}\right) \exp\left[\frac{\Gamma}{C_r}(x - x_e)\right] \\ + \frac{1}{\rho_0 g f} \int_{x_e}^x \frac{g'}{C_r} \nabla \times \tau\left(x', y, t + \frac{x - x'}{C_r}\right) \exp\left[\frac{\Gamma}{C_r}(x - x')\right] dx' \quad (3)$$

² Rossby waves with small zonal and meridional wave number and long wave length (approaching the origin of the wave dispersion graph) can be treated as non-dispersive (i.e. frequency = constant*k) and propagate westward at the speed $C = C_g = -\beta L_r^2$ (where L_r = Rossby radius). Assuming typical parameters to estimate L_r at 20N yields $L_r = 50\text{Km}$ (and less at higher latitudes) and the phase speed of long Rossby waves at this latitude is $\sim 5\text{cm/s}$. It would take around 6 years for these waves to cross 10,000 km, typical distance of Pacific Ocean at 20N. This leaves enough time for tropical Oceans to adjust to forcing over decadal time scales and to attain a quasi-steady state. This useful limit where the wave speed is fast compared to the time scales under consideration is known as "fast wave" limit (e.g. Neelin 1990).

The first term on the right-hand side of (3), (say F1), represents sea-level signals propagating westward from the eastern boundary at a Rossby wave speed C_r and the second term on the right-hand side (say F2) represents Rossby waves forced by the interior wind stress curl. This equation essentially provides the total sea-level response of the basin to a given wind forcing over the basin, away from the equator. In this thesis, we do not extensively discuss the influence of signals radiated from the eastern boundary (the F1 term) but demonstrate that decadal sea level variations are generally well explained by the F2 term, i.e. with decadal wind forcing in the basin interior, which propagate further west as Rossby waves.

A good approximation for the phase speed of long Rossby wave is:

$$C_r = \beta c^2 / f^2 = c^2 / (\beta y^2) \quad (4)$$

where $\beta = df/dy$ is the meridional gradient of f , y is latitude and c is the characteristic speed (speed of first mode baroclinic Kelvin wave generally approximated to be ~ 2.5 m/s in these kind of models; see McCreary 1983 for example). Equation (4) shows that Rossby waves propagate more slowly at higher latitudes. The mid-latitude oceanic adjustment to a given wind forcing hence requires longer time than that near the equator (i.e. the ocean requires much more time to reach a steady state). However within the tropics, the oceanic Rossby waves travel much faster. Equatorial Kelvin and Rossby waves can, for example, go back and forth (in two different forms) across the equatorial Pacific in about 2-9 months, i.e. a time period that is much shorter than decadal wind variations. The travel time of waves can thus be neglected at those time scales (an approximation which is usually known as the “fast wave limit”) and one can consider that the ocean response is quasi-steady (i.e. a steady state balance between the pressure gradient and the force exerted by the wind on the ocean) on time scales greater than a year (Philander 1979).

Under the assumption of no local acceleration (i.e. $\frac{\partial}{\partial t} = 0$) and no wind-stress curl in the vicinity of the equator, the governing equations of the reduced gravity model discussed above reduces to much simple forms (see Clarke 2008) that yield $(u, v) = 0$; it implies that there is no horizontal flow in the absence of surface wind-stress curl. This further gives:

$$g'h_x = -\tau^x / (\rho_o H_1) \quad (5)$$

where h is the thermocline displacement (anomaly) and H_1 is the depth of the top layer (mixed layer). τ_x is the zonal wind-stress anomaly. (5) can also be written in terms of sea-level gradient using the model expression:

$$\text{sea level displacement } (\eta) = -\varepsilon h \quad (6); \text{ where, } \varepsilon = (\rho_2 - \rho_1) / \rho_o.$$

So that, (5) becomes, in terms of sea-level gradient:

$$\rho_o g \eta_x = \tau^x / H_1 \quad \text{i.e.} \quad \eta_x = \frac{1}{\rho_o g} \left(\frac{\tau^x}{H_1} \right) \quad (6)$$

Expression (6) describes a balance between the force exerted by the wind stress on the ocean and the pressure gradient. For instance, one expects the average eastward wind-stress found along the equatorial Indian Ocean on an annual average to tilt the sea level up toward the east (end to tilt the thermocline down in the proportions given by equation 6). We can summarise that, when the forcing time scales are larger compared to wave propagation across the basin, the ocean response is quasi-steady, and the zonal pressure gradient balances the zonal wind-stress forcing. As a first approximation, one thus expects the equatorial zonal sea-level gradient to be proportional to decadal zonal wind-stress variations. In the following chapters, we will find results that are consistent with this simple theory.

2.4 Tropical Indo-Pacific annual mean state

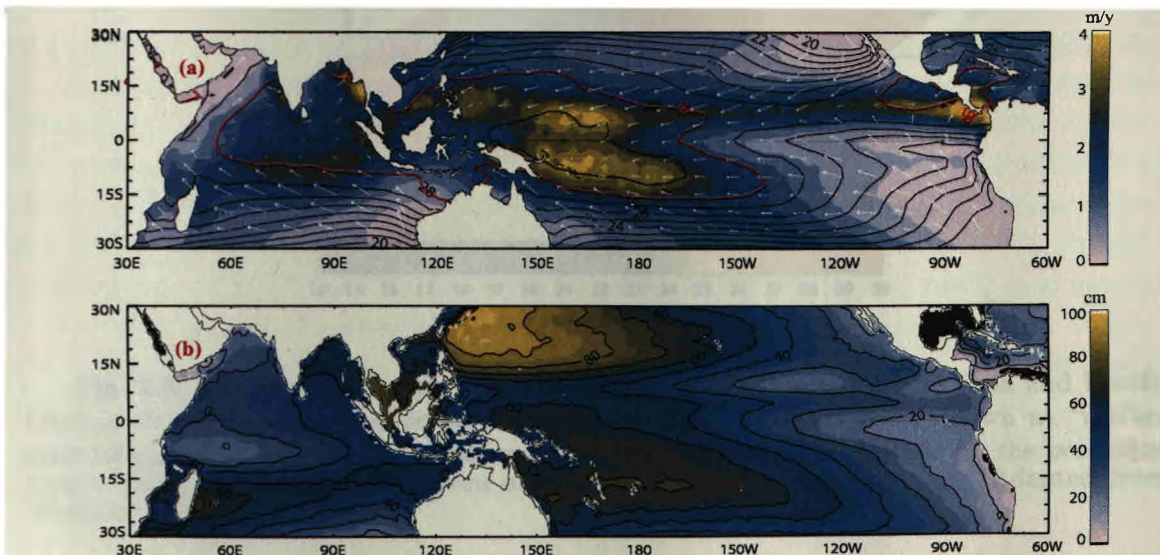


Fig. 2.5: (a) Annual-mean sea-surface temperature (SST, contour), wind stress (vector) and precipitation (shade) in the tropical Indo-Pacific Ocean (30E:290E; 30S:30N). Annual-mean SST is more than 28°C in the western Pacific and eastern IO, a region collectively known as “Indo-Pacific warm pool” (region bounded by the 28°C isotherm as shown by red contours on panel a). The warm pool drives deep atmospheric convection and the region is wetter than other parts of the basin. Annual mean easterlies over the tropical Pacific and westerlies over the equatorial IO blow toward this warm pool. The mean position of the Inter-tropical Convergence Zone (ITCZ) in the tropical Pacific can be seen as a band of maximum precipitation (~5-10N) where trades from both hemispheres converge. (b) Mean dynamic topography over the tropical Indo-Pacific during 1993-2002 as observed from satellite altimetry. HadISST, wind stress and precipitation from 20CR and dynamic height from altimeter during 1993-2013 are used to produce this figure.

The tropical western Pacific and eastern IO host the warmest surface waters in the world ocean, with annual mean SST above 28°C (Fig. 2.5a). This threshold is a necessary condition for maintaining deep atmospheric convection above the ocean (Gadgil et al. 1984, Graham and Barnett 1987). The Indo-Pacific ‘warm pool’ hence maintains an almost permanent deep-atmospheric convection on top

of it, whose mid-tropospheric heating drives surface easterlies over the eastern and central Pacific and annual-mean westerlies over the western and central IO (e.g. Gill, 1982). The deep atmospheric convection above the warm pool supports a 'net upwelling' of air masses over this region. The circulation is closed by upper tropospheric westerly flow over the Pacific and easterly flow over the IO. This large-scale east-west overturning circulation is known as the *Walker circulation* (Fig. 2.6, Bjerknes 1969). As seen in equation (5), the westward surface equatorial easterlies make the thermocline deeper in the western Pacific and shallower in the eastern Pacific, with an opposite annual mean-slope in the IO (figs. 2.5a and 2.6). Thus, the existence of the Indo-Pacific warm pool can be understood as consequence of the equatorial easterlies in the Pacific and westerlies in the IO that pile up warm waters on either side of the maritime continent.

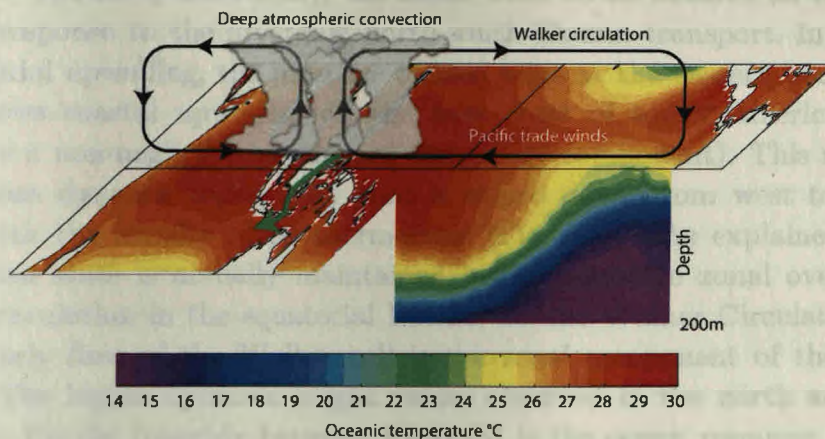


Fig. 2.6: Two zonal atmospheric circulation cells in the equatorial Indian and Pacific Oceans driven by deep convection over the Indo-Pacific warm pool, known as “Walker circulation”. The warm water piled up in the western equatorial Pacific by the persistent trade winds flow toward IO (green arrow) via Indonesian through flow. Adapted from Vialard (2015).

Through its impact on the Walker circulation, the warm pool influences a large domain on both sides of it (~29,000 km), bridging the tropical Indian and Pacific Oceans together (Bjerknes 1969). We will see in the following chapters that the interannual variability in the tropical Pacific induces a zonal shift in the Walker circulation, thereby inducing anomalous convection or subsidence over it and influences the IO sea surface temperatures (e.g. Klein et al. 1999, Lau and Nath 2000). This is known as the 'atmospheric bridge' between the Indian and Pacific Oceans. In the equatorial band (say 5S-5N), the westward forcing by the prevailing Pacific easterlies is, to the first order, balanced by a zonal tilt in thermocline and sea level. Since the winds are stronger and have a longer zonal fetch in the Pacific, the thermocline (steric height) is deeper (higher) in the western equatorial Pacific than in the eastern IO (Fig. 2.5b). The resulting pressure gradient drives a flow from the western Pacific to the eastern equatorial IO (to the south of ~9S in the southeast IO; see Clarke 2008 for a dynamical consideration) through a gateway of narrow deep sills in the Indonesian

Archipelago called the *Indonesian Throughflow* (ITF, Fig. 2.6). This ocean tunnel has profound importance in shaping the Indo-Pacific climate variability, especially at long time scales as the ITF transports a significant amount of warm water and heat from the Pacific to the IO (e.g. Wijffels et al. 2008, England and Huang 2005). At the same time, the thermocline and sea-level anomalies (SLA) in the western equatorial Pacific are also transmitted to the southeast IO through coastally trapped waves (Feng et al. 2004, 2010). As we will see in the coming chapters, the variability of the western Pacific can thus be transmitted to the southeast IO via the Indonesian throughflow in the form of both mass transport and oceanic waves. This is known as the 'oceanic bridge' between the Indian and Pacific Oceans.

Surface easterlies prevail in the tropical Pacific throughout the year. In the vicinity of the equator ($\sim 2.5^{\circ}\text{N}$ - 2.5°S), the zonal wind stress induces an equatorial upwelling in response to the diverging north-south Ekman transport. In addition to this equatorial upwelling, the presence of land mass at the eastern boundary of the basin allows coastal upwelling off the west coast of south America (where easterlies have a non-negligible northward alongshore component). This results in an annual mean dynamic topography that is sloped down from west to east in accordance with the zonally tilted thermocline (Fig. 2.5b). As explained above, the mean ocean state is actually maintained by a large-scale zonal overturning atmospheric circulation in the equatorial Pacific, i.e. the Walker Circulation. The low-level easterly flow of the Walker cell is the zonal component of the Pacific trade winds. The higher dynamic height values observed in the north and south of the western Pacific (roughly between 10 - 30°NS) is the ocean response to large-scale negative wind-stress curl generated by trade winds and mid-latitude westerlies over the interior ocean. The convergence and downward Ekman pumping causes sea surface to "bump" in the interior ocean, which gradually propagate westward as Rossby waves (see section 2.3) and induce positive sea-level anomalies in the western boundary as seen in Fig. 2.5b.

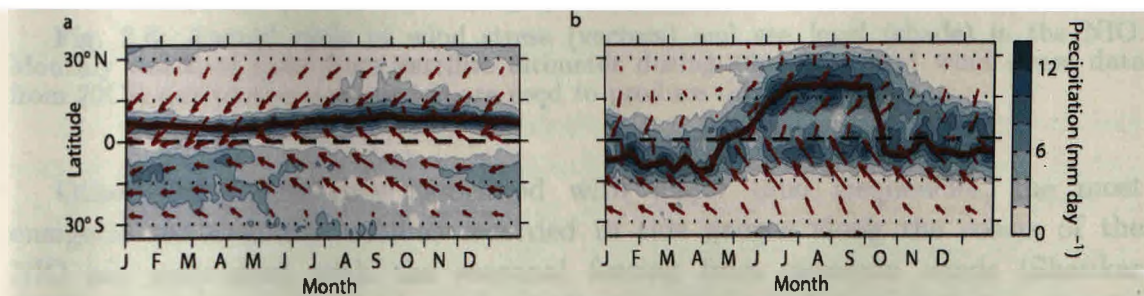


Fig. 2.7: Seasonal migration of the ITCZ over the Pacific and in the south Asian monsoon sector. (a) Mean precipitation (colour) and surface winds (vector) as a function of months averaged zonally over the Pacific. The ITCZ (precipitation maxima) is highlighted by red line. The seasonal migration of ITCZ is rather weak over the Pacific, with zonal winds remaining easterly year-round. (b) Same for the IO. There are abrupt and large shifts of ITCZ marking the onset and retreat of summer monsoon, with zonal wind north of the equator shifting to westerly during the monsoon onset. However, south IO experiences easterly winds year-round. This seasonal migration of ITCZ and reversing winds constitute a strong seasonal cycle in the north IO with marked changes in currents and sea level. Adapted from Schneider et al. (2014).

The position of ITCZ remains nearly steady (centred around 5-10N) in the Pacific Ocean over the course of the year (Fig. 2.7a). This ITCZ is associated with converging trade winds and precipitation maxima (Waliser & Gautier 1993; Philander et al. 1996). The scenario is strikingly different in the IO. Generally, the Indo-Pacific warm pool induces westerlies in the equatorial IO that deepen the thermocline in the east and cause it to shoal in the west. During May-September, the ITCZ shifts northward dramatically (nearly up to 20N) and shifts southward during November-February. These two periods are characterised by southwesterly and northeasterly winds in the north IO (NIO) respectively, characterizing two distinct monsoon systems (the summer and winter monsoon, Gadgil et al. 1984). The wind reversal during these two periods drives a reversal of the circulation in the equatorial and NIO. This seasonal reversal in surface circulation is a very unique feature of the NIO, not observed in any part of the world ocean (Schott and McCreary 2001, Shankar et al. 2002). However, the zonal winds in the equatorial IO (EIO) are weak during the monsoons while relatively strong westerlies develop in the EIO during the transition periods of these two monsoons, i.e. during spring (April-May) and fall (October-November). These westerlies drive strong eastward equatorial currents in the IO known as Wyrtki (1973) jets, whose speed generally exceeds 1 m.s^{-1} . These strong currents accumulate warm water and deepen the thermocline in the eastern EIO. Hence climatologically, the eastern EIO is warmer, and associated with higher SST, heat content and deeper mixed layer than the western EIO. Consequently, the atmosphere above the eastern EIO experiences more deep convection than that in the west.

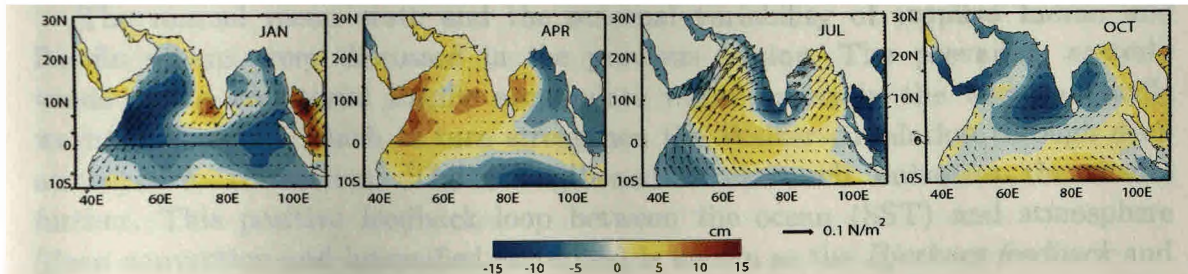


Fig. 2.8: Annual cycle of wind stress (vectors) and sea level (shade) in the NIO. Monthly sea-level data from satellite altimeter during 1993-2013 and wind stress data from 20CR during the same period are used to produce this figure.

Other than variability associated with major tidal frequencies, the most energetic sea-level fluctuations recorded in tide gauges along the coasts of the NIO are associated with the seasonal forcing from monsoon winds (Shankar 2000). Seasonal sea level along the Indian coasts and the associated seasonally reversing coastal currents are not well correlated to the local along-shore winds, because they are partly driven remotely through coastal Kelvin waves. The unique geometry of the Indian Ocean indeed allows equatorial Kelvin waves induced by the EIO wind stress variations to propagate into the entire NIO coastal waveguide when they hit the eastern boundary. This observation led to the development of a dynamic framework for the north IO coastal currents and sea level that consider the equatorial IO, the Bay of Bengal (BoB) and the

Arabian Sea (AS) as a 'single dynamical entity' (Shankar 2000). Remote forcing by the seasonally reversing monsoon winds over the EIO is a key feature of the north IO seasonal sea-level variations. The seasonal basin-scale sea-level signals shown in Fig. 2.8 are largely the result of the integration of wind forcing (zonal wind at the equator and wind curl away from it), with some non-local effects due to planetary wave propagation (e.g. McCreary et al., 1993). During winter (Fig. 2.8a), the downwelling signal observed at the southern tip of India is, for example, opposed to the effect of alongshore wind forcing. This signal is indeed results from remote forcing from the BoB, that propagate counter clockwise along the coasts as a coastally-trapped Kelvin wave. This signal further extends northward along the Indian west coast as downwelling coastal Kelvin waves, and eventually radiate westward into the Arabian sea as Rossby waves. On the other hand, the shallow thermocline along the eastern and northern rim of the Bay of Bengal results from remote forcing by the equatorial westerlies in October–December that yields an equatorial upwelling Kelvin wave that propagates into the BoB as coastally trapped Kelvin wave. Sea-level patterns in summer (Fig. 2.8c) are usually opposite to those found during the winter season (Figure 2.8a). In particular, the summer alongshore winds off Java and Sumatra induce coastal downwelling and high sea level (readers may refer to Shankar (1998) for a comprehensive description of NIO seasonal variability based on sea level).

2.5 Indo-Pacific interannual climate and sea-level variability

2.5.1 The El Niño Southern Oscillation

The annual mean state and the seasonal variability of tropical Indian and Pacific oceans were discussed in the previous section. The prevailing easterly winds in the equatorial Pacific accumulate warm waters in the western Pacific warm-pool region, which in turn strengthen the Walker circulation through deep atmospheric convection. The strengthened Walker cell enhances the trades further. This positive feedback loop between the ocean (SST) and atmosphere (deep convection and intensified easterlies) is known as the *Bjerknes feedback* and is at the heart of the El Niño–Southern Oscillation (ENSO) phenomenon.

ENSO is the most prominent interannual fluctuation of the tropical climate system and impacts weather patterns across the globe (McPhaden et al. 2006a). ENSO arises from air-sea interaction in the tropical Pacific, and results in positive (El Niño) or negative (La Niña) SST anomalies in central eastern-tropical Pacific, with anomalous deep atmospheric convection, rainfall and surface wind in the western/central Pacific (Fig. 2.9a). ENSO temporal evolution is not a perfectly periodic and display irregularities. The temporal and spectral characteristics of ENSO however display the most energetic fluctuations at ~2-7 years time scales. A robust feature of the warm ENSO events is the tendency for their peak to preferentially occur in boreal winter, that is, from November to January (Rasmusson and Carpenter 1982; Harrison and Larkin 1998).

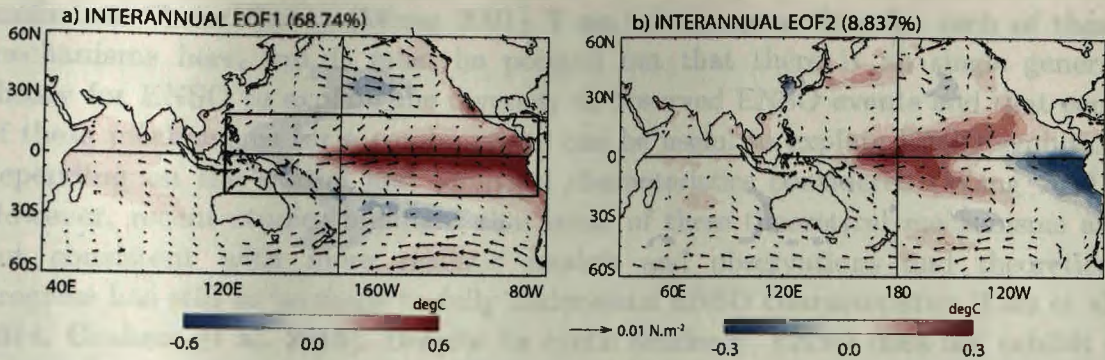


Fig. 2.9: (a) First and (b) second EOF pattern of interannual SST anomalies over the tropical Pacific (120E-290E, 20S-20N; shown by a black rectangle on (a)). The percentage of variance explained by each mode is shown on top of each panel. Though the EOFs are performed over the tropical Pacific, spatial patterns are shown for the entire Indo-Pacific domain by regressing the SST and wind anomalies onto normalized PCs. The first EOF represents typical canonical ENSO events while the second EOF is representative of ENSO Modoki events (see text). HadISST and wind stress from 20CR for the period 1960-2010 are used to produce this figure.

Even though the mechanism of the initiation of an El Niño event is still debated, climate scientists have a good understanding on the mechanisms driving the El Niño growth and decay once the event gets started (McPhaden 2006). An El Niño event grows as the result of the Bjerknes ocean-atmosphere feedback. In essence, the Bjerknes positive feedback (between warm SST anomalies in the central-eastern Pacific and westerly wind anomalies in the western Pacific) provides the necessary instability for an El Niño to grow: a positive SST anomaly in the central Pacific induces an increase in deep atmospheric convection and westerly wind anomalies in the central/western Pacific (e.g., Gill 1980). The eastward surface current and deeper thermocline response to this wind anomaly in turn reinforces the initial warming. Observational analysis and modelling studies indeed suggest that zonal advection of warm surface waters from the west contributes significantly to the SST anomalies in the central Pacific while vertical movements of the thermocline dominate the SST changes in the east (Gill 1983; Fu et al. 1986; McPhaden and Picaut 1990; Picaut and Delcroix 1995; Picaut et al. 1996). This eventually leads to the development of an El Niño event, usually peaking towards the end of the calendar year. This positive feedback mechanism is offset by several negative feedbacks: the instantaneous negative feedback from air to sea fluxes (e.g. Lloyd et al. 2010), non-linear interactions of convective anomalies with the seasonal cycle (e.g. Lengaigne et al. 2006) and delayed negative feedbacks from ocean dynamics (e.g. Boulanger et al. 2004).

However, favourable grounds are needed for the Bjerknes feedback to be able to result in an El Niño. The role of the tropical Pacific heat content, initially suggested by Wyrtki (1975), is now widely recognized under the framework of the discharge/recharge oscillator, which is the most widely accepted conceptual paradigm to explain ENSO cycle today (Jin 1997a,b). There are, of course, other mechanisms proposed to explain ENSO, including the western Pacific Oscillator (Wang et al. 1999), the advective-reflective oscillator (Picaut et al. 1997) and the

unified oscillator theory (Wang 2001). I am not going to describe each of these mechanisms here, but it must be pointed out that there is no single general theory for ENSO to explain the diversity of observed ENSO events and that each of these mechanisms (or a combination) can be useful to explain ENSO evolution depending on the spatial and temporal characteristics considered (Wang 2001). However, recent studies highlight that some of these theoretical mechanisms are not consistent with more realistic models and observations and theoretical progress has still to be made to fully understand ENSO characteristics (Linz et al. 2014, Graham et al. 2015). Despite its cyclic tendency, ENSO does not exhibit a periodicity, but can be rather viewed as a damped harmonic oscillator forced by stochastic noise (e.g. Jin et al. 2007, Linz et al. 2014). In addition, the non-linear processes involved in ENSO dynamics favour stronger El Niños than La Niñas events (e.g. Larkin and Harrison 2002, An and Jin 2004). A more detailed description of the dynamics of ENSO may be found in Clarke (2008).

Observations since the 1970's showed frequent warm episodes in the equatorial Pacific, which differ from canonical El Niño events. During these events, the maximum warming does not occur in the eastern Pacific (Niño3.4 region)³, but in the central Pacific. An Empirical Orthogonal Function (EOF) analysis of interannual SST during this period reveals these warming events as the second mode of variability (the first mode being the canonical ENSO) as shown in Fig. 2.9b. The central Pacific warming (second mode of interannual SST) has been given various names such as “El Niño Modoki” (meaning *pseudo-El Niño* in Japanese; Ashok et al. 2007), central Pacific El Niño (Kao et al. 2009), warm pool El Niño (Kug et al. 2009) etc. I will refer to ENSO for canonical ENSO (Fig. 2.9a) and Modoki for second interannual mode (Fig. 2.9b) in this thesis for both interannual and decadal time scales⁴. Modoki events have been shown to have specific global teleconnection patterns of SST and precipitation anomalies (Ashok et al. 2007, Trenberth 2001, Wang et al. 2007). Even though Modoki has been viewed as a coupled phenomenon distinct from ENSO in some studies (Ashok et al. 2007, Wang et al. 2007), the current view considers these two phenomenon as “different flavours” of the same climate mode (see review of Capotondi et al. 2015), with Modoki being viewed as moderate El Niño events associated with a mild eastward displacement of the warm-pool eastern edge (as compared to

³ Niño3.4 region is classically defined as the region of maximum warming during an El Niño in the equatorial Pacific. The geographic boundaries of this oceanic region are [120W:170W; 5S:5N]. Time series of monthly SST anomalies averaged over Niño3.4 region (known as Niño3.4 index) is being widely used as an index for ENSO variability in the literature.

⁴ Based on the tripolar structure of the El Niño Modoki, Ashok et al. (2007) derived an index for this mode by averaging SST anomalies over three regions in the tropical Pacific. (i.e. El Niño Modoki Index, $EMI = [SSTA]_A - 0.5*[SSTA]_B - 0.5*[SSTA]_C$). Where A [165E–140W, 10S–10N], B [110W–70W, 15S–5N] and C [125E–145E, 10S–20N] are the geographic coordinates considered to average the SST anomalies. This definition of EMI is used in chapter 4 of this thesis.

extreme El Niño; Takahashi et al. 2011). In this paradigm, Modoki is considered merely a part of ENSO diversity within an ENSO continuum.

Even though ENSO develops in the equatorial Pacific, its influence extends far beyond, through both oceanic and atmospheric teleconnections. The warming of the central equatorial Pacific during an El Niño is associated with an eastward shift of deep atmospheric convection over the equatorial Pacific. The anomalous convection during warm and cold phases of ENSO affects the equatorial Pacific atmospheric temperature and winds. On average, the tropical troposphere (approximately the lower 17 km of the atmosphere) warms by about 0.5°C all around the Earth during warm ENSO phase through anomalous latent heat release (Horel and Wallace 1981; Yulaeva and Wallace 1994). This atmospheric heating associated with ENSO has profound implications on the global atmospheric circulation and heat transport from tropics to higher latitudes. This is illustrated in Fig. 2.9a, which shows the SST and wind-stress anomalies associated with the warm phase of canonical ENSO events over the entire Indo-Pacific ocean. The excess heat and momentum fluxes in the upper atmosphere is channelled toward higher latitudes as atmospheric Rossby waves that are “guided” by the zonal mean atmospheric circulation. These fluxes deepen the extra-tropical low pressure systems and strengthen the mid-latitude westerlies over the North and South Pacific (Fig. 2.9a). The enhanced mid-latitude westerlies result in negative SST anomalies in the north and south Pacific (i.e. the well known “horseshoe” pan-Pacific SST pattern of El Niño), a remote oceanic response driven by El Niño teleconnections (Bjerknes 1969, Alexander 1990; Lau and Nath 1994; Lau and Nath 1996; Alexander et al. 2002).

Zonal movements of the Pacific Walker circulation during ENSO influence other tropical Ocean basins too (e.g. Klein et al. 1999; Lau and Nath 2000). The atmosphere, in fact, acts like a bridge that connects the tropical Pacific variability to sea-level pressure and surface wind variations in other tropical oceanic regions, leading to significant heat flux and SST signature of El Niño (e.g. Zhang et al. 1997). An eastward shift and weakening of the Pacific Walker cell induces anomalous subsidence in the tropical IO and thus weakens the IO Hadley cell (Klein et al. 1999). This anomalous subsidence reduces the surface wind speed and upward latent heat flux in the tropical IO basin and the reduced cloudiness allows more solar radiation to reach the ocean surface and eventually sea surface warms (Fig. 2.9a, Klein et al. 1999, Lau and Nath 2000, Ohba and Ueda 2005). This mode of SST variability (surface warming/cooling of the tropical IO following El Niño/La Niña in the Pacific) is known as the IO Basin-wide warming Mode (IOBM) (Klein et al. 1999; Ohba and Ueda 2005, 2009b), which can be maintained until the following summer by local air-sea interactions (e.g. Xie et al. 2009).

2.5.2 The Indian Ocean Dipole (IOD)

The annually reversing monsoon winds in the IO have prompted the oceanographers worldwide to test the concepts of the prevailing dynamical theories in the IO in the 1970's and 80's. For example, the equatorial linear wave theory was found to be a good candidate to explain many of the observed circulation features in the IO like Wyrtki jets (Wyrtki, 1973) or the reversing Somali current (Lighthill, 1969). ENSO has been known for long to influence the tropical IO (e.g. Walker 1924). However, until the late 1990's, the IO was widely considered as a climatically passive ocean with little influence on the global climate variability. Reverdin et al. (1986) was the first to suggest a possible ocean-atmosphere feedback loop in the IO in boreal fall, with strong interannual zonal wind anomalies related to opposite precipitation anomalies in the western and eastern IO. This led at the turn of the century to the discovery of an intrinsic mode of climate variability in the Indian Ocean, now known as the Indian Ocean Dipole or the IOD (Saji et al. 1999, Webster et al. 1999, Murtugudde et al. 2000).

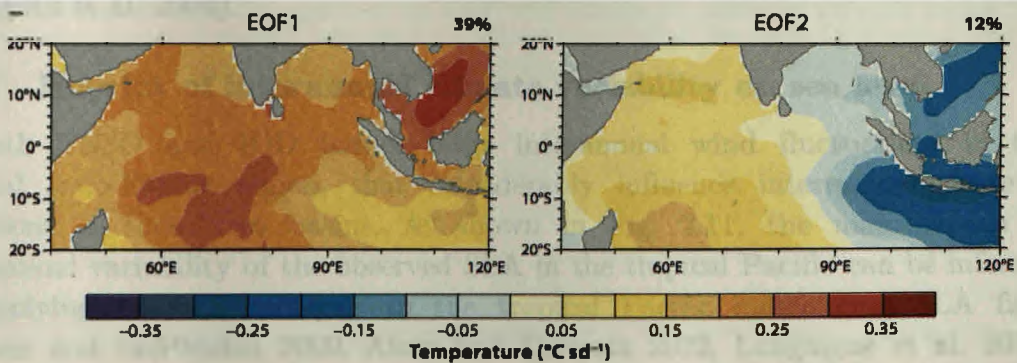


Fig. 2.10: First two leading modes EOF of monthly SST anomalies in the tropical IO: the first mode (left panel) shows a basin-wide warming signal often referred as the 'IO Basin Mode (IOBM)', and the second mode (right panel) is a *dipole* structure typical of the IOD signature. While the IOBM is largely a remote response to ENSO, the IOD is an "intrinsic" mode of the IO basin, that can occur independently of an El Niño (there is however a tendency of El Niño events to trigger an IOD so that IODs & IOBMs often occur simultaneously). Adapted from Deser et al (2010).

An EOF analysis of interannual IO SST anomalies indeed reveals the two main modes of interannual climate variability in the IO: the first mode is directly related to El Niño, with a basin-wide warming (IOBM) discussed in the previous section and the IOD shows up as the second mode of variability (see Fig. 2.10). Saji et al. (1999) defined an index for the IOD as the difference between the SST anomalies averaged over the western (50E-70E; 10S-10N) and the southeastern (90E-110E; 10S-0) regions of the tropical IO, now widely known as the Dipole Mode Index (DMI).

The positive phase of the IOD is associated with anomalous easterlies in the central IO and cold SST anomalies off the west coasts of Java and Sumatra and positive SST anomalies west of ~80E (Fig. 2.10). This east-west SST gradient induces a positive feedback loop involving SST and surface winds (Reverdin et al. 1986, Webster et al. 1999, Saji et al. 1999), similar to the Bjerknes feedback

mechanism critical to the ENSO development. The anomalous easterlies raise the thermocline and cool the SST (hence suppressing atmospheric convection) in the eastern part of the basin and together with the equatorial Rossby wave responses, they deepen the thermocline and warm the SST in the western IO, resulting in characteristic zonal dipole-structure in both sea level and SST (e.g. Feng and Meyers, 2003; Murtugudde et al., 2004; Rao et al., 2002). A negative IOD phase features anomalies of opposite sign over similar regions (Meyers et al. 2007, Vinayachandran et al. 2002). Similar to ENSO, IOD events are phase-locked to the seasonal cycle. IOD starts developing during boreal spring, peaks around October, and decays by the end of the calendar year. Observations suggest that IOD events generally co-occur with ENSO, which acts as an external trigger for IOD events by setting up an initial wind anomalies over the IO in spring through atmospheric teleconnections (e.g. Annamalai et al. 2003, Gualdi et al. 2003, Fischer et al. 2005). However, a number of studies pointed that IOD can also occur independently of ENSO, and is thus considered as an independent climate mode (Saji et al. 1999, Fischer et al. 2005, Meyers et al. 2007, Song et al. 2007, Yamagata et al. 2004).

2.5.3 Imprint of interannual climate variability on sea level

Both ENSO and IOD induce large interannual wind fluctuations in the tropical Indo-Pacific region, that considerably influence interannual sea-level variations in these two basins. As shown in Fig. 2.11, the main modes of interannual variability of the observed SLA in the tropical Pacific can be inferred by applying an EOF analysis to the tropical Pacific interannual SLA field (Meinen and McPhaden 2000, Alory and Delcroix 2002, Lengaigne et al. 2012; Widlansky et al. 2015). The first mode represents an “east-west tilting” mode pivoting around 150W. The SLA pattern can be explained by the equatorial waves forced by ENSO-related zonal wind stress anomalies, i.e. the vertical displacement of the thermocline associated with Kelvin waves induces a sea-level rise in the eastern equatorial Pacific while the westward propagating upwelling Rossby waves result in a sea-level drop in the equatorial and off-equatorial western Pacific. El Niño also triggers coastally-trapped Kelvin waves along the eastern boundary of the Pacific basin transmitting equatorial signals poleward along the western coast of north and south America (Fig. 2.11a). It is interesting to note that, even though El Niño strengthens the mid-latitude westerlies in the north Pacific and induces sharp SST anomalies (Fig. 2.11b), the SLA signature of ENSO over this region is very weak or nearly absent. We will come to this point in chapter 4. The second mode of interannual SLA in the tropical Pacific consists of a north–south tilting along an axis centred around 5N coinciding with the North Equatorial Counter-current pathway and maximum along the equator in the central and western Pacific. This second mode can be viewed as the sea-level response associated with the equatorial “discharge-recharge” phase of ENSO discussed earlier. This second mode, in fact, leads the east–west tilting mode by about 8 months (Meinen and McPhaden 2000), consistent with the theoretical recharge-discharge oscillator of Jin (1997a). Hence the leading modes of

interannual sea-level variability in the tropical Pacific consist of two different phases of ENSO, a zonal and a meridional see saw representing the “mature state of El Niño/La Niña” and “discharge-recharge” respectively.

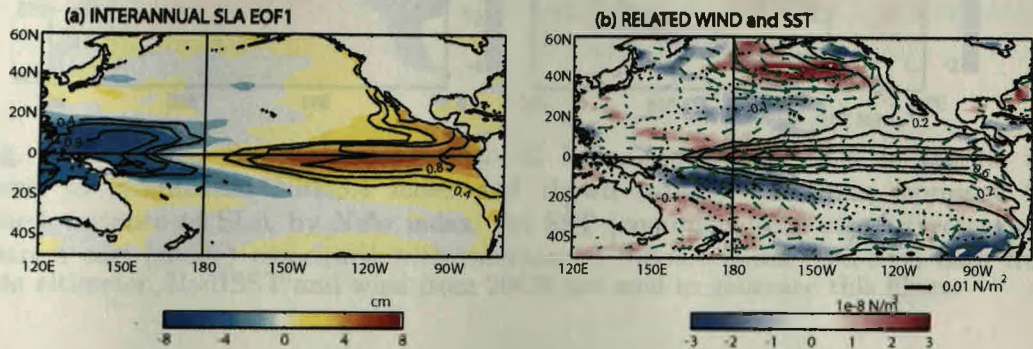


Fig. 2.11: (a) Pacific sea-level pattern associated to EOF1 of interannual SLA (satellite data during 1993-2013) performed over the tropical Pacific (120E-290E; 20S-20N). Interannual SLA over the entire Pacific are regressed onto the PC1 (shade). Contours show the variance of SLA explained by PC1. (b) Regressed patterns of wind stress curl (shade), wind stress (vector) and SST (contour) onto PC1. Sea-level data from TP/J, HadISST and 20CR wind field for the period 1993-2013 are used to construct this plot.

As for the SST, the sea-level signature associated with Modoki differs markedly from the canonical El Niño signature. The thermocline (and sea level) evolution during the development of a Modoki has been shown in Ashok et al. (2007; their figure 6). Unlike canonical ENSO for which the thermocline slopes down towards the eastern Pacific (where maximum sea-level anomalies hence also occur), the thermocline anomalies during an El Niño Modoki display deeper thermocline anomalies in the central equatorial Pacific (east of the dateline) and shallower anomalies on either side of it (i.e. in the west and east Pacific), with minimum variability over the eastern equatorial Pacific.

The IO sea level also exhibits a signature of El Niño (Fig. 2.12a). A number of observational and modelling studies (Clarke 1991, Clarke and Liu 1993, Meyers 1996, Masumoto and Meyers 1998, Potemra 2001, Potemra et al. 2002, Wijffels and Meyers 2004, Cai et al. 2005a, Cai et al. 2005b, Feng et al. 2003, Feng et al. 2005) showed that the western Pacific negative SLA forced by the westward propagating Rossby waves force coastally trapped waves along the coast of Papua-New Guinea, which eventually propagate southward to the north Australian and west Australian coasts (see Fig. 2.12a). In a series of papers, Feng et al (2003, 2004, 2010) demonstrated the “oceanic bridge” between the western equatorial Pacific and west Australian coast by analysing the sea level from the record of Fremantle tide gauge, located at the south-west coast of Australia (115E, 32S). They showed that a large fraction of low-frequency sea-level changes off the west Australian coast (WAC) is indeed driven by remote wind forcing from the equatorial Pacific associated with ENSO.

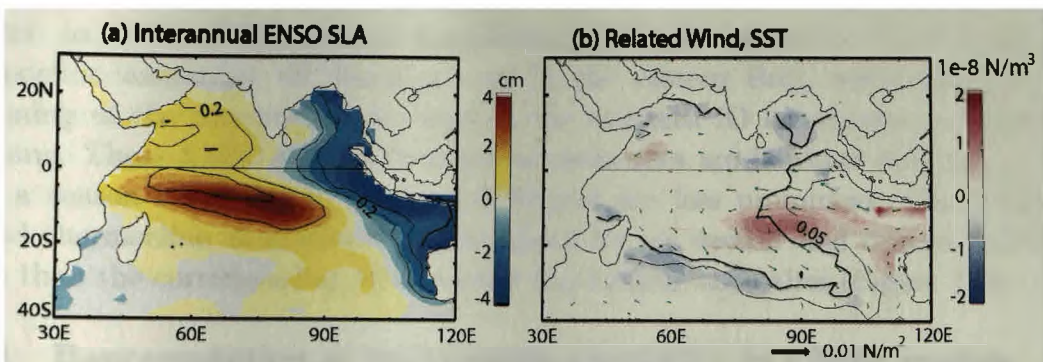


Fig. 2.12: (a) IO Sea-level response to El Niño. Interannual SLA in the IO are regressed to interannual Niño3.4 index and shown (shade). Contours represent the explained variance of SLA by Niño index. (b) SST (contour), wind stress (vector) and wind-stress curl (shade) associated with interannual Niño3.4 index. Sea-level data from satellite altimeter, HadISST and wind from 20CR are used to generate this figure.

Easterlies in the equatorial IO associated with both positive IOD and ENSO events force an upwelling Kelvin wave response in the eastern IO. These anomalous equatorial easterlies produce a dynamical response in the IO, characterized by a dipole sea-level structure (Fig. 2.12a,b). The equatorial wind forcing related to ENSO/IOD drives an equatorial sea-level signature in the IO that propagates into the northern BoB as coastally-trapped waves (Fig. 2.12a). The wind curl associated with easterly anomalies in the southern hemisphere also drive downwelling Rossby waves south of the equator (Masumoto and Meyers 1998, Xie et al. 2002, Yu et al. 2005, Rao and Behera 2005, Nagura and McPhaden 2010, Currie et al. 2013, Tozuka et al. 2010, McPhaden and Nagura, 2013). As positive IOD events very often co-occur with El Niño events in the Pacific, it is difficult to distinguish their respective impacts on the IO. In agreement with Yu et al. (2005) and Rao et al. (2002), Currie et al. (2013) showed a less-extensive and weaker ENSO influence on tropical IO thermocline variations than that of IOD (Figure 2.13).

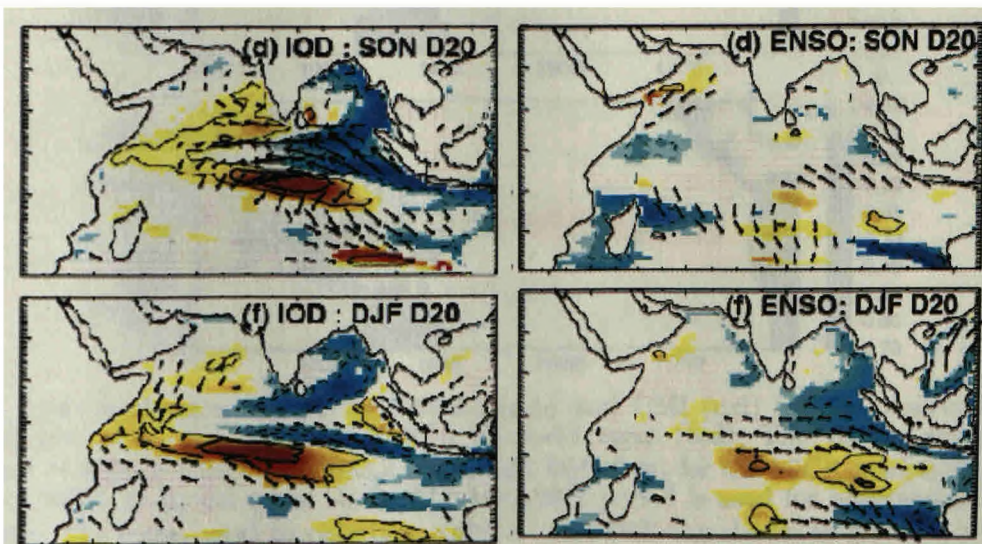


Fig. 2.13: Wind and thermocline signature of “pure positive IOD” (left) and “pure El Niño” (right) obtained from a partial regression approach applied to an Indian Ocean simulation. Adapted from Currie et al. (2013).

Similar to IOD, ENSO-related anomalous equatorial easterlies cause shallow thermocline anomalies off Sumatra and in the eastern BoB, while concurrent deepening of the thermocline develops in the southern IO in response to Ekman pumping. These ENSO-related thermocline anomalies are however delayed by at least a season compared to those of IOD and are less prominent. The ENSO-related thermocline anomalies in the southern IO are weaker and centred further south than the corresponding IOD-related thermocline anomalies (Figure 2.13).

2.5.4 Representation of interannual variability in CMIP models

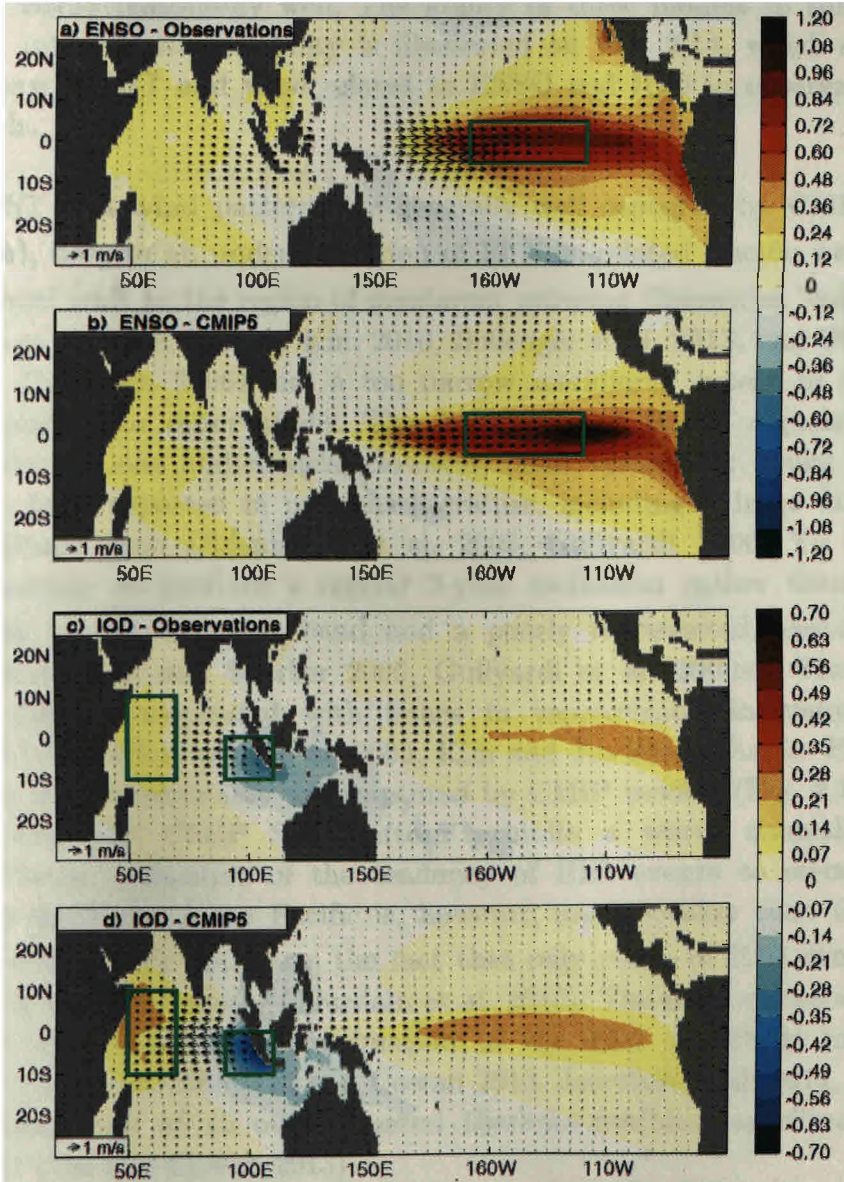


Fig. 2.14: Regression of SST on Niño3.4 (a,b) and DMI (c,d) for the observational multi-dataset mean (a,c) and the CMIP5 21-model mean (b,d). The vectors show the regression of surface winds on Niño3.4 (a,b) and DMI (c,d) for the 20CR reanalysis (a,c) and the CMIP5 21-model mean (b,d). The 1891-2010 period is used for observations and reanalyses. The boxes used to calculate Niño3.4 and DMI are shown in green. Adapted from Jourdain et al. (2016).

ENSO and IOD are hence the leading modes of interannual climate variability in the tropical Indo-Pacific Ocean, which involve several ocean-atmospheric coupled interactions. I have discussed them so far through studies mainly based on observations and forced ocean models. As stated in section 2.2, coupled simulations from CMIP3 and CMIP5 are the most widely used tools to study the impacts of anthropogenic activities on climate. Therefore, it is of utmost importance to assess their ability to simulate these major modes of interannual variability in the Indo-Pacific region. Published literature suggests that CMIP models capture the main observed characteristics of ENSO (Kim and Yu 2012; Bellenger et al. 2014; Taschetto et al. 2014; Jourdain et al. 2016) and IOD (Cai and Cowan 2013) reasonably well. The ability of these models to simulate the Indo-Pacific interannual variability is illustrated on Fig. 2.14, which shows the spatial pattern of SST and wind related to ENSO and IOD in observations and CMIP models.

ENSO SST and wind patterns are generally well captured by CMIP models (Fig. 2.14a,b), despite an underestimation of El Niño-related Pacific westerlies, a slight westward shift in the region of maximum warming (known as “cold-tongue” bias; Leloup et al. 2008, Yu and Kim 2010, Bellenger et al. 2013, van Oldenborgh et al. 2005, Guilyardi 2006) and a too narrow meridional extent of equatorial anomalies relative to observations. The ENSO-related IOBM signals are also similar in observations and models. However, other systematic biases in CMIP models have been reported in previous literature, including a large diversity of ENSO amplitude (van Oldenborgh et al. 2005, Guilyardi 2006, Yu and Kim 2010), a tendency to produce a regular 2-year oscillation rather than a broad spectral peak in the 2–7 year band and a poorly represented seasonal phase locking (Achuta Rao and Sperber 2006, Guilyardi et al. 2009a). These ENSO biases are directly associated with issues in representing individual ENSO mechanisms (van Oldenborgh et al. 2005, Kim and Jin 2011). As for ENSO, the IOD pattern is also reasonably well captured by CMIP models (Fig. 2.14c,d). As in observations, the CMIP SST pattern exhibits a warm anomaly in the equatorial Pacific, indicative of the tendency of IOD events to co-occur with ENSO. This signature in the Pacific is, however, much weaker than the ENSO related signature which illustrates the fact that only ~50% of IOD events occur independently of ENSO events (Jourdain et al. 2016). The main discrepancy with observations arise from an overestimation of the IOD amplitude in coupled simulations (Saji et al. 2006, Cai and Cowan 2013, Jourdain et al. 2014, 2016), as a direct consequence of an overestimated Bjerknes feedback amplitude in the equatorial IO (Cai and Cowan 2013).

The recent generation of CMIP models also reasonably well capture ENSO teleconnection patterns (Langenbrunner and Neelin 2013). In a recent paper, Kim et al. (2016) showed that even though the CMIP models simulate the extra-tropical teleconnections well, they still fail to reproduce some of the sub-seasonally varying features of the atmospheric circulation over the north Pacific. The systematic errors in ENSO teleconnection observed in CMIP models are

shown to be related to errors in tropical precipitation associated with ENSO. These studies suggest CMIP models can be used to better understand ENSO variations and associated climate variability, even though there are still a lot of possible improvements in these models. However, only a couple of studies have so far investigated the ability of CMIP simulations to capture the sea-level signature associated with ENSO (e.g. Widlansky et al. 2015) and the IOD (Du et al. 2013). These studies generally illustrate that CMIP models simulate the salient features of interannual sea-level variability in the tropical Indo-Pacific reasonably well. Most of the CMIP5 models also capture the downwelling oceanic Rossby wave in the southern IO forced by a wind curl anomaly over the southern IO triggered by ENSO (Du et al. 2013).

2.6 Indo-Pacific decadal climate and sea-level variability

2.6.1 Pacific decadal climate variability

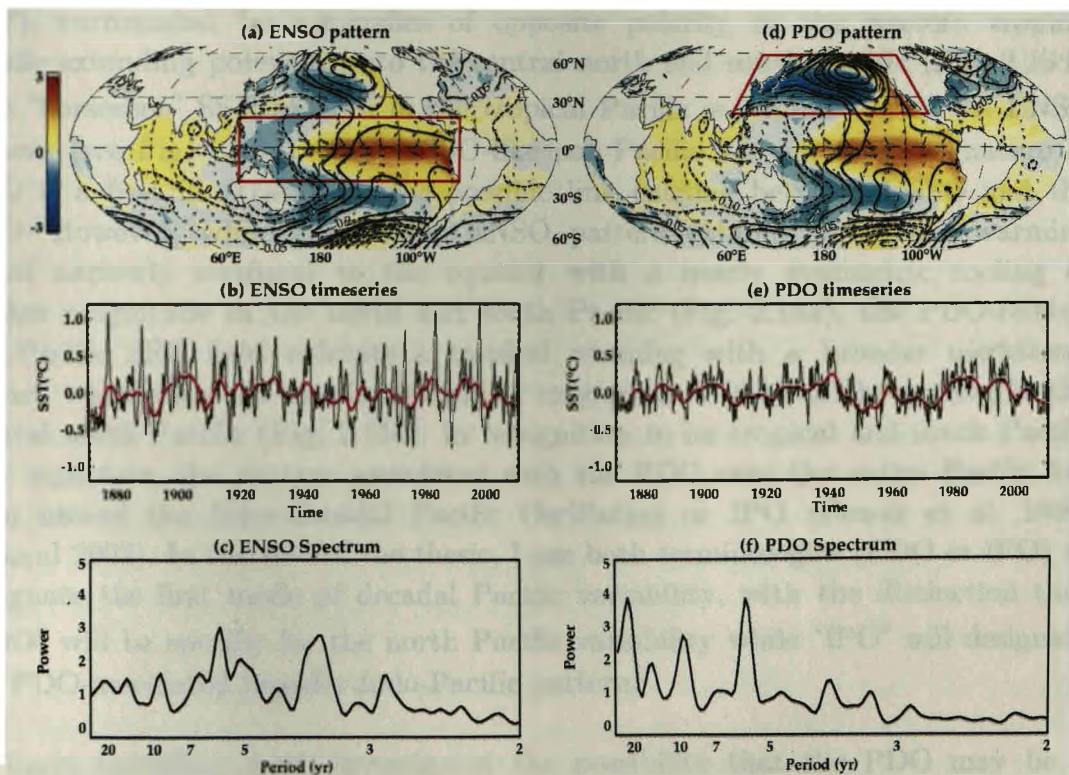


Fig. 2.15: El Niño Southern Oscillation defined as (a) the leading EOF of monthly SST anomalies over the tropical Pacific (120E-80W; 20N-20S, red frame) for HadISST dataset over the 1871-2010 period, it's (b) associated principal component (PC) time series (black curve) and corresponding low frequency (≥ 7 yrs) component (red curve) and (c) power spectrum of the normalised PC. The EOF pattern is normalized by its spatial root mean square so that the PC is a measure of the ENSO amplitude. The spatial pattern is obtained globally by regressing the SST anomalies (color), wind stress anomalies (vectors) and mean sea-level pressure anomalies (contours) onto the PC. (d-f) Same as (a-c) but for Pacific Decadal Oscillation defined as the leading EOF of monthly SST anomalies over the north Pacific (110E-110W; 20N-60N). Monthly SST anomalies are calculated by removing the mean seasonal cycle and the global mean SST time series. A linear trend is further removed from each grid point before computing the EOFs. SST pattern and spectra are unit less while SST time series are in $^{\circ}\text{C}$ and wind vectors have $\text{N}\cdot\text{m}^{-2}\cdot^{\circ}\text{C}^{-1}$ units.

The leading mode of SST variability in the north Pacific (region outlined by the red frame in Fig. 2.15d) is known as the Pacific Decadal Oscillation (PDO; e.g. Zhang et al. 1997; Mantua et al. 1997). This climate mode has clear impacts on ecosystems and marine fisheries in the North Pacific (Mantua et al. 1997; Overland et al. 2010; Schwing et al. 2010). The main characteristics of PDO have recently been described in detail in several review papers (e.g. Deser et al. 2010; Alexander 2010; Liu 2012) and are briefly reminded hereafter. PDO time series display clear decadal phase shifts (apparent “regime changes”) in the 1920’s, 1940’s and 1970’s (Fig. 2.15e) - this is why it is called Pacific *Decadal* Oscillation, although it also exhibits prominent interannual variations (in the 2 to 7 years window). A positive phase of the PDO (Fig. 2.15d) consists of cold SST anomalies in the central north Pacific and warm anomalies along the western coast of north America and in the central and eastern equatorial Pacific.

PDO also exhibits a clear SST signature outside the north Pacific, with positive SST anomalies in the central and eastern equatorial Pacific (Zhang et al. 1997), surrounded by anomalies of opposite polarity in the western tropical Pacific extending poleward into the central north and south Pacific (Fig. 2.15d). This “horseshoe” SST pattern in the tropical Pacific is reminiscent of the ENSO pattern (see Fig. 2.15a). This ENSO-like pan-Pacific as well as IO signature of PDO is a first illustration of the possible link existing between ENSO and the PDO. However, while the Pacific ENSO pattern exhibits a tropical warming signal narrowly confined to the equator with a nearly symmetric cooling of weaker magnitude in the north and south Pacific (Fig. 2.15a), the PDO-related pan-Pacific SST field exhibits a tropical warming with a broader meridional extent, which also has an almost similar magnitude to that of the cooling in the central north Pacific (Fig. 2.15d). In recognition to its tropical and south Pacific SST signature, the pattern associated with the PDO over the entire Pacific has been named the Inter-decadal Pacific Oscillation or IPO (Power et al. 1999, Folland 2002). In the rest of the thesis, I use both terminologies (PDO or IPO) to designate the first mode of decadal Pacific variability, with the distinction that “PDO” will be specific for the north Pacific variability while “IPO” will designate the PDO-associated broader Indo-Pacific pattern.

Early modelling work investigated the possibility that the PDO may be a coupled ocean-atmosphere mode of the north Pacific (e.g. Latif and Barnett 1994; LB1994 hereafter), with the time scale of the “oscillation” arising from the ocean dynamics (i.e. the spin-up time of the oceanic gyre). This study designates the north Pacific decadal variability as an inherent air-sea coupled mode with an oscillation period around 20 years. In this paradigm, the ocean memory plays an important role: the ocean indeed “slowly” adjusts to the past wind-stress variations over the north Pacific through large-scale planetary waves and advection and the time scale of this adjustment determines the ‘decadal timescale’ of the mode. The ocean response conveys a positive feedback to the atmosphere and the system evolves as a decadal coupled mode. The importance of ocean dynamics in shaping the north Pacific decadal variability and its evolution

as a coupled air-sea mode has been highlighted in a few studies a decade later (e.g. Wu et al. 2007, Zhong et al. 2008). This picture of north Pacific decadal variability as a “coupled mode” did however contradict results from other studies (Trenberth and Hurrell 1994; Graham 1994; Jacobs et al. 1994) who argued that low-frequency tropical Pacific variability drive signals in the north Pacific via atmospheric/oceanic teleconnections and/or planetary waves. One of the interesting aspects of LB1994 theory is that the atmosphere over the north Pacific is sensitive enough to mid-latitude SST anomalies to provide a positive feedback to the ocean to sustain the coupled mode.

But, is the PDO really a regional coupled ocean-atmosphere process in the north Pacific as hypothesized by LB1994?. Climate science witnessed a huge number of observational and modelling studies that addressed this question over the last fifteen years (see review by Alexander 2010). There is now a growing body of evidences that a large fraction of the PDO variance arises from the integration of atmospheric stochastic forcing by the ocean, i.e. forced by the atmosphere rather than the result of air-sea coupling. The mid-latitude ocean responds to atmospheric forcing in accordance with Hasselman’s (1976) stochastic climate model. The stochastic climate model paradigm (SCM) initially introduced by Frankignoul and Hasselmann (1977) is the seminal theory that allows understanding the mid-latitude oceanic variability at low frequencies (especially decadal to multi-decadal time scales). The paradigm is basically a first order explanation of the ocean mixed layer temperature response to random atmospheric variability via surface fluxes and Ekman currents. The atmospheric mid-latitude variability is structured spatially, but display a very flat spectrum, that can be considered as a white noise. This “white noise” atmospheric forcing is integrated by ocean mixed layer to yield a “red noise” SST response, leading larger amplitudes of the oceanic response in the lower frequency part of the spectrum. This simple SCM paradigm is widely accepted as the leading paradigm for the “*null hypothesis*” of SST variability in mid and high latitudes where random atmospheric forcing is a good approximation.

Thus the null hypothesis for mid-latitude SST variability is that the random (unpredictable) atmospheric forcing induces much slower SST response in the ocean simply due to the thermal inertia associated with the deep mixed layer. The SST response, according to this hypothesis enhances the low-frequency part of the atmospheric forcing according to a first-order auto-regressive process. The large-scale spatial pattern of the PDO arises from the fact that the atmospheric “stochastic” (i.e. random at time scales longer than a few days) forcing is spatially organised at large spatial and temporal scales (e.g. Feldstein 2002). The PDO is indeed strongly related to fluctuations of the north Pacific Aleutian low (contours on Fig. 2.15d), with a deeper Aleutian low/negative sea-level pressure anomalies over the North Pacific inducing a positive PDO response (Pierce et al. 2000; Alexander et al. 2002). Part of these SST anomalies *re-emerge* through entrainment into the mixed layer during the following winter through a process called ‘re-emergence mechanism’ (for more details, see Namias and Born 1974;

Alexander and Deser 1995; Deser et al. 2003). This integration of the atmospheric forcing by the ocean increases the PDO variance in the low frequency part of its spectrum, i.e. at decadal to multi-decadal time scales (Fig. 2.15f). The time series and power spectrum of the PDO are also in agreement with the SCM paradigm i.e., it is consistent with a red-noise spectrum at low frequency (greater than ~10 years), with no clear spectral peaks in this spectral range. Due to the limited length of the observational record, it is however difficult to ascertain whether the PDO has a robust spectral peak at decadal to multi-decadal time scales or if the spectrum at these time scales is essentially red (Pierce 2001; Qiu et al. 2007). Some studies however hint toward a significant peak at about 20-year period in both historical SST data (Minobe 1997; Minobe 1999; Deser et al. 2004) and reconstructions from paleo-proxies (Biondi et al. 2001; Gedalof et al. 2002).

The SCM paradigm however does not explain the spectral peak of the PDO time series at interannual time scales nor the similarity between ENSO and the PDO spatial patterns (Fig. 2.15). Newman et al. (2003) showed that PDO is actually influenced by ENSO at all time scales through the well-known mid-latitude atmospheric teleconnection, which modulates the variability of the Aleutian low at ENSO time scales. This influence of ENSO on PDO translates into a ~0.6 correlation between ENSO and PDO time series in observations, with ENSO leading the PDO evolution about 1-2 months (Fig. 2.15b,e). As a result, the pan-Pacific expression of the PDO (IPO) bears a strong resemblance with that of ENSO, except for a stronger weighting in the north Pacific relative to the tropical Pacific (Fig. 2.15d). The SST anomalies resulting from the combined influence of ENSO and stochastic forcing in the North Pacific (mid-latitude surface wind and heat-fluxes being largely modulated by synoptic weather events) are then detrained from the mixed layer at the end of the winter and persist in the seasonal thermocline through summer, isolated from the atmospheric influence. Part of those anomalies re-emerge through entrainment into the mixed layer during the following winter. Newman et al. (2003) showed that the observed PDO spectrum is compatible with that obtained from a simple autoregressive model accounting for ENSO influence, stochastic atmospheric forcing and re-emergence process. In this “*extended null hypothesis*” (ENH) of PDO (the standard null hypothesis considers solely the oceanic integration of atmospheric white noise forcing), the PDO can simply be described as a reddened response to both ENSO and atmospheric white noise forcing.

Fig. 2.16 illustrates the influence of ENSO on the PDO as well as the re-emergence mechanism by providing the lead/lag-correlation between ENSO and PDO. ENSO leads PDO throughout the year by a few months (typically by ~2-3 months lag; Fig. 2.16), illustrating the forcing of ENSO onto the PDO. The simultaneous correlation is weaker during November to March and the lag of maximum correlation between ENSO and PDO varies from nearly 2 months (summer) to ~5 months (early winter). During winter and spring, ENSO one-year lead correlation with PDO remains statistically significant, which is what we would expect from the aforementioned “winter-to-winter” re-emergence of mixed

layer temperature anomalies. The relationship between ENSO and PDO extends beyond the interannual time scales. Torrence and Compo (1998) and Newman et al. (2003) indeed showed that ENSO and PDO power spectra were also coherent at lower frequencies (decadal/multi-decadal periods). However, the PDO spectrum is much redder than that of ENSO (Fig. 2.15c,f), illustrating the fact that at longer (shorter) periods the PDO signal tends to be stronger (weaker) than ENSO signal due to the ocean reddening process. In fact, about 54% and 32% of the PDO and ENSO variance respectively occurs at periods of 10 years and greater (Newman et al. 2003).

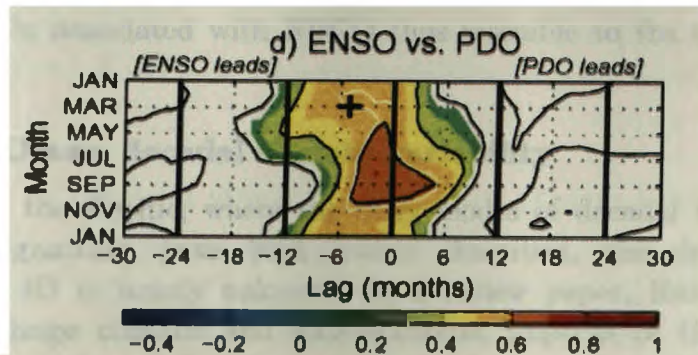


Fig. 2.16: Annual cycle of cross-correlation between ENSO and PDO. ENSO leads PDO for negative lags and vice versa for positive lags. The month ordinate refers to the PDO; e.g. cross represents correlation between Mar PDO and Oct (lag -5) ENSO. Adapted from Newman et al. (2003).

As already discussed briefly, many studies have attempted to understand the various physical processes that shape the observed PDO. Results from Newman et al. (2003) strongly suggest that PDO characteristics can largely be understood through the ENSO direct forcing, the re-emergence of north Pacific SST in winter and the atmospheric white noise forcing, suggesting that north Pacific ocean dynamics play a minor role in shaping the PDO variability. By expanding the ENH of Newman et al. (2003), Schneider and Cornuelle (2005), however, demonstrated that accounting for the ocean dynamics of the north Pacific gyres yield to a better representation of the PDO at multi-decadal timescales. They also suggested that the vertical mixing of temperature anomalies triggered by the wind-driven Rossby waves had little impact on PDO. What all these studies imply is that PDO may not be a single physical mode but rather the sum of several phenomena (see also Barlow et al. 2001, Newman 2007, Alexander et al. 2008).

In the previous section, we have seen that the IPO/PDO is the leading mode of decadal climate and sea-level variability in the Pacific Ocean. Recent papers have reported another mode of decadal climate variability in the North Pacific. This second climate mode has been referred to as the North Pacific Gyre Oscillation (NPGO; Di Lorenzo et al. 2008). This mode emerges as the second dominant mode of SLA variability in the region (when extracted through an EOF analysis) and is significantly correlated with salinity, nutrients and chlorophyll fluctuations found in long-term records of the California Current and Gulf of

Alaska. It is **also** related to variations in the intensity of the central and eastern branches of the North Pacific gyre circulations. The NPGO atmospheric forcing pattern (SLP and wind) significantly differs from that of the PDO. While the PDO is associated with low-frequency fluctuations of the Aleutian low, The NPGO forcing pattern resembles to that of the North Pacific Oscillation, which corresponds to a northward/southward shift of the Aleutian low. While the PDO is forced by canonical ENSO variations, the NPGO variability is dynamically linked to Modoki discussed in section 2.5.1. Modoki indeed drives low-frequency changes in the extra-tropical atmospheric circulation that are integrated by the ocean to form the decadal NPGO (Di Lorenzo et al. 2010). The SST anomalies in the tropical Pacific associated with NPGO thus resemble to the typical Modoki SST pattern.

2.6.2 Indian Ocean decadal climate variability

In contrast to the Pacific, where the main modes of decadal variability and their sea-level signatures have been widely described, the decadal climate variability in the IO is largely unknown. In a review paper, Han et al. (2014) pointed out the huge climatic and socio-economic impacts of the IO decadal climate variability and sea-level changes for the Indian sub-continent and low-lying islands in the IO. This study concludes that our understanding of IO decadal variability is “primitive” compared to that of the Pacific and Atlantic Oceans. While decadal variability of the IOBM is tied to decadal variability of ENSO, observational studies (Ashok et al. 2004; Song et al. 2007; Tozuka et al. 2007) suggest that decadal modulations of the IOD are not strongly tied with decadal ENSO variations but may be more related to the asymmetry between positive and negative IOD events (Tozuka et al. 2007). An EOF analysis of the IO and Pacific SST at decadal time scales performed by Han et al. (2014) reveals some intriguing features (Fig. 2.17). This analysis shows that the first mode of IO decadal SST variations exhibits a basin-wide warming pattern, reminiscent of the one discussed earlier for interannual time scales. While this basin mode mimics the IPO variations until the 1980's, their relationship reverses during the last three decades (Fig. 2.17c).

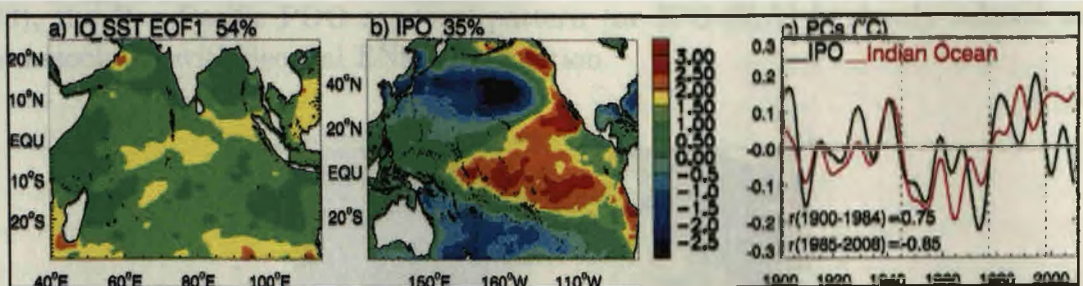


Fig. 2.17: (a) EOF1 structure of decadal SST in the IO and (b) Pacific. (a) shows a homogeneous basin wide pattern (similar to ENSO-related IOBM) that accounts for 54% of the total SST variance. (b) is IPO SST pattern (35%) as we discussed in previous sections, IPO being the leading mode of climate variability in the Pacific. (c) shows the PC1 of IO EOF (red) and Pacific EOF (black). Interestingly, both times series show a similar evolution until the mid 1980's (correlation=0.75) to be then in opposite phase during the last three decades (correlation=-0.85). Adapted from Han et al. (2014).

Several proxy-based reconstructions in the southwest IO have also highlighted decadal SST variations nearly in phase with decadal ENSO or IPO (Cole 2000; Cobb and Charles 2001; Crueger et al. 2008; Grove et al. 2013). The reasons behind the reversal of the relationship during the recent period remain unclear but Han et al. (2014) indicate that the IO may play an increasing role in shaping the Indo-Pacific decadal climate variability or that forced or internally generated natural variability could explain this behaviour. Thus, the details and relative importance of variability internal to the Indian Ocean versus Pacific forcing of the IO decadal variations remains an open question. Both the decadal IPO and decadal IOD have been reported to contribute to IO decadal variability, but the relative roles of IO internal variability, air-sea interactions, and stochastic atmospheric forcing in shaping IO decadal variability remains a largely uncharted territory.

2.6.3 Imprint of decadal climate variability on sea level

The imprint of the PDO or IPO on the decadal sea-level variability in the Pacific region is now relatively well established. As shown by Di Lorenzo et al. (2008), the leading mode of SLA variability in the north Pacific is driven by the PDO. Fig. 2.18 shows the SLA pattern associated with the PDO. This pattern is obtained through a linear regression of SLA onto the PDO index over the 1993-2012 period. We have seen earlier that the Pan-Pacific pattern of SST associated with PDO (IPO SST pattern) closely resembles the ENSO pattern (Fig. 2.15a,d) due to the ENSO contribution to forcing of the PDO (Newman et al. 2003). The PDO sea-level pattern also bears a strong resemblance with the IPO SST map, with a symmetric distribution of SLA about the equator (negative SLA in the western and positive in the eastern and central Pacific regions). Positive SLA maximum occurs in the central equatorial Pacific (around 140W) and maximum negative anomalies are seen over the tropical western Pacific and Kuroshio Extension region (Fig. 2.18). The strong SLA variability in the tropical north-western Pacific has also been monitored in tide gauges records (Merrifield et al. 2012). The decadal IPO sea level pattern is described in detail in chapters 4 and 6. But, I want here to emphasize that, owing to the close relationship between ENSO and PDO, as shown in many of the previous studies (e.g. Newman et al. 2003), the Pan-Pacific PDO sea-level pattern (or IPO-SLA) is closely related to that associated with decadal ENSO modulation.

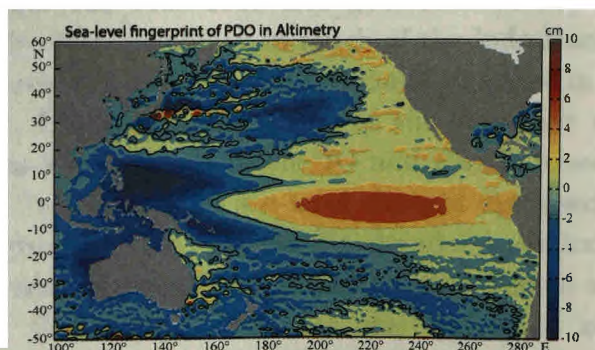


Fig. 2.18: Pacific sea-level pattern obtained by regression of altimeter SLA (during 1993-2012) onto PDO index. Adapted from Si and Xu (2014).

The most remarkable influence of the Pacific on the IO variability has been found in the sea-level variations along the west coast of Australia (WAC). A strong decadal SLA signature of the IPO along the WAC has been evidenced from the analysis of altimetry data (Fig. 2.19) and longer tide gauge records (Feng et al. 2004, 2010). By analysing three long tide gauge records in the tropical Indo-Pacific, Feng et al. (2010) indeed revealed coherent decadal sea-level variability in the western tropical Pacific and the WAC, with sea-level decadal variations from Fremantle record mimicking the one at Pohnpei (Fig. 2.19). These coherent sea-level variations between the western equatorial Pacific and WAC occurs through an oceanic teleconnection mechanism similar to the one discussed in section 2.5.2 for interannual time scales. Feng et al. (2010) also pointed out that about 80% of the decadal sea-level variance in the equatorial Pacific can be explained by the equatorial zonal winds, which is consistent with the equatorial balance found in Pacific, i.e. a quasi-steady state of the ocean against equatorial zonal winds at lower frequencies (Yu and McPhaden 1999; also see section 2.3). About 70% of the decadal variance of Fremantle sea level is explained by equatorial wind variations in the Pacific, while local along-shore winds explains only 20%. The Leeuwin current and ITF are also shown to co-vary with equatorial wind in the Pacific at decadal time scales. There is no wonder why Feng et al. (2004) called the Fremantle sea-level record a “footprint” of decadal climate variability in the tropical Pacific.

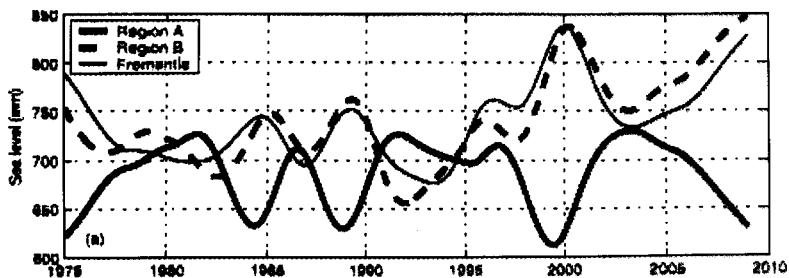


Fig. 2.19: Decadal evolution of tide-gauge sea-level at Christmas (eastern tropical Pacific; thick solid curve), Pohnpei (western tropical Pacific; thick dashed curve and Fremantle (western coast of Australia; thin solid curve). Adapted from Feng et al. (2010).

The satellite data analysis performed by Lee and McPhaden (2008; hereafter LM08) also revealed substantial decadal SLA reversals consistent over the entire Indo-Pacific region over the 1993-2000 and 2000-2006 period (Fig. 2.20). These large-scale coherent decadal variability in much of the Indo-Pacific sector over the recent period was further associated with decadal changes in the Pacific trade wind curl (Fig. 2.20). LM08 is perhaps one of the very first description on the large-scale decadal sea-level pattern in the IO and Pacific based on observations. The features of Indo-Pacific decadal sea-level changes discussed in LM08 provide very interesting insights on the Indo-Pacific decadal variations. First of all, it points out that large-scale decadal SLA in the tropical Pacific and Indian Oceans are coherent (during the satellite altimeter era) and could be related to each other. Secondly, the observed sea-level pattern in each of these basins is dynamically consistent with large-scale wind variations. Besides, the decadal

phase change in sea level seen in most of the regions at the turn of twentieth century could be associated with the decadal phase change seen in IPO/ENSO during the same period. This study also highlights that the phase change in the tropical Pacific tends to occur earlier than elsewhere, suggesting a potential role of the tropical Pacific in driving decadal variability of the entire Indo-Pacific region via the atmospheric (through the Walker circulation) and oceanic (through the coastally trapped waves and the ITF) teleconnections discussed in section 2.5.

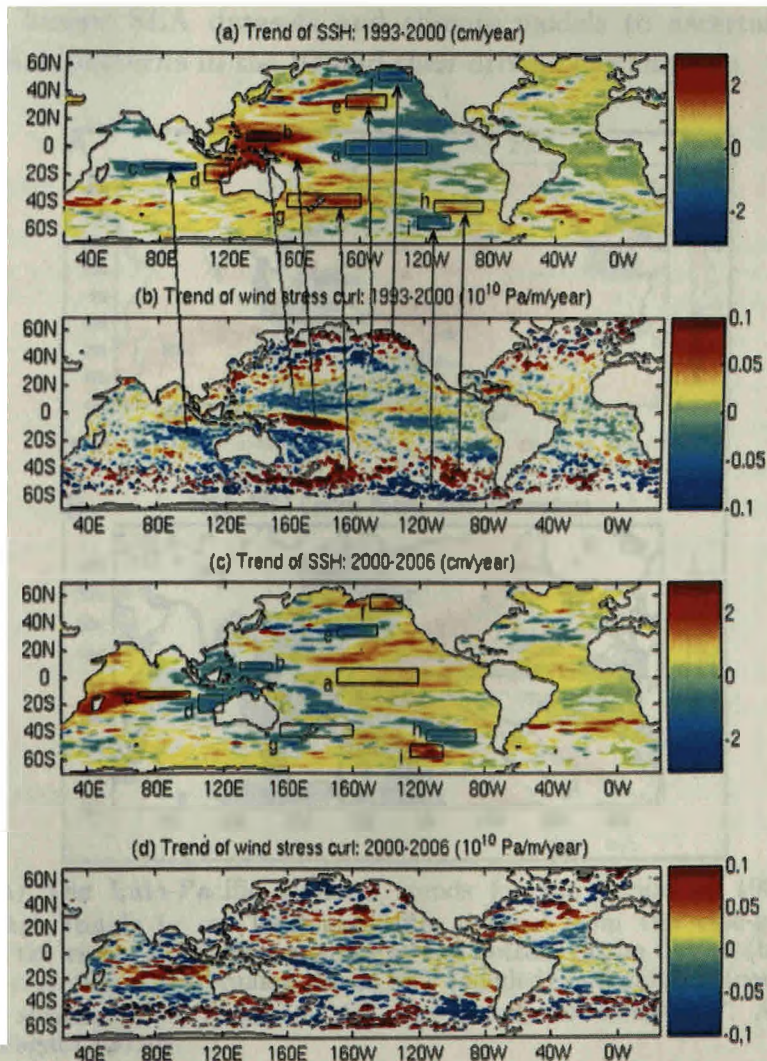


Fig. 2.20: (a) 1993 - 2000 sea-level linear trend from satellite altimeter. Positive trends are seen over western tropical Pacific and along the west Australian coast spreading across the south east IO. Central-to-eastern tropical Pacific and SWIO experience sea-level drop. (b) Wind-stress curl trend for the same period highlighting the agreement between sea level and wind during 1993-2000. (c-d) Same as (a-b) but over the 2000-2006 period. Adapted from Lee and McPhaden (2008).

As for the canonical ENSO, the Modoki variability described in section 2.5 also induces decadal fluctuations in sea level (e.g. Behera and Yamagata 2010). Behera and Yamagata (2010) characterised the Modoki imprint over the tropical Indo-Pacific in terms of SLA, wind, and sea-level pressure over the satellite altimeter period (Fig. 2.21). Their analysis suggests a possible remote influence of decadal Modoki in the southwestern IO. In this scenario, the ENSO Modoki

would strengthen the subtropical high in the southern IO (Mascarene high), which drives a cyclonic wind-stress curl and elevates the sea level through Ekman convergence in the upper ocean. Hence the positive SLA found east of Madagascar is attributed to Modoki atmospheric teleconnections by Behera and Yamagata (2010), while it was attributed to ENSO by Lee and McPhaden (2008). This discrepancy may arise from the limited number of effective degrees of freedom in these two seminal satellite-based studies. It is indeed very difficult to derive robust decadal signals from 20 years long data. This calls for further analyses using longer SLA datasets and climate models to ascertain the large-scale decadal SLA patterns in the IO and their driving mechanisms.

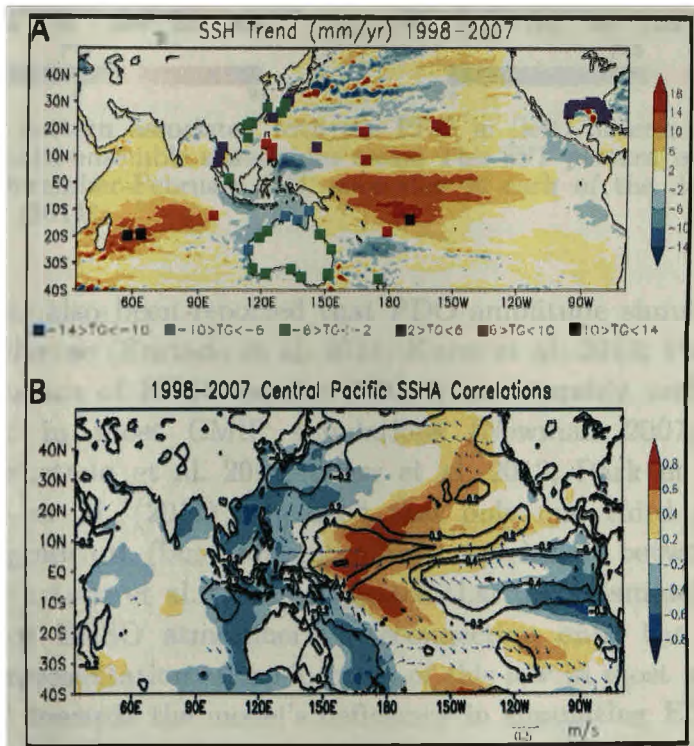


Fig. 2.21: (a) The Indo-Pacific sea-level trends for the period of 1998–2007. The squares denote the trends in sea level anomalies derived from the tide-gauge records. Colour codes for the range of trends are given at the bottom of the figure. (b) The central Pacific sea-level correlation with anomalies of SST (shaded) and rainfall (contour) and its regression with surface wind anomalies for the decade of 1998–2007. Adapted from Behera and Yamagata [2010].

2.6.4 Representation in CMIP models

Past literature have shown that most models from the CMIP3 database reproduce reasonably well the spatial pattern of the PDO in the North Pacific (Furtado et al. 2011; Kwon et al. 2012; Park et al. 2013; Yim et al. 2014). For instance, Fig. 2.22 compares the leading mode of SST anomalies in the north Pacific from observations to the mean EOF pattern from the models. The model ensemble-mean compares visually well with the observations, with negative SST anomalies in the central and western North Pacific and positive SST anomalies in the eastern North Pacific. There is however a slight difference between the distributions of the model ensemble mean and observation. The maximum negative SST anomalies are indeed located over the central Pacific in the

observations, whereas they are located near the western boundary in the CMIP models. Yim et al. (2013) suggested that this maximum cooling near the western boundary could be related to ocean dynamical process rather than atmospheric processes.

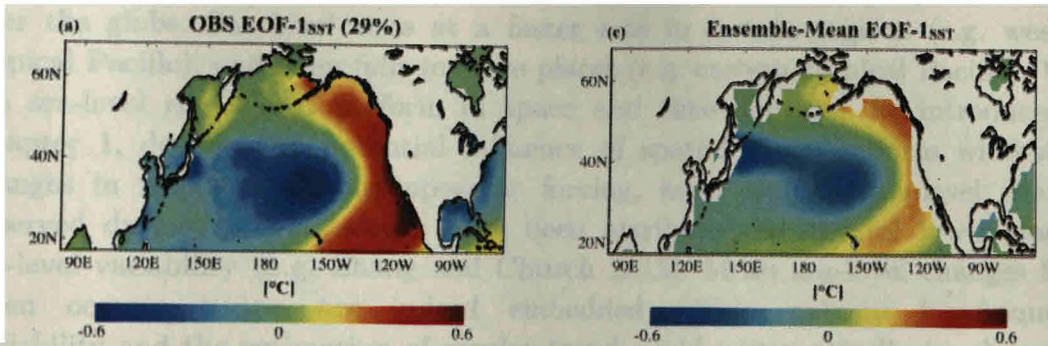


Fig. 2.22: SST pattern associated with the PDO in (left) observations and (right) CMIP3 historical multi-ensemble simulations mean. This SST pattern is derived from an EOF analysis of December-February SST anomalies in each of the datasets. Adapted from Furtado et al. (2011).

However, it has also been reported that PDO amplitude simulated by CMIP models are very diverse (Furtado et al. 2011; Kwon et al. 2012; Park et al. 2013) and that the influence of ENSO on the PDO is considerably underestimated or even non-existent in most CMIP simulations (Newman 2007; Oshima and Tanimoto 2009; Furtado et al. 2011; Deser et al. 2012; Park et al. 2013). For instance, Furtado et al. (2011) concluded that only one third of the CMIP3 models display significant (but underestimated) correlation between ENSO and the PDO. While Furtado et al. (2011) suggested that this mismatch arises from a weak projection of ENSO atmospheric teleconnection onto the Aleutian Low because of a misrepresentation of the location of this low in most models. Park et al. (2013) pointed towards the model's deficiency in simulating ENSO amplitude and centres of actions. In contrast, Lienert et al. (2011) showed that the simulated amplitude of ENSO-related signals in the North Pacific as well as the time-lag between PDO and ENSO were overestimated in these models possibly because of an overestimated mixed layer depth and underestimated air-sea feedbacks in the North Pacific. However, the assessment of the tropical Pacific decadal variability and its relationship with the PDO has not been conducted yet in CMIP5 models. In addition, although the influence of ENSO on the Indian Ocean SST variability at interannual timescales has already been discussed in CMIP models (see section 2.5.4), the interactions between Indian and Pacific Oceans at decadal time scales in these models have yet to be explored.

2.7 Aliasing of long-term sea-level trend by decadal variability

In a detailed discussion on the effects of decadal variability on observed sea-level trend, Houston and Dean (2013) wrote: *“If decadal variation in a tide gauge record causes a low trend at the beginning of the record and high trend at the end, the variation will cause a positive acceleration and trend difference, with the reverse situation producing a negative acceleration and trend difference”*. This

statement technically summarises an intriguing problem that climate scientists face today: the aliasing of long-term trends associated with anthropogenic effects by the background natural low-frequency variability for any climatic variable. We may revisit Fig. 2.3 that shows the global map of sea-level trend estimated from satellite SLA data for the period 1993-2012. These trends are clearly not uniform over the globe. Sea level rises at a faster rate in certain regions (e.g. western tropical Pacific), and even falls in some places (e.g. eastern tropical Pacific). Why the sea-level rise is not uniform in space and time domain? As introduced in Chapter 1, despite the potential influence of spatially non-uniform wind-stress changes in response to anthropogenic forcing, most regional sea-level changes observed during recent decades have been attributed to natural low-frequency sea-level variability (e.g. Zhang and Church 2012). Mean sea-level changes for a given oceanic region are indeed embedded within natural low-frequency variability and the estimation of secular trend could systematically be aliased by this natural variability.

In the following, we will focus the mean sea-level trends in the Indian and Pacific basins and the possible aliasing in the trend estimation. The typical amplitude of tropical sea-level decadal variability is about 5 cm (Feng et al. 2004, Frankcombe and Dijkstra 2009), although it can vary up to 15 cm regionally. The rate of global mean sea-level rise during the last two decades is estimated to be $\sim 3 \text{ mm yr}^{-1}$ from altimetry (Nerem et al. 2010, Church and White 2011); i.e. a ~ 6 cm rise in mean sea level over the altimeter period. Hence the amplitude of decadal variability and mean sea-level change are of similar magnitude for, at least, the short satellite altimetry record. This results in a large uncertainty in the trend estimation driven by anthropogenic forcing, specifically in regions of strong natural decadal variability. The tropical Indo-Pacific is such a region, with strong natural low-frequency variations, discussed in detail in the previous sections. This scenario largely explain the close relationship between observed sea-level trend pattern and the natural low-frequency variability patterns. Recent sea-level research has intended to correct the low-frequency signals before estimating the long-term trend that could be attributed to climate change. This “correction” is usually performed by removing the natural low-frequency variability from the sea-level record through statistical techniques. This method, however, requires a clear understanding of the natural low-frequency variability in observations.

For example, IPO being the main mode of decadal variability in the Pacific Ocean, a proper estimation of long-term sea-level trend in the Pacific requires removal of IPO related signals from the sea-level record. Zhang and Church (2012) made such an attempt in order to separate the low-frequency IPO signal from the anthropogenic trend. A multiple linear regression technique based on ENSO and IPO indices allowed them to detect sea-level signals (trend) unrelated to the Pacific low-frequency climate variability (ENSO and PDO). The trends derived from this method appears to be very different from the one directly derived from a simple linear regression in time. They indeed attributed most of the intensified sea-level trend in the western tropical Pacific to the IPO

variability, while the weak decreasing trend in the eastern Pacific is a combined effect of IPO-related sea-level fall and global mean sea-level rise (see Fig. 2.23). This study clearly illustrates that a short record, such as the altimeter sea-level data, cannot be used for anthropogenic trend estimation without accounting for natural decadal variability.

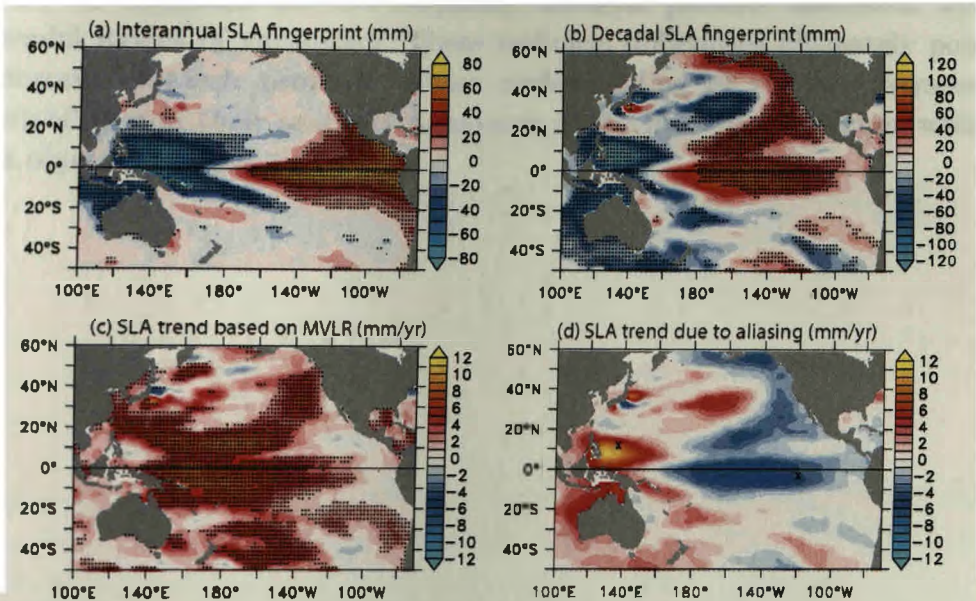


Fig. 2.23: This figure shows how the IPO aliases the sea-level trend estimation in the Pacific from Satellite altimetry data. (a) Sea-level signature of interannual ENSO and (b) sea-level signature of decadal IPO. (c) Sea-level trend pattern obtained from a multiple linear regression by considering ENSO and PDO as additional independent variables. (d) Spatial map of sea-level trend aliasing by climate modes (mainly by the IPO). Adapted from Zhang and Church (2012).

Similarly, the IO sea-level trends are strikingly different over the altimeter period (Fig. 2.3) and over longer periods (see IO sea-level trends for 1960–1999 in Alory et al. 2007, for 1961–2008 in Han et al. 2010 and the sea-level trends estimated from tide gauge records in the NIO by Unnikrishnan and Shankar 2007). Fig. 2.3 shows that sea level is substantially decreased in the south tropical IO, while it has increased elsewhere. Han et al. (2010) attributed this basin-wide feature of sea-level trend to changes in the surface winds partly attributable to rising levels of anthropogenic greenhouse gases. Alory et al. (2007) and Schwarzkopf and Boning (2011) suggested that the trend discussed by Timmermann et al. (2010) in the Pacific may also be transmitted to the IO by the ITF and hence partly explain the observed sea level decrease in the south tropical IO.

However, in a more recent study, Frankcombe et al. (2014) showed that the IPO signature, both the amplitude and the spatial pattern (obtained through regression onto the PDO index) is different over the satellite period compared to longer records from reconstructed datasets. This means that the regression of sea-level onto IPO is sensitive to the time window used. Frankcombe et al. (2014) wrote: “Window lengths on the order of 50 years (or longer) are required for

robust regressions of SSH on to low-frequency variability such as the PDO". The method that Zhang and Church (2012) used to isolate trend from natural variability is efficient only if the low-frequency signal that they derive is representative of the signature of targeted natural mode. The length of the sea-level record is obviously a strong caveat to reach such a goal and longer records are necessary to ascertain the low-frequency sea-level pattern associated with natural decadal modes of variability. These technical difficulties ultimately point to an important research problem: better understanding of the low-frequency climate variability and their sea-level signatures in the Indo-Pacific region; which is the main objective of this thesis.

Decadal and long-term sea-level variability in an OGCM

As mentioned in Chapter 2, Lee and McPhaden (2008) (hereafter LM08) revealed a near coherent large-scale decadal variability in much of the Indo-Pacific sector over the satellite altimeter period with a phase change at the end of the 20th century (i.e. opposite trends during the 1993-2000 and 2000-2006 periods). Fig. 3.1b is identical to LM08 sea-level trend estimate over the 2000-2006 period, and hence provides an estimate of typical decadal sea-level variations over the satellite altimetry era. As discussed in LM08, the opposite sea-level variations in the western and central Pacific are accompanied by opposite variations along the WAC and a region in the central IO located northeast of Madagascar. LM08 further showed that trade winds and sea-level variations in the tropical Pacific and in the south IO (SIO) are anti-correlated during the 1993-2006 period, implying anti-correlated variation of the sub-tropical cells in the two oceans. However, as clearly stated by LM08, the exact relationship of these decadal sea-level signals and decadal ENSO (or IPO) variations needs to be further assessed. Similar to the findings in LM08, but based on longer tide gauge sea-level data, Feng et al. (2004, 2010) showed that the decadal and multi-decadal sea-level variations along the WAC are coherent with those in the western Pacific.

Apart from the potential influence of the IPO on Indo-Pacific sea-level fluctuations, Behera and Yamagata (2010) suggested, based on an analysis of the short satellite altimetry record that decadal sea-level variations in central Pacific were strongly related to decadal Modoki variations, with a strong imprint on sea-level fluctuations east of Madagascar through atmospheric teleconnections. Even though these studies (LM08, Feng et al 2004, 2010, Behera and Yamagata 2010) highlight basin-scale interactions and coherent low-frequency sea-level changes in the tropical Indo-Pacific Ocean potentially associated with known decadal Pacific climate modes, the observational data (altimeter and tide gauge sea level) used in these studies were limited in time and space domains and prevents definitive

conclusions on the robustness of these findings. Satellite altimetry provides high resolution data with near-global coverage but available only for the last two decades (since 1992). On the other hand, some tide gauge data are available for more than a century in the tropical Indo-Pacific Ocean (as it is the case for the Fremantle tide gauge record located along the WAC used in Feng et al. studies), but these gauges are largely confined to coastal regions and thus preventing a thorough assessment of open ocean variability.

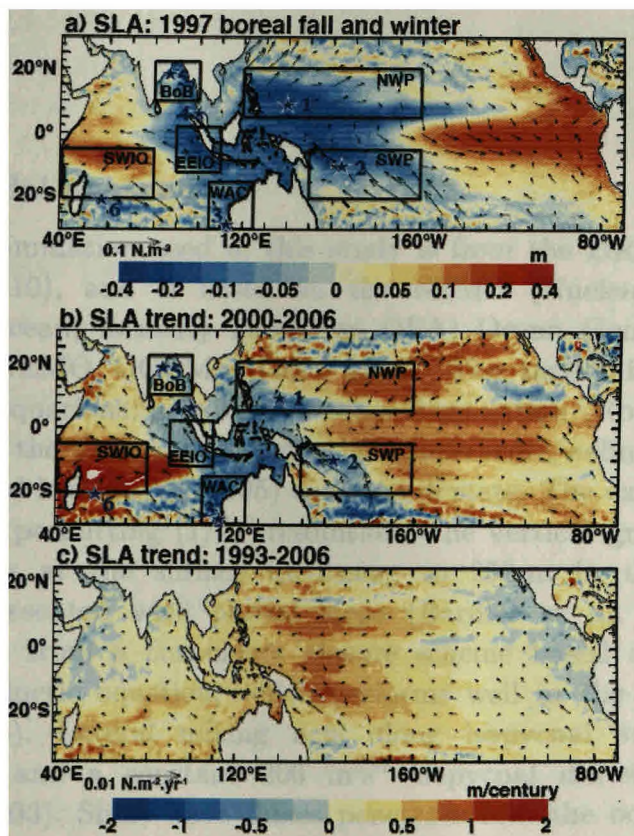


Fig. 3.1: (a) Satellite SLA averaged during October 1997–March 1998 (color) and associated wind anomalies derived from NCEP (arrow). (b) Satellite SLA linear trend for the 2000–2006 period (color) and associated NCEP wind stress trend (arrow). (c) Satellite SLA linear trend for the 1993–2006 period (color) and associated NCEP wind stress trend (arrow). The mean seasonal cycles were removed from both SLA and wind datasets. The stars on panels (a) and (b) indicate locations of the tide-gauges used to validate the model steric sea level. The selected gauge locations are (1) **Yap B** (138E, 9.5N), (2) **Honiara II** (161E, 9.5S), (3) **Fremantle** (115.7E, 32S), (4) **Langkawi** (99.8E, 6.4N), (5) **Paradip** (86.7E, 20.3N) and (6) **Port Louis** (57.5E, 20.15S). Boxes on panel (a) and (b) indicate the regions where model SLA are validated to satellite observations. The selected boxes are the North West Pacific (**NWP**), the West Australian Coast (**WAC**), the Southwest Pacific (**SWP**), the Eastern Equatorial IO (**EEIO**), the Bay of Bengal (**BoB**) and the Southwest IO (**SWIO**). Panel (b) is identical to fig. 1c of Lee and McPhaden (2008), i.e. an estimate of decadal sea-level change over that period. Panel (c) provides an estimate of long-term sea-level trends over 1993–2006, the period consistent with the study by Lee and McPhaden (2008).

The lack of reliable “long and basin-wide” observational sea-level data is in fact a strong limitation for investigating the decadal sea-level variability of the world oceans. This is particularly true in the case of IO, which is one of the least sampled oceanic regions in the world. Only a few studies have so far investigated the decadal sea-level variability in the IO, either focusing on the recent satellite

period (e.g. LM08, Behera and Yamagata 2010) or on the western Pacific-WAC oceanic connection using tide gauge data (Feng et al. 2010). In this chapter, I aim at describing and understanding the decadal variability of the Indo-Pacific region using 42 years of an OGCM simulation (1966-2007) validated with available observations. Although my focus is more on the IO, I consider the entire Indo-Pacific region owing to the known linkages between Indian and Pacific Oceans via atmospheric and oceanic teleconnections (Klein et al. 1999, Feng et al. 2004), and also discuss Indo-Pacific interannual variability as a basis of comparison for decadal fluctuations.

3.1 Data

3.1.1 Ocean model experiment

The numerical simulation used in this study is from the DRAKKAR project (Brodeau et al. 2010), and is based on the NEMO (Nucleus for European Modelling of the Ocean, formerly known as OPA) Ocean General Circulation Model (hereafter, NEMO OGCM, Madec 2008). The model is based on the standard primitive equations, uses a free surface formulation (Roullet and Madec 2000) and computes the density from potential temperature, salinity and pressure using the Jackett and McDougall (1995) equation of state. The experiment in this study uses an eddy permitting $(1/4)^0$ resolution. The vertical grid has 46 levels with a 6-m spacing at the surface increasing to 250-m in the deep ocean. Bathymetry is represented with partial steps (Barnier et al. 2006). Vertical mixing is computed from a turbulence closure scheme based on a prognostic vertical turbulent kinetic equation, which performs well in the tropics (Blanke and Delecluse 1993). Lateral mixing acts along isopycnal surfaces, with a Laplacian operator and a constant $200 \text{ m}^2\text{s}^{-1}$ isopycnal diffusivity coefficient (Lengaigne et al. 2003). Short-wave fluxes penetrate into the ocean based on a single exponential profile (Paulson and Simpson 1977) corresponding to oligotrophic water (attenuation depth of 23 m).

The model is forced with the 1958-2004 DFS3 wind, described in detail in Brodeau et al. (2010). This forcing is essentially based on the corrected ERA-40 reanalysis (Uppala et al. 2005, and ECMWF operational analyses beyond 2002) for near surface meteorological variables and on the corrected ISCCP-FD radiation product (Zhang et al. 2004) after 1984. No surface temperature restoring is used and salinity is restored to climatological values, with a relaxation time scale of 33 days (for a 10m thick layer). The model simulation is initialized with Levitus et al. (1998) climatology. The model is then run over the 1958-2007 period, using the DFS3 forcing. As this study aims at investigating interannual to decadal time scales, the beginning of this simulation is discarded (until the model has “forgotten” the initial shock at the beginning of 1958). I did discard the first 8 years of this simulation (1958-1965) and analysed the output only for the 1966-2007 period. This choice of discarding the first 8 years can be justified as follows: i) EOF analysis of the steric sea level over the full period (1958-2007) showed a first EOF whose principal component changes steeply over the first 8 years and

then remain quite flat; ii) the typical first-baroclinic mode Rossby wave phase velocity is about 0.05 m.s^{-1} at 30° latitude (i.e., 12000 km in 8 years), and about 0.1 m.s^{-1} at 20° latitude i.e. 24000 km in 8 years (Chelton and Schlax 1996) that leaves enough time for basin-scale adjustment within the tropics.

The NEMO OGCM has been extensively validated with various forcing strategies in uncoupled mode (e.g. Vialard et al. 2001, Cravatte et al. 2007) and in coupled mode (e.g. Lengaigne et al. 2006, Lengaigne and Vecchi 2009). This model well simulates the equatorial dynamics and basin wide structures of currents and temperature in the tropics. The particular simulation analysed in this paper reproduces observed equatorial currents and interannual variations of the heat content in the tropical Pacific (Lengaigne et al. 2012) and mixed layer depth in the IO (Keerthi et al. 2012) as well.

3.1.2 Observational datasets

Altimeter sea surface height and measurements of sea level from tide gauges are used to validate the model steric sea-level variations. The satellite data combine the joint US-French missions Topex/POSEIDON (October 1992 to October 2002) and JASON-1 or Envisat (October 2002 to present; sea-level data from this combined satellite missions will be referred as TP/J from hereafter). The data have been processed by CLS Space Oceanography Division and distributed over weekly intervals on a one-third degree Mercator grid. The weekly data were converted into monthly-averaged sea-level data and the monthly data are used in the present study. Since the sea-level data from altimetry covers only the last two decades, historical tide gauge data obtained from the Permanent Service for Mean Sea Level (PSMSL - Woodworth and Player, 2003) are also used in this study. As many of the gauge stations in the Indian and Pacific Oceans suffer from large data gaps, a few tide gauge records are selected (with minimum gaps in regions of largest decadal variability). The selected tide gauge records, shown as stars on Fig. 3.1 are 1.Yap B (138E; 9.5N), 2.Honiara II (161E; 9.5S), 3.Fremantle (115.7E; 32S), 4.Langkawi (99.8E; 6.4N), 5.Paradip (86.7E; 20.3N) and 6.Port Louis (57.5E; 20.15S).

Century-long records of SST (HadISST) and wind fields are also used in the present study. HadISST is based on blended *in-situ* and satellite data sources after 1981 and sparse ship datasets prior to that period (Rayner et al. 2003), with an optimal interpolation to fill the gaps in data-sparse oceanic regions. Estimates of long-term variations from reanalyses (such as the ERA-40 reanalysis, on which the model forcing is based) are subject to spurious variations caused by changes in the observing system, or measurement methods (e.g. the effect of anemometer height discussed in Tokinaga and Xie 2011). To assess the robustness of the model wind forcing, I compared the decadal variability with other wind datasets covering the entire 1958-2007 period, namely the NCEP and 20th Century (20CR) reanalyses and the WASWind dataset. The NCEP/NCAR reanalysis uses a state-of-the-art analysis/forecast system to perform data assimilation using past data from 1948 to the present, with an original $\sim 1.9^\circ$ resolution (Kalnay et al. 1996).

The 20CR reanalysis project (Compo et al. 2010) is an effort to produce a reanalysis dataset spanning the entire twentieth century, assimilating sea level pressure observations from the International Surface Pressure Databank station component version 2 (Yin et al. 2008), International Comprehensive Ocean-Atmosphere Data Set (ICOADS, Woodruff et al. 2009) and from the International Best Track Archive for Climatic Stewardship (IBTrACS, Knapp et al. 2010). This dataset offers 6-hourly wind data from 1870 to 2008. A new surface wind dataset constructed from the wind speed and wind wave-height ship observations archived in the ICOADS database is also considered. This Wave and Anemometer-based Sea surface Wind (WASWind; Tokinaga and Xie 2011) dataset is corrected for spurious upward trend due to increases in anemometer height and provides wind velocity and scalar speed at monthly resolution on a $4^\circ \times 4^\circ$ longitude–latitude grid from 1950 to 2008. All these datasets were interpolated onto the regular $2.5^\circ \times 2.5^\circ$ grid to ease comparison.

3.2 Method

3.2.1 Model steric sea level

Changes in temperature and salinity in an oceanic water column result changes in vertical height of the layer, referred to as 'steric' sea-level variations (Pattullo et al. 1955). Changes caused by temperature and salinity variations are respectively referred as the *thermosteric* and *halosteric* sea-level anomalies (hereafter TSLA and HSLA). The sum of TSLA and HSLA is the total steric sea-level anomaly (SSLA). SSLA variations are computed for the upper thousand meter layer of the tropical Indo-Pacific ocean from the model temperature and salinity fields, following Antonov et al. (2002) as:

$$TSLA = \int_{z=0}^{1000} \frac{1}{v} \frac{\partial v}{\partial T} \Delta T dz \quad HSLA = \int_{z=0}^{1000} \frac{1}{v} \frac{\partial v}{\partial S} \Delta S dz$$

where v is specific volume, z is depth and ΔT and ΔS are the temperature and salinity anomalies computed by subtracting the mean temperature and salinity field for the entire period from the raw values at each standard depth. Specific volume v has been computed at each standard depth level as a function of monthly mean temperature and salinity fields and pressure using the UNESCO equation of state for sea water (UNESCO 1981; Millero and Poisson 1981).

Since the model uses the Boussinesq approximation, the model global average sea level does not account for a sea-level rise due to a global average thermal (or haline) expansion/contraction (Greatbatch 1994), i.e. the global average ocean mass can vary under the effect of a surface buoyancy flux imbalance, but not the global average *sea level*. I hence use steric sea-level variations, rather than the sea level in the free-surface NEMO simulation in our analyses because:

(i) it can account for a globally uniform sea-level increase due to a uniform buoyancy flux.

(ii) it does not include the long-term sea-level drift caused by unbalanced freshwater (evaporation minus precipitation and runoff) over the global ocean in the forcing dataset.

(iii) since the changes in steric sea level are an important contribution to local changes in sea level on seasonal and climatic time scales (Pattullo et al. 1955, Church et al. 1991, Gregory 1993), it is reasonable to assume that the steric sea-level variations discussed in this study are more or less equivalent to sea-level variations, especially in the tropical regions.

3.2.2 Time scale definition

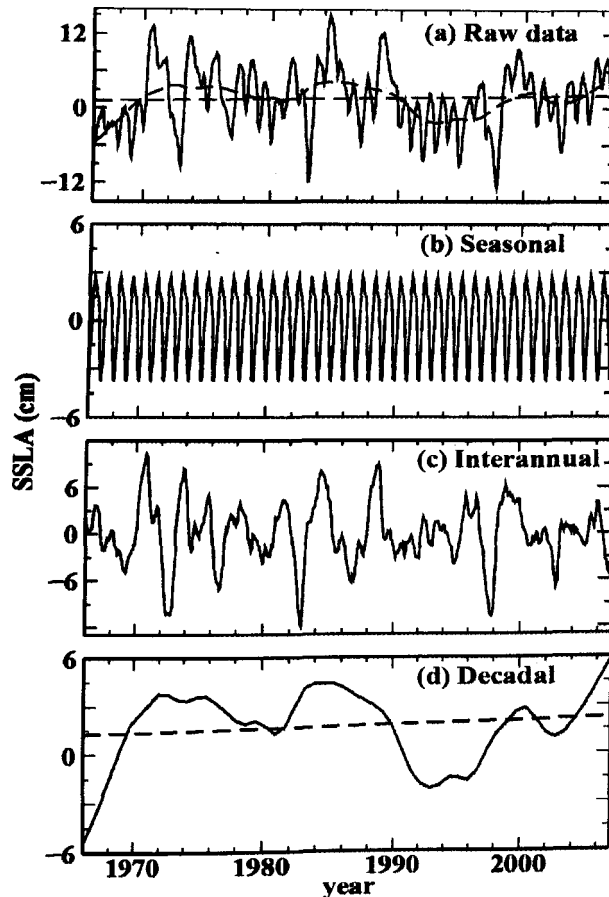


Fig. 3.2: Time series of model steric sea-level variations in the NWP, extracted by STL method. (a) raw data (black curve), (b) seasonal, (c) interannual and (d) low-frequency component. Linear trend associated with either a long-term change or multi-decadal variability is shown as a dashed line in panel (d). This linear trend has been subtracted from estimates of STL derived "low-frequency" component to get the 'decadal' component (see text). The low-frequency component shown in panel (d) are also shown in panel (a).

The interannual and decadal signals of the monthly SSLA data are extracted using the STL (Seasonal-Trend decomposition procedure based on loess¹) filtering method as described in (Cleveland et al. 1990). STL is a robust iterative non-parametric regression procedure using loess smoother, which allows decomposing a time series into seasonal, low-frequency and remainder components. As for all non-parametric regression methods, STL requires subjective selection of a smoothing parameter to define the low frequency component. I chose a 7-year cut-off to extract low-frequency component in the steric sea-level data. Results from this procedure are illustrated on fig. 3.2 for SSLA variations in the Northwest Pacific. The STL method successfully extracts the seasonal variations (Fig. 3.2b) as well as the low-frequency evolution (Fig. 3.2d), which accounts for SSLA variations with time scales larger than 7 years. The remainder (Fig. 3.2c) is the residual of the full field, once the seasonal and low-frequency components are subtracted, and is referred to as *interannual sea level* in the following sections (and for all the analysis/variables described in this thesis). Sensitivity tests using cut-off period ranging from 4 to 8 years were performed for the extraction of low-frequency component and I found that the main results and conclusions of this study are not altered. This method of time series filtering is applied both to the steric sea-level field and to the various wind products described above to extract signals above seven year periodicity (also for various datasets used throughout in this thesis). I have isolated the long-term (multi-decadal) changes, either linked to anthropogenic or natural long-term climate variations, from the linear trend of the STL-derived low-frequency component over the 1966-2007 period (see Fig. 3.2d for an example). Hence, *decadal variability* is defined as the difference between the STL derived low-frequency component and this linear trend.

3.2.3 Definition of climate indices

As we have seen in Chapter 2 and in the introductory section of this chapter, the tropical Pacific climate variability could potentially affect climate and sea-level variations not only in the tropical Pacific but in other oceanic basins, especially the IO through atmospheric as well as oceanic bridges. This strong control led me to define indices for the main tropical Pacific climate modes in order to analyse how they relate with the sea-level variability in various regions of the tropical Indo-Pacific basin. As discussed in Chapter 2, there are two major climate modes in the tropical Pacific, namely ENSO and Modoki, which are usually defined by the climate indices Niño3.4 index (for ENSO) and ENSO Modoki Index (EMI) (for Modoki variability; see Chapter 2 for the definitions of these indices). These two climate indices are, however, being correlated significantly at 0.55 and 0.71 at interannual and decadal time scales respectively². Using uncorrelated indices would ease the assessment of the percentage of sea-level variance explained independently by these two modes. To do so, I define the main tropical Pacific climate modes as the first two EOFs of

¹ loess is an acronym for "local regression" (see Jacoby 2000).

² These correlations are computed for the period 1960-2010 period from HadISST data. This must be noted that these numbers may be altered with respect to a change in dataset used or for a different period considered.

SST anomalies in the tropical Pacific for the period 1960-2010 (dashed frame on Fig. 3.3a), computed separately for interannual and decadal time scales. This strategy allows the climate indices (represented by the corresponding PCs) to be orthogonal at both interannual and decadal time scales.

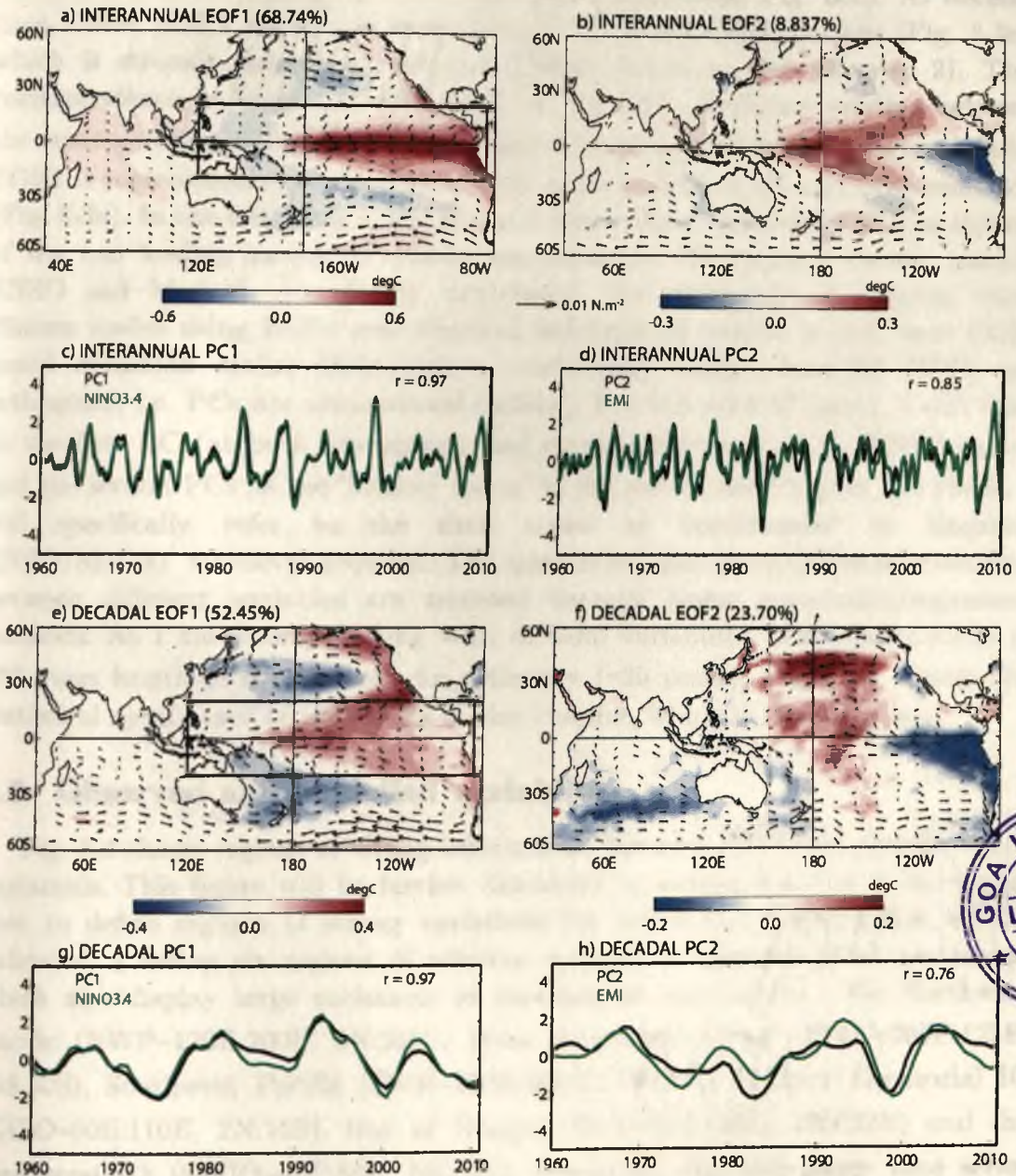


Fig. 3.3: First two EOFs of tropical Pacific (120E-70W, 20S-20N; black rectangle on a&e) SST at interannual and decadal time scales over the period 1960-2010. (a, b) SST (color) and wind-stress (arrow) anomalies associated with EOF1 and EOF2 at interannual time scales and (c, d) their principal components. (e-h) Same as (a-d) but for decadal time scales. Niño3.4 and EMI indices are overlaid on PC1 and PC2 respectively for both time scales (the correlation coefficient between the timeseries is also given in each panel). Even though the EOFs are computed for the tropical Pacific, the SST and wind are regressed onto the corresponding normalized PCs over the entire Indo-Pacific region to illustrate their Indo-Pacific signature.



Fig. 3.3 demonstrates that these new indices are actually representative of ENSO and Modoki variability for both interannual and decadal time scales. At interannual time scales, EOF1 pattern resembles the typical ENSO SST pattern (Fig. 3.3a), while EOF2 pattern is reminiscent to that of Modoki (Fig. 3.3b). Indeed, interannual PC1 and PC2 strongly correlate with interannual Niño3.4 and EMI indices respectively (0.97 and 0.85 correlations; Fig. 3cd). At decadal time scales, EOF1 pattern is very similar to the IPO SST pattern (Fig. 3.3e), which is strongly related to decadal ENSO variations (see Chapter 2). This correspondence is further demonstrated by the 0.97 correlation existing between the corresponding PC1 and decadal Niño3.4 index (Fig. 3.3g). Similarly, decadal EOF2 is representative of decadal Modoki pattern (Fig. 3.3.f) and time evolution (Fig. 3.3h). In the following, I will hence consider these normalized PCs as indices of the two leading modes of climate variability in the tropical Pacific, namely ENSO and Modoki. As already mentioned, the advantage of defining these climate modes using EOFs over classical definition of indices is that their EOF-based definition makes these indices statistically independent (as EOFs are orthogonal, i.e. PCs are uncorrelated indices). For the sake of clarity, I will refer to the first PC (at both interannual and decadal time scales) as “ENSO index” and the second PCs as the “Modoki index” in the rest of the Chapter and thesis. I will specifically refer to the time scales as ‘interannual’ or ‘decadal’ ENSO/Modoki’ whenever required. The qualitative and quantitative relationships between different variables are assessed through linear correlation/regression methods. As I am mainly dealing with decadal variability from observations of ~50 years length or even shorter for altimetry (~20 years), I will not discuss the statistical significance of the results in this chapter, which is obviously low.

3.3 Observed and modelled variability

Fig. 3.4 shows regions of strong interannual, decadal and multi-decadal SSLA variations. This figure will be further discussed in section 3.4, but is mentioned here to define regions of strong variations for which the model SSLA will be validated. I define six regions of relative maxima in decadal SSLA variations, which also display large variations at interannual time scales - the Northwest Pacific (NWP–120E:200E, 5N:20N), West Australian Coast (WAC–105E:125E, 15S:30S), Southwest Pacific (SWP–150E:200E, 5S:20S), Eastern Equatorial IO (EEIO–90E:110E, 2N:12S), Bay of Bengal (BoB–80E:100E, 10N:22N) and the Southwest IO (SWIO–40E:80E, 5S:20S). I selected one tide-gauge time series record within each of these regions. The representativeness of the location of tide gauges with respect to the large-scale variability (in terms of variability over regions shown by boxes in Figs. 3.1 and 3.4) is illustrated in Table 1, which displays the correlation between the box-averaged model SSLA and the SSLA at the corresponding tide gauge location, at interannual and decadal time scales. In the western Pacific (NWP, SWP), in the EEIO and WAC, the selected tide gauges are very representative of the region at both interannual and decadal time scales (correlation ranging from 0.79 to 0.96). The Paradip tide gauge is less

representative of the entire BoB, which shows correlations of ~ 0.65 at both time scales. The interannual sea-level evolution at the Port Louis tide gauge record is not representative of the interannual evolution in the SWIO box ($r=0.33$), while it is more representative at decadal time scales ($r=0.56$).

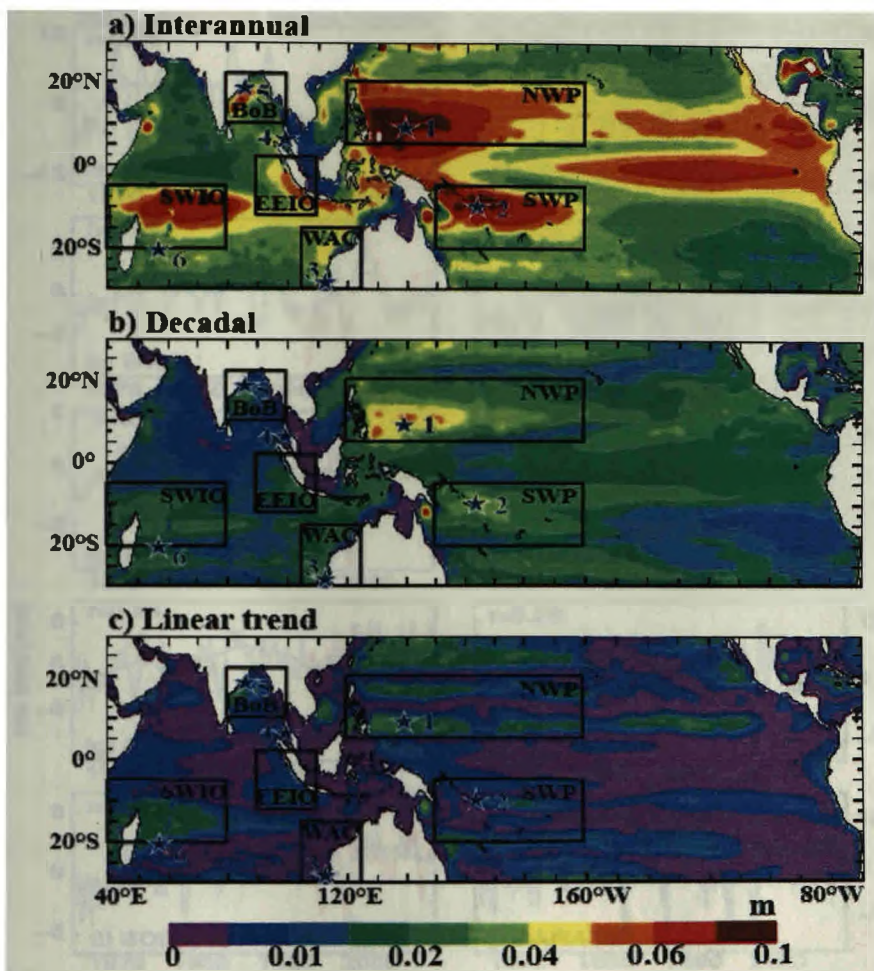


Fig. 3.4: Standard deviation of model SSLA over the 1966-2007 period for (a) interannual time scales (b) decadal time scales and (c) long-term linear trend. The boxes on each panel indicate regions of strong interannual and decadal variability. The locations of tide gauge data used in this study are indicated by stars.

Region / Tide gauge	Interannual	Decadal
NWP / Yap B	0.83	0.93
WAC / Fremantle	0.79	0.89
SWP / Honiara	0.86	0.85
EEIO / Langkawi	0.91	0.96
BOB / Paradip	0.68	0.63
SWIO / Port Louis	0.33	0.56

Table 3.1: Correlation coefficient between model SSLA evolution averaged over the box (see fig. 3.1 and 3.3) and at the corresponding tide gauge location at interannual and decadal time scales over the 1966-2007 period.

The ability of the model to simulate sea-level variability in the selected regions is illustrated in Fig. 3.5, which compares the evolution of the model SSLA (green curves) with regionally-averaged altimeter SLA (red curves, left panel) and selected tide gauge SLA (blue curves, right panel).

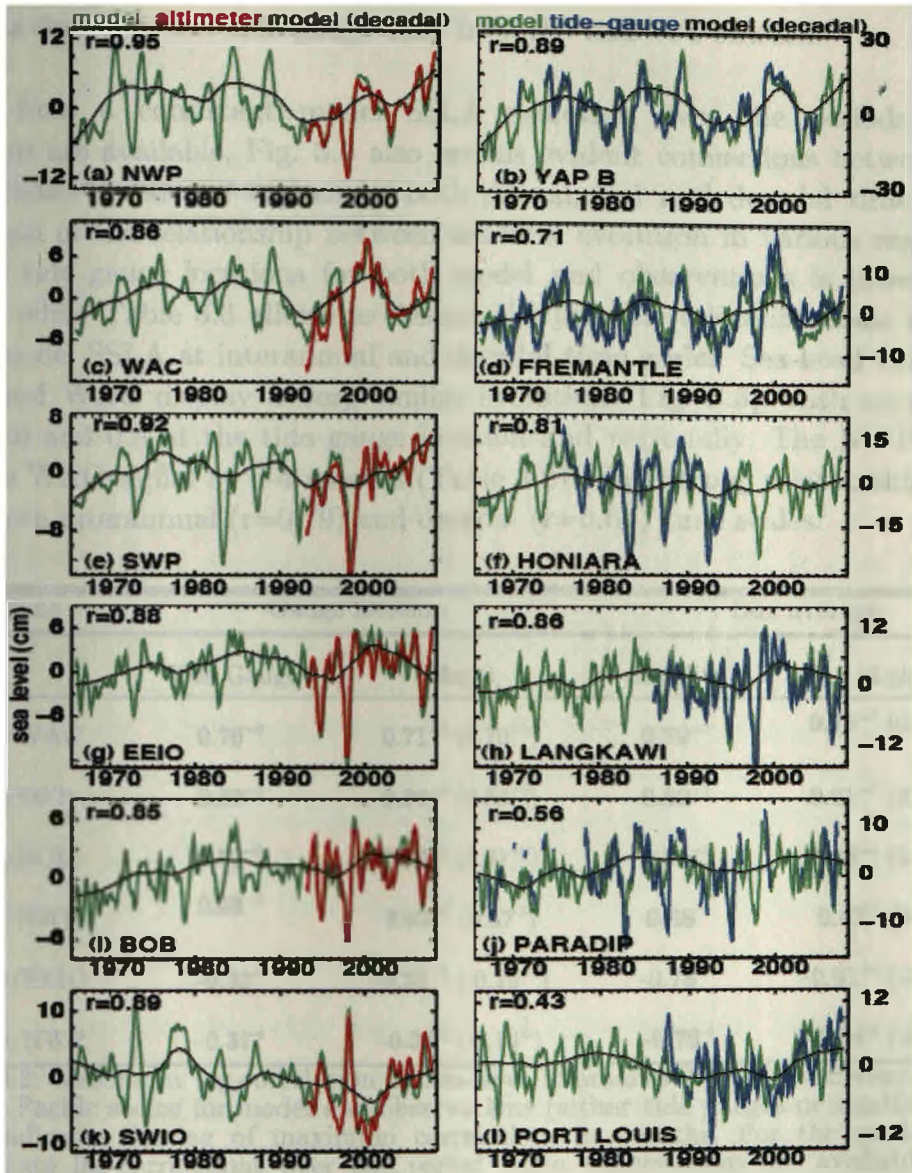


Fig. 3.5: Comparison of monthly model SSLA with altimeter (left panel) and tide gauge sea level anomalies (right panel). Time series on the left panels are averaged over the regions shown on Fig 3.1 and 3.3 while time series on the right panels are extracted at the corresponding tide gauge locations indicated by stars on Figs 3.1 and 3.3. The monthly anomalies were calculated by removing the mean seasonal cycle and a 5 months smoothing is further applied to the time-series. The linear correlation coefficient between the model and observed time series is given on the top left of each panel. The black line indicates the model decadal signal (including long-term linear trend).

Interannual and decadal variations in model SSLA compare well with both satellite and tide gauge SLA in the NWP, SWP and WAC (correlations ranging from 0.71 to 0.95). The model SSLA evolution at decadal time scales in the NWP and WAC also agrees well with the Feng et al. (2010) observational analysis using tide gauge data (Fig. 3 in their paper). In the EEIO, the model SSLA

compares well with the satellite sea level with a correlation of above 0.85. Model and tide gauge sea level also display a good agreement at Langkawi in the EEIO and a reasonably good match at Paradip station along the western BoB. At Port Louis, on the southern border of the SWIO region, the model does not capture interannual sea-level variations properly. On the other hand, the decadal evolution is similar to the tide gauge data from the mid-80's onward.

Apart from a consistent model SSLA evolution over the periods where observations are available, Fig. 3.5 also reveals evident connections between sea-level variability in several regions at both interannual and decadal time scales. The strength of the relationship between sea-level evolution in various regions or at various tide gauge locations for both model and observations is provided in Table 3.2, while Table 3.3 allows to discuss the possible teleconnections inferred from the model SSLA at interannual and decadal time scales. Sea-level variations in NWP and WAC display a very similar evolution (Fig. 3.5), with correlation between 0.6 and 0.8 at the tide gauge location and regionally. The NWP signal leading the WAC signal by 0-4 months (Table 3.2). This strong relationship holds good for both interannual ($r=0.79$) and decadal ($r=0.64$) time scales.

Regions	Gauge location		Box average	
	Tide Gauge	Model	Satellite	Model
NWP/WAC	0.76 ⁺⁰	0.71 ⁺² (0.76 ⁺¹)	0.79 ⁺³	0.75 ⁺³ (0.74 ⁺⁴)
NWP/SWP	0.52 ⁺⁶	0.36 ⁺⁸ (0.53 ⁺⁶)	0.62 ⁺⁷	0.61 ⁺⁷ (0.58 ⁺⁸)
EEIO/BOB	0.79 ⁺⁰	0.89 ⁺⁰ (0.81 ⁺⁰)	0.91 ⁺¹	0.86 ⁺² (0.80 ⁺¹)
EEIO/NWP	0.68 ⁺⁰	0.62 ⁺⁰ (0.57 ⁻¹)	0.68 ⁻¹	0.67 ⁻¹ (0.61 ⁻²)
SWIO/EEIO	-0.33 ⁻³	-0.35 ⁺² (-0.19 ⁺¹)	-0.78 ⁺³	-0.91 ⁺³ (-0.72 ⁺²)
SWIO/NWP	-0.37 ⁻¹	-0.36 ⁻² (-0.14 ⁻⁵)	-0.76 ⁻¹	-0.84 ⁻¹ (-0.47 ⁻⁵)

Table 3.2: Maximum lag-correlation of sea-level anomalies between different regions in the Indo-Pacific sector for model and observations (either tide gauges or satellite). The exponent indicates the lag of maximum correlation, in months. For the model, bold values indicate lag-correlations over the period when observations are available while values in parentheses indicate lag-correlations for the entire 1966-2007 period. Anomalies have been calculated by removing the mean seasonal cycle and the long-term linear trend. A five months smoothing is further applied to the resulting time series.

At interannual time scales, there are indeed relative minima during El Niño events (e.g. in 1972, 1982, 1987, 1997) and relative maxima during La Niña events (e.g. in 1975, 1984, 1988, 1999)³ for these two locations. The NWP and WAC regions also display a comparable decadal evolution (black curves), with a maximum in the mid-1970's, mid-1980's and around 2000 and a minimum in the

³ ENSO and IOD years are taken from Ummenhofer et al. (2009)

1960's, in the early 1980's, in the early 1990's and in the mid-2000's in both regions.

Regions	Interannual	Decadal
NWP / WAC	0.79 ⁺⁴	0.64
NWP / SWP	0.63 ⁺⁸	0.71
EEIO / BOB	0.79 ⁺¹	0.85
EEIO / NWP	0.65 ⁻¹	0.47
SWIO / EEIO	-0.84 ⁻²	-0.42
SWIO / NWP	-0.69 ⁻⁵	0.08

Table 3.3: Correlation coefficient of model steric sea-level evolution between selected regions in the Indo-Pacific sector at interannual and decadal time scales. The various regions are shown on Figs 3.1 & 3.4.

Regionally-averaged sea-level signals from the model SSLA and satellite measurements in the SWP and NWP also display a good agreement, with a correlation about 0.6. The agreement is however weaker ($r \sim 0.5$, Table 3.2) when considering the tide gauge locations. As illustrated in Table 3-3, this co-variability between NWP and SWP holds for both interannual and decadal variations. At interannual time scales, both locations display relative minima during El Niño events and relative maxima during La Niña, the SWP lagging the NWP signal by ~ 6 months (Table 3.2 and Table 3.3). This relationship is even slightly stronger for decadal time scales ($r = 0.71$) compared to interannual time scales ($r = 0.63$).

The EEIO exhibits very clear signatures of IOD events at interannual time scales with negative SSLA during positive IOD events (e.g. in 1982, 1994, 1997, 2007) and positive SSLA during negative IOD events (e.g. in 1985, 1988/89, 1996). Most of these extremes are also present in the BoB, which displays a very similar sea-level evolution to the EEIO, with correlations above 0.8 (with no lag) for both model and observations (Table 3.2). At decadal time scales, variations in the BoB agree well with variations in the EEIO ($r = 0.85$; Table 3.3) with an increase from the late 60's until the early 80's, a minimum in the mid-90's and a maximum in the early 2000's (Figs. 3.5g, 3.5i). The SSLA evolution averaged over the regions (boxes shown in Fig. 3.1) indicates that variations in the SWIO region are anti-correlated with those in the EEIO and NWP, with correlation below -0.7 (Table 3.2). The relationship between the variability in the SWIO and EEIO/NWP regions is evident at interannual time scales, with positive IOD events associated with positive sea level anomalies in SWIO and negative in EEIO (e.g. in 1994 and 1997). When considering tide gauge locations, this anti-correlation is considerably weaker (correlation ~ -0.35) for both model and

observations. This mismatch between the results for box averages and tide gauge locations can be understood as follows: the IOD signal is rather weak at Port Louis station, which is located at the very southern border of the SWIO box (Fig. 3.1a and Table 3.1). Sea-level signal at Port Louis is dominated to a large extent by decadal variations (in contrast to the box average) - at this timescale, the SWIO stands out as partly independent from other regions (last two rows of Table 3.3) - while SWIO and EEIO exhibit opposite decadal evolution during the last 10 years of the simulation, there is no obvious relationship during the early part of the simulation (Fig. 3.5g,k).

Finally, the long-term linear trends computed from the simulated SSLA and observed sea level at tide gauge locations are given in Table 3.4. This table first illustrates that for the six regions, the model displays a long-term trend of the same sign as the considered tide gauge, with a sea-level rise at all stations in the IO (Fremantle, Langkawi, Paradip and Port Louis) and a decrease in the western Pacific (Yap B and Honiara). While the model reasonably captures the amplitude of the observed long-term trend at Honiara, Langkawi, Paradip and Port Louis, the model SSLA trend is larger than the tide gauge trend at Yap B and weaker at Fremantle.

Tide gauge location	Tide-gauge (m/Century)	Model (m/Century)
Yap B	-0.055	-0.126 (0.137)
Fremantle	0.137	0.029 (0.034)
Honiara	-0.482	-0.446 (-0.001)
Langkawi	0.067	0.053 (0.077)
Paradip	0.092	0.069 (0.089)
Port Louis	0.203	0.311 (-0.006)

Table 3.4: Linear trend of observed sea level and model steric sea level at tide gauge locations. For the model, bold values indicate linear trends calculated over the period when observations are available while the values in parenthesis indicate the linear trend calculated over the entire 1966-2007 period.

When the SSLA trend is calculated over the entire model period (values in bracket), its value varies considerably, even changing in sign at Yap B and becoming negligible at Port Louis and Honiara. This illustrates the strong sensitivity of the sea-level trend to the period considered, which can partly be attributed to the aliasing by the interannual and decadal variability. To summarize, the above results demonstrate that the simulation captures interannual and decadal sea-level variations reasonably well over periods where observational data from satellite and tide gauge are available. In addition, our analysis suggests that interannual and decadal variations in both model and observations are very similar among the WAC, NWP and SWP regions and

between the EEIO and BoB while the SWIO region stands out as partly independent from other regions of the Indo-Pacific sector at decadal time scales. In the following, I therefore use the modelled SSLA with some confidence to infer the interannual and decadal sea-level variability at the basin scale over the 1966-2007 period and investigate the main processes responsible for these changes.

3.4 Decadal sea-level variations and related mechanisms

Fig. 3.4a-b shows the standard deviation of the model SSLA at both interannual and decadal time scales. Regions of maximum decadal variability are also home to strong interannual fluctuations in the western Pacific and the IO (NWP, SWP, SWIO, EEIO, WAC and BOB). This may indicate some relationship between the variability at these two time scales, even though the amplitudes at decadal time scales are nearly half of those in interannual variations in NWP, SWP and WAC and half to one-third in EEIO, BoB and SWIO.

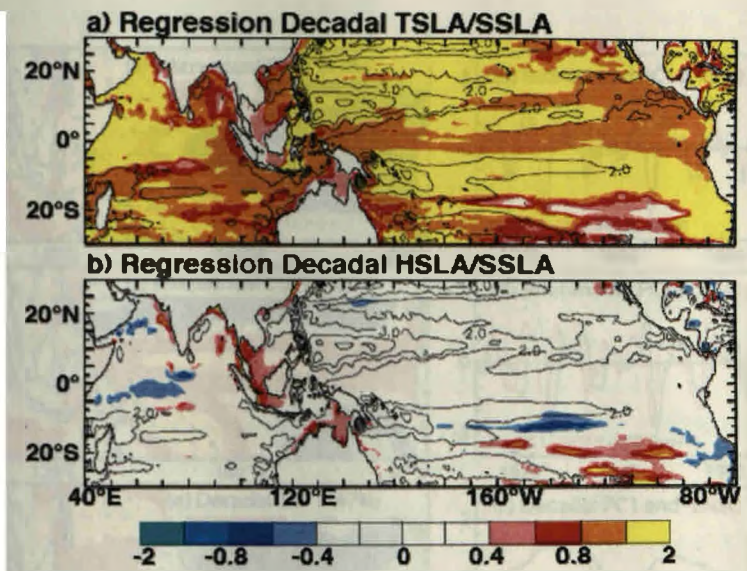


Fig. 3.6: Regression coefficients of model (a) thermosteric and (b) halosteric sea level to steric sea level at decadal time scales. The standard deviation of decadal steric sea level is also shown by contours on each panel.

It is however to be noted that, while interannual variability displays a clear maximum in the eastern equatorial Pacific explained by Kelvin wave response to interannual wind anomalies in the equatorial Pacific (see Chapter 2), no such maximum appears at decadal time scales. The strong long-term change diagnosed in the model for the SWIO (Fig. 3.4c) region has been discussed earlier by Han et al. (2010), who suggested that it is due to an intense Walker and Hadley circulation in the tropical IO, partly attributable to rising levels of atmospheric greenhouse gases. Fig. 3.4, however, illustrates that this long-term trend has weaker amplitude in most of the Indo-Pacific sector as compared to both interannual and decadal variations, ranging from a bit less than half of decadal variations in the BoB and SWIO. As seen in Fig. 3.6, decadal SSLA variations are almost entirely driven by thermosteric variations, with halosteric variations playing a significant role in only a few regions (e.g. western Indonesian seas and

north of Australia, along the rim of eastern and northern BoB and off the west coast of India, north of 10N). A similar conclusion can be drawn for interannual time scales (not shown). Large-scale interannual and decadal sea-level variations discussed in the following sections are hence essentially associated with temperature changes in the upper thousand meters layer over the Indo-Pacific ocean.

3.4.1 Basin-scale pattern of sea-level

The large-scale interannual and decadal SSLA variations in the tropical Indo-Pacific region are inferred using EOF analysis over the domain (40E:80W; 15S:15N). The first two EOFs and the corresponding principal components (PC) for both interannual and decadal time scales are displayed in Fig. 3.7. The regression coefficients of the zonal and meridional wind stress to the normalized PC of each EOF have also been overlaid in each panel as vectors.

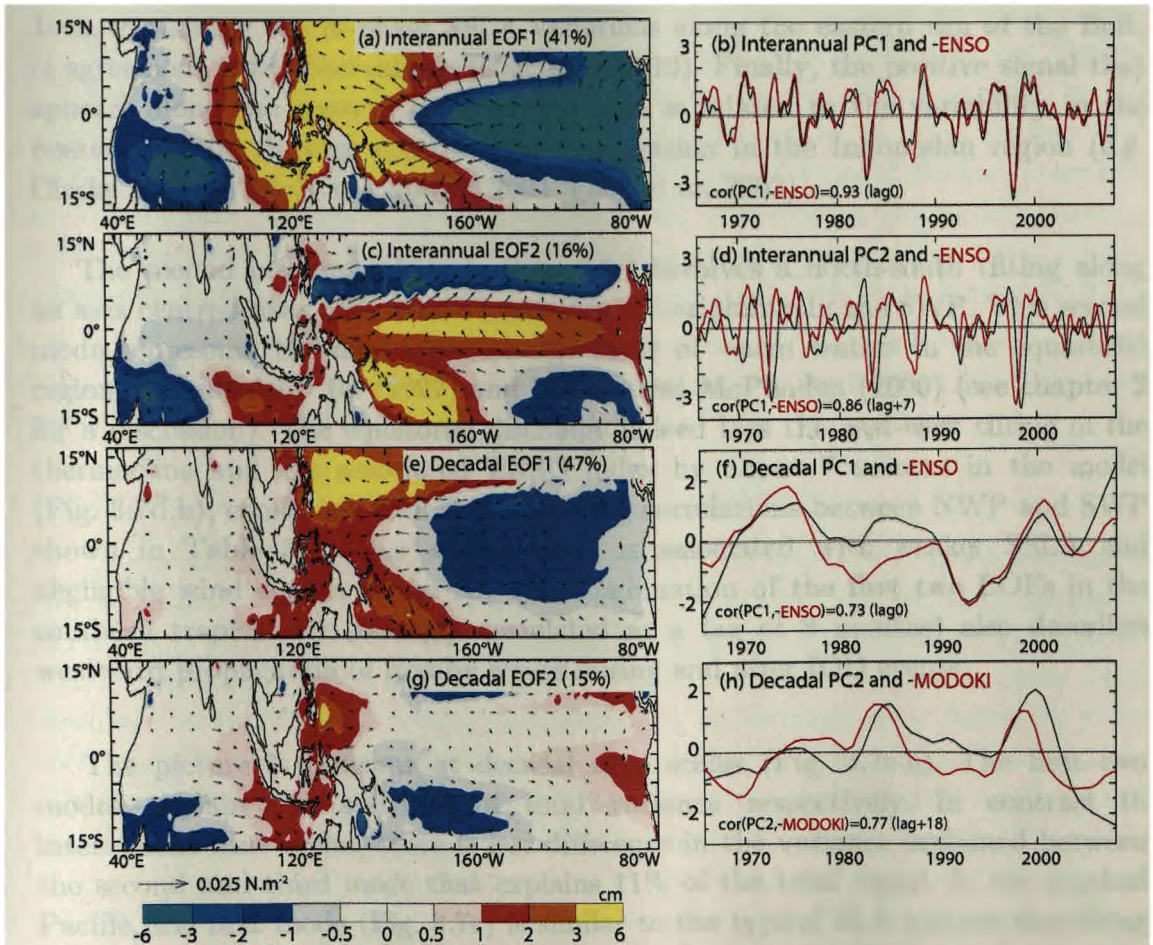


Fig. 3.7: First two EOF patterns of the model SSLA over the Indo-Pacific sector (left panels) and their corresponding normalized principal components (right panels) at interannual (a-d) and decadal time scales (e-h). The arrows show the wind stress (u, v) components regressed onto each normalized PCs. The percentage of total variance explained by each EOF is shown in brackets. Interannual ENSO index is overlaid on panels b and d, decadal ENSO index on panel f and decadal Modoki index on panel h (these indices are multiply by -1 for a better visual agreement). The maximum lag-correlation between PC and corresponding index is also shown in each panel. A positive lag indicates index leads PC.

At interannual time scales, the first two modes respectively explain 41% and 16% of the total variance with each of the higher modes representing less than 5%. These EOF modes for interannual time scales agree well with analysis by Meinen and McPhaden (2000) over the 1980-1999 period (their Fig. 3). The first mode (Fig. 3.7a) represents an east-west tilting mode in the tropical Pacific, typical of the mature phase of La Niña events with an anomalously shallow thermocline in the east, deep thermocline in the west and related easterly wind anomalies at the equator (Harrison and Larkin 1998). The corresponding PC is indeed correlated (0.93) with the interannual ENSO index at zero lag (Fig. 3.7b). Minima of EOF1 time series (Fig. 3.7b) are observed during the largest El Niño events during the past 50 years (1972, 1982, 1986 and 1997). As IOD events tend to co-occur with ENSO events, EOF1 also displays typical features of negative IOD events (Saji et al. 1999, Webster et al. 1999), i.e. positive SSLA in the eastern IO along the coast of Java and Sumatra and negative SSLA in the SWIO (Fig. 3.7a). IOD-related wind anomalies generate equatorial Kelvin waves that further propagate northward as coastally-trapped Kelvin waves as they reach Java, explaining the in-phase SSLA variations along the eastern rim of the BoB, in agreement with observations (Rao et al. 2010). Finally, the positive signal that appears along the western coast of Australia is related to the variability in the western Pacific through coastal wave propagation in the Indonesian region (e.g. Clarke 1991, Wijffels and Meyers 2004, Feng et al. 2003).

The second interannual mode (Fig. 3.7c) involves a north-south tilting along an axis centred near 5°N, with a maximum of variability in the SWP. This second mode represents the discharge-recharge mode of warm waters in the equatorial region, described by Jin (1997) and Meinen and McPhaden (2000) (see chapter 2 for a discussion). The equatorial discharge indeed lags the east-west tilting of the thermocline and the associated ENSO index by about 7 months in the model (Fig. 3.7d,b), consistent with theory and lag correlations between NWP and SWP shown in Table 3.3. This second mode is associated with weaker SSLA and negligible wind signals in the IO. The combination of the first two EOFs in the southern tropical IO (strongly correlated at a lag of 8 months) also describes westward propagation of Rossby waves during and after IOD events.

The picture is different at decadal time scales (Fig. 3.7e-h). The first two modes explain 47% and 15% of total variance respectively. In contrast to interannual time scales, there is less difference in the variance explained between the second and third mode that explains 11% of the total signal. In the tropical Pacific, the first mode (Fig. 3.7e) is similar to the typical SLA pattern describing decadal variations of the subtropical cells (see Fig. 1 of LM08), which has been related to decadal ENSO (or IPO) variability. Decadal PC1 indeed correlates well (0.73) with decadal ENSO index (Fig. 3.7f). The wind pattern of Fig. 3.7e indeed induces a typical Kelvin/Rossby upwelling/downwelling response. The geostrophic flow associated with these waves results in an increase of equatorward convergence of pycnocline waters, i.e. a strengthening of the lower branch of the Pacific sub-tropical cells since the early 1990s (Fig. 3.7f, LM08) and a weakening

before (Fig. 3.7f, McPhaden and Zhang 2002). This pattern is related to a sea-level rise along the WAC, consistent with the decadal variability in this region being forced remotely by winds in the tropical Pacific and transmitted via the Indonesian Archipelago (Feng et al. 2010), similar to interannual time scales. Interestingly, this first mode is neither related to SSLA anomalies nor to any wind signals anywhere in the vicinity of equatorial IO. These results are in apparent contradiction with LM08, who revealed a near-coherent large-scale decadal variability in much of the Indo-Pacific region, with trade winds, SLA and sub-tropical cells anti-correlated at decadal time scales in the two oceans. This will be further discussed in the following section.

The second mode (Fig. 3.7g) displays smaller scale patterns as compared to the first mode. This mode shows decadal variations in the far western Pacific in the Mindanao dome region (see also Kashino et al. 2009), varying in phase with the west Australian and Indonesian coast. Opposite signals are found in the central Pacific near the dateline and in the SWIO region. In contrast to the first mode, this Indo-Pacific SSLA pattern is associated with wind anomalies in both the Indian and Pacific Oceans, reminiscent of decadal modulation of the Walker circulation intensity: easterlies in the far western Pacific, and westerlies in the eastern equatorial and south tropical IO. This Indo-Pacific sea-level pattern and related wind variations is reminiscent of the imprint of decadal Modoki described by Behera and Yamagata (2010; their Fig. 2a). The related PC indeed shows a 0.77 correlation with decadal Modoki index at 18 months lag (Fig. 3.7h). Depending on the period considered, the temporal evolution of the first two EOFs for decadal time scales can either vary in phase (as during the late 1990's where they both show a decrease), or vary in phase opposition (as seen at the end of the period).

3.4.2 Mechanisms of regional decadal variability

The possible driving mechanisms of decadal SSLA variability in each region is discussed in this section. I chose not to present the same analysis for interannual variability, because it shows well-known ENSO and IOD patterns (and inter-basin connection between the western Pacific and WAC), which have been discussed in the previous section and elsewhere in literature (e.g. Landerer et al. 2008, Wijffels and Meyers 2004). Prior to entering to this section, readers may refer back to chapter 2 for a theoretical considerations on large-scale sea-level and thermocline adjustments to a prescribed wind field.

SSLA in the NWP and SWP largely co-varies at decadal time scales, with a 0.71 correlation (Table 3.3). Decadal variations in the western tropical Pacific (NWP and SWP) are both strongly related to variations in the extra-equatorial wind stress curl that occur east of the sea-level variability (Figs. 3.8a and 3.8e). These SSLA patterns and associated wind structures are similar to those of the first EOF of Indo-Pacific decadal variations displayed in Fig. 3.7e, with rather weak wind signals in the IO.

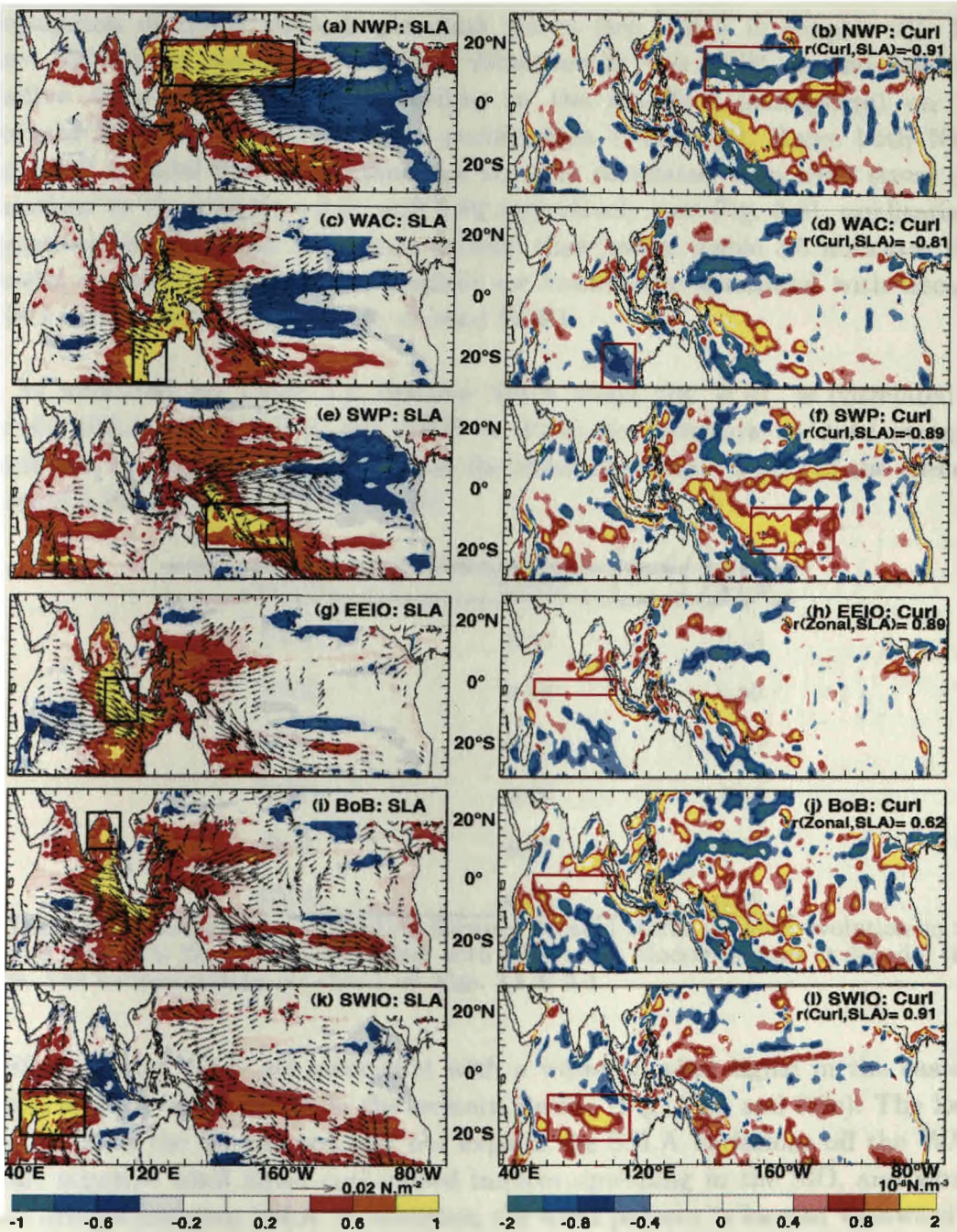


Fig. 3.8: (a) Correlation of model SSLA averaged over the NWP to the entire Indo-Pacific region (color) and regression of wind stress components (arrows) to the model normalized SSLA averaged over NWP. (b) Regression of wind stress curl to the normalized model SSLA averaged over NWP. Same for WAC (c-d), SWP (e-f), EEIO (g-h), BoB (i-j) and SWIO (k-l). The numbers provided below the title in the right column indicate the correlation coefficient between the average SSLA within the black frame (on the left) and average zonal wind stress (or wind stress curl) within the red frame (on the right).

The northern flank of the equatorial easterly wind perturbation (Fig. 3.8a) results in a negative wind stress curl (i.e. downwelling in the northern hemisphere; red box on Fig. 3.8b) east of the maximum SSLA variability in NWP. This is hence coherent with wind-driven downwelling, and westward

propagation of SSLA through planetary waves (see eqn 3 in chapter 2)⁴. The same mechanism accounts for SSLA variations in the SWP, as the result of positive wind stress curl (downwelling in the southern hemisphere) on the southern flank of the easterly wind perturbation (Fig. 3.8e). Hence both NWP and SWP decadal SSLA variations are strongly correlated with wind stress curl variations to the east ($r=-0.91$ and 0.89 respectively; see Fig. 3.8), qualitatively suggesting the Sverdrup balance at decadal time scales. Table 3.5 indicates that decadal variations in these two regions are moderately correlated with decadal ENSO variations, consistent with decadal EOF1.

As indicated on Table 3.3, decadal SSLA along the WAC is correlated to decadal SSLA variations in the NWP ($r=0.64$) and displays an even stronger correlation ($r=0.89$) with SSLA within the Mindanao Dome region in the western equatorial Pacific (5N-5S; 120E-160E).

Regions	ENSO	Modoki
NWP	-0.57	0.33
SWP	0.37	0.00
WAC	0.52	-0.71
EEIO	-0.26	-0.36
BoB	-0.07	-0.49
SWIO	-0.08	0.19

Table 3.5: Maximum lag-correlation between decadal steric sea-level evolution in the selected regions in the Indo-Pacific sector with ENSO and Modoki indices at decadal time scales. The various regions are shown on Figs. 3.1 & 3.3.

SSLA in the WAC are associated with a westerly wind signal in the eastern IO and easterly wind signals in the western Pacific (Fig. 3.8a and 3.8c). The local wind signal in the IO can however not explain the SSLA variations off the WAC as this negative wind stress curl indeed induces upwelling in the SIO, and would hence drive a negative SSLA. In addition, the wind pattern is located westward of the maximum SSLA perturbation, which is not consistent with the westward propagation of SSLA signals by planetary waves. The signal at the WAC is hence linked to the upstream influence of the western Pacific through the Indonesian throughflow at decadal time scales (e.g. Feng et al. 2004, 2010). These decadal fluctuations along the WAC are more strongly tied to decadal Modoki

⁴ If the variation of Coriolis parameter f with latitude is considered, the Ekman pumping velocity induced by interior wind forcing has two terms:

$$W_{Ek} = \frac{1}{\rho_{of_0}} \left[\nabla \times \vec{\tau} + \frac{\beta f}{f_0} \tau^x \right]$$
 .. (a); and the second term in the R.H.S. of (a) indicates the convergence/divergence due to the latitudinal gradient of the meridional Ekman transport due to beta effect (a change in magnitude of f with change in latitudes; $\beta = f_y$, being stronger equatorward, the meridional Ekman transport will be also stronger equatorward). Hence the beta effect also contribute to the Ekman pumping velocity.

fluctuations (-0.71) rather than that of decadal ENSO (0.52). This result is in line with the very strong correlation of WAC variations with SSLA variations in the Mindanao dome region, a typical feature associated with decadal Modoki variability (Fig. 3.8g). The dynamical arguments stated above suggest that those changes should be balanced by zonal wind stress changes in the equatorial Pacific. The high (0.8) correlation between the SSLA in the WAC and zonal wind stress to the west of the dateline in the equatorial Pacific (not shown) further supports this hypothesis. Local wind variations in the IO may however limit the westward expansion of remotely-driven decadal sea level variations at the WAC, as they will tend to counteract the Rossby wave signals radiated from the WAC region.

With the exception of WAC and BoB, most of the decadal SSLA variability over the key regions (the regions of maximum variability) in the IO can directly be related to large-scale wind perturbations. EEIO and BoB decadal SSLA are in phase ($r=0.86$; Table 3.3) and are both strongly related to zonal wind variations over the central and eastern equatorial IO (Figs. 3.8g and 3.8i). Equatorial westerly wind stress anomalies indeed generate downwelling Kelvin waves, which induce SSLA variations in the eastern equatorial IO, and then propagate into the BoB as coastally-trapped Kelvin waves, as observed at intra-seasonal (Vialard et al. 2009), seasonal (McCreary et al. 1996) and interannual (Rao et al. 2010) time scales. The strong correlation between the wind variations in the equatorial IO and SSLA variations in the EEIO and BoB ($r=0.89$ and 0.62 respectively) further support this hypothesis. Decadal variability in these regions is not strongly related to variations in the western Pacific, with correlations between EEIO and NWP smaller than 0.5 at decadal time scales (Table 3.3), and only very modestly related to decadal Modoki variations (-0.36/-0.49 correlation).

In contrary to the variability at interannual time scales, SWIO SSLA variability stands out as largely independent from the north west Pacific variations ($r=0.08$; Table 3.3) and to a lesser extent from the variations in other regions in the IO, such as the EEIO ($r=-0.42$; Table 3.3). SSLA decadal variations in the SWIO are highly correlated ($r=0.91$) with wind stress curl further east (Fig. 3.8l), hence suggesting a similar mechanism (wind stress curl forcing in the fast-wave limit) as in the NWP and SWP. In the model, the wind stress curl in the SIO is weakly (~ 0.23 , Table 3.5) correlated with equatorial Pacific decadal zonal wind stresses, hence explaining the weak connection between the SWIO and the western Pacific ($r=0.08$, Table 3.3). Similarly, SWIO SSLA decadal variations is only weakly correlated with the two main modes of decadal Pacific variability (Table 3.5). The wind stress curl in the SIO is moderately related to equatorial IO zonal wind stress anomalies ($r=-0.62$). This is probably due to the fact that wind stress curl in the SIO is not only influenced by equatorial wind stress, but also by wind variations further south. This influence of extra-equatorial wind stress is hence explaining the relatively weak correlation ($r=-0.42$, Table 3.3) between the SWIO and EEIO SSLA variability at decadal time scales.

3.5 Robustness of the decadal wind forcing

The results discussed so far have been obtained from the NEMO OGCM forced with ERA-40 derived wind stress and these results may largely rely on the forcing wind field, as decadal wind variability may not be well constrained before the satellite era due to the scarcity of in-situ near surface wind observations. Hence, I analysed decadal wind variability in the NCEP, 20CR reanalyses and WASWind datasets over the model forcing period (1958-2007) to assess the robustness of the model results.

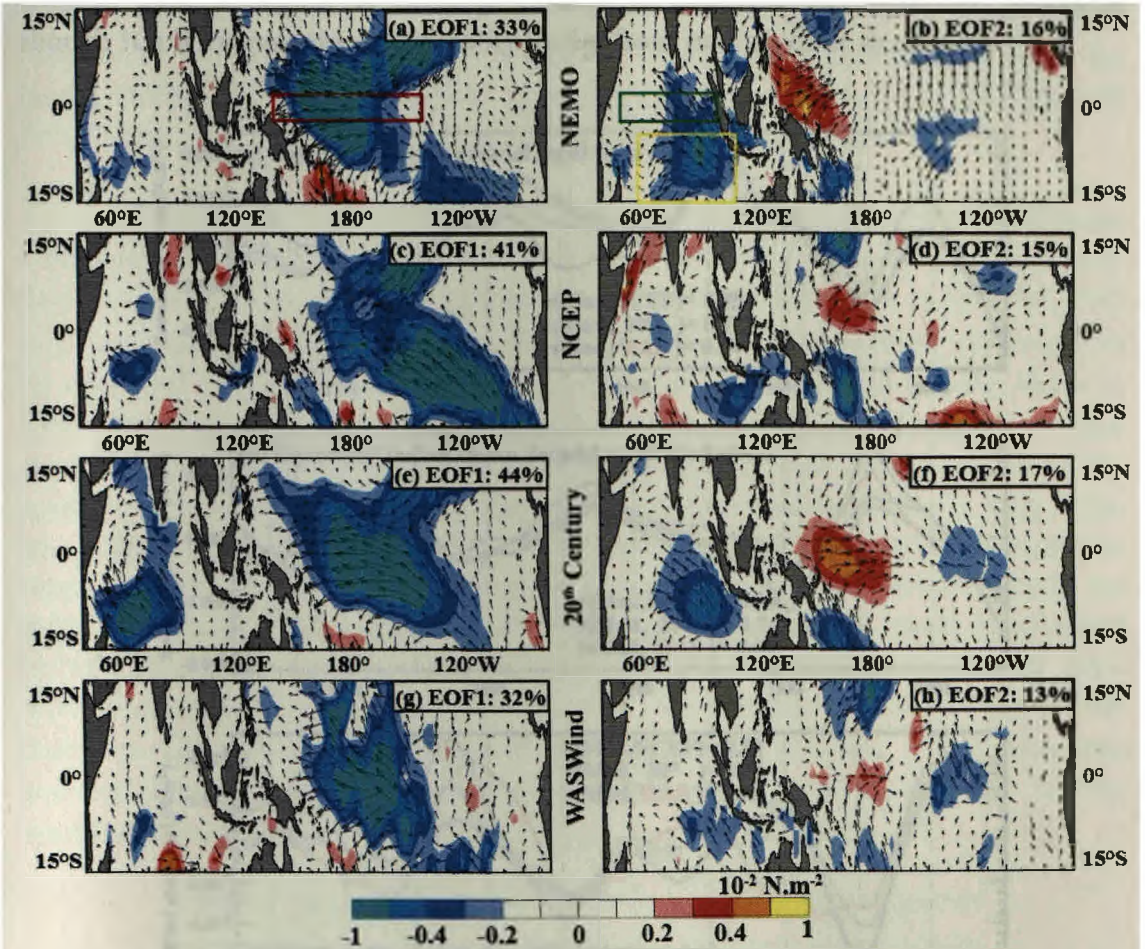


Fig. 3.9: First two EOF patterns of the zonal wind stress over the Indo-Pacific sector at decadal timescale for (a-b) model forcing, (c-d) NCEP reanalysis, (e-f) 20CR and (g-h) WASWind product. The arrows indicate the wind stress components regressed onto the normalized PCs. The percentage of variance explained by each EOF is shown in brackets.

An EOF analysis is done to extract the main mode of wind decadal variability depicted by each dataset. The first EOF mode displays similar patterns in each of the products (Fig. 3.9). It explains between 32% (WASWind) and 44% (20CR) of the total variance and exhibits strong easterly wind anomalies in the central Pacific for all products. This wind pattern is reminiscent of the wind variations associated with model decadal SSLA in the NWP and SWP (Fig. 3.9a and 3.7e, whose associated principal components are correlated at 0.92) and is largely related to the decadal ENSO (not shown). Despite the broad pattern agreement in the Pacific, there is more discrepancy in the IO. In most datasets, the wind

signature in this basin is rather weak, except in the 20CR reanalysis, where strong south-easterly anomalies in the SWIO co-vary with the equatorial Pacific wind signal. The second mode of decadal wind variability also displays some similarities between the different datasets and explains between 13% (WASWind) and 17% (20CR) of the total variance (right panel of Fig. 3.9). It consists of south-easterly wind anomalies in the southeastern IO combined with westerly wind anomalies in the far western Pacific. The amplitude and location of these wind signals, however, considerably vary from one dataset to another. This EOF analysis hence reveals that the spatial structure of the decadal variability in the tropical Pacific region is broadly consistent amongst the different products, though it's IO signature considerably varies from one product to another.

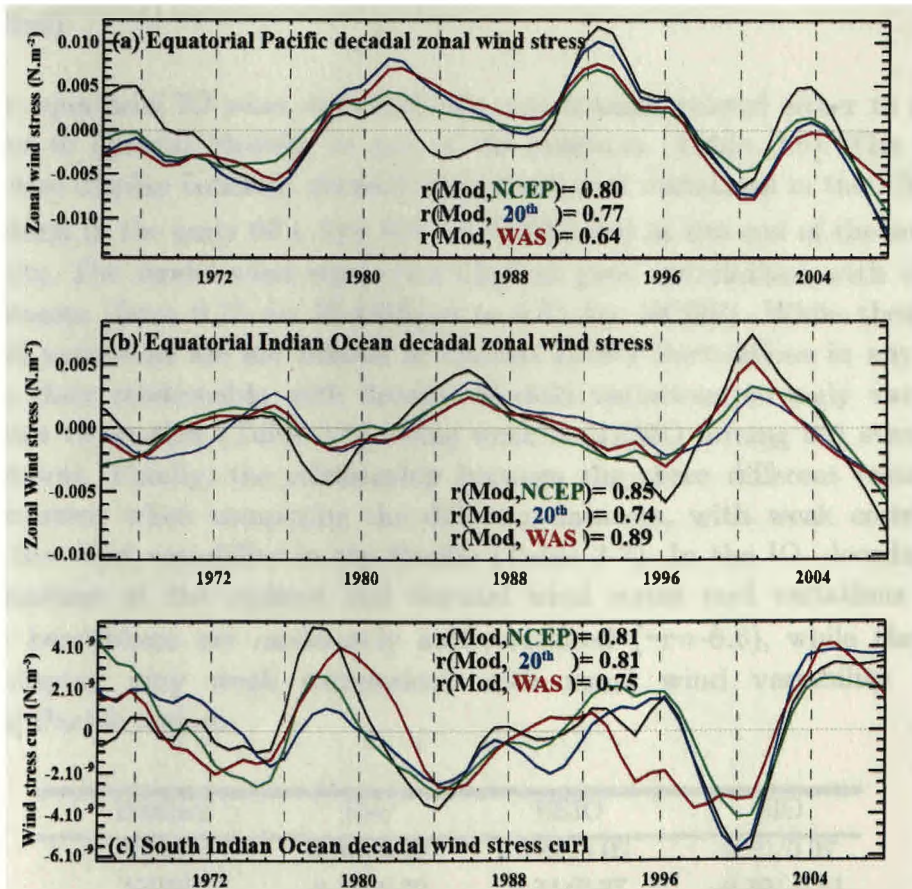


Fig. 3.10: Time series of decadal (a) equatorial Pacific zonal wind stress (140E-140W; 2.5-N-2.5S; red box on Fig. 3.8a), (b) equatorial IO zonal wind stress (60E-100E; 2.5N-2.5S; green box on Fig. 3.8b) and (c) south IO wind stress curl (60E-110E; 20S-5S; yellow box on Fig. 3.8b) from model output (black line, similar to ERA40), NCEP reanalysis (green line), 20th century reanalysis (blue line) and WASWind dataset (red line). The correlation between the model forcing and other datasets is indicated on each panel.

Mechanisms of decadal SSLA variability outlined in Section 3.4 stress the importance of wind variations in three key regions of the tropical Indo-Pacific ocean. Zonal wind variations in the western equatorial Pacific largely drive decadal SSLA in the western Pacific and along the WAC. Zonal wind variations in the equatorial IO drive decadal SSLA in the EEIO Ocean and the BoB. Wind stress curl variations in the Southeast IO drive SSLA in the SWIO. Decadal

evolution of wind field in these three regions are displayed in Fig. 3.10, for the four datasets (ERA-40 NCEP, 20CR, WASWind). The four datasets display coherent decadal zonal wind variations in the equatorial Pacific region (Fig. 3.10a), with local maxima in the early-70's, early-80's and early-90's and around 2004. Model wind variations have correlations with the winds in other products ranging from 0.64 (WASWind) to 0.80 (NCEP). As shown in Table 3.6, these Pacific wind variations are strongly tied to decadal ENSO variations for all products, with correlation ranging from -0.79 to -0.89, and not strongly related to decadal Modoki variations. Similarly, all wind datasets display very coherent decadal zonal wind fluctuations in the equatorial IO (Fig. 3.10b), with local maxima in the mid-70's, mid-80's and around 2000 and correlation between the model forcing and other products ranging from 0.74 (20CR reanalysis) to 0.89 (WASWind).

These equatorial IO wind variations are not strongly related either to decadal ENSO nor to decadal Modoki in any of the products (Table. 3.6). The various datasets also display coherent decadal wind stress curl variations in the SIO, with local maxima in the early 60's, late 70's, early 90's and at the end of the record in all datasets. The model wind stress curl displays good correlations with those in other datasets (from 0.75 for WASWind to 0.81 for NCEP). While these wind stress curl variations are not related to decadal ENSO fluctuations in any of the products, their relationship with decadal Modoki variations strongly vary from one product to another (Table 3.6), being weak in NEMO forcing but stronger in other datasets. Finally, the relationship between the three different regions are quite consistent when comparing the different datasets, with weak correlations between the wind variability in the Pacific (Table 3-7). In the IO, decadal zonal wind variations at the equator and decadal wind stress curl variations in the Southern hemisphere are moderately anti-correlated ($\sim r=-0.6$), while these two regions display very weak correlations with zonal wind variability in the equatorial Pacific region.

Dataset	Pac	EEIO	SIO
NEMO	-0.89/0.22	-0.42/0.02	0.20/0.07
NCEP	-0.79/0.20	0.41/0.37	-0.30/-0.61
20CR	-0.83/0.25	0.16/0.40	-0.15/-0.66
WASWind	0.80/-0.28	-0.41/-0.35	0.06/0.51

Table 3.6: Maximum lag-correlation between decadal Indo-Pacific zonal wind stress PC1 and PC2 with decadal ENSO and Modoki index respectively for the four wind stress datasets considered. A positive lag indicates that the climate index leads zonal wind stress variations.

	Model	NCEP	20CR	WASWind
Zonal(Pac)/Zonal(EIO)	-0.18	-0.10	0.08	-0.25
Zonal(Pac)/Curl(SIO)	0.23	0.21	-0.03	0.18
Zonal(EIO)/Curl(SIO)	-0.62	-0.76	-0.64	-0.56

Table 3.7: Cross-correlation between decadal wind stress variations in selected regions of the Indo-Pacific sector, for different datasets. Zonal(Pac) refers to the equatorial Pacific zonal wind stress (140E-140W; 2.5N-2.5S; red box on Fig. 3.8a), Zonal(EIO) to the equatorial IO zonal wind stress (50E-100E; 2.5N-2.5S; green box on Fig. 3.8b) and curl(SIO) to south IO wind stress curl (60E-110E; 20S-5S; yellow box on Fig. 3.8b).

3.6 Long-term trends

3.6.1 Pattern of steric sea-level long-term trend

IO SSLA trends on Fig. 3.11a are similar to those obtained by Timmerman et al. (2010) using the SODA ocean reanalysis. The picture is also similar to modelling results in Han et al. (2010). This is somewhat normal considering the fact that these studies also used ERA-40 to force their ocean models, as I did. SSLA has decreased substantially in the SWIO whereas it has increased elsewhere in the IO during this period (Fig. 3.11a). This decrease is also evident from Fig. 3.4k. This trend pattern is likely to be driven by long-term changes in surface wind fields. The trend of surface wind stress pattern displays an enhanced convergence around 15S owing to the anomalous north-westerly winds from the equator (Fig. 3.11b). These wind changes result in a large negative wind stress curl anomaly around 10S in the IO, dynamically consistent with the SSLA decrease in the SWIO region.

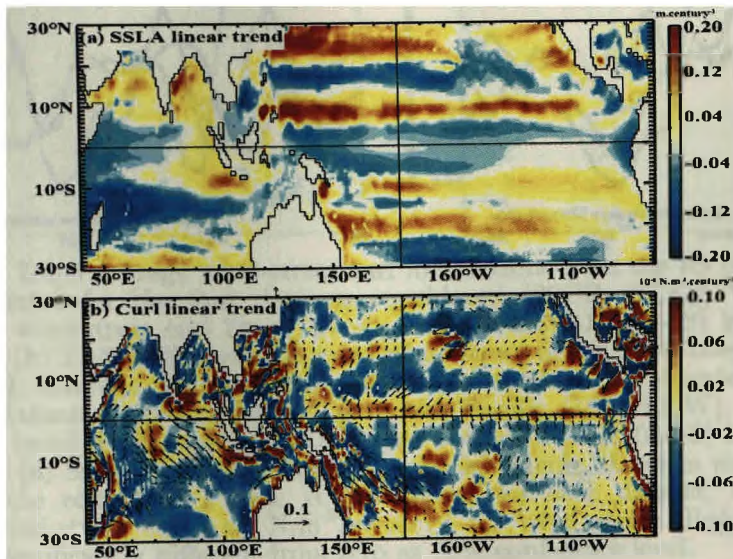


Fig. 3.11: Linear trend over the 1966-2007 period for (a) model steric sea level and (b) model wind stress curl (in colors). The vectors on panel (b) show the wind-stress linear trend. Unit is m.century^{-1} for steric sea level, $\text{N.m}^{-3}.\text{century}^{-1}$ for wind-stress curl and $\text{N.m}^{-2}.\text{century}^{-1}$ for wind stress.

3.6.2 Robustness of the wind forcing trends

In this section, I assess the robustness of the model SSLA long-term trends in the Pacific and IO in evaluating the robustness of the wind linear trend estimate across wind products (model forcing (ERA-40), WASWind, NCEP, 20CR) and to the trend estimation period. Fig. 3.12 displays regional long-term trends in the four wind datasets. While wind stress decadal variations display some consistency (section 3.5), it is not the case for the long-term linear trends. While the model forcing exhibits a significant negative Ekman pumping signal in the southern IO between 30S and 10S, trends are very different in other datasets. 20CR displays a positive trend in Ekman pumping south of 10S and a negative trend further north (with a minimum around 5S). NCEP displays a positive Ekman pumping trend north of 20S. When averaging between 20S and 5S (where largest SSLA trends are found in the southwestern IO, Fig. 3.11a), it appears that the model dataset is showing a significant negative trend (consistent with the SSLA decrease in this region), while NCEP is showing a positive curl trend and the two other datasets showing no significant trends.

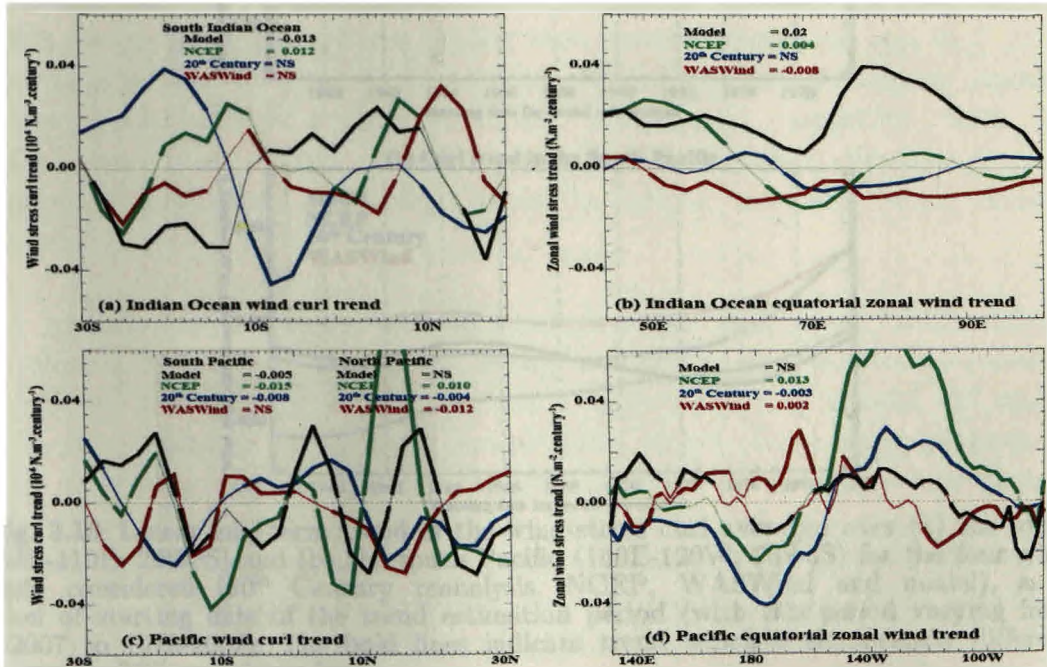


Fig. 3.12: (a) Zonal average wind-stress curl linear trend over the IO (60E-110E) over the 1966-2007 period for the four datasets considered (20CR, NCEP, WASWind and model). Average wind-stress curl linear trend in the South IO (20S-5S) is also indicated for each dataset. (b) 2.5N-2.5S averaged zonal wind stress linear trend over the 1966-2007 period in the IO. Average zonal wind stress linear trend in the equatorial IO is also shown for each dataset. (c) Same as (a) but in the Pacific (160E-120W). Average wind-stress curl linear trend in the north (5N-20N) and south Pacific (20S-5S) is also indicated for each dataset. (d) Same as (b) but in the equatorial Pacific. Average zonal wind stress linear trend in the equatorial Pacific is also shown for each dataset. Units are $\text{N}\cdot\text{m}^3\cdot\text{century}^{-1}$ for wind-stress curl and $\text{N}\cdot\text{m}^2\cdot\text{century}^{-1}$ for wind stress. Bold lines indicate trends that are significantly different from zero at 95% confidence level.

Similarly, IO equatorial zonal wind stress linear trends largely differ amongst the datasets (Fig. 3.12b): the model displays a significant positive zonal wind

stress trend all over the equatorial region, WASWind exhibits a negative trend while NCEP and 20th century reanalysis display latitude bands where trend is alternatively positive and negative. When averaged within the equatorial waveguide, results still vary depending on the wind product: the model displays a positive trend, while other products display weak or insignificant changes. Wind products exhibit similar trend discrepancies in the Pacific, with opposite signs for the averaged trends of north Pacific wind stress curl (Fig. 3.12c) and equatorial Pacific zonal wind stress (Fig. 3.12d). The only region where the trend is reasonably consistent amongst the datasets is the South Pacific where all the three products display a negative trend, consistent with the SSLA decrease discussed in Timmermann et al. (2010).

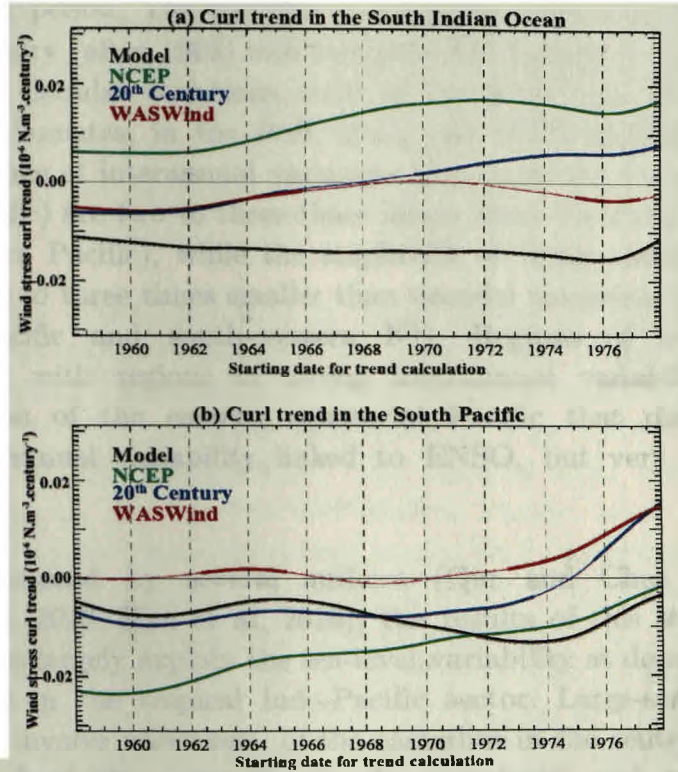


Fig. 3.13: Linear long-term trend of the wind-stress curl averaged over (a) the south IO (60E-110E; 20S-5S) and (b) the south Pacific (160E-120W; 20S-5S) for the four wind datasets considered (20th Century reanalysis, NCEP, WASWind and model), as a function of starting date of the trend estimation period (with this period varying from 1958-2007 to 1978-2007). The bold lines indicate trend which is significantly different from zero at 95% confidence level.

The trend is not only sensitive to the dataset used but also to the period over which it is estimated. Fig. 3.13 provides the average wind-stress curl trend estimate in the South IO and South Pacific as a function of the starting date (with the trend computation period varying from 1958-2007 to 1978-2007). In the SIO (Fig. 3.13a), while NCEP and the model forcing exhibit a consistent wind-stress curl trend for the range of periods considered (positive for NCEP, negative for the model), trends estimation for WASWind product and the 20th century reanalysis varies depending on the estimation period, being either negative if the starting date to calculate the trend is chosen before 1966 or insignificant or positive if the starting date is chosen after 1966. Results are more coherent for

the South Pacific where three datasets (model forcing, 20th century and NCEP reanalysis) show a consistent negative wind-stress curl if the starting date to calculate the trend is chosen before 1974 while the WASWind trend generally remains insignificant. Similar discrepancies are seen among products by also varying the end-date, or by changing the box definition (not shown). This indicates that long-term trends are even less consistent than decadal variations of the wind field in current reanalysis products.

3.7 Summary

In this chapter, I investigate the decadal steric sea-level variations and long-term trends in the Indo-Pacific sector using results from an OGCM simulation over the 1966–2007 period. The simulation compares favourably with sea level from satellite altimetry (after 1993) and available tide gauges in the Indo-Pacific region. The largest decadal variations occur in the NWP and SWP, along the coast of Java and Sumatra, in the BoB, along the WAC and SWIO. In these regions, the amplitude of interannual variations (up to 10 cm standard deviation in the western Pacific) are two to three times larger than the decadal ones (up to 5 cm in the western Pacific), while the amplitude of linear trend over the full record is about two to three times smaller than decadal variations (up to 2 cm in the northwest Pacific and south-western IO). Regions of largest decadal variations coincide with regions of strong interannual variability, with the noticeable exception of the eastern equatorial Pacific that displays a clear maximum of interannual variability linked to ENSO, but very small decadal variability.

As already discussed by several authors (Qiu and Chen 2006; LM08, Timmermann et al. 2010; Han et al. 2010), the results of this study confirmed that wind variations largely explain the sea-level variability at decadal and multi-decadal time-scales in the tropical Indo-Pacific sector. Large-scale patterns of decadal variability involve variations of the easterlies in the central and western Pacific Ocean, and of the westerlies in the equatorial and south IO. The equatorial decadal wind variations are relatively independent between the Indian and Pacific Oceans, in contrast to variations at interannual time scales, which are clearly linked through the tendency of ENSO and the IOD to co-occur. The strong decadal wind stress curl fluctuations on the northern and southern flanks of the western Pacific force Rossby waves, responsible for decadal variations in the NWP and SWP regions. Oceanic teleconnections transmit this signal from the western Pacific to the WAC, through equatorial and coastal waveguides. This results in the decadal variability along the WAC that varies in phase with that in the western Pacific, in a similar way to what happens at interannual time scales (correlation around 0.7 for both time scales over 1966–2007 period). These results confirm the strong relationship between these two regions at interannual time scales (e.g. Clarke 1991; Wijffels and Meyers 2004; Feng et al. 2005), but also the observational analysis from tide gauge data performed by Feng et al. (2010) at decadal time scales.

In the IO, the results further reveal the modulation of the strength of the equatorial trade winds that drive Kelvin waves, which propagate to the EEIO and BoB through the equatorial and coastal wave guides. As a result, SSLA variations in these two regions are highly correlated ($r = \sim 0.8$) at both interannual and decadal time scales. While Rao et al. (2010) discussed this connection using satellite data for interannual time scales, it had not been reported earlier for decadal time scales. Ekman pumping variations south of the equator in the IO, drive planetary waves that induce decadal sea level variations in the SWIO. Interannual variations of SSLA in the SWIO, encompassing Seychelles-Chagos thermocline ridge, have a -0.7 correlation with those in the EEIO, but this correlation considerably weakens (-0.4) at decadal time scales. This weaker association at decadal time scales probably comes from the fact that the strength of equatorial easterlies is not the only factor controlling the Ekman pumping south of the equator at decadal time scales. In addition, decadal steric sea level variations in the south-western and to a lesser extent in the eastern equatorial IO are independent of decadal variations in the NWP in agreement with the independency found in the decadal wind forcing over the Indian and Pacific oceans.

In agreement with Timmermann et al. (2010), most of the steric sea level decadal signals in our model experiment are dynamically consistent with large-scale wind stress forcing. I have hence investigated the robustness of the decadal wind stress forcing in our model by comparing it with three other products (WASWind product, NCEP and 20CR). The decadal wind evolution in key regions (zonal winds in the western and central Pacific, zonal winds in the equatorial Indian ocean and wind stress curl in the SIO) are generally consistent among the different wind products. The relationships between these decadal wind variations are also very consistent among these products, with an independency between the decadal variability in the IO and the Pacific Ocean. In addition, decadal zonal wind variations in the equatorial Pacific is strongly related to decadal ENSO fluctuations in all wind products, while decadal zonal wind variations in the equatorial IO are rather independent of both decadal ENSO and Modoki variations. The decadal wind stress curl variations in the SIO are not related to decadal ENSO variations but their relationship with decadal Modoki is variable across products, illustrating the sensitivity of IO decadal wind variations to decadal Pacific climate modes.

Decadal and interannual SSLA variability shares a lot of common features such as strong variability in the western Pacific, along the coast of Java and Sumatra, in the BoB, along the WAC and SWIO. There is a strong co-variability between the western Pacific and the WAC and between the EEIO and the BoB through equatorial and coastal waveguides with similar forcing mechanisms at interannual and decadal time scales. There are also noticeable differences between interannual and decadal steric sea-level variability, such as a weaker amplitude of SSLA at decadal period compared to interannual variability, a weaker association of the Pacific and IO winds at decadal time scales, no noticeable SSLA variability

in the eastern equatorial Pacific at decadal time scales and a weaker association between the eastern equatorial and southwestern Indian ocean SSLA at decadal time scales.

Regarding the long-term linear trend of SSLA over the 1966–2007 period, results in this study agree with previous findings of Han et al. (2010) and Timmermann et al. (2010). SSLA decreases substantially in the SWIO, in response to a large negative wind stress curl trend south of the equator, whereas it increases elsewhere in the IO. In the Pacific, zonally oriented bands of alternating signs, dynamically consistent with the linear trend of curl characterize the long-term sea level trend. The very broad agreement with the results of Han et al. (2010) and Timmermann et al. (2010) is not surprising as the wind forcing used in these studies is similar to the one used in our simulation (ERA40). However, comparison of our model wind forcing with other products reveal a very strong dependence of the long-term wind stress trend to the wind product as well as a moderate dependence to the length of the period over which the trend is estimated. This reveals that estimates of long-term trends in sea level from forced ocean models need to be interpreted with caution.

3.8 Discussion

Results from this study indicate that a large part of the large-scale decadal sea-level variations in the Pacific are driven by decadal ENSO (or IPO). The related sea-level IPO pattern in the Pacific (see Fig. 3.7e) is consistent with recent analysis of altimeter data (LM08, Han et al. 2013), reconstructions (Meyssignac et al. 2012; Hamlington et al. 2013, 2014) and reanalysis (Han et al. 2013). More interestingly, the results point towards a significant role of decadal Modoki variations in shaping the decadal sea-level variations in this region, being associated with a localized but strong signature in the Mindanao dome region and a broader signature in the central equatorial and south tropical Pacific. These findings confirm the findings of Behera and Yamagata (2010), who suggested such a Modoki imprint on the Indo-Pacific decadal sea-level variations from a 12-yr satellite altimetry data analysis.

The oceanic teleconnection between western Pacific and SIO was established in observations earlier mainly through tide gauge sea-level analysis and temperature profiles from XBTs. Feng et al. (2010) described the remote influence of Pacific equatorial winds on the decadal sea-level variations along the western Australian coast. They suggested a teleconnection through the equatorial and coastal waveguide in the Indonesian throughflow, similar to what is described at interannual time scales (Clarke 1991, Clarke and Liu 1993, Meyers 1996, Masumoto and Meyers 1998, Potemra 2001, Potemra et al. 2002, Wijffels and Meyers 2004, Cai et al. 2005a, Cai et al. 2005b, Feng et al. 2003, Feng et al. 2005). The results from the present study are fully consistent with Feng et al. (2010) and other more recent works discussing the link between sea-level along the WAC and the western Pacific at decadal time scales (e.g. Scharzkopf and Boning 2011, Trenary and Han 2013, Wang et al. 2015). My model analysis

further suggests that decadal Modoki variations may have a stronger contribution than decadal ENSO variations in these Indo-Pacific oceanic teleconnections.

On the other hand, results in this study appear to contradict LM08 who suggested a possible inter-basin connection between Pacific and IO wind and sea-level decadal variability. Indeed, apart from the WAC region discussed above, I find that the model sea-level variability in other regions of the IO are relatively independent of that in the Pacific. Over the 1993-2006 period, the period studied by LM08, the principal components describing the sea-level variations over both basins (Fig. 3.6e-h) are largely in phase, with a phase change in 2000 consistent with LM08. This tendency considerably weakens over the entire 1966-2007 period (figs. 3.4a and 3.4e; Table 3.3). The present study hence suggests that the in-phase wind and related sea-level variations between the IO and IPO related variations in the tropical Pacific is not necessarily a general feature of decadal variations in those basins. This weak control of the IPO on the decadal wind variability over the IO is slightly surprising in the context of interannual variability, where ENSO and IOD shows a general tendency for equatorial wind co-variability in these two basins. These results remind those from Han et al. (2013) who showed that the IO decadal SST variability was largely in phase with the IPO before 1985, analogous to ENSO impact on the interannual IO basin mode, but out of phase since 1985. This may reflect an increasingly role of the IO in shaping Indo-Pacific decadal climate under global warming (Han et al. 2014) or simply a sign of natural variability in the IO which is independent from the Pacific. The possibility of an independency of decadal IO climate variability is further strengthened by the lack of IPO influence on decadal IOD variations (Song et al. 2007; Tozuka et al. 2007).

Results for the IO are consistent with most recent results discussing the causes of the decadal sea-level variations in the SWIO region (Trenary and Han 2013, Zhuang et al. 2013, Li and Han 2015, Wang et al. 2015). These studies indeed conclude that the decadal sea-level variations in the SWIO region (north of 20S) are primarily driven by wind stress curl in the SIO, with a minor influence from the remote Pacific oceanic bridge. This study further suggest that the SWIO SSLA variability is largely independent from decadal ENSO but the different wind products analysed show variations in their relationship with decadal Modoki in this region. It may hence well be that a large part of the IO climate variability at decadal time scales is independent of the Pacific, but the processes that could generate this internal variability are currently unknown (Han et al. 2014).

The model SSLA displays a negative trend of steric sea level over 1966-2007 in the SIO, consistent with Han et al. (2010) and Timmerman et al. (2010), who used the same forcing (ERA-40) on different periods (1958-2001 and 1961-2001 respectively). This study agrees with those two studies in attributing the sea-level decrease to long-term changes in wind field in the SIO, but not in accordance with Scharzkopf and Boning (2011) who attributed it to oceanic teleconnections with the Pacific Ocean. The discrepancies between these studies are probably

related to the wind products used to force the ocean models. While myself, Han et al. (2010) and Timmerman et al. (2010) forced their respective model with ERA-40 winds, Scharzkopf and Boning (2011) used NCEP reanalysis winds. The large discrepancy in the wind trends depicted by these two datasets (see Fig. 3.11) could largely explain these contradicting results. In the Pacific Ocean, our results differ more from those of Timmermann et al. (2010), who showed a ~ 20 cm per century sea-level decrease in the western Pacific between 15S and 5S. When not considering the end of the record (i.e. 1966-2001 instead of 1966-2007), the steric sea-level trends in our model is more consistent with Timmermann et al. (2010, not shown). It is important to understand long-term changes of the Indo-Pacific winds and Walker circulation because they largely drive the spatial structures of IO sea-level and thermocline changes. As shown in section 3.6.2, there is however no consensus on trends in equatorial IO westerly winds and off equatorial wind-stress curl and the Indo-Pacific Walker circulation over the past 50 years. This clearly illustrates that long-term sea-level changes derived from forced ocean simulations must be taken with great care, given the wide spread in the wind forcing trends.

The time span of the OGCM experiment discussed in this study (1966-2007, i.e. 42 years) is short, given the time scales considered in the present chapter (~ 7 years and longer). This results in a low number of degrees of freedom in our analysis (≤ 12) and hence a low statistical significance of correlations that I provide. Whereas some confidence is provided by the dynamical consistency of the simple physical mechanisms that I propose, the association between steric sea-level variability in various regions in this study will therefore need further verifications. This chapter however clearly illustrated some inconsistencies in the different wind products at both decadal and longer time scales, especially in the IO basin. This calls for the need to revisit the decadal and long-term IO climate and sea-level variations, including their remote connection with the Pacific decadal variability by performing an extensive intercomparison of the available long-term SST, winds and sea-level products. Also, given the short period of data for most available "observational" products, analysing the long simulations available in the CMIP (Coupled Model Intercomparison Project) datasets would be helpful to ascertain any robust decadal feature of the Indo-Pacific climate and related sea-level variations. These are the main contents in the following chapters.

Robustness of Indo-Pacific decadal sea-level variability

In chapter 3, I have described the tropical Indo-Pacific large-scale sea-level decadal variability simulated by an ocean model forced by winds derived from ERA-40. I also showed that the decadal sea-level variability in this simulation is tightly related to the decadal wind forcing, consistent with other studies such as Timmerman et al. (2010). The intercomparison of different wind products however point towards inconsistencies in the decadal and long-term wind variations depicted by different wind products, especially in the IO. This suggests that the sea-level variations described in the previous chapter may not be robust when compared to other available sea-level datasets. In this chapter, I address the following questions: do all sea-level products (see section 4.1.3 for the details of sea-level products analysed in this thesis) exhibit a similar decadal sea-level variability over the tropical Indo-Pacific? Is the IO decadal sea-level variability depicted by existing sea-level products largely independent from the main decadal climate variability in the Pacific, in agreement with results obtained from NEMO simulation?. Is there any robust sea-level signal in the IO associated with known decadal climate modes? To address these questions, I compare the Indo-Pacific decadal sea-level variability from a large set of sea-level observations, reconstructions and reanalysis data. This will allow me to assess the Indo-Pacific regional variability: i.e. the regions in which decadal sea-level variations are robust and regions for which these products should be considered cautiously.

The most reliable and directly available sea-level data are those derived from tide gauges and satellite altimetry. The modern satellite altimetry offers sea-level measurements with a near-global coverage but only spans about twenty years. On the other hand, tide gauge sea-level measurements are confined to coastal regions and islands, preventing a thorough assessment of open ocean variability. The lack of “long” near-global observational data to study the long-term sea-level changes hence prompted the scientific community to reconstruct past sea-level from a

combination of various ocean data and ocean models by using sophisticated statistical techniques. This eventually led to the development of a number of different sea-level reconstructions (e.g. Church et al. 2011, Hamlington et al. 2009, Meyssignac et al. 2012) and reanalysis products (e.g. Carton and Giese 2008; Balmaseda et al. 2013), providing global sea-level estimates for at least the past fifty years. Note that these sea-level data are referred as observational “*products*” hereafter, since these estimates are derived from observations, but are not pure observations. Complementary to tide gauge and satellite data, I use these gridded sea-level products to describe the Indo-Pacific decadal sea-level variability in this chapter.

Sea-level data from reanalysis/reconstructed products have been used in conjunction with observations and models to discuss the large-scale low-frequency sea-level variations in the Pacific Ocean (e.g. McPhaden and Zhang 2002; Lee and McPhaden 2008; Qiu and Chen 2012; Bromirski et al. 2011; Merrifield et al. 2012, Zhang and Church 2012; Hamlington et al. 2014). Some of the findings of these studies have already been discussed in Chapters 2 and 3. The decadal to multi-decadal zonal wind variations in the equatorial Pacific, characterized by phase changes in the mid 70’s and at the turn of the 20th century have been related, amongst others, to opposite decadal sea-level variations in the western Pacific (Merrifield et al. 2012) and along the west coast of North America (Bromirski et al. 2011), a modulation of shallow meridional overturning circulation in the Pacific (McPhaden and Zhang 2002) and variations in the bifurcation of the north equatorial current (Qiu and Chen 2012). These low-frequency sea-level variability are largely attributed to the dominant decadal climate mode in the Pacific, i.e. the IPO (e.g. Zhang and Church 2012; Han et al. 2013). Results from the previous chapter also suggest an influence of decadal Modoki in shaping the sea-level variations in the tropical Pacific, in line with the results of Behera and Yamagata (2010) derived from satellite altimetry.

The IO decadal sea-level variability has been much less studied than those in the Pacific. Apart from the well-established oceanic bridge between the western equatorial Pacific and WAC via the coastal wave guide in the ITF region (Feng et al. 2004, 2010; Trenary and Han 2008, 2013; Schwarzkopf and Boning 2011; Nidheesh et al. 2013), there is no consensus on the Pacific influence on the decadal sea-level variability elsewhere in the IO. While Lee and McPhaden (2008) suggested a control of the IPO on the basin-wide Indo-Pacific decadal sea-level variations, results from the previous chapter point towards largely independent IO decadal sea-level variations. Except along the WAC, the respective influence of remote and local wind forcing on the decadal IO sea-level variability appears to vary considerably depending on the period and dataset considered (e.g. Lee and McPhaden 2008; Nidheesh et al. 2013; Schwarzkopf and Boning 2011; Trenary and Han 2013; Zhuang et al. 2013).

The present chapter aims at assessing the robust patterns of decadal sea-level variations in the Indo-Pacific sector and their relationship with the two main

modes of Pacific decadal climate variability, namely decadal ENSO and Modoki. To that purpose I compare sea-level variations depicted by a large set of long-term sea-level products.

4.1 Data

4.1.1 Satellite altimeter

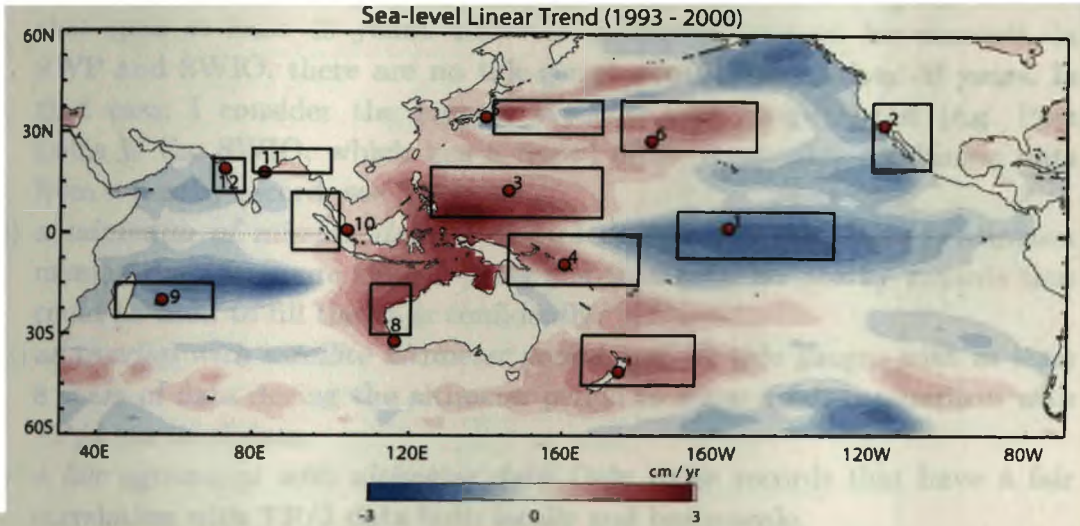


Fig. 4.1: Sea-level linear trend estimated from TP/J data over the 1993-2000 period. The mean seasonal cycle and global mean sea level are removed before estimating the linear trend. The tropical Indo-Pacific Ocean experienced a decadal phase shift around 2000. The 1993-2000 period is characterized by a transition from a warm to a cold phase of decadal ENSO (Zhang and Church 2012). The geographical locations of tide gauges used in this study are shown by red dots. The selected tide gauges are: 1. Christmas 2. San Diego 3. Guam 4. Honiara 5. Uchiura 6. Midway 7. Wellington 8. Fremantle 9. Port Louis 10. Raffles 11. Visakhapatnam 12. Mumbai. See Table 4.1 for more details of the tide gauges.

The combined altimeter data from TOPEX/Poseidon, Jason 1 and 2 (TP/J) distributed by the Commonwealth Scientific and Industrial Research Organization over the 1993-2013 period are used in this study. (<http://www.cmar.csiro.au/sealevel/sl/data/cmar.html>). These monthly mean SLA distributed on a $1^\circ \times 1^\circ$ near-global grid are used to assess the ability of the tide gauges in capturing the offshore variability (see section 4.1.2). This dataset, re-gridded on the $2.5^\circ \times 2.5^\circ$ grid, is used for all other analyses in this study, in order to ensure a fair comparison with coarser long-term gridded sea-level products.

4.1.2 Tide gauge sea level

The present study also uses the monthly-mean sea-level data obtained from the archives of PSMSL (<http://www.psmsl.org>). Twelve tide-gauge records selected in regions of large decadal sea-level variations in the Indo-Pacific region (see Fig. 4.1 and Table 4.1) are used in the present study. Fig. 4.1 highlights the regions which underwent a sharp decadal sea-level phase change in the 1990's. These regions have nearly the same extent as those identified for maximum

decadal sea-level variability in chapter 3 (Fig. 3.4). For each of these key regions, a single tide gauge has been selected based on its ability to capture the large-scale decadal sea-level variations and the length of the time series. This selection procedure is detailed below. Since most of the regions of large decadal sea-level variability generally encompass more than one tide gauge (especially in the Pacific), I have chosen an objective selection procedure. The main criteria are:

- (i) *the length of the tide-gauge record*: I consider all the tide gauge records that span at least 40 years. However, in certain regions, for example, in SWP and SWIO, there are no tide-gauge records longer than 40 years. In that case, I consider the longest available tide gauge record (e.g. Port Louis in the SWIO, which has a record of 39 years after combining data from a nearby record; see Table 4.1).
- (ii) *a minimum of missing data*: I discard the records that have continuous missing data for more than 2 years and that have no nearby records that could be used to fill the gaps confidently.
- (iii) *an overlap with satellite altimeter period*: I select tide gauges with at least 8 years of data during the altimeter period to allow a fair comparison with TP/J sea-level data.
- (iv) *a fair agreement with altimeter data*: Only those records that have a fair correlation with TP/J data both locally and basin-scale.

Fig. 4.2 is an illustration of this tide gauge selection procedure for the NWP framed on Fig. 4.1 and 4.2a. In this region, the Guam tide-gauge has one of the longest record (1948-2015), with few missing data (6%; Table 4.1) and an extended overlap with altimeter data (18 years). This record is also representative of sea-level variability over the entire NWP region, with a 0.95 correlation with TP/J sea-level data averaged over the box shown in Fig 4.2a. Correlation map between Guam tide gauge and gridded TP/J data is reminiscent of the IPO sea-level fingerprint described by Zhang and Church (2012; see their Fig. 4). This suggests that this tide gauge is representative of the basin scale sea-level variability, at least for the altimeter period. I then consider the possibility of filling the 6% of missing data in Guam tide gauge record with the nearby Yap B (the location is shown in fig. 4.2a as a black dot) tide gauge record (Fig. 4.2c). Before doing so, I first checked that Yap-B sea-level variations correlate well with both altimeter data over the NWP region ($r=0.93$; Fig. 4.2c) and with tide gauge data at Guam ($r=0.71$; Table 4.1). Once these consistency checks have been performed, the missing data of the parent tide gauge (Guam in this case) are filled with the data from this nearby record (Yap-B). In case data are not available for the entire missing fields from nearby tide gauge data, short gaps (less than 5 months) are filled through a linear interpolation method. The final continuous record of Guam is shown in Fig. 4.2d and the points where data are filled are plotted as green segments. This continuous record allows to perform a low frequency time series filtering using the STL method detailed in chapter 3 with a cut-off period of 7 year. This procedure allows to extract the decadal component of the Guam tide gauge record (blue curve in Fig. 4.2d).

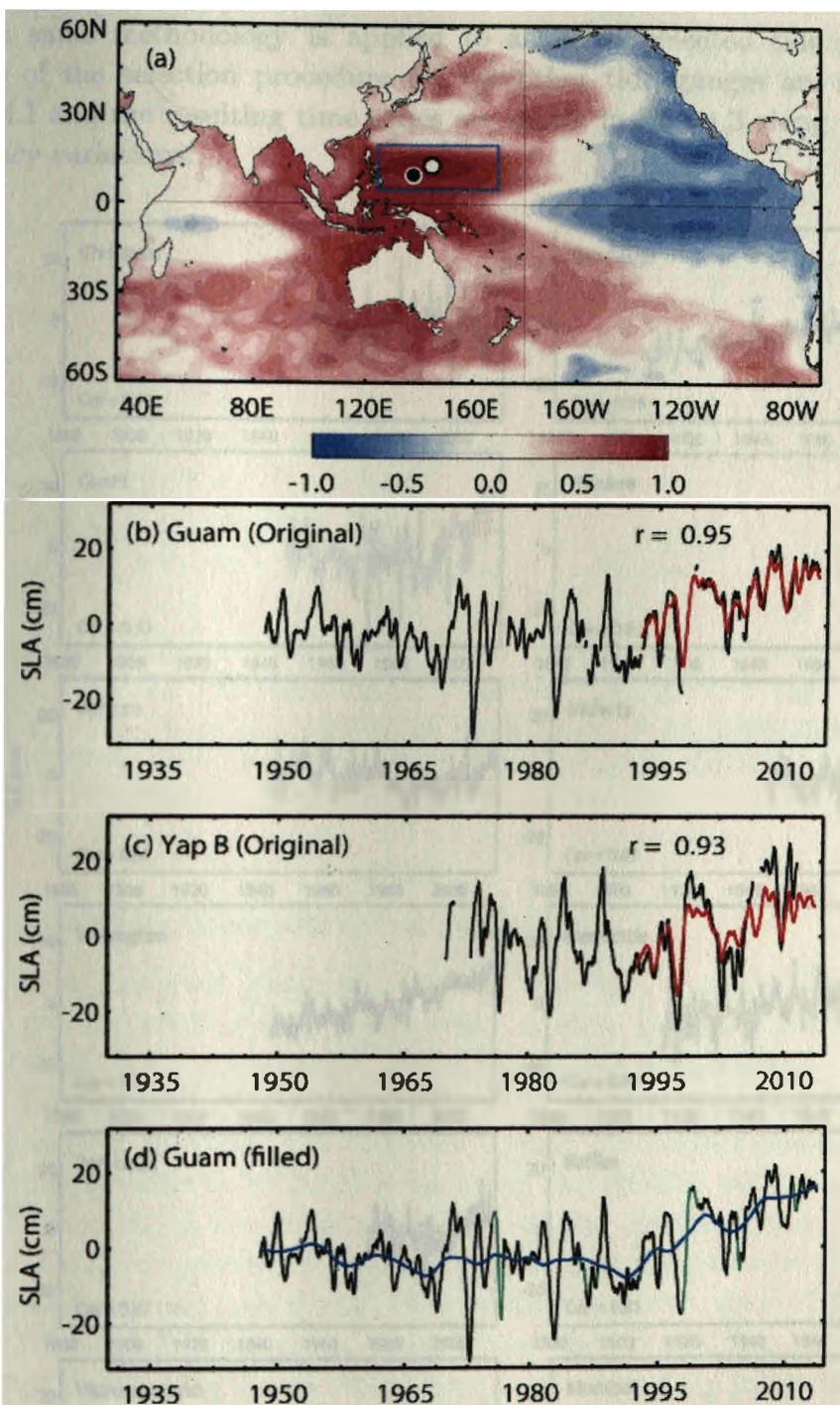


Fig. 4.2: The basic procedure applied to select a tide gauge for each region is summarised in this figure for the case of Guam tide gauge in the NWP. (a) Spatial map of linear correlation coefficients between Guam tide-gauge record (white dot) and TP/J sea level over their common period (1993-2013). The region in the vicinity of the tide-gauge location that exhibits maximum correlation is shown by the blue frame (all the regions considered in this way in the Indo-Pacific region are shown in Fig. 4.1). (b) Original sea level time series from Guam tide gauge data (black curve) and TP/J data averaged over the box shown in panel a (red curve). The correlation coefficient between the two time series is also indicated on upper right of this panel. (c) Sea-level time series from Yap-B tide gauge record (black dot in panel a), the nearby tide gauge used to fill the gaps in Guam dataset (see Table 4.1). (d) Filled time series of Guam dataset with its decadal component (blue curve) overlaid. The segments where the data are either filled from Yap tide gauge data or by linear interpolation are shown as green curve.

The same methodology is applied to all other selected tide gauge records. Details of the selection procedure for the other tide gauges are summarised in Table 4.1 and the resulting time series are shown in Fig. 4.3 along with their low-frequency variations.

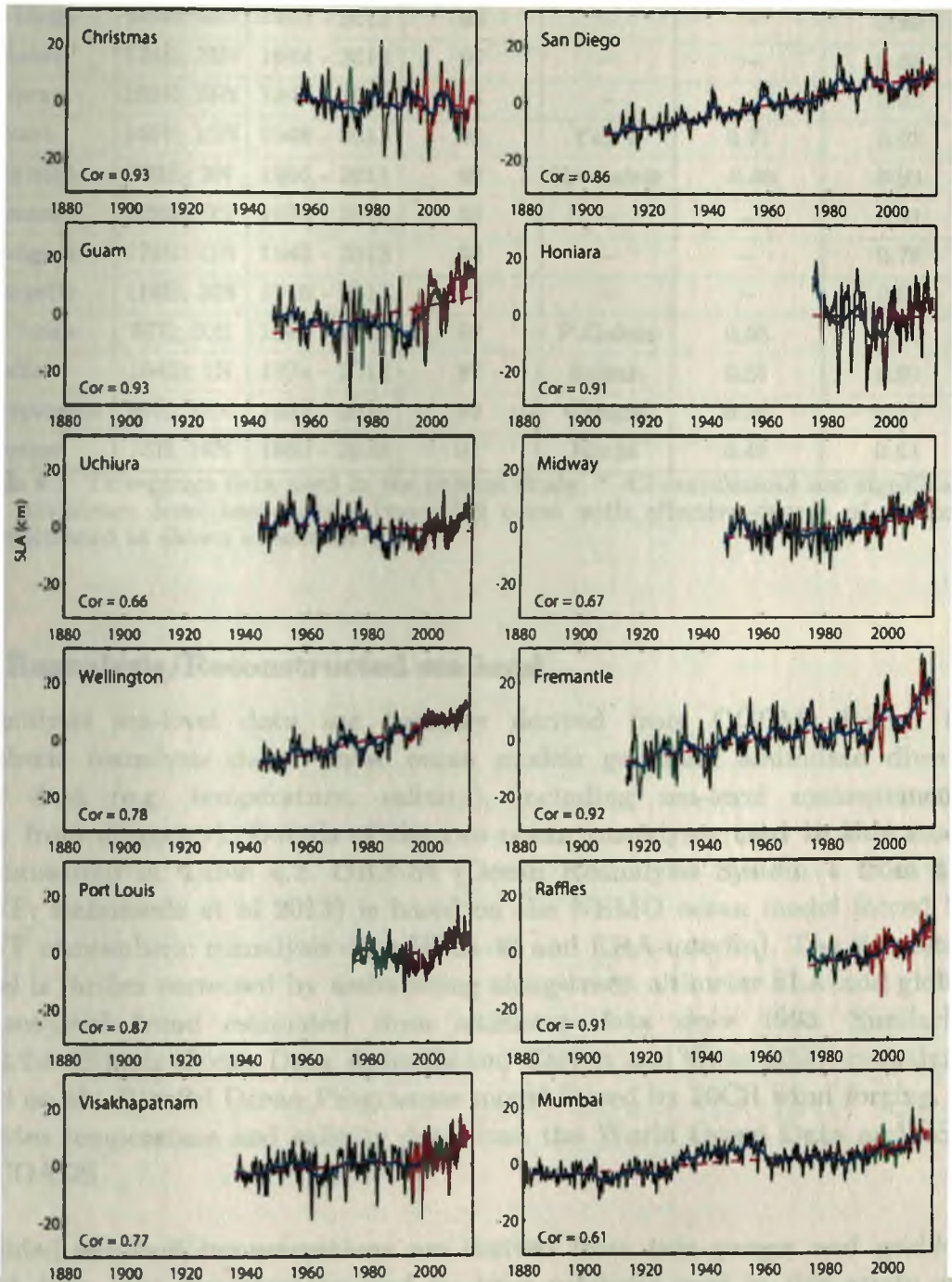


Fig. 4.3: Original tide-gauge time series (black) filled using either data from nearby gauges or through linear interpolation (green). The low-frequency component (periodicity greater than 7 years) of the resulting continuous time series is shown by the blue curve (see text for a description of the procedure applied to fill these tide gauge records). The linear trend estimated from this blue curve is shown as a dashed purple line. Sea level from altimetry averaged over the boxes shown in fig. 1 is overlaid as a red curve. Linear correlation between tide gauge and altimeter sea level over their common period is also given at the bottom left of each panel. These anomalies have been computed by removing the mean seasonal cycle and a 5 month running mean was further applied to each time series. See table 4-1 for more details on the used tide gauges.

Parent Tide gauge	Location	Period	% of data availability	Tide gauge used to fill the gap / combine		Correlation with TP/J sea level (1993-2013)
				Tide gauge	Correlation with parent gauge*	
San Diego	243E; 33N	1906 - 2013	98	--	--	0.86
Uchiura	139E; 35N	1944 - 2013	99	--	--	0.66
Midway	183E; 28N	1947 - 2012	95	--	--	0.67
Guam	145E; 13N	1948 - 2013	94	Yap B	0.71	0.93
Christmas	203E; 2N	1956 - 2011	92	Kwajalein	-0.68	0.93
Honiara	160E; 9S	1975 - 2013	93	--	--	0.91
Wellington	175E; 41S	1945 - 2013	94	--	--	0.78
Fremantle	116E; 32S	1915 - 2013	92	--	--	0.92
Port Louis	57E; 20S	1987 - 2013	97	P Galets	0.53	0.87
Raffles	104E; 1N	1974 - 2013	87	Sultan	0.81	0.91
Visakhapatnam	83E; 18N	1937 - 2010	86	Gangra	0.75	0.77
Mumbai	73E; 19N	1880 - 2010	91	Kochi	0.48	0.61

Table 4.1: Tide-gauge data used in the present study. * All correlations are significant at 95% confidence level based on a two-tailed t-test with effective degree of freedom (EDF) calculated as shown in section 4.2.2.

4.1.3 Reanalysis/Reconstructed sea level

Reanalysis sea-level data are basically derived from OGCMs forced by atmospheric reanalysis data. These ocean models generally assimilate diverse oceanic data (e.g. temperature, salinity), including sea-level measurements (mainly from altimetry). Details of the two ocean reanalyses used in this study are summarized in Table 4.2. ORA-S4 (Ocean Reanalysis System 4 from the ECMWF; Balmaseda et al 2013) is based on the NEMO ocean model forced by ECMWF atmospheric reanalysis data (ERA-40 and ERA-interim). The simulated sea level is further corrected by assimilating along-track altimeter SLA and global mean sea-level trend estimated from altimeter data since 1993. Similarly, SODA2.2.4 (Simple Ocean Data Assimilation; Carton and Giese 2008) reanalysis is based on the Parallel Ocean Programme model forced by 20CR wind forcing. It assimilates temperature and salinity data from the World Ocean Data and SST from ICOADS.

Gridded sea-level reconstructions are derived from tide gauges and gridded sea-level data. The five reconstructed sea-level products used in this study are listed in Table 4.2. In Church et al. (2011) and Hamilton et al. (2011) reconstructed sea-level products (referred to as C&W and CCAR respectively), the sea level is reconstructed by decomposing the satellite altimeter data into EOFs and then subsequently using these basis functions to interpolate in situ tide gauge measurements back in time.

Product	Summary
WOD	Thermosteric sea level (for the upper 2000 m) constructed by using updated data from World Ocean Database (2009) and improved ARGO profiles. Reference: Boyer et al (2009), Levitus et al, (2012).
ORA-S4	Model: NEMO V3.0 Resolution: Horizontal 1x1o. 42 vertical levels, about 10m level thickness in upper 200 m. Period: 1958-2013. Data assimilated: Temperature and Salinity profiles from the EN3 v2a XBT bias corrected database (1958-2009), including XBT, CTD, Argo, Mooring, and from real time GTS thereafter. Along-track altimeter sea level anomalies and global mean sea-level trend from AVISO. SST and sea-ice are from the ERA-40 archive prior to November 1981, from the NCEP OI v2 weekly product (1981 until December 2009) and from OSTIA analysis from January 2010 onwards. Forcing and relaxation used: Daily surface fluxes of heat, momentum and fresh water. Prior to 1989, the surface fluxes are from the ERA-40 atmospheric reanalysis. For 1989-2009, the surface fluxes are from ERA-Interim reanalysis. From 2010 onwards, when ORAS4 started operational running, daily surface fluxes were derived from the operational ECMWF atmospheric analysis. Reference: Balmaseda et al (2013).
SODA2.2.4	Model: Simple Ocean Data Assimilation model based on Parallel Ocean Program (POP) physics. Resolution: 0.25°x0.4°x40-level. Period: 1871-2011. Data assimilated: WOD09 standard level T&S, ICOADS 2.5 SST. Forcing and relaxation used: 20CRv2 surface wind stress and variables for bulk formulae. Reference: Carton and Giese (2008).
CCAR	Data: Monthly mean sea-level data from 409 tide gauge records obtained from the archives of PSMSL database over the period 1950 – 2009 as well as sea-level data from the combined mission of Topex/Poseidon, ERS-1&2, Geosat Follow-On, Envisat, Jason-1, and OSTM satellites (1993-2009 period) were used for the sea-level reconstruction. Method: Cyclostationary Empirical Orthogonal Functions (CSEOFs) derived from altimeter data are fit through a least-square method to the selected tide gauge records extending back to 1950. Period: 1950:2010. Reference: Hamilton et al (2011).
C&W	Data: Monthly mean sea-level data from 426 tide gauge records obtained from the archives of PSMSL database over the period as well as sea-level data from the combined mission of Topex/Poseidon, ERS1&2, Geosat Follow-On, Envisat, Jason-1, and OSTM satellites (1993-2009 period) were used for the sea-level reconstruction. Method: Global covariance structures of sea level are produced by EOF analysis of gridded satellite sea-level data and the amplitude of these structures are reconstructed for the past by using long tide gauge records. Period: 1950 - 2012. Reference: Church et al (2004, 2011).
M-ALTI M-ORA M-SODA	Data: Monthly mean sea-level data from 91 tide gauge records obtained from PSMSL database and three different gridded sea-level data: (i) sea level from Ocean Reanalysis System-4 (ii) the SODA Ocean reanalysis (3) 17-year long satellite altimetry data. Method: EOFs decomposed from the gridded sea-level data mentioned above are used to reconstruct past sea level by using historic tide gauge data through a reduced optimal interpolation method as described by Kaplan et al. (1998). Reference: Meyssignac et al (2012).

Table 4.2: A brief summary of gridded sea-level datasets used in this study.

It results in a dataset with the spatial resolution of satellite altimetry and the record length of tide gauges. However, Meyssignac et al. (2012) showed that the altimeter record may be too short to capture the full range of variability, especially at decadal time scales, and that regional variability derived from reconstructed products may hence be sensitive to the basis functions considered. To address this issue, they developed different reconstructed sea-level products with basis functions derived from different gridded sea-level data, i.e. from (i) satellite altimetry (referred as M-ALTI in this study), (ii) ORA-S4 (M-ORA) and (iii) SODA (M-SODA)¹.

I have also analysed the thermosteric sea-level dataset computed from the World Ocean Data (Boyer et al 2009, Levitus et al 2012) as an independent observational dataset (referred to as WOD). The eight gridded sea-level datasets listed in Table 4.2 are interpolated onto the regular $2.5^0 \times 2.5^0$ NCEP grid to ease comparison. The multi-product analysis is then performed over their common period, i.e. 1960-2010.

4.1.4 SST and wind

Century long HadISST SST product is also used in this study. It is based on blended *in-situ* and satellite data sources after 1981 and sparse ship data sets prior to that period (Rayner et al. 2003), with an optimal interpolation to fill the gaps in data-sparse oceanic regions. I also use the three wind datasets, already discussed in chapter 3, namely the 20CR, NCEP/NCAR and WASWind products (see Section 3.1.2 for a brief description and related references). All the data are interpolated onto the regular $2.5^0 \times 2.5^0$ grid to ease comparison.

4.1.5 The LCS model

In addition to these observational products, a Linear Continuously Stratified (LCS) numerical model is also used to understand the respective influences of local and remote forcing from the Pacific Ocean on the decadal sea-level variability in IO. This model was initially formulated by McCreary (1980, 1981) to understand the equatorial dynamics in the Pacific region. It is based on an expansion of the linearized equations of motion into vertical modes, each follows shallow water equations and being solved separately (see McCreary et al. 2007 for more details). The LCS model avoids the complexity of an OGCM, while providing relevant insights on the dynamics of the SLA response to wind forcing as it includes the essential physics required to simulate thermocline and related sea-level variations.

Here, I use an Indo-Pacific configuration described in Izumo et al. (2015). The model has a 0.5 horizontal resolution and a coastline defined by 200m isobaths, allowing for a realistic representation of the ITF as in McCreary et al. (2007). Background vertical stratification (and thus vertical modes structure) are derived from the World Ocean Atlas 2009 (for depth less than 1500m) and Levitus (for

¹ I thank Dr. Meyssignac for providing the dataset through personal communication.

depth greater than 1500m) temperature and salinity climatologies in the tropical Indo-Pacific Ocean. I used the first five vertical modes, a reasonable approximation since the first two modes dominate the sea-level variability in tropical regions (see Chen et al. 1995, Han 2005). While the first mode has a rather constant celerity and Rossby radius in the tropical Indo-Pacific region, the vertical stratification and vertical modal structure can be significantly different poleward of 15 (Chelton et al. 1998). As we are also interested in the extra-equatorial SLA response, I use a scaling of the simulated SLA to the observed SLA as described in Timmerman et al. (2010) to overcome that caveat. The scaling is empirically obtained by comparing the LCS and TP/J SLA standard deviations, and fitted to an idealised Gaussian depending only of latitude (a good approximation as shown by Timmerman et al. 2010). The relatively good comparison between the model and satellite SLA variations in the Indo-Pacific region (not shown) suggests that this approach is reasonable.

4.2 Method

4.2.1 Time scale definition

The low-frequency component (variability above 7 year periodicity) of sea level in all the gridded sea-level products as well as for the selected tide gauges is extracted using STL method described in Chapter 3 (section 3.2.2). For the gridded products, the following procedure is followed to isolate the “decadal” time series that is used in this thesis for all further analysis.

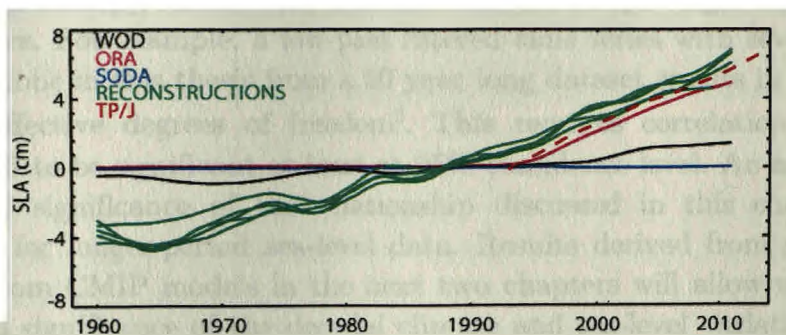


Fig. 4.4: Global mean sea-level (GMSL) time series from nine gridded products (including TP/J) analysed in this study: WOD (black), ORA (purple), SODA (blue), CCAR, C&W, M-ALTI, M-ORA, M-SODA (green) and TP/J (red). The decadal component of sea level is spatially averaged at each time step over 65N to 65S to obtain the GMSL for all the gridded products listed in Table 2 as well as for the gridded altimeter data.

As shown in Fig. 4.4, the Global Mean Sea Level (GMSL) time series has been estimated for all these products from the low-frequency component. The GMSL rise is steady and very consistent for all reconstructed sea-level products (CCAR, C&W and Meyssignac’s sea-level products (MESSIs hereafter)) over the 50 year period considered, but very different from the GMSL derived from reanalysis products (ORA and SODA) and observations (WOD). ORA GMSL shows a sharp sea-level rise from 1993 onwards, as the system started assimilating satellite

sea-level from that year onwards. Before the satellite era, SODA and ORA GMSL rise is virtually absent, because the models based to build these reanalyses use the Boussinesq approximation (Greatbatch 1994). Finally, the WOD GMSL slope is far smaller than those from satellite and reconstructions, as this product accounts only for the ocean thermal expansion and not the addition of mass into the global oceans due to the melting of the continental glaciers and ice sheets under global warming (see chapter 2). Because of these very diverse GMSL rise in various products and my focus on natural decadal sea-level variability, the GMSL time series is removed from each gridded product before performing my analysis. In order to isolate the decadal variability from possible regional trends and from multi-decadal changes (e.g. the 60-year oscillation suggested from an analysis based on global-network of tide-gauge by Chambers et al. 2012), I further removed the linear trend of sea level at each grid-point over analysed the 50-years period. Decadal variability (≥ 7 years) discussed in this study hence excludes GMSL rise and long-term sea-level trends.

4.2.2 Definition of climate indices

Owing to the strong control of the tropical Pacific on the entire Indo-Pacific climate, I also use the EOF-based climate indices of the tropical Pacific (interannual/decadal ENSO and Modoki indices) introduced in the previous chapter (see section 3.2.3) to assess the influence of ENSO and Modoki on the Indo-Pacific sea-level. The qualitative and quantitative relationships between different variables are assessed through linear correlation/regression methods. As I am focusing on decadal variations from at most ~ 50 years long records (or even shorter for altimetry), I do not discuss the statistical significance of the correlation here. For example, a low-pass filtered time series with seven year cut-off period as done in this thesis from a 50 year long dataset results in a maximum of $\sim 12-13$ effective degrees of freedom². This requires correlation coefficients larger than 0.5 to be significant at least at 95% confidence level. An assessment of the statistical significance of the relationship discussed in this chapter would certainly call for longer-period sea-level data. Results derived from century-long simulations from CMIP models in the next two chapters will allow us to discuss the statistical significance of the decadal climate and sea-level variations in more details.

The assumption of having two degrees of freedom for a seven year cycle as made above is typically consistent with the EDF estimated using the equation (1) below. Smoothing of the decadal component increase the auto-correlation of the time series and reduce the total number of degrees of freedom considerably. Hence the effective degrees of freedom (EDF), N^* , for such a smoothed time series having N time points can be estimated by the formula (following Leith 1973):

$$N^* = N / 2T \quad (1);$$

where T is the time interval over which the autocorrelation of the time series drops to $1/e$. Also note that, the EDF to compute the significance of the correlation between original tide gauge records discussed in section 4.1.2 is estimated by (1). I also verified this assumption with the eqn. 30 given in Bretherton et al. 1999.

4.3 Sea-level products evaluation

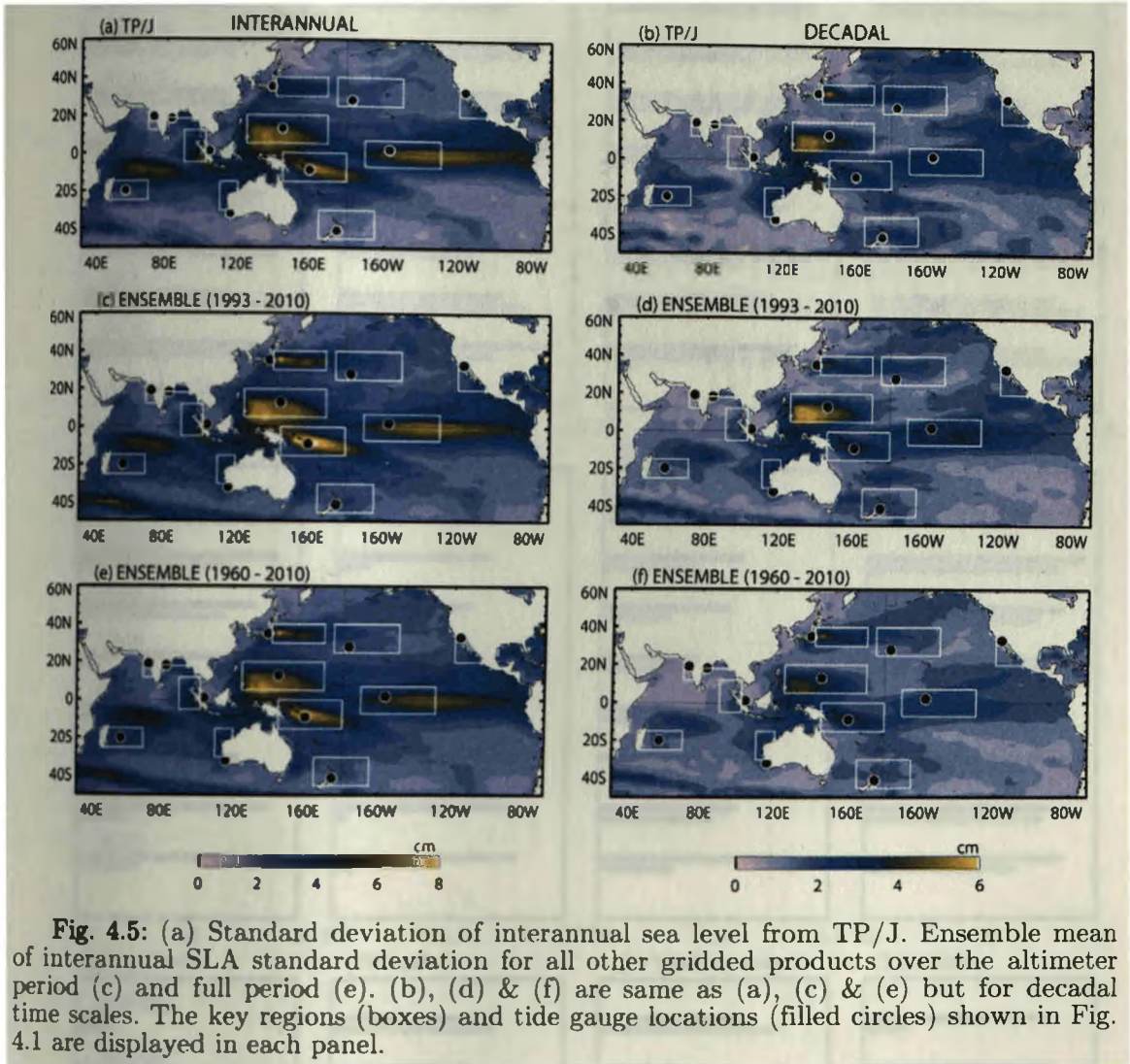


Fig. 4.5: (a) Standard deviation of interannual sea level from TP/J. Ensemble mean of interannual SLA standard deviation for all other gridded products over the altimeter period (c) and full period (e). (b), (d) & (f) are same as (a), (c) & (e) but for decadal time scales. The key regions (boxes) and tide gauge locations (filled circles) shown in Fig. 4.1 are displayed in each panel.

Fig. 4.5 shows sea-level standard deviation map from TP/J and other gridded products at interannual and decadal time scales. The standard deviation for the gridded products is computed for two different periods: (i) the altimeter period (1993-2010; Fig. 4.5c,d) and (ii) the entire period (1960-2010; Fig. 4.5e,f). Comparing Fig. 4.5a,b with Fig. 4.5c,d shows that the reanalysis/reconstructed products are able to capture the main regions of maximum interannual and decadal sea-level variability depicted by the altimeter data in the Indo-Pacific region. The only noticeable difference is a tendency for reanalysis/reconstructed products to display a maximum decadal variability in the SWIO that is shifted northward relative to the TP/J dataset. There is an overall reduction in the amplitude of the signals when extending this analysis over the 1960-2010 period in several regions, including the equatorial and northwest Pacific and the WAC at decadal time scales. Whether this reduction is realistic or related to caveats in the sea-level products remains an open question. It must also be noticed that the main regions of maximum variability shown in Fig. 4.5 agree well with those derived from our ocean model analysis in the previous chapter.

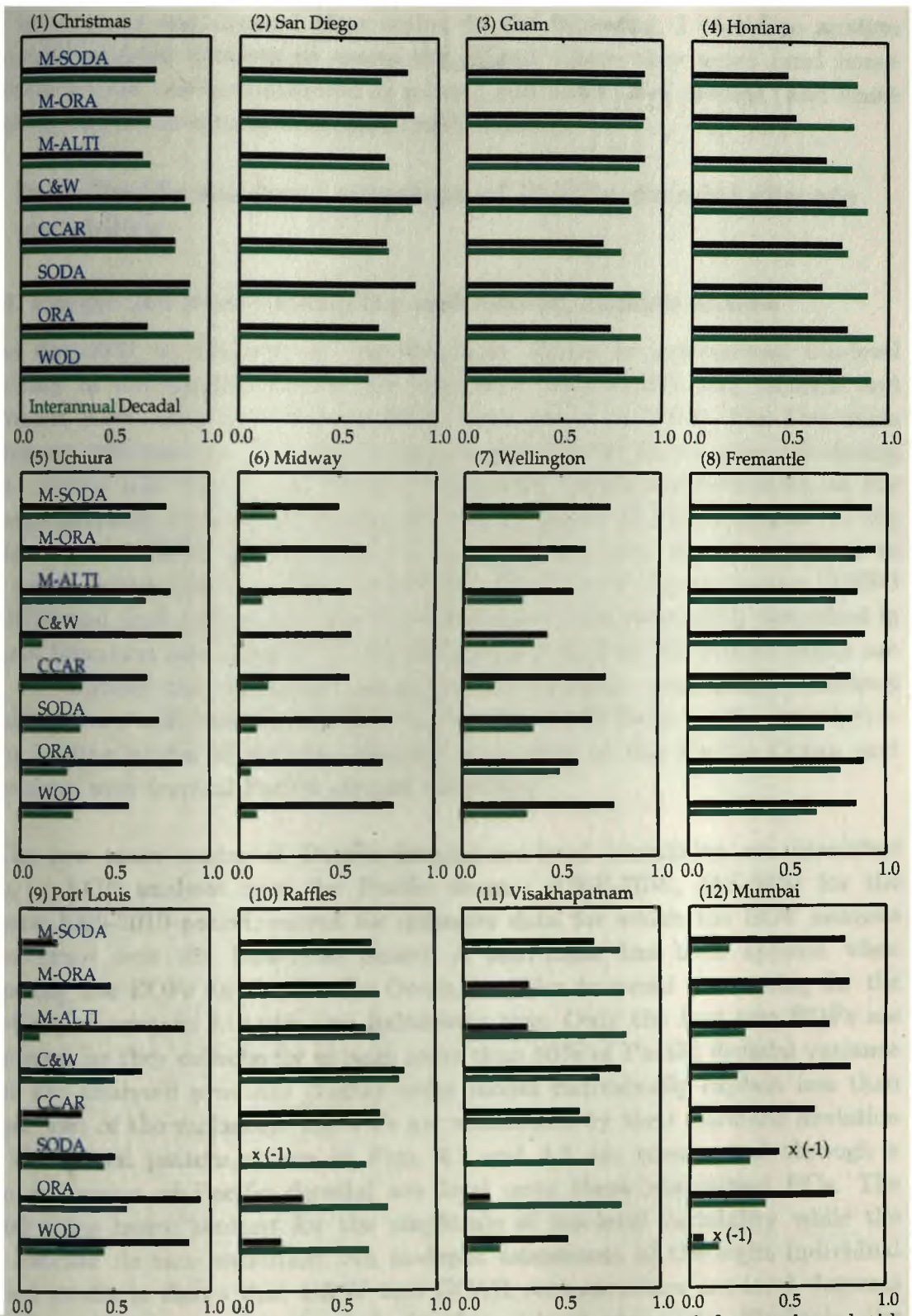


Fig. 4.6: Bars represent correlation coefficient between sea level from selected tide gauges in the Indo-Pacific region and average sea level over the boxes shown in Fig. 4.1 and 4.5 for all sea-level products at both interannual (green bars) and decadal (black) time scales. Negative correlations are labelled by "x(-1)".

Although some products are better than others in reproducing the observed sea-level variability in specific regions, this analysis reveals that no single product clearly outperforms the others at the scale of the entire Indo-Pacific region for

both interannual and decadal time scales. In the following, I therefore analyse these eight gridded datasets to assess the regions where they agree (and hence where the signals can be considered as robust) and where they diverge (and hence where the signals have to be considered with caution).

4.4 Indo-Pacific sea-level signature of Pacific decadal climate variability

4.4.1 Pacific sea-level variability and related climate modes

As described in Chapter 2, the dominant modes of interannual sea-level variability in the tropical Pacific are associated with ENSO (e.g. Meinen and McPhaden 2000; Alory and Delcroix 2002, Lengaigne et al. 2012). The first mode displays an east-west sea-level seesaw representative of the thermocline tilt during ENSO events and the second mode a basin-wide signal representative of the recharge-discharge that occurs during the mature phase of ENSO events. In the IO, interannual ENSO forcing results in a dipolar sea-level signature related to IOD events, which often co-occur with ENSO. Interannual climate modes (ENSO and IOD) and their related sea-level signatures have been extensively described in the past literature (see Chapter 2). All the products used in the present study are able to capture the dominant modes of Indo-Pacific interannual sea-level variability very well (not shown). For conciseness, I will focus on the description of the leading modes of decadal sea-level variability in the Pacific Ocean and relate them with tropical Pacific climate variability.

The two main modes of Pacific decadal sea-level variability are identified using an EOF analysis over the Pacific domain [120E-70W, 45S-60N] for the common 1960-2010 period, except for altimeter data for which the EOF analysis is performed over the 1993-2010 period. A land-mask has been applied when computing the EOFs for the Pacific Ocean, in order to avoid accounting for the variability of western Atlantic and Indonesian seas. Only the first two EOFs are considered, as they collectively explain more than 50% of Pacific decadal variance for all the analysed products (higher order modes individually explain less than ten per cent of the variance). The PCs are normalised by their standard deviation and the spatial pattern shown in Figs. 4.7 and 4.8 are constructed through a linear regression of Pacific decadal sea level onto these normalised PCs. The spatial maps hence account for the amplitude of sea-level variability while the PCs indicate its time evolution. An in-depth assessment of the eight individual gridded products shows that C&W and CCAR reconstruction sea-level datasets generally exhibit a very similar Indo-Pacific sea-level variability. Similarly, the three Meyssignac's (MESSIs hereafter) reconstructed products are also rather consistent with each other, as do ORA, SODA and WOD products. This led me to perform a subjective classification into three groups: (i) Reanalyses and WOD (ORA, SODA, WOD). (ii) C&W and CCAR Reconstructions and (iii) MESSIs reconstructions. Since TP/J is our ground truth product, which only spans about 20 years, I consider it separately in the following. For conciseness, average EOF

patterns are provided for the three groups (see Figs. 4.7 to 4.10) but a statistical assessment is also provided for each individual product.

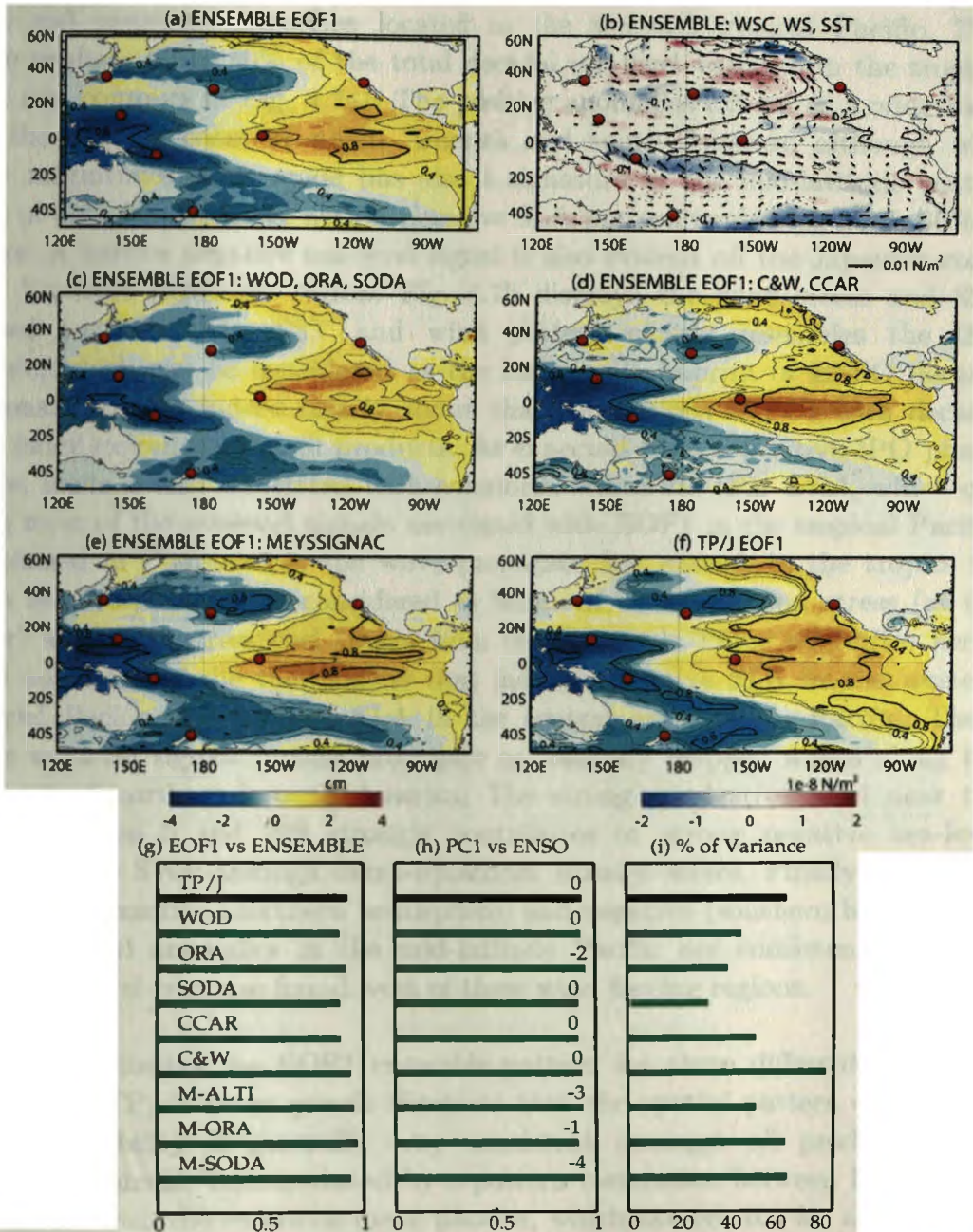


Fig. 4.7: (a) Ensemble average of Pacific decadal SLA 1st EOF patterns across all products (shade). The % of sea-level variance explained by the 1st PC is overlaid as contours. (b) Corresponding pattern for decadal wind stress curl (WSC, shade), wind stress (arrow) and SST (contour), obtained by regression on PC1. Ensemble average of Pacific decadal SLA 1st EOF patterns for (c) WOD, ORA and SODA (d) C&W and CCAR (e) M-ALTI, M-SODA and M-ORA. (f) Pacific decadal SLA 1st EOF for TP/J. The location of selected tide gauges (filled circles) in the Pacific is also shown. (g) Pattern correlation between the 1st EOF ensemble average for all products and individual datasets. (h) Maximum lag-correlation of PC1 of each product with decadal ENSO (with the corresponding lag, in months, is indicated with positive lags indicating that the PC leads ENSO). (i) Percentage of sea-level variance explained by the 1st EOF for each product. The region for which EOFs have been computed is outlined by a black rectangle on panel a, but with a masking to avoid regions in the western Atlantic and Indonesian seas.

Fig. 4.7a shows the ensemble-mean EOF1 spatial structure from the 8 gridded products (TP/J excluded). This pattern exhibits a large-scale sea-level seesaw in the tropical Pacific, with positive anomalies over the central/eastern tropical Pacific and negative anomalies located in the western tropical Pacific. This pattern explains 60 to 80% of the total decadal sea-level variance in the tropical Pacific (see contours in Fig. 4.7a). The positive anomalies extend as a wide band along the western coast of north America and south America, although with weaker magnitudes. This mode has also a signature in the mid-latitude central Pacific of both hemispheres, with a negative SLA pattern explaining 40 to 60% of variance. A narrow negative sea-level signal is also evident off the Japanese coast in the Kuroshio extension region. Fig. 4.7b displays the wind stress and SST regressed on PC1. The SST and wind pattern closely resembles the IPO signature, which can be considered as the basin scale imprint of ENSO decadal variations. Fig. 4.7h indeed clearly shows that correlations of PC1 with decadal ENSO index exceed 0.9 for all products. As expected from a positive IPO phase, this first mode is also associated with equatorial westerlies (Fig 4.7b), which can explain most of the sea-level signals associated with EOF1 in the tropical Pacific. As explained in Chapter 2.3, the wave propagate fast enough in the tropics for the sea level response to be considered as balanced by zonal wind stress (at the equator) and wind stress curl (away from the equator). These westerlies hence force a zonal tilt of the thermocline that induces negative SLA in the western equatorial Pacific and positive SLA in the central and eastern Pacific. These positive sea-level signals further propagate as coastally trapped waves along the west coast of north and south America. The strong wind stress curl near the dateline between 0 and 20S strongly contributes to strong negative sea-level response in the SWP through extra-equatorial Rossby waves. Finally, the IPO-related strong positive (northern hemisphere) and negative (southern hemisphere) wind stress curl anomalies in the mid-latitude Pacific are consistent with the negative sea-level response found west of these wind forcing regions.

Fig. 4.7c-f display the EOF1 ensemble pattern for three different groups of products and TP/J. These panels illustrate that the spatial pattern of the first mode of variability is generally very consistent amongst all products. This consistency is further demonstrated by a pattern correlation between EOF1 from each product with the ensemble-mean pattern, which exceeds 0.8 for all products (Fig. 4.7a). Two discrepancies can however be noted from Fig. 4c-f. First, the negative SLAs in the NWP are usually weaker for WOD, ORA and SODA compared to reconstructions and TP/J. Second, the positive sea-level signal in the central tropical Pacific is equatorially confined in reconstructions compared to other products. Reconstructions are mostly based on EOFs that are not performed separately for each time scale. Hence, these EOF patterns are generally dominated by interannual variations, that generally exceed the decadal ones in amplitude (see Fig. 4.5). This may explain why reconstructed products decadal patterns resemble the interannual ones. Despite these relatively minor differences, EOF1 patterns are very robust across products. The main discrepancy between products actually lies in the percentage of total sea-level variance explained by

EOF1 in the Pacific, which is systematically larger for reconstructions and TP/J compared to other datasets. While this percentage varies between 30-40% for WOD and reanalysis products, it exceeds 50% in reconstructions and TP/J, even reaching 80% for C&W.

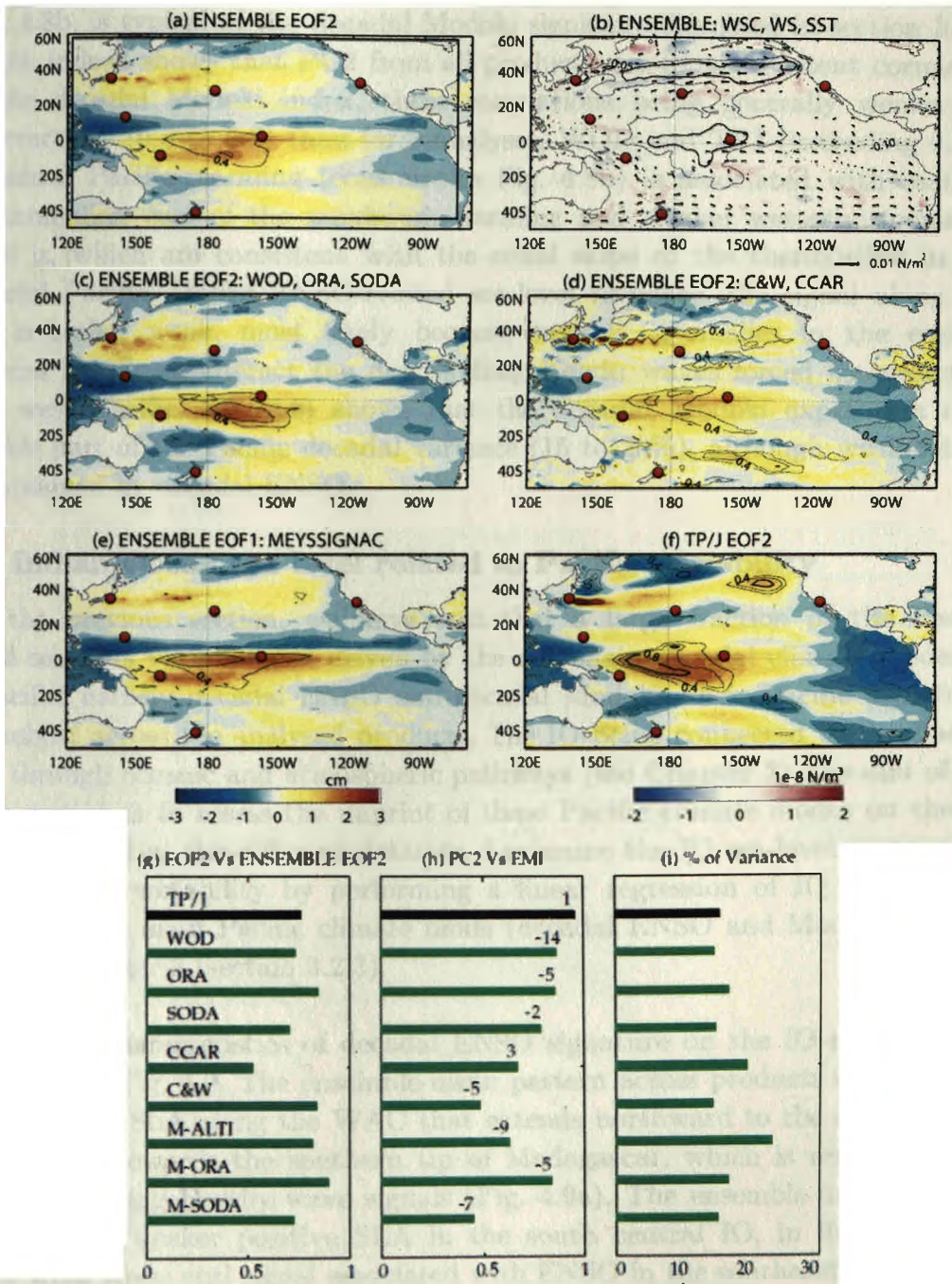


Fig. 4.8: Same as fig. 4.7 but for Pacific decadal sea-level 2nd EOF.

The main characteristics of the second mode of Pacific decadal sea-level variability are summarized in Fig. 4.8. The ensemble-mean pattern (Fig. 4.8a) is characterized by positive SLAs over the central equatorial Pacific (between 150E and 140W), which explain 40 to 60% of the total decadal sea-level variance near the dateline (contours in Fig. 4.8a). This mode is also related to negative SLA in the far north western tropical Pacific (7N; 130E) and far eastern equatorial

Pacific and a narrow band of positive SLA off the east coast of Japan but explains less than 20% of decadal sea-level variance in these regions. This spatial pattern is rather consistent amongst different products, with a spatial pattern correlation between ensemble and individual maps ranging from 0.5 to 0.8 (Fig. 4.8h). This sea-level pattern, along with the projected SST and wind field shown in Fig. 4.8b, is typical of the decadal Modoki signature discussed in section 3.2.3. Fig. 4.8h indeed shows that PC2 from all products are to some extent correlated with the decadal Modoki index, these correlations being generally weaker for reconstructions (0.5 to 0.8) than for reanalyses, WOD and TPJ (exceeding 0.75). The central Pacific warming (contours in Fig. 4.8b) is associated with easterly wind anomalies, east of the maximum warming and weaker westerly anomalies west of it, which are consistent with the zonal slope of the thermocline in the equatorial Pacific. Unlike ENSO-related sea-level response, the signal along the WAC is rather weak, most likely because easterly anomalies in the eastern equatorial Pacific counteract the downwelling Kelvin waves forced by westerlies in the west Pacific. Fig. 4.8i shows that the decadal Modoki explains a non-negligible part of the Pacific decadal variance (15 to 20%), although weaker than that explained by decadal ENSO.

4.4.2 Indian Ocean sea level related to Pacific variability

In the previous section, we have seen that a large fraction of the Pacific decadal sea-level variability is driven by the two main decadal climate modes in the Pacific: namely decadal ENSO and decadal Modoki, their Pacific signatures being robust across the analysed products. The IO being connected to the Pacific Ocean through oceanic and atmospheric pathways (see Chapter 2), the aim of the present section is to assess the imprint of these Pacific climate modes on the IO decadal sea-level in the different datasets. I examine the IO sea-level response to Pacific decadal variability by performing a linear regression of IO decadal sea level to the two main Pacific climate mode (decadal ENSO and Modoki) indices defined in Chapter 3 (section 3.2.3).

The main characteristics of decadal ENSO signature on the IO sea level are summarised in Fig. 4.9. The ensemble-mean pattern across products consists of a strong negative SLA along the WAC that extends northward to the eastern BoB and westward towards the southern tip of Madagascar, which is reminiscent of westward-radiating Rossby wave signals (Fig. 4.9a). The ensemble-mean pattern also exhibits a weaker positive SLA in the south central IO, in line with the positive wind stress curl signal associated with ENSO in the southeast IO (weaker than at interannual time scales; not shown). However, the intensity of these signals varies strongly from one dataset to another. The most consistent signal amongst products is the negative SLA along the WAC (Fig. 4.9b-d), underlining the ability of all products to accurately capture the oceanic teleconnection between the western Pacific and the WAC, associated with the decadal ENSO forcing. The westward extension of these negative SLA around 30S and northward extension into the BoB is highly variable across products, with reconstructions and TP/J showing the clearest signals. Similarly, the positive

SLA signature in the south central IO is only found in reconstructions (Fig. 4.9cd) and TP/J to some extent, being virtually absent in the reanalyses and WOD. As a result, the ENSO-related sea level in the IO depicted by reconstructions consists of a dipole-like pattern with negative signals centred over southeastern IO (and extending along the entire part of IO eastern boundary) and positive signal in the SWIO, a pattern very similar to that of IOD events at interannual timescale (not shown; e.g. Rao and Behera, 2005). On the other hand, reanalyses suggest that, apart from the oceanic connection between the western Pacific and the WAC, the IO decadal sea-level response to ENSO is very weak elsewhere in the basin. This is in line with the results obtained from NEMO OGCM in Chapter 3, which suggested a strong independency of the IO decadal sea-level variations from the Pacific. Consequently, the percentage of IO sea-level variance explained by ENSO is rather low in reanalysis products and WOD (<15%; Fig. 4.9h) and higher for reconstructions ($\geq 20\%$). C&W clearly stands out as an outlier compared to the other products in terms of explained variance, with 70% of the decadal sea-level variance in the IO explained by ENSO.

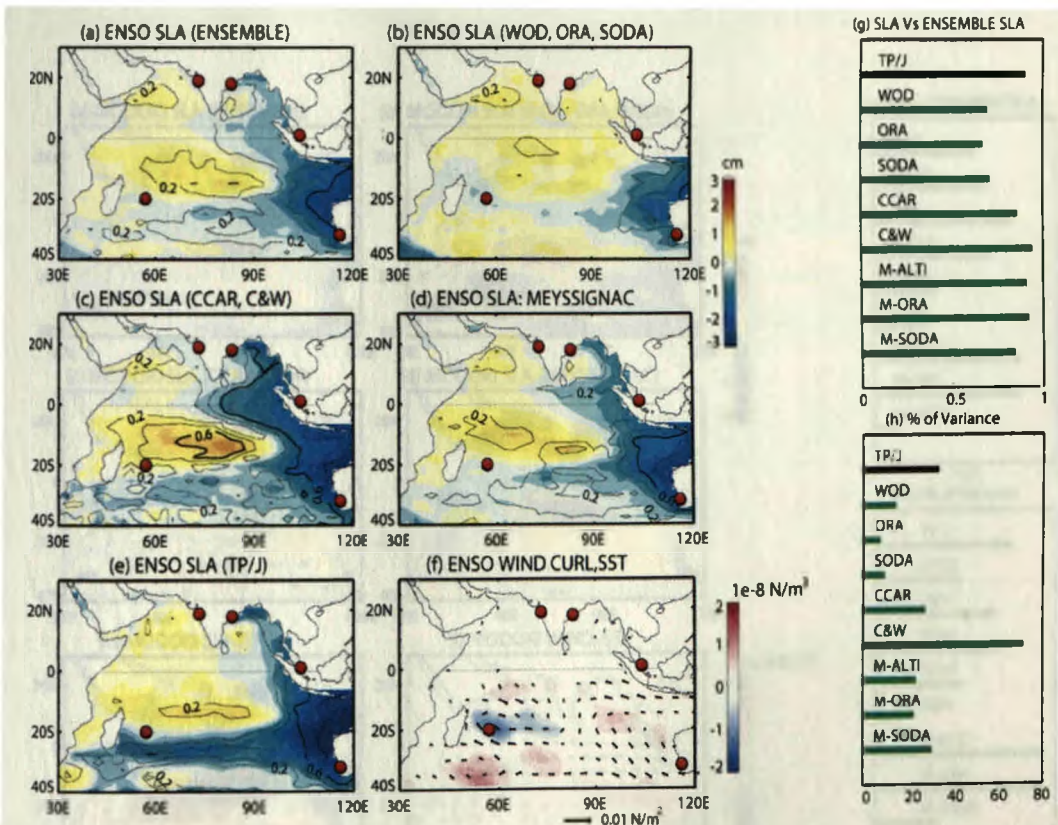


Fig. 4.9: (a) Ensemble-mean regression pattern of IO decadal SLA to decadal ENSO for all products (shade). The explained variance of SLA (computed as the square of the correlation coefficient between SLA and ENSO index) by decadal ENSO is overlaid as contours. Ensemble-mean regression pattern for (b) WOD, ORA and SODA (c) C&W and CCAR (d) Meyssignac and (e) TP/J. (f) Regression of decadal wind stress curl (shade), wind stress (arrow) and SST (contour) on decadal ENSO. (g) Pattern correlation of ensemble-mean SLA pattern for all products (shown in a) with those of individual datasets. (h) Percentage of IO decadal SLA variance explained by decadal ENSO for each dataset. Red dots indicate locations of selected tide gauges in the IO.

Fig. 4.10 summarises the IO decadal sea level, wind and SST response to decadal Modoki. The most noticeable feature in the ensemble-mean pattern (Fig. 4.10a) is a positive SLA in the south central IO (at $\sim 10S$). This signal is however not consistent amongst the products, being very weak in C&W and CCAR (Fig. 4.10c) and stronger in TP/J (Fig. 4.10e) compared to MESSIs, reanalyses and WOD products (Fig. 4.10b,d). The geographic location of this positive SLA also varies across products (Fig. 4.10b-e). This explains the rather poor agreement between the ensemble pattern and individual patterns, especially for C&W, CCAR and M-SODA (Fig. 4.10g). The second interesting feature on this figure is that the oceanic teleconnection between western equatorial Pacific and WAC is much weaker than that associated with ENSO, in contrast to what has been diagnosed in the NEMO model in the previous section. The wind response to ENSO Modoki is associated with a positive wind stress curl over the southeastern IO, which is slightly stronger and broader than that associated with ENSO in the same region. As demonstrated in the next section, this wind signal largely explains the positive SLA found in the south IO. Except for C&W and M-SODA, the decadal Modoki modulation explains a broadly similar percentage of IO decadal sea-level variance to that associated with decadal ENSO (10-20%).

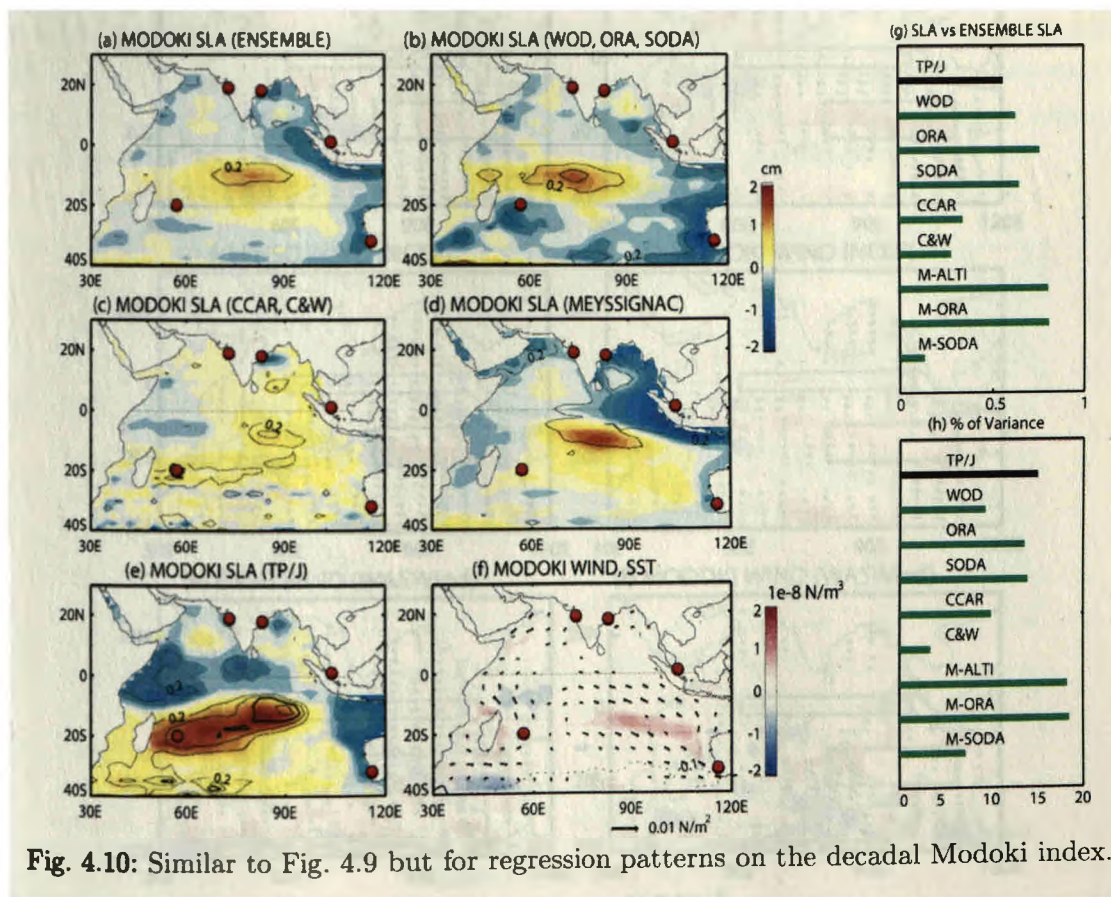


Fig. 4.10: Similar to Fig. 4.9 but for regression patterns on the decadal Modoki index.

4.4.3 A destructive interference between ENSO atmospheric and oceanic teleconnections in the IO

Previous section described the IO SLA response to Pacific decadal variability. The tropical Pacific decadal variability has a robust Pacific signature amongst various datasets. On the other hand, its IO remote signature varies depending on the dataset. Except for the WAC, there is no evident ENSO-related sea-level signature in the IO in the reanalyses and WOD, in contrast to what is found in reconstructions. On the other hand, most of the products, except C&W and CCAR display a Modoki-related signal in the south central IO. Since reanalysed sea-level products partly depend on the ocean model wind forcing, I first briefly assess the robustness of the IO sea level response to decadal ENSO and Modoki forcing diagnosed from several wind products. If these wind signatures are not consistent, this will further question the reliability of IO decadal sea-level variability in reanalyses. The IO wind patterns associated with decadal ENSO and Modoki and diagnosed from three wind products (20CR, NCEP and WASWind) are shown in Fig. 4.11.

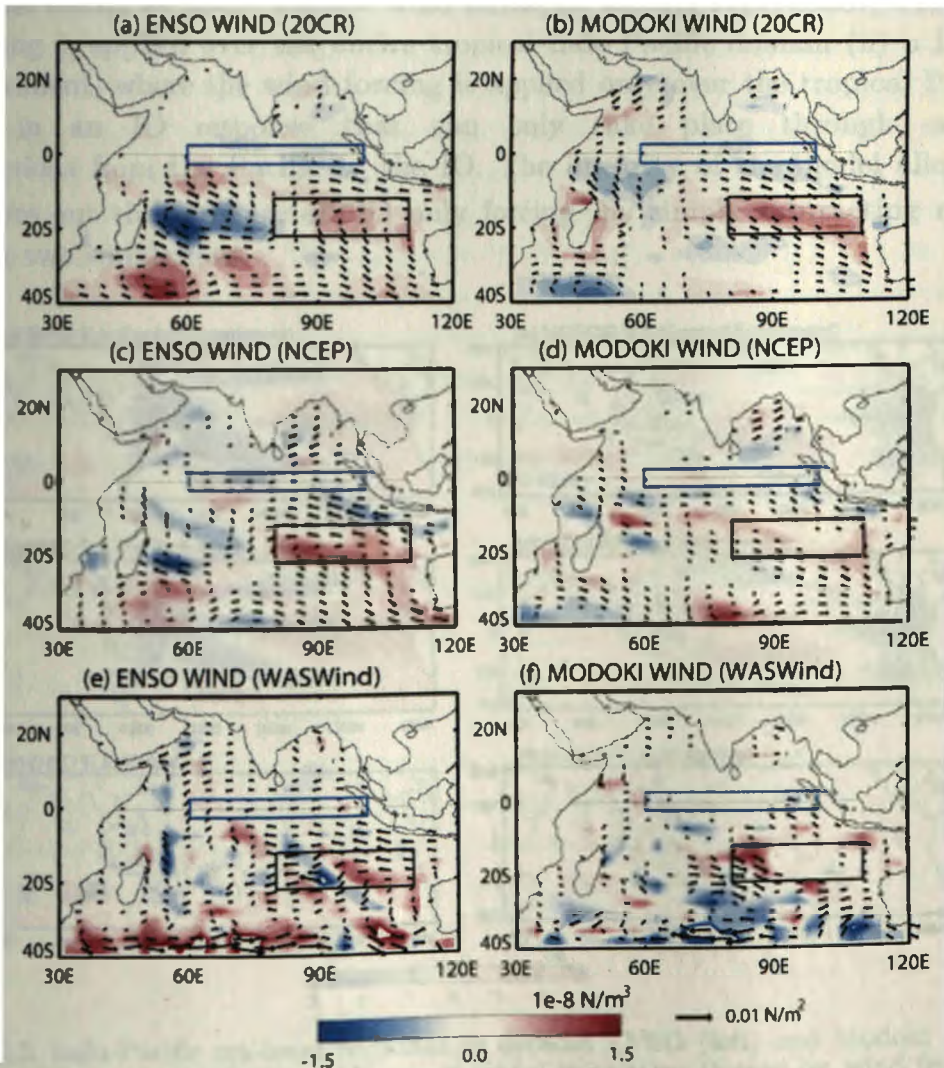


Fig. 4.11: Regression coefficients of IO decadal wind stress curl (color) and wind stress (vectors) on decadal ENSO (left) and Modoki (right) for 20CR, NCEP and WASWind data. The key regions discussed in the text (equatorial IO and southeastern IO) are outlined by rectangles.

The wind signals associated with decadal ENSO and Modoki are rather similar, as expected from a Matsuno-Gill (Matsuno 1966, Gill 1980) response to reduced convective activity over the maritime continent during an El Niño (e.g. Xie et al. 2002). They both display a positive wind stress curl over the southeastern IO. This is rather surprising as we have previously seen that there is no notable SLA signal associated with decadal ENSO in the south central IO in reanalyses products and in WOD (see section 4.3.2), while there is one for decadal Modoki. The absence of ENSO-related SLA in the south IO may be related to the negative wind stress curl anomalies associated with decadal ENSO west of the southeastern IO positive curl anomalies (left panels of fig. 4.11). These positive and negative curl anomalies may hence partly cancel each other. In contrast to decadal ENSO wind signature, there is no decadal Modoki-associated negative curl signal west of the southeastern IO region (right panel of fig. 4.11). This may explain the larger decadal Modoki positive SLA in the south central IO compared to that associated with decadal ENSO in reanalyses and WOD (fig. 4.9b and 4.10b). In the following, I address this specific issue by using the LCS model presented in section 4.1.5. Using this model, I have performed two kinds of experiments forced by 20CR surface wind stress: (i) control experiment, where the wind forcing is applied over the entire tropical Indo-Pacific domain (ii) a Pacific only experiment, where the wind forcing is applied only over the tropical Pacific, resulting in an IO response that can only take place through oceanic teleconnections from the Pacific to the IO. The linearity of the model allows to easily figure out the response of “IO only forcing” by simply subtracting results from these two simulations.

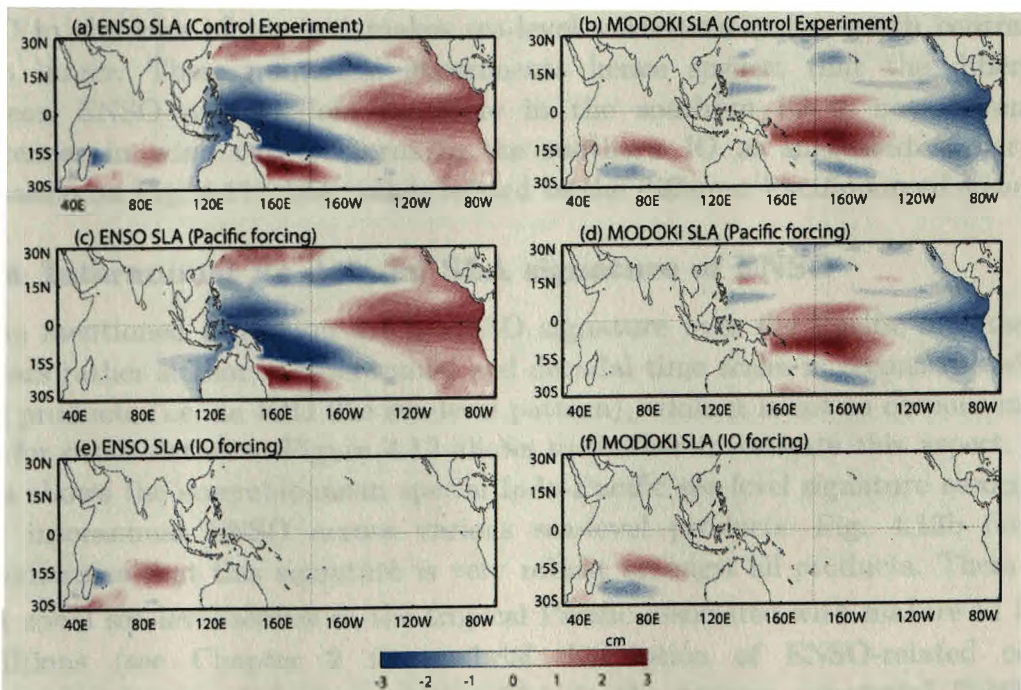


Fig. 4.12: Indo-Pacific sea-level response to decadal ENSO (left) and Modoki (right) wind stress signals, obtained from LCS ocean model simulation (forced by wind from the 20CR reanalysis). (a-b) Control experiment with wind forcing applied over the entire Indo-Pacific. (c-d) Pacific wind forcing only. (e-f) IO forcing only (this is obtained by subtracting the results of Pacific forcing experiment from control experiment).

Fig. 4.12 summarises the sea-level response to decadal ENSO and Modoki in these experiments (estimated using a linear regression to the corresponding climate indices). Fig. 4.12a,b show that when the wind forcing is applied over the entire Indo-Pacific region, the ENSO and Modoki sea-level signatures from the model are broadly consistent with those seen in reanalyses and WOD (Fig. 4.9b Fig.4.10b), suggesting that this simple tool can be used to investigate this issue. As seen in these products, the south IO sea-level response is indeed larger and broader in response to Modoki than to ENSO forcing. When applying the wind forcing over the IO only, the Modoki signature of the IO remains very similar, while the positive south central IO SLA signal related to ENSO is considerably larger and broader, a pattern that now resembles to the one related to Modoki. This suggests that the difference between ENSO and Modoki related IO signature largely arises from the Pacific wind forcing. Indeed, the “Pacific only forcing” (Fig. 4.12 c-d) shows that the south central IO sea-level signal related to decadal ENSO consists of a negative SLA along the WAC that are driven remotely from western Pacific through coastally trapped waves and that radiate westward as Rossby waves into the south central IO. On the other hand, this oceanic passage and the associated southern IO sea-level response is virtually absent for Modoki (essentially because the Pacific anomalies associated with the Modoki do not lead to a large sea-level anomaly at the entrance of the Indonesian throughflow). In essence, these results suggest that the positive SLA in the south IO driven by ENSO-related local wind curl destructively interferes with negative SLA triggered by Rossby waves radiated from WAC originally forced by Pacific wind, implying a rather weak ENSO-related SLA response in the south central IO. On the other hand, the absence of such oceanic connection between western equatorial and WAC in the case of Modoki makes sea-level variations in the south central IO much larger. These numerical experiments hence suggest that the difference between ENSO and Modoki signature in the southern IO is not driven by differences in wind curl patterns in the southern IO as suggested earlier (cf. discussion on Fig. 4.11), but rather related to the different Pacific-forced signals.

4.4.4 Interannual Vs decadal SLA signature of ENSO

As mentioned in section 4.4.2, ENSO signature over the Pacific and the IO appears rather similar at interannual and decadal time scales in reconstructed sea level products (i.e. an IOD like sea-level pattern), while it is not so obvious in the case for other datasets. Figure 4.13 allows to further investigate this aspect. Fig. 4.13a shows the ensemble-mean spatial Indo-Pacific sea-level signature associated with interannual ENSO across various sea-level products. Fig. 4.13b further demonstrates that this signature is very robust amongst all products. There is a clear zonal sea-level seesaw in the tropical Pacific associated with mature El Niño conditions (see Chapter 2 for a brief description of ENSO-related ocean dynamics). As expected, the negative SLA in the western equatorial Pacific is transmitted to the WAC through coastally trapped Kelvin waves. Coastally trapped SLA signals (but of the opposite sign) are also seen along the west coast of south and north America.

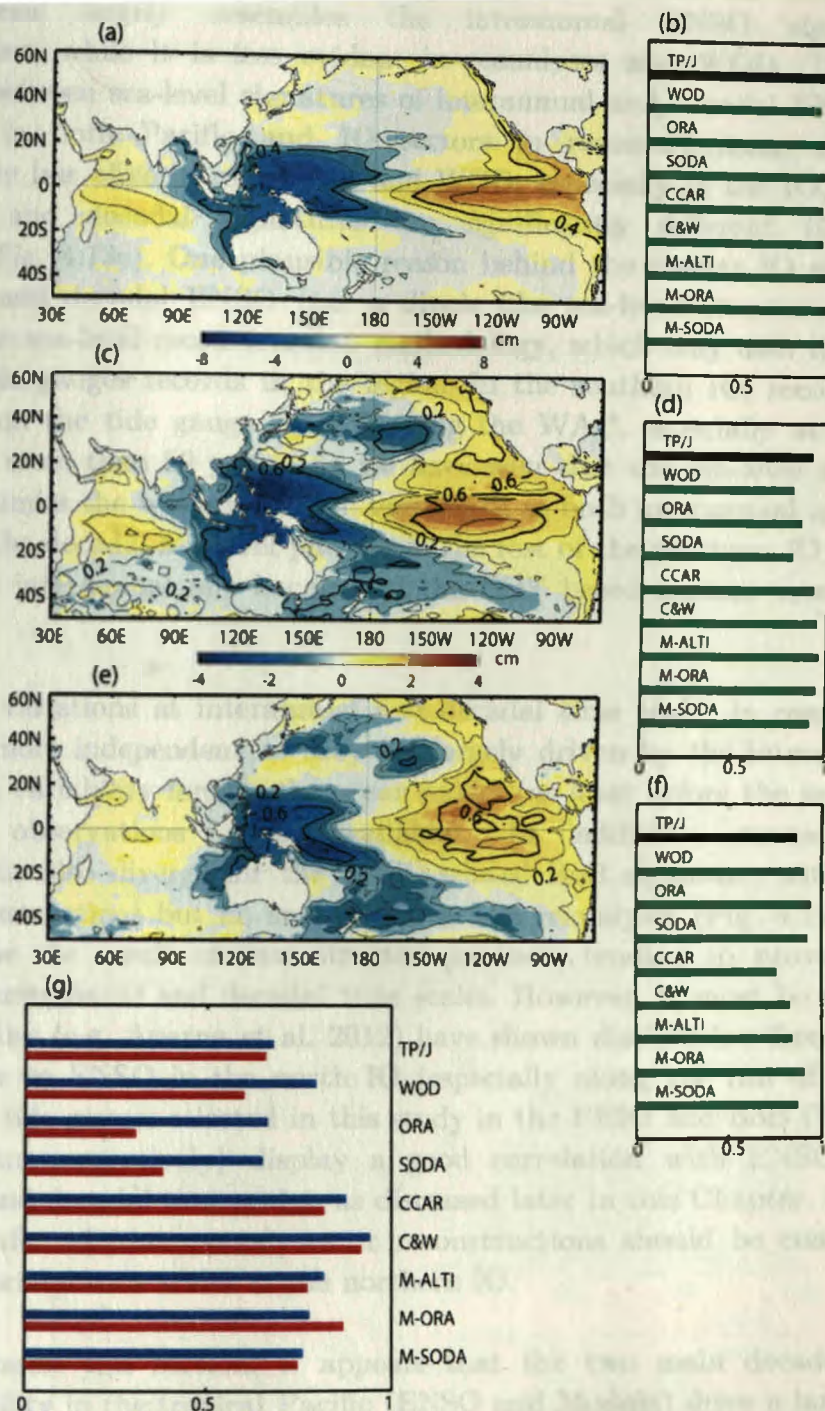


Fig. 4.13: (a) Ensemble-mean of SLA regression pattern onto interannual ENSO index in the Indo-Pacific region for all products. (b) Pattern correlation between the ensemble mean shown in (a) and regression pattern for individual products. (c-d) Same as (a-b) but for decadal ENSO-related SLA for reconstruction ensemble. (e-f) Same as (c-d) but for the reanalysis and WOD ensemble. (g) Pattern correlation between the regression patterns to interannual and to decadal ENSO in the Pacific (blue) and IO (red) for each gridded product.

At decadal time scales, we have seen in Fig. 4.9 that the ENSO sea-level signature is relatively consistent between reconstruction and reanalyse products in the Pacific but not in the IO. This discrepancy is likely to arise from the different techniques used to produce reanalyses and reconstructions. Fig. 4.13a,b,c highlight that the decadal ENSO-driven sea-level response in the tropical Indo-

Pacific Ocean largely resembles the interannual ENSO signature in reconstructions, while it is less evident in reanalyses and WOD. The pattern correlation between sea-level signatures of interannual and decadal ENSO indeed exceed 0.8 in both Pacific and IO sectors in reconstructions, while these signatures are less alike in reanalyses and WOD, especially in the IO, where the interannual and decadal signatures are significantly different (0.3 to 0.6 correlation; Fig. 4.13e). One plausible reason behind the similar IO signature to interannual and decadal ENSO (i.e. a dipole like sea-level structure) could be related to the sea-level reconstruction methodology, which only uses the sea-level from long tide gauges records in the region. In the southern IO, reconstructions largely rely on the tide gauge records along the WAC, especially at Fremantle which spans more than 50 years. As we have seen that the sea-level recorded at this gauge mimics the western Pacific variability at both interannual and decadal time scales, the decadal sea-level pattern in the rest of the southern IO is likely to resemble the interannual one because of the EOF based pattern reconstruction technique.

Sea-level variations at interannual and decadal time scales in reanalyses are likely to be more independent as they are largely driven by the interannual and decadal wind variability forcing the ocean model (at least before the satellite era, when less observations were available). In addition, reanalyses and reconstructions also diverge for the ENSO-related BoB signature, with negative SLA in reconstructions but no such signal in the reanalyses (Fig. 4.13b,c). This may again be the result of reconstructed products tending to provide similar patterns at interannual and decadal time scales. However, it must be noted that previous studies (e.g. Aparna et al. 2012) have shown distinct low-frequency sea-level response to ENSO in the north IO (especially along the rim of BoB) and that the two tide gauges selected in this study in the EEIO and BoB (Raffles and Visakhapatnam respectively) display a good correlation with ENSO at both interannual and decadal time scales, as discussed later in this Chapter. It is hence difficult to infer whether reanalyses or reconstructions should be considered as realistic at decadal time scales in the northern IO.

To summarise this section, it appears that the two main decadal climate modes variability in the tropical Pacific (ENSO and Modoki) drive a large part of the decadal sea-level variability in the Pacific, their signatures being very robust amongst the different products analysed. In contrast, there are large discrepancies in sea-level signatures from these climate modes in the IO (except along the WAC). In reanalyses and WOD, the decadal Modoki is associated with a strong signature in the central IO, while the ENSO-related signature is confined to the WAC, despite a similar IO wind forcing by these two climate modes. The weak sea-level response to ENSO forcing in the southern IO can be explained by the destructive interference between the ENSO-related oceanic bridge that force negative sea-level signals emanating from the WAC and the ENSO-related atmospheric bridge (see Chapter 2, section 2.5) that force positive SLA in the same region. In reconstructions, the IO ENSO signature is very similar at

interannual and decadal time scales, a feature that may be related to the EOF-based reconstruction technique. In any case, the control of the tropical Pacific climate variability on the IO sea-level appears to be rather modest in most of the analysed products (~20-30% of the total decadal sea level variance over the IO), except for C&W (80%). In the next section, I investigate the main modes of decadal sea-level variability in the IO and how they relate to Pacific variability (i.e. decadal ENSO and Modoki).

4.5 Modes of IO decadal sea-level variability

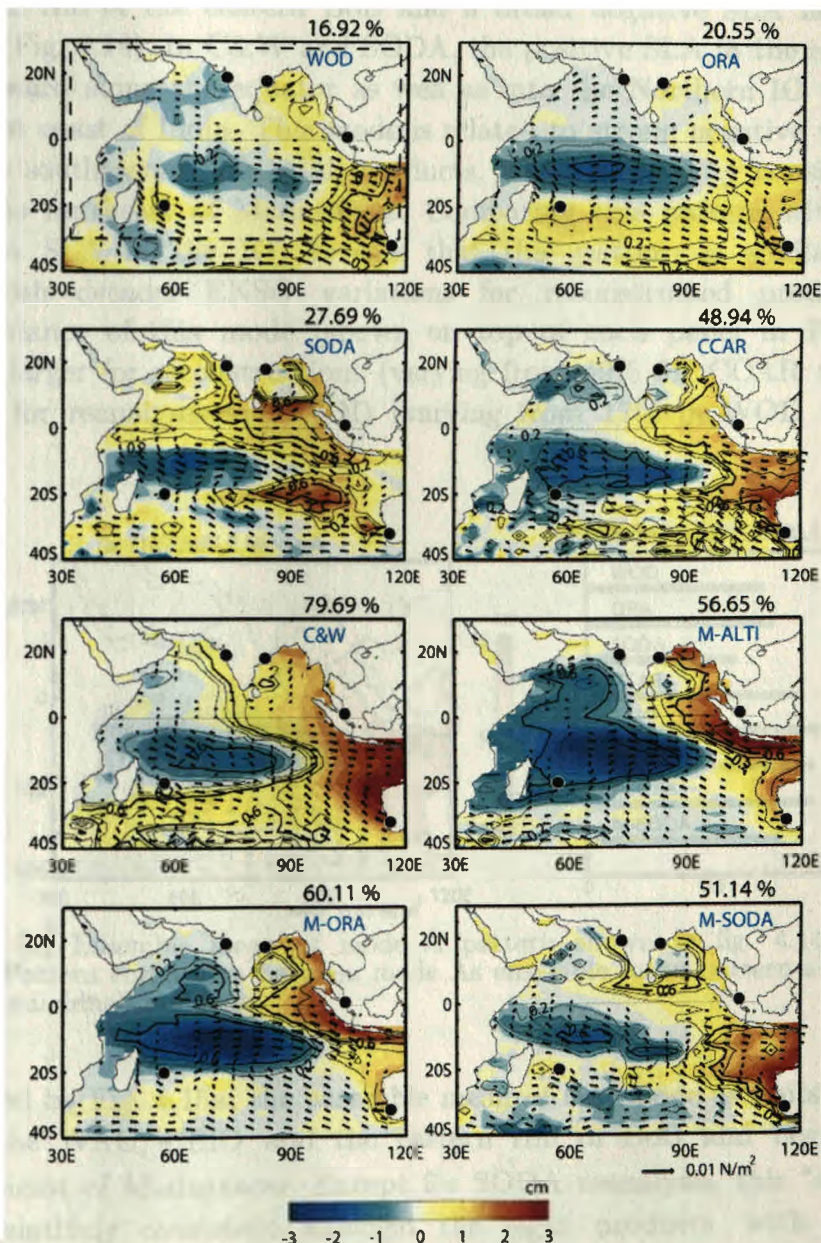


Fig. 4.14: Mode A EOF pattern (see text) of IO decadal SLA (shade) and associated 20CR wind stress (vectors). The region where the EOF is computed is outlined by the dashed frame on the first panel. Seas around the Maritime continents are excluded from the EOF. The percentage of SLA variance explained by the corresponding PC is indicated by contours. The percentage of total variance explained by this EOF mode is shown on the top of each panel. Locations of selected tide gauges in the IO are also shown (black dots).

A separate EOF analysis is now performed for the IO decadal sea level (over the 30E-120E; 30S-30N domain). Amongst the first two EOFs, there is one mode that systematically looks like the IOD sea-level signature in the IO. This pattern is depicted by EOF2 in WOD and ORA and EOF1 for all other products. I refer to this IOD-like mode as mode A. The other decadal IO mode (EOF1 for WOD and ORA and EOF2 for the others) will be referred to as mode B.

Fig. 4.14 shows this mode A for the eight gridded products. 20CR decadal wind stress is regressed to the normalised PC and shown as vectors in each panel. Sea level shows a “basin-scale” pattern with positive SLA along the WAC, EEIO and along the rim of the eastern BoB and a broad negative SLA northeast of Madagascar (Fig. 4.14). In C&W and SODA, the positive SLA in the eastern side spreads westward along the equator as well as into the Northern IO waveguide, up to the west coast of India. This mode is related to strong negative wind stress curl over the southeastern IO in all products, which is broadly consistent with negative SLAs northeast of Madagascar. Comparing this pattern with Fig. 4.9 (ENSO-driven SLA in the IO) reveals that this pattern is similar to that associated with decadal ENSO variations for reconstructed products. The explained variance of this mode (shown on top of each panel in Fig.4.14) is considerably larger for reconstructions (varying from 49% for CCAR to 80% for C&W) than for reanalyses and WOD (varying from 17% in WOD to 27% in SODA).

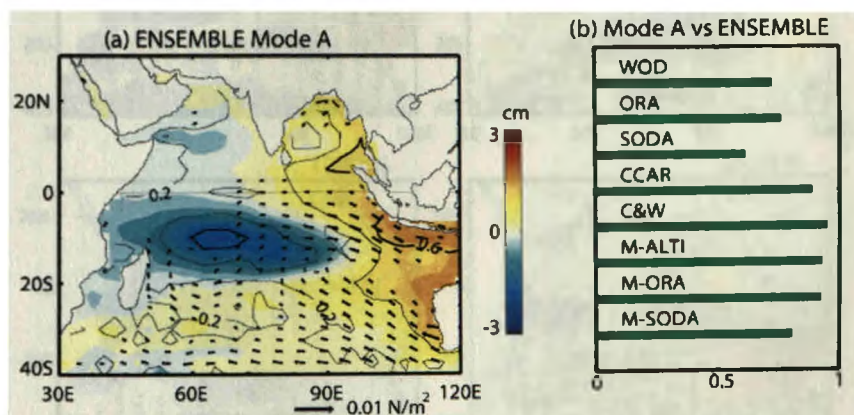


Fig. 4.15: (a) Ensemble mean of mode A pattern shown in fig. 4.14 across all products. (b) Pattern correlation between mode As ensemble mean pattern shown in (a) and those for individual products.

As revealed by Fig. 4.15a, the ensemble mean of this mode exhibits a positive SLA along the WAC, EEIO and the eastern rim of BoB and negative SLA centred northeast of Madagascar. Except for SODA reanalysis, this “dipole like” pattern is relatively consistent amongst the eight products, with individual correlation patterns with the ensemble mean exceeding 0.7 (Fig. 4.15b).

Unlike mode A for which all products display a consistent basin-scale SLA signature, mode B pattern is very diverse amongst sea-level products (Fig. 4.16). Only ORA (with 36% of explained variance) and M-ORA (18%) exhibit similar

patterns, with a maximum variability located in the SWIO. Mode B from WOD also exhibits strong signal east of Madagascar, but shifted eastward and slightly noisy. Both CCAR and C&W display a confined variability in the western part of the tropical IO, which is not surprising as most of the SLA variance elsewhere is already captured by mode A in these products (and explained by decadal ENSO as we will see towards the end of this section). M-ALTI displays a strong positive SLA in the southeastern IO. Finally, SODA and M-SODA display a strong variability in the sub-tropical IO. Overall, this analysis further supports the idea that the IO decadal sea-level variability is not consistent amongst sea-level products.

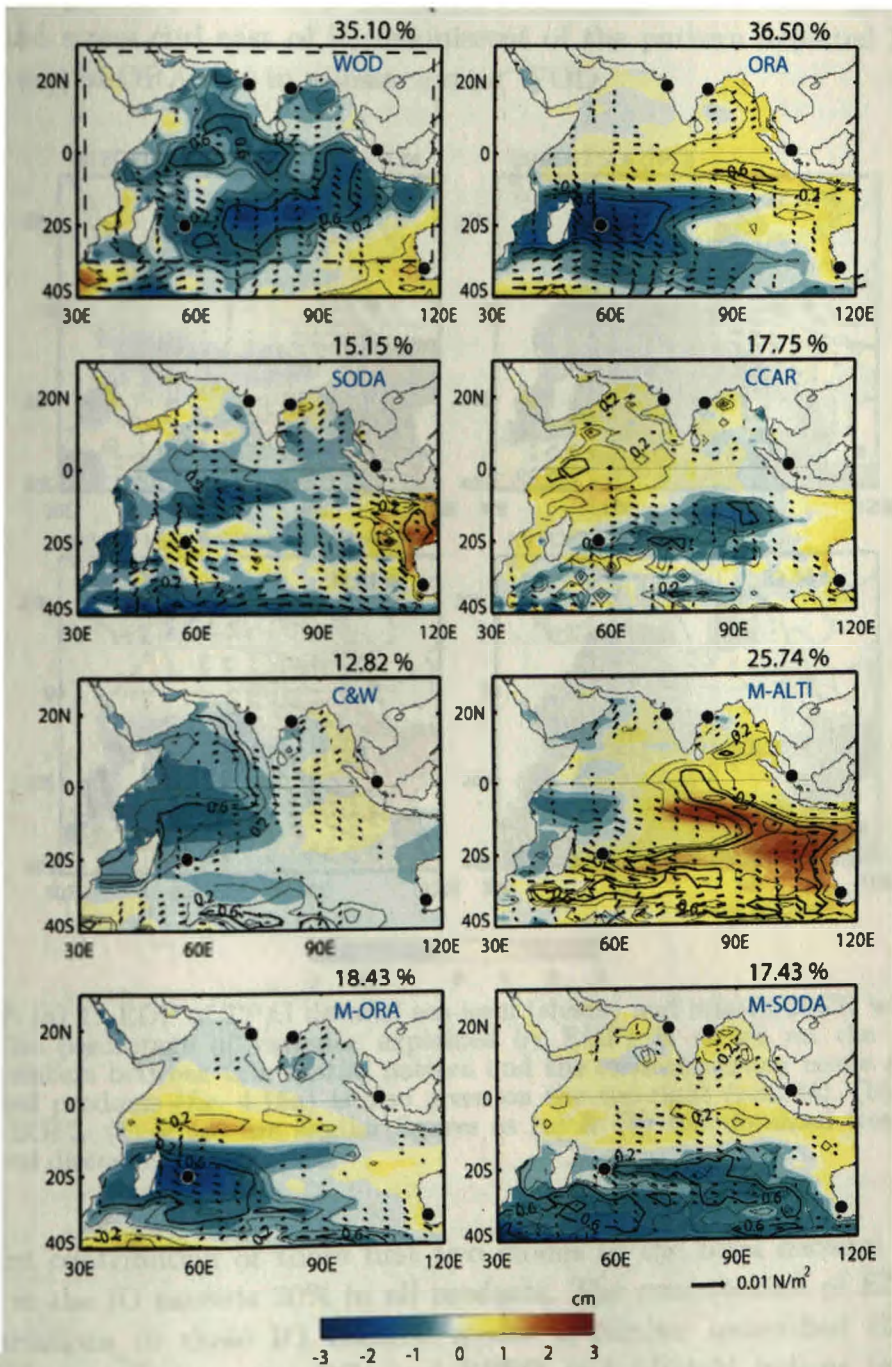


Fig. 4.16: Same as fig. 4.14 but for mode B (see text) EOF pattern.

Figure 4.17 shows the EOF1 and EOF2 of decadal sea level in the IO from TP/J and NEMO. Since these two products have a different time period (1993-2010 for TP/J and 1966-2007 for NEMO) compared to other gridded products (1960-2010), results are presented separately for these two products. Interestingly, the EOF1 pattern of both TP/J and NEMO (Fig. 4.17a,c) agrees very well with the ensemble-mean IOD-like mode A pattern (Fig. 4.15a) in terms of SLA (pattern correlation of 0.84 for TP/J and 0.76 for NEMO) and wind. The TP/J spatial pattern resembles the ENSO-related SLA signature shown in this product in Fig. 4.9e. This result suggests that this “dipole like” basin wide pattern is probably a robust feature of the decadal IO sea-level variability. The second mode in these products exhibits a maximum variability east of Madagascar with negative wind stress curl east of it, reminiscent of the pattern depicted by mode B for ORA and M-ORA and to a lesser extent WOD.

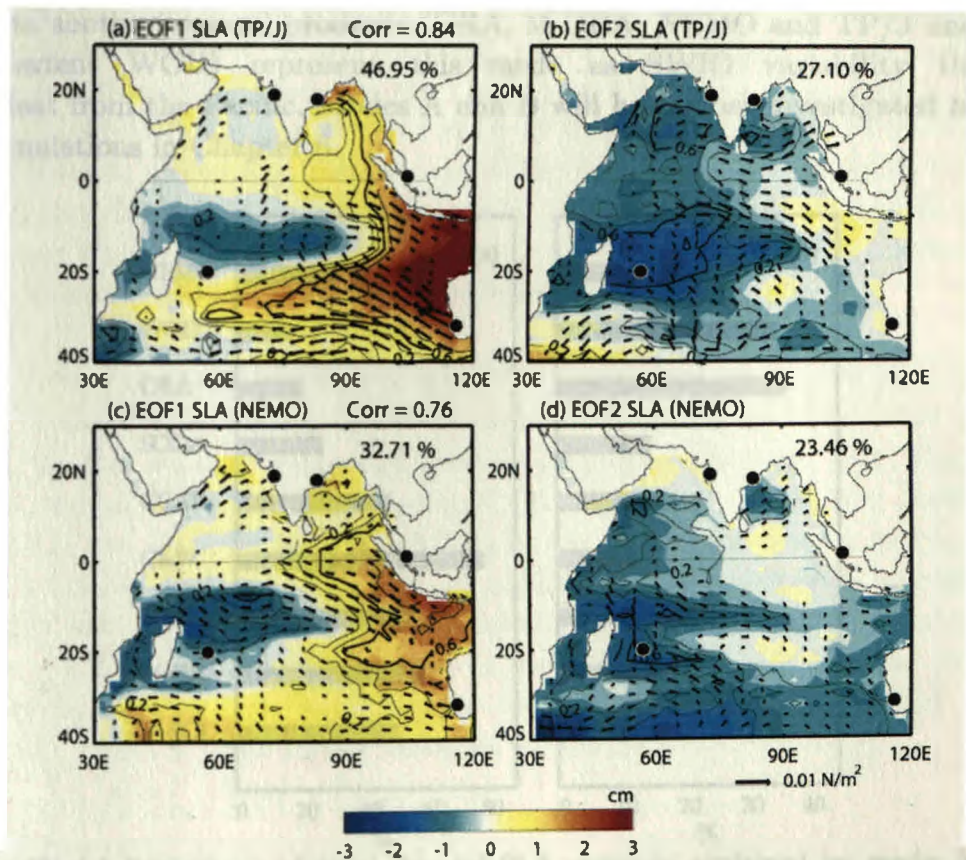


Fig. 4.17: (a) 1st EOF of TP/J decadal sea-level (shade) and related 20CR wind stress (vectors). The percentage of variance explained by EOF1 is shown on the top. The pattern correlation between this spatial pattern and the ensemble-mean mode A pattern for all gridded products (fig. 4.15a) is also given on the top-right ($r=0.84$). (b) Same as (a) but for EOF2. (c) & (d) are similar figures as (a) & (b) but obtained from NEMO steric sea level discussed in chapter 3.

The joint contribution of these first two modes to the total decadal sea-level variability in the IO exceeds 50% in all products. The contribution of ENSO and Modoki variations to these IO decadal modes is further quantified through a linear correlation between the PCs and ENSO and Modoki indices (explained variance computed as the square of the linear correlation coefficient) and

presented in Fig. 4.18. As previously suggested, mode A in C&W, CCAR and M-SODA is mainly driven by decadal ENSO variations. For reanalysis and NEMO products, the control by Modoki is larger than that of ENSO. For WOD, M-ORA and M-ALTI both ENSO and Modoki show a similar control on mode A. In any case, it appears that that this decadal IO sea-level mode is strongly controlled by the decadal climate variability in the Pacific. The relative control of ENSO and Modoki, however, depends on the sea-level product considered. There is also a significant part of the variance unexplained by the Pacific modes (ENSO and Modoki), suggesting that other climate modes, probably rooted in the IO (e.g. the portion of decadal IOD fluctuations which is independent of ENSO), partly control this mode of variability.

In contrast to mode A, mode B is nearly independent of Pacific variability (Fig 4.18b). While the pattern associated to this mode is very different from one product to another, several products (ORA, M-ORA, NEMO and TP/J and to a certain extent WOD) represent this mode as SWIO variability that is independent from the Pacific. Modes A and B will be further investigated in long CMIP simulations in Chapter 6.

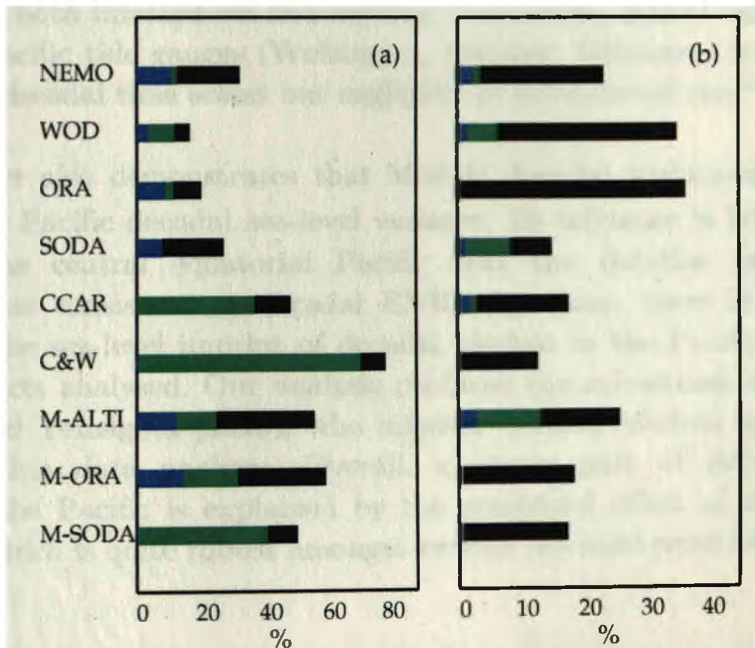


Fig. 4.18: (a) Percentage of total decadal SLA variance explained by mode A. The fraction of variance explained by decadal ENSO (green) and Modoki (blue) are also shown. (b) Same as (a) but for mode B explained variance.

4.6 Summary and discussion

The present chapter aims at assessing the robustness of conclusions drawn based on the analysis of a single ocean model in Chapter 3. This is performed by comparing the decadal sea-level variability in the Indo-Pacific sector using a large set of long-term (~50 years) gridded sea-level products based on either *in situ* observations (thermometric SLA from WOD), reanalyses/models (ORA, SODA, NEMO) and reconstructions (CCAR, C&W and three different products from

Meyssignac reconstructions, referred to as M-ORA, M-ALTI and M-SODA). The main results are summarized below.

4.6.1 Pacific decadal sea-level variability

Our results confirm that decadal ENSO (IPO) variations control a large part of decadal sea-level variance in the Pacific Ocean (50% and more in reconstructions and ~30-40% in reanalysis and WOD), not only in the tropics but also in the mid-latitudes. All products generally display a very consistent Pacific sea-level pattern associated with decadal ENSO, similar to the one depicted by the short-period altimeter data, suggesting that any of these products can confidently be used to describe ENSO-related decadal Pacific sea-level variability. The decadal pattern is somewhat different from the Pacific ENSO sea-level response at interannual time scales, where the sea-level response is largely confined to the tropical Pacific (see Fig. 4.13). The strong control of ENSO on the interannual sea-level in the tropical Pacific and weaker control at mid-latitudes is further confirmed by the tide gauges analysis (Fig. 4.19a). ENSO explains 40 to 60% of the sea-level variance for tide gauges located in the tropical Pacific (Honiara, Christmas, Guam) and along the west coast of north America (San Diego) at both interannual and decadal time scales. ENSO influence on the mid-latitude Pacific tide gauges (Wellington, Midway, Uchiuara) is, on the other hand, large at decadal time scales but negligible at interannual ones³.

This chapter also demonstrates that Modoki decadal variations also control ~15-20% of the Pacific decadal sea-level variance. Its influence is however mainly confined to the central equatorial Pacific near the dateline (see Fig. 4.8). Although not as consistent as decadal ENSO signature, there is a reasonable agreement in the sea-level imprint of decadal Modoki in the Pacific amongst the different products analysed. Our analysis confirms the robustness of the findings from Behra and Yemagata (2010), who inferred decadal Modoki imprint from a 15 years satellite data analysis. Overall, a major part of decadal sea-level variability in the Pacific is explained by the combined effect of decadal ENSO and Modoki, which is quite robust amongst various sea-level products.

³ There are two possibilities for this distinction of ENSO related SLA signature over mid-latitudes at interannual and decadal time scales. (i) *signal to noise ratio*: at interannual time scales, the sea-level signature of ENSO's teleconnection in the North Pacific is dominated by the stochastic part of the forcing. But this signal emerges at longer time scales, because of its integration by the ocean. (ii) *adjustments by planetary waves*: SLA become evident only at decadal time scales in mid-latitudes because the slow-moving mid-latitude long Rossby waves get enough time to travel and marks its signatures at decadal time scales but the interannual wind forcing relatively alternates faster and the mid-latitude ocean adjustment can only be forced by lower frequency wind variations in these regions (conversely interannual wind forcing can force SLA within the tropics because of much faster waves propagation).

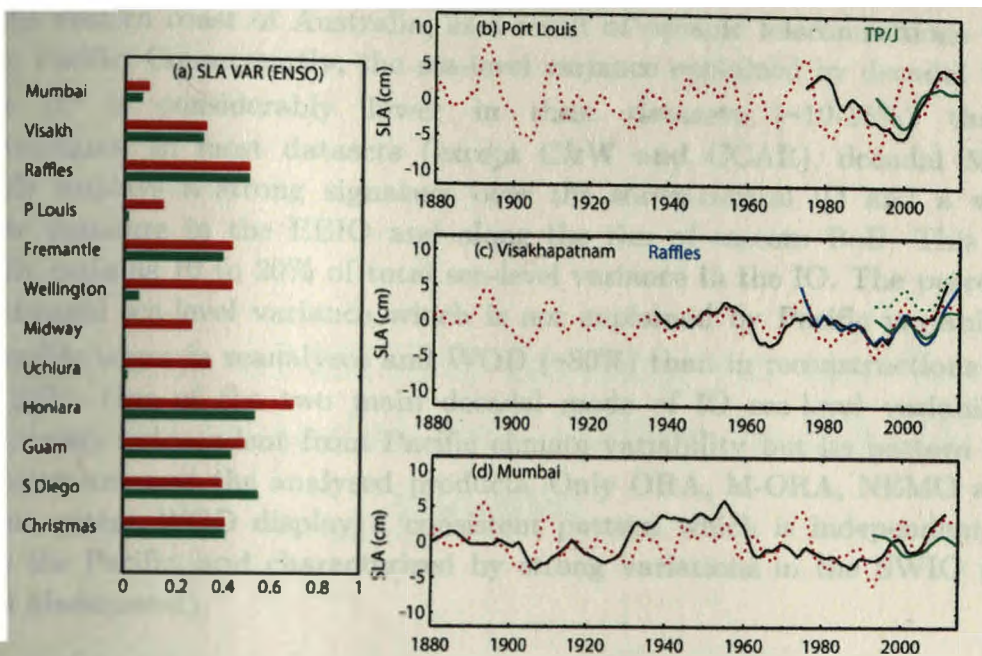


Fig. 4.19: (a) Percentage of tide gauge sea-level variance explained by ENSO at both interannual (green) and decadal (red) time scales. Decadal sea-level variations from tide gauge (black/blue) and altimeter (green) at (b) Port Louis, (c) Visakhapatnam & Raffles (d) Mumbai. The decadal ENSO index is overlaid as a dashed red line on each panel (scaled by the STD of sea-level time series for presentation purposes).

4.6.2 Indian Ocean decadal sea-level variability

While the Pacific decadal sea-level variability is robust across sea-level products, it is not the case for the IO. The IO variability described by reconstructions generally differs from that described by other products (reanalysis and WOD). The Pacific control on the IO decadal sea-level indeed appears to be larger in reconstructed sea-level products. The first dominant mode of decadal IO sea-level variability in these products exhibits a pattern that strongly resembles the IO signature of ENSO at interannual time scales (a dipole-like pattern reminiscent of the IOD sea-level signal) and explains more than 50% of the IO variance. In these products, this mode is strongly related to the Pacific decadal variability. This is particularly the case for C&W dataset, where ~80% of the decadal sea-level variance in the IO is explained by this mode, which is almost entirely controlled by decadal ENSO. This strong control of the Pacific on the decadal IO sea-level in these products is probably spurious and may be related to sparse tide-gauge records in the southern IO.

One of the two dominant modes of decadal IO sea-level variability in reanalyses and WOD exhibits a basin-wide seesaw pattern, which is however more independent from Pacific decadal climate modes compared to reconstructions. The decadal ENSO signature is also generally confined to the WAC in reanalysis and WOD, most likely because of a destructive interference between the sea-level responses triggered by ENSO-driven oceanic and atmospheric teleconnection over the southern IO. The positive SLAs in the SIO triggered by ENSO-related wind stress curl in the southeastern IO oppose the negative SLAs induced by the ENSO-driven upwelling Rossby waves radiated

from the western coast of Australia, as a result of oceanic teleconnections to the western Pacific. Consequently, the sea-level variance explained by decadal ENSO in the IO is considerably lower in these datasets (~10-15%) than in reconstructions. In most datasets (except C&W and CCAR), decadal Modoki generally displays a strong signature over the south-central IO and a weaker opposite signature in the EEIO and along the rim of eastern BoB. This mode generally explains 10 to 20% of total sea-level variance in the IO. The percentage of IO decadal sea-level variance which is not explained by Pacific variability is considerably larger in reanalyses and WOD (~80%) than in reconstructions (from 65 to 20%). One of the two main decadal mode of IO sea-level variability is indeed largely independent from Pacific climate variability but its pattern is not very robust amongst the analysed products. Only ORA, M-ORA, NEMO and to a certain extent WOD display a consistent pattern which is independent from that in the Pacific, and characterized by strong variations in the SWIO region (east of Madagascar).

It is difficult to infer which long-term product is the most reliable for analysing IO decadal sea-level variations from available direct sea-level observations (altimetry and tide-gauges). Analysis of the short altimeter record shows an ENSO influence on IO decadal sea-level that lies in-between those diagnosed from reconstructions and reanalyses (Fig. 4.9), with a strong negative sea-level signal along the WAC that expands westward along 30S and a weak positive signal north of it. In line with some long-term gridded products (ORA, M-ORA, NEMO and to a certain extent WOD), this dataset also reveals a strong decadal sea-level variability east of Madagascar, that is independent from ENSO (Fig. 4.17). It is however very difficult to draw definite conclusions on decadal variability from such a short record. Similarly, the IO tide gauge coverage is very poor. Only two tide gauges span more than 30 years in the southern IO. The analysis of the 100-year long Freemantle tide gauge confirms the strong influence of ENSO along the WAC at both interannual and decadal time scales (Fig. 19a), in agreement with all the gridded products analysed. On the other hand, the strong decadal sea-level variability at Port Louis in the SWIO are not influenced by ENSO (Fig. 19a). This could either be due to its geographic location outside of the regions of maximum ENSO influence (Fig. 4.9). Analysis of long tide gauge data in the EEIO (Raffles) and the BoB (Visakhapatnam) suggests a possible influence of decadal ENSO on the northern IO sea level, through coastal Kelvin wave propagating from the equatorial region (Fig. 4.19a,d). However, the sea-level variability along the west coast of India (Mumbai) is dominated by multi-decadal changes, which are not related to decadal ENSO variations.

The results suggest that a large part of the IO decadal variability may be controlled by processes rooted in the IO and not related to those in the Pacific. However, the inconsistencies between the analysed observational products do not allow to draw definitive conclusion on this issue, which will be further investigated in Chapter 6 using the large database with long records offered by CMIP models.

Influence of ENSO forcing on the Indo-Pacific decadal variability in CMIP models

Chapters 3 and 4 revealed that the description of decadal sea-level and wind variations in the IO is not consistent amongst the analysed products. There are two major caveats that arise from the analysis of these observationally-derived products. First, the very sparse in-situ measurements of sea level in the IO before the satellite era does not constrain these products enough, which largely explains their inconsistent behaviour. Second, these products generally cover a relatively “short” period (~50 years) with regards to the time scales we are interested in (decadal to multi-decadal time scales), which clearly restricts the statistical significance of our results. The analysis of CMIP models can alleviate these two major issues. First, the pre-industrial simulations in these models are considerably longer (~500 years) than the observational datasets and their analysis will hence allow a statistically robust assessment of their simulated decadal variability. Second, although these models exhibit certain biases (see chapter 2), these simulations provide climate datasets without any gaps or measurements uncertainty, as compared to observationally derived datasets. Pre-industrial simulations also do not include any anthropogenic forcing, which allows to clearly attribute all the variability they exhibit to intrinsically generated variability, that is not aliased by external and anthropogenic forcing as in observations.

The present chapter assesses the ability of CMIP models to accurately simulate ENSO and its teleconnections to the Indo-Pacific Ocean, especially at decadal time scales. Given the importance of ENSO for Indo-Pacific decadal variations, this preliminary assessment is a necessary prerequisite to ascertain the degree of confidence that we can have in the realism of the natural decadal sea-level variability simulated by these models, which will be discussed in chapter 6. The ‘observed’ low-frequency (both interannual and decadal) climate variability in the tropical Indo-Pacific basin has been extensively described in the literature in terms SST and wind variations associated with ENSO and PDO (e.g. Bjerknes

1969, Mantua et al. 1997, Power et al. 2002, Deser et al. 2004, Newman et al. 2003). The analysis performed in this chapter hence includes climate variables such as SST, wind, precipitation and sea-level pressure but *not* sea level, a variable which will be investigated in the next chapter. This will allow to assess the extent to which CMIP models represent the “observed” low-frequency climate features in the Indo-Pacific Ocean.

ENSO is the leading mode of global interannual climate variability. The salient features of ENSO have been discussed in Chapter 2 and I’ll just revise here the features that are important for understanding the present chapter. El Niño manifests itself in the central and eastern tropical Pacific Ocean as a widespread positive SST anomalies, that enhances deep atmospheric convection and tropospheric diabatic heating over the central Pacific. This heating drives an atmospheric planetary wave response, resulting in global-scale impacts through atmospheric teleconnections (e.g. Alexander et al. 2002). The tropical Pacific anomalies associated with ENSO is indeed channelled toward higher latitudes by atmospheric Rossby waves guided by the zonal mean circulation, acting to deepen the extra-tropical low pressure systems and strengthen the westerlies over the north and South Pacific (e.g. Alexander 1990; Lau and Nath 1994; Lau and Nath 1996; Alexander et al. 2002). ENSO also affects rest of the tropics via zonal shift of the Pacific Walker circulation (e.g. Klein et al. 1999; Lau and Nath 2000). The atmosphere thus acts like a bridge linking the tropical Pacific variability to sea-level pressure and surface wind variations in other oceanic regions, leading to a large heat flux, wind and SST signature of ENSO outside the tropical Pacific (e.g. Zhang et al. 1997). ENSO exhibits its most energetic fluctuations at interannual time scales but also displays lower-frequency fluctuations at decadal/multi-decadal time scales.

The prominent mode of low-frequency SST variability in the north Pacific is named the Pacific Decadal Oscillation (PDO; e.g. Zhang et al. 1997; Mantua et al. 1997). As discussed in Chapter 2, this mode is driven by fluctuations of the north Pacific Aleutian low (Pierce et al. 2000; Alexander et al. 2002) and strongly influenced by ENSO that modulates the intensity of this low through the atmospheric teleconnections. The influence of ENSO on PDO translates into a ~ 0.6 correlation between observed ENSO and PDO time series, with ENSO leading the PDO evolution by 1-2 months. As a result, the pan-Pacific expression of the PDO, also known as the Inter-decadal Pacific Oscillation (IPO, Power et al. 1999; Folland 2002), bears a strong resemblance with that of ENSO, except for a stronger weighting in the north Pacific relative to the tropical Pacific.

The SST anomalies in the north Pacific are detrained from the mixed layer at the end of winter and persist in the seasonal thermocline through summer, isolated from the atmospheric influence. Part of those thermal anomalies *re-emerge* through entrainment into the mixed layer during the following winter (a process called “*re-emergence mechanism*”; Namias and Born 1974; Alexander and Deser 1995; Deser et al. 2003, 2010). The resulting integration of the atmospheric

forcing by the ocean (e.g. Frankignoul and Hasselman 1977) acts to increase the PDO variance in the low frequency part of its spectrum, i.e. at decadal and multi-decadal time scales. Newman et al. (2003) showed that the observed PDO spectrum was compatible with that obtained from a simple autoregressive model accounting for ENSO influence, stochastic atmospheric forcing and re-emergence process. In this paradigm, the PDO can be described as a reddened response to ENSO and north Pacific atmospheric stochastic forcing, also known as “*Extended Null Hypothesis (ENH hereafter)*” for PDO. There are however evidences that the north Pacific gyre anomalies and local air-sea coupling processes also contribute to the PDO at multi-decadal time scales (e.g. Deser and Blackmon 1995; Wu et al. 2003; Schneider and Cornuelle 2005; Qiu et al. 2007), leading other authors to suggest that the PDO may not be explained from a single physical mode but rather the sum of several phenomena (Schneider and Cornuelle 2005; Liu 2012; Newman 2013).

As discussed in Chapter 2, ENSO also influences the Indian Ocean through zonal shifts in the Walker circulation, resulting in a tropical Indian Ocean basin-wide warming persisting even after ENSO demise (Klein et al. 1999; Xie et al. 2009). There is thus a clear influence of the Pacific on the Indian Ocean at interannual time scales. How this influence translates at decadal time scales, or whether an independent mode of Indian Ocean variability exists at this time scale, however, remains largely unexplored (Han et al. 2014). Proxy-based reconstructions further suggest that a large part of SST decadal variations in the southwest Indian Ocean are related to decadal ENSO variability (Cole 2000; Cobb and Charles 2001; Crueger et al. 2008; Grove et al. 2013) and could in turn modulate Indian summer monsoon rainfall (Krishnan and Sugi 2003). This is a strong motivation to investigate decadal variations in the Indian Ocean.

The ability of CMIP models to simulate ENSO and the PDO has been discussed in the past literature. Most CMIP3 models reproduce the spatial pattern of the PDO in the north Pacific reasonably well (Furtado et al. 2011; Kwon et al. 2012; Park et al. 2013; Yim et al. 2014) but the influence of ENSO on the PDO has been reported to be far weaker or even non-existent in most CMIP simulations (Newman 2007; Oshima and Tanimoto 2009; Furtado et al. 2011; Deser et al. 2012; Park et al. 2013). Previous studies hypothesized that this mismatch could be either attributed to a weak projection of ENSO atmospheric teleconnections onto the Aleutian Low (Furtado et al. 2011) or to underestimated ENSO amplitude (Parks et al. 2013). On the other hand, the influence of ENSO on the decadal IO SST variability has not yet been explored in CMIP models.

5.1 Data

5.1.1 Observational data

Observational datasets which span at least the entire 20th century are only considered in this attempt as the goal here is to describe interannual to decadal SST variations in the Indo-Pacific region. To infer the robustness of the

conclusions regarding PDO/IPO characteristics in observations, I analysed three gridded SST products. The baseline dataset is the HadISST dataset available from 1870 onwards, already described in the previous chapters. I compared the results obtained from HadISST with two other SST reconstruction products that also use blended in-situ and satellite data and statistical techniques to fill the gaps: ERSSTv3 available from 1854 (Smith et al. 2008) and Kaplan v2 available from 1856 (Kaplan et al. 1998). We also used surface wind stress, sea-level pressure (SLP) and precipitation fields available over the entire 20th century, namely, the previously described 20CR dataset (Compo et al. 2011). To allow for a fair comparison, all these datasets are interpolated onto a common 2.5°x2.5° horizontal grid and are analysed at monthly resolution over their common period, i.e. 1871-2010.

5.1.2 CMIP models

CMIP3 models				
No.	Model Name	Short Name	Length (yr)	Class
1	CGCM3.1	CGCM	500	II
2	GFDL-CM2.0	GFDL2.0	500	II
3	GFDL-CM2.1	GFDL2.1	500	I
4	GISS-AOM	GISSAO	250	II
5	GISS-ER	GISSER	500	II
6	IPSL-CM4	IPSL4	500	I
7	MIROC3.2(m)	MIROC3	500	I
8	ECHO-G	ECHO-G	340	I
9	MRI-CGCM2.3.2	MRI2.3.2	350	II
10	UKMO-HadCM3	HadCM3	340	II
CMIP5 models				
11	BCC-CSM1.1	BCCCSM	500	II
12	CanESM2	CanESM	500	I
13	CCSM4	CCSM4	500	I
14	CNRM-CM5	CNRM	500	II
15	CSIRO-Mk3.6.0	CSIRO	500	I
16	FIO-ESM	FIO	500	II
17	GFDL-CM3	GFDL3	500	I
18	GFDL-ESM2G	GFDL2G	500	II
19	GFDL-ESM2M	GFDL2M	500	I
20	GISS-E2-R	GISSE2R	500	II
21	HadGEM2-ES	HadGEM	500	I
22	INM-CM4	INMCM	500	II
23	IPSL-CM5A-LR	IPSL-LR	500	I
24	IPSL-CM5A-MR	IPSL-MR	300	I
25	IPSL-CM5B-LR	IPSL5B	300	II
26	MIROC5	MIROC5	500	I
27	MPI-ESM-LR	MPI-LR	500	I
28	MPI-ESM-MR	MPI-MR	500	II
29	MPI-ESM-P	MPI-P	500	I
30	MRI-CGCM3	MRI3	500	II
31	NorESM1-M	Nor-M	500	I
32	NorESM1-ME	Nor-ME	252	I

Table 5.1: List of models from CMIP3 and CMIP5 database. Model name, short name used in figures and discussion, length of pre-industrial control simulation analysed and Class of the model (see text) are also indicated.

Readers may refer to section 2.1.2 for a brief introduction to CMIP coupled models. Models from both CMIP3 (Meehl et al. 2007) and CMIP5 (Taylor et al. 2012) archives are used in this study. To avoid potential aliasing of the natural variability by anthropogenic forcing, we focused on multi-century pre-industrial control simulations, with a constant CO₂ concentration of about 280 ppm. As the focus of the present study is on decadal variability (greater than 7 years), we analysed only those models that provide at least 250 years of simulations to ensure statistical robustness of the spectral characteristics of decadal variability. This criterion has led to the selection of 10 CMIP3 and 22 CMIP5 simulations, which are listed in Table 5.1.

5.2 Method

5.2.1 Climate indices definition

Following Zhang et al. (1997) and Mantua et al. (1997) seminal papers, PDO-related literature usually defines the PDO from the leading EOF of monthly SST anomalies over the north Pacific after removing the global mean SST time series. We used a similar method in the present study. SST anomalies are calculated by removing the monthly climatology. The global mean SST and a linear trend are then removed from each grid point and a five-month running mean is applied before performing the EOF analysis. For the PDO, the EOF is performed over the 110E-110W; 20N-60N region. Similarly, ENSO is defined as the leading EOF of the monthly SST anomalies over the tropical Pacific (120E-80oW; 20N-20S) as defined in Newman et al. (2003). The first EOF over the north (tropical) Pacific and corresponding principal components are used to define the PDO (ENSO) spatial pattern and time evolution. The EOF spatial pattern is normalized by its spatial root mean square (rms) over either the tropical (ENSO) or north Pacific (PDO) where EOF is performed, so that the PC accounts for the amplitude. The standardised global signature associated with each of these climate modes is computed by regressing different variables (SST, SLP, wind and precipitation) onto the corresponding PC time series.

The interannual and decadal components of the ENSO/PDO time series and all the variables discussed in this study are extracted using the STL filtering method, described in chapter 3.

5.2.2 Statistical analysis

Re-emergence of north Pacific SST anomalies from the previous winter, ENSO forcing through mid-latitude teleconnections and the atmospheric white noise forcing are key components in setting the temporal characteristics of the PDO. Newman et al. (2003) built a simple linear model of the PDO evolution that incorporates these three processes. In this model, PDO and ENSO indices are annually averaged from July to next June and the PDO evolution is modelled using a first-order auto-regressive (AR-1) model as:

$$P_n = \alpha P_{n-1} + \beta E_n + \eta_n \quad (1)$$

where P is the normalized PDO index, E is the normalized ENSO index, n is time (in years), and η is the atmospheric white noise. The β parameter is obtained by regressing the PDO index onto the ENSO index. The α parameter is obtained by regressing the residual ($P_n - \beta E_n$) on the previous year's PDO index P_{n-1} . Hence in this model, α represents the strength of the re-emergence process while β accounts for the influence of ENSO on the PDO.

Applying this AR-1 model to HadISST data over the 1900-1999 period, Newman et al. (2003) showed that the model PDO time series yields a 0.74 correlation with observed PDO index, a significantly better skill than when only either ENSO or re-emergence is accounted for. They also concluded that the observed spectrum is well within the 95% confidence interval of the spectrum derived from the AR-1 model (eq. 1), suggesting that the PDO observed evolution can largely be explained by accounting only for atmospheric stochastic forcing, re-emergence and ENSO influence. The relatively short 100 years of observational record however translates into uncertainties in the spectrum at decadal and multi-decadal time scales. As suggested by Schneider and Cornuelle (2005), this simple analysis does not preclude other processes, such as changes in the gyre circulation in the north Pacific, to operate. To assess the role of ENSO on the PDO in CMIP simulations, we applied the linear model described by equation (1) to the CMIP PDO time series as described in Section 5.3.

To calculate the PDO power spectrum, the PDO index, defined in section 5.2.1 as the leading PC in the north Pacific, is first converted into June-July averaged yearly values and then normalized by its standard deviation to have unit variance. A Fourier transform is then applied to obtain the raw power spectrum. To reduce the statistical noise which is inherent to spectrum calculation of finite time series, we use the Daniel's estimator approach (well-suited for the case of continuous time series as in the present study), with the Daniel's filter being here a triangle filter to reduce noise: an N -point double running-mean (i.e. a triangle filter of $2N$ length) is used, where N has to be chosen to give a good compromise between accurate amplitude and accurate bandwidth (see Storch and Zwiers 1999 for details). We have found $N=3$ to be adequate for the 140 years-long observational record over the 1871-2010 period. For CMIP models, we chose N as the integer closest to $3N_y/140$ (where N_y is the number of years available for any given CMIP model) to obtain a bandwidth comparable to the observations which allows a fair comparison. This choice indeed results in a similar spectral resolution for all computed spectra.

The PDO power spectrum is then compared to the spectrum computed from Newman's model (eq. 1). For this purpose we used a similar approach as Newman et al. (2003). Three steps are necessary. First, we generate 1000 time series of random numbers (which is considered as the white noise time series) whose

amplitude is chosen to be equal to the standard deviation of the residual of equation (1) (i.e. the time series obtained once the ENSO and re-emergence influence is removed linearly from the original PDO time series). This allows generating 1000 samples of Newman's model time series, and thus to calculate 1000 power spectra. The mean of these 1000 spectra is considered as the average Newman's model spectrum and the two-sided t-distribution of these 1000 spectra is considered for the 95% confidence level of the average model PDO spectrum.

5.3 ENSO-PDO relationship in CMIP models

Observations suggest that PDO is at least partly driven by the tropical Pacific variability (Garreaud and Battisti 1999; Shakun and Shaman 2009). In this section, I will show that the strength of the ENSO/PDO relationship varies considerably amongst CMIP models and that the strength of this relationship holds a key-role in shaping the PDO pan-Pacific (or IPO) spatial pattern. CMIP models exhibit a large range of ENSO/PDO correlation (Fig. 5.1), with all correlations being significant and varying from 0.15 (CNRM) to 0.75 (MIROC5). 17 models exhibit a maximum ENSO/PDO lag-correlation within the range of that observed (≥ 0.5 ; shown by green bars) while the remaining 15 models underestimate the ENSO/PDO relationship (red bars).

As in observations, ENSO systematically leads the PDO in all CMIP models. Except for the FIO model, this lead-time (lag of PDO) is larger in CMIP models (from 3 to 8 months) than in observations (~ 1 -2 months). In the following, we further divide CMIP models into two classes depending on the strength of the simulated ENSO/PDO time series correlation. We define Class-I models as those with a maximum ENSO/PDO lag-correlation above 0.5 (green bars in Fig. 5.1a). These models exhibit an average correlation of 0.58 very close to the observational average (thick bars on Fig. 5.1a). Each of these individual models except MIROC5 indeed exhibit correlations within the range of observed estimates (between 0.52 and 0.61) when calculating these correlations over the same length as the observational records (140 years; see black frames at the tip of each bar on Fig. 5.1a). Class-II models are defined as models with a maximum ENSO-PDO lag correlation below 0.5 (with an average correlation of 0.35 that is weak compared to that deduced from observations; red bars in Fig. 5.1a). Most of these individual models except three (GFDL2G, CGCM and MRI3) indeed exhibit correlations systematically below the range of the observed estimates within the uncertainty limits (see black frames on Fig. 5.1a). Re-computing these statistics separately for interannual and decadal time scales for ENSO and PDO time series (Fig. 5.1b,c) shows that the observed ENSO/PDO relationship is slightly stronger at decadal (correlation of ~ 0.7) than at interannual time scales (~ 0.55). In addition, models with large ENSO/PDO lag-correlation at interannual time scales also generally display large lag-correlation at decadal ones, with Class-I and Class-II models respectively displaying an average maximum lag-correlation of 0.6/0.38 at interannual and 0.58/0.36 at decadal time scales.

ENSO PDO Lag-correlation

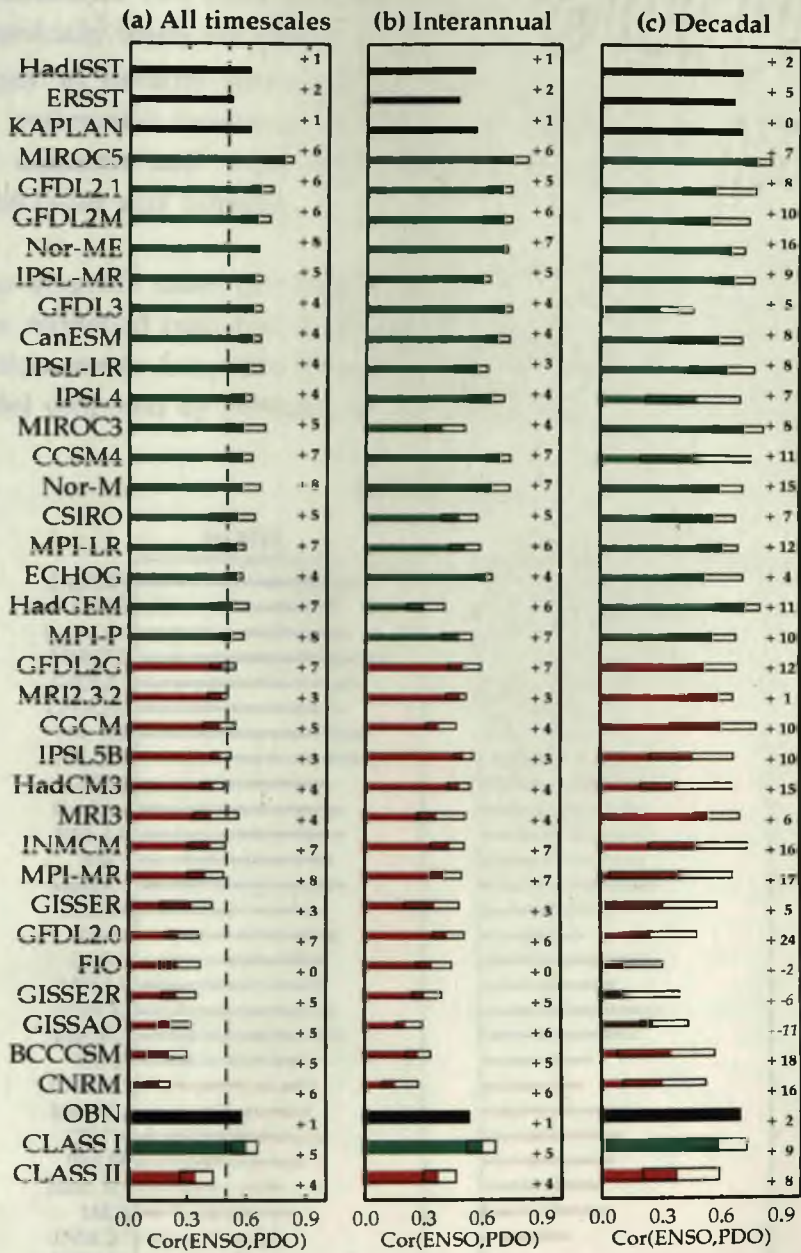


Fig. 5.1: Maximum lag-correlation coefficient between the ENSO and PDO time series at (a) all time scales (including both interannual and decadal periodicities), (b) interannual and (c) decadal time scales. The number shown to the right of each bar indicates the lag (in month) of the maximum correlation, with positive lag indicates ENSO leading the PDO. The lag is indicated in italic when the correlation is not significantly different from zero based on a t-test. CMIP models are divided into two classes depending on the maximum lag-correlation between PDO and ENSO at all time scales: **Class-I** models (green bars) with correlation above 0.5 and **Class-II** models (red bars) below that threshold. The transparent bar at the tip of the colour bars indicates the minimum and maximum correlation obtained for each CMIP model when evaluating the correlation over sliding windows of the same length of the observed datasets (i.e. 140 years). Average correlation for observations, Class-I and Class-II models are indicated as thick bars on the bottom of each panel along with the average uncertainty for the classes of models.

As expected, correlation uncertainties are generally larger at decadal than at interannual time scales in CMIP models (see black frames on Fig. 5.1b,c): this

results in ENSO/PDO lag-correlations falling within the observed range at decadal time scales for two third of CMIP models. This analysis also reveals that ENSO systematically leads the PDO at both time scales, with a tendency for the lag to be larger at decadal time scales (~8 months vs ~4 at interannual time scales). This systematic tendency of ENSO to lead the PDO across models, observational datasets and time scales suggests that ENSO forces the PDO, rather than the other way around.

In order to quantify more precisely how much of the PDO variability can be explained as a reddened response to ENSO and atmospheric stochastic forcing, I fit the PDO time series from the three observational and 32 CMIP models with the AR-1 model proposed by Newman et al. (2003) (eq. (1) in Section 5.2).

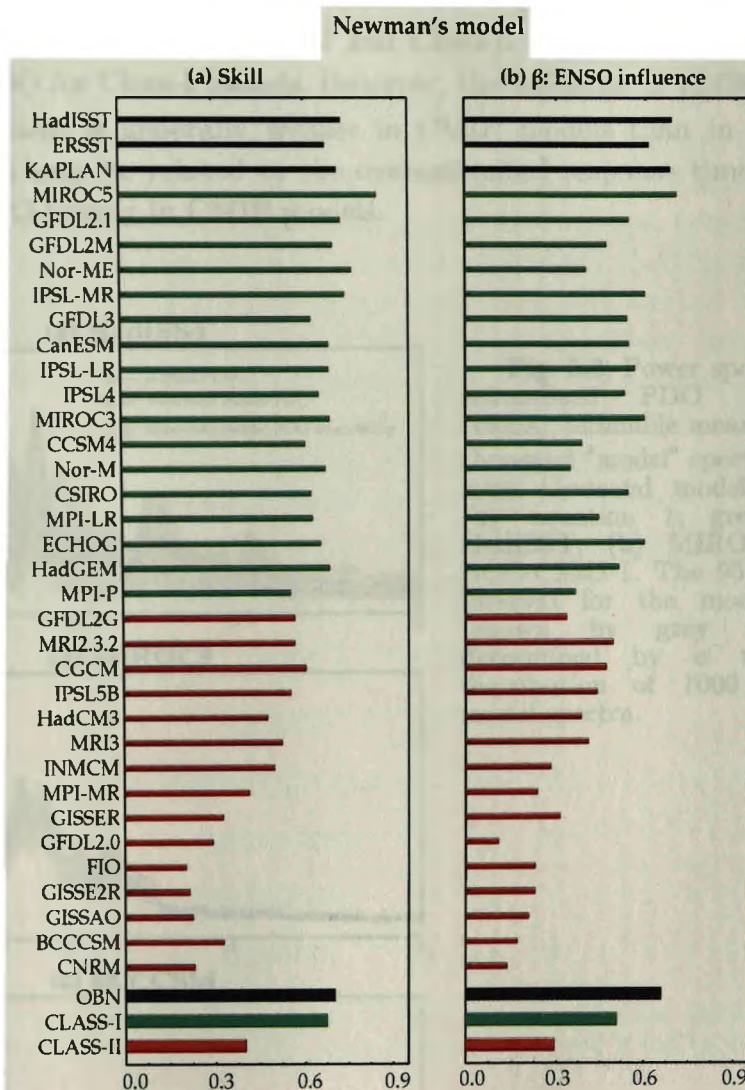


Fig. 5.2: (a) Correlation between original PDO time series and computed PDO time series using the AR-1 model (equation 1) for CMIP models and observations and (b) ENSO coefficient obtained for the AR-1 model. Class-I models are indicated in green and Class-II models in red as defined in the text and in the caption of Fig. 2. Average values for observations, Class-I and Class-II models are shown as thick bars on the bottom of each panel.

Fig. 5.2a evaluates the performance of this AR-1 model in capturing the PDO variability. The influence of ENSO forcing on the PDO evolution is represented by the β coefficient in equation (1), shown on Fig. 5.2b. In line with Newman et al. (2003) results, this AR-1 model accurately captures the PDO variability in observations, with a “skill” (defined as the correlation between original PDO time series and computed PDO time series using the AR-1 model (equation 1)), ranging between 0.67 and 0.73 depending on the observational dataset considered (black bars on Fig. 5.2a). The AR-1 model also performs well in reproducing Class-I models PDO evolution: all Class-I models except one (MPI-P) exhibit a correlation above 0.6, with a 0.67 average correlation, very close to observations. In contrast, the average correlation of Class-II models is 0.4 and all Class-II models tend to exhibit a weaker correlation than Class-I models. As expected from the ENSO-PDO correlations shown on Fig. 5.1a, there is a striking difference between β values of Class-I and Class-II models, with a larger ENSO influence on PDO for Class-I models. However, the influence of ENSO as depicted by the β coefficient is generally weaker in CMIP models than in observational products, which may be related to the overestimated response time of the PDO relative to ENSO forcing in CMIP models.

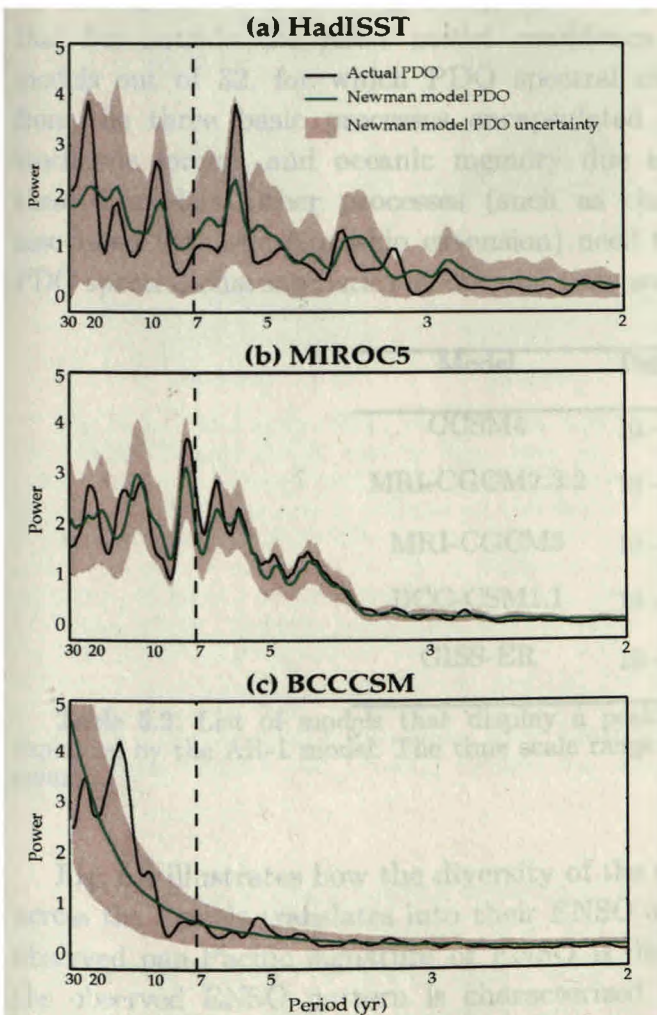


Fig. 5.3: Power spectrum of the normalized PDO time series (black), ensemble mean spectrum of thousand “model” spectra computed from thousand model time series (by equation 1; green) for (a) HadISST, (b) MIROC5 and (c) BCC-CSM2-1. The 95% confidence interval for the model spectrum (shown by grey shading) is determined by a two-sided t-distribution of 1000 samples of model spectra.

The AR-1 model (eq. 1) allows to test whether the reddened response to ENSO and atmospheric white noise can explain the main PDO spectral characteristics in CMIP models. As an illustration, Fig. 5.3 compares the actual PDO spectrum with that derived from the AR-1 model for HadISST and two selected models with contrasted behaviours. Accounting for the influence of ENSO on the PDO allows reproducing the PDO spectrum at interannual and decadal time scales in HadISST data (Fig. 5.3a): the actual PDO spectrum (black curve) lies within the 95% confidence interval of that derived from equation (1). In line with Newman et al. (2003) results, the observed PDO spectrum is therefore well captured from the reddened response to ENSO and atmospheric white-noise forcing (this is also the case in other observed datasets; not shown). As for observations, the PDO spectrum of the MIROC5 model (which displays the highest skill and largest ENSO influence on PDO, see Fig. 5.2) is very close to that derived from equation (1) (Fig. 5.3b). In fact, the actual PDO spectrum lies well within the confidence interval of AR-1 model spectrum for 27 out of the 32 CMIP models analysed in this study (not shown). This suggests that the PDO spectral characteristics can be understood as a reddened response to ENSO and atmospheric white noise forcing in most CMIP models. Only 5 models out of 32 (four of them belonging to Class-II), exhibit a spectral peak at decadal time scales that cannot be explained by the AR-1 model (see Table 5.2). This is for instance the case for BCC-CSM1 (Fig. 5.3c), which displays a peak around 12 year period that lies outside the AR-1 model confidence interval. There are thus only 5 models out of 32, for which PDO spectral characteristics cannot be explained from the three basic processes encapsulated in ENH model - ENSO forcing, stochastic forcing and oceanic memory due to re-emergence processes, i.e. for these 5 models, other processes (such as changes in oceanic gyre circulation associated with the Kuroshio extension) need to be accounted for to explain the PDO spectral characteristics at decadal time scales.

Model	Period	Class
CCSM4	10 – 20	I
MRI-CGCM2.3.2	10 – 15	II
MRI-CGCM3	10 – 20	II
BCC-CSM1.1	10 – 20	II
GISS-ER	10 – 30	II

Table 5.2: List of models that display a peak at decadal time scales which is not explained by the AR-1 model. The time scale range of this peak is indicated in the second column.

Fig. 5.4 illustrates how the diversity of the simulated ENSO/PDO relationship across the models translates into their ENSO and PDO pan-Pacific patterns. The observed pan-Pacific signature of ENSO is displayed on Fig. 5.4a. As expected, the observed ENSO pattern is characterized by an equatorial Pacific warming associated with tropical SLP seesaw and converging westerly wind anomalies west

of the maximum warming (Fig. 4.5a). The ENSO pattern also exhibits a strong extra-tropical signature in both hemispheres. For instance, a broad area of negative SLP anomaly characterizes the central and eastern north Pacific (highlighted by the black dashed frame on Fig. 5.4a), to the southeast of the Aleutian low climatological position. In this region, anomalous surface winds are roughly in geostrophic balance with the Aleutian low fluctuations, with maximum westerly and negative SST anomalies south of the anomalous low (highlighted by the grey dashed frame on Fig. 5.4a).

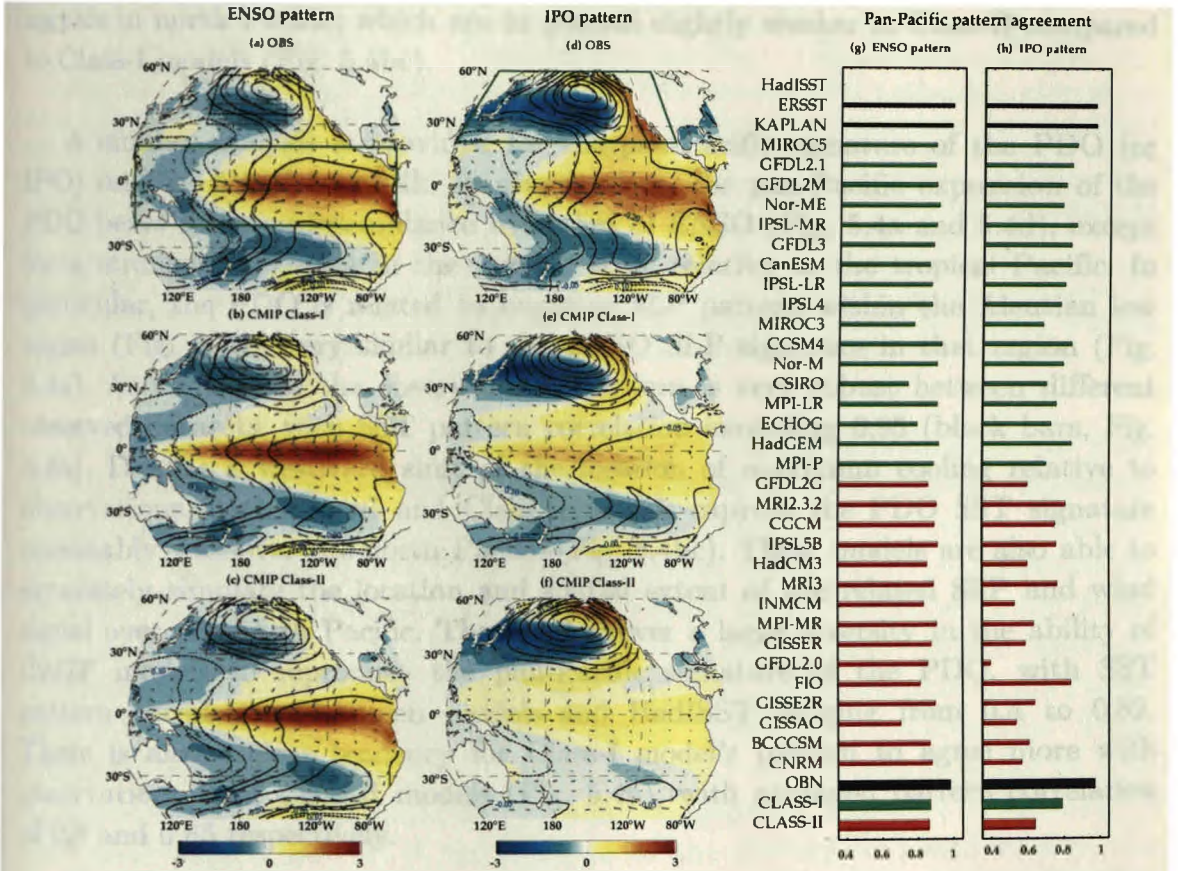


Fig. 5.4: Pan-Pacific SST, wind stress and sea-level pressure signature of ENSO for (a) HadISST and 20CR (as in Fig. 1a), (b) Class-I and (c) Class-II CMIP models ensemble mean (Class-I and Class-II models are defined in the text and in the caption of Fig. 5.1). ENSO pattern is defined as the leading EOF of SST anomalies in the tropical Pacific (120E-80W; 20N-20S, green rectangle on panel a) normalized by its spatial root mean square so that the PC is a measure of the ENSO amplitude. The pan-Pacific signature of ENSO is obtained by regressing the SST (color), surface pressure (contours) and wind stress (vectors) anomalies onto the first PC time series. (d-f) Same as (a-c) but for the pan-Pacific signature of the PDO. SST pan-Pacific pattern correlation of each dataset with HadISST for (g) ENSO and (h) PDO. SST patterns are unit less and wind stress vectors have $N.m^{-2}.^{\circ}C^{-1}$ units. On panels g and h, observational datasets are plotted in black, Class-I models in green and Class-II models in red. Average values for observations, Class-I and Class-II models are indicated as thick bars on the bottom of each panel.

A similar sea-surface cooling associated with westerly wind anomalies equatorward of the maximum negative SLP anomalies is also observed in the South Pacific (Fig. 5.4a). The ENSO pan-Pacific signature on Fig. 5.4a is very robust between different observed datasets, with SST pattern correlation exceeding 0.95

(black bars, Fig. 5.4g). Both Class-I and Class-II models accurately reproduce the observed pan-Pacific ENSO pattern (Fig. 5.4a-c), with only three models (GISS-AOM, MIROC3, CSIRO-Mk3) having pattern correlations below 0.75 (Fig. 5.4g). Both classes of models are able to accurately simulate the location and amplitude of the negative SLP signature over the north Pacific and the associated westerly anomalies south of it (Fig. 5.4bc). Class-I and Class-II models however share some common biases (Fig. 5.4bc), such as a westward shift of the equatorial warming and of the north Pacific cooling. The only apparent difference between the two classes of models relates to the amplitude of the low pressure and cooling signals in north Pacific, which are in general slightly weaker in Class-II compared to Class-I models (Fig. 5.4bc).

A similar analysis is provided for the pan-Pacific signature of the PDO (or IPO) on Fig. 5.4d-f and 5.4h. In observations, the pan-Pacific expression of the PDO bears a strong resemblance with that of ENSO (Fig. 5.4a and 5.4d), except for a stronger weighting in the north Pacific relative to the tropical Pacific. In particular, the PDO is related to negative SLP pattern within the Aleutian low region (Fig. 5.4d), very similar to the ENSO SLP signature in that region (Fig. 5.4a). As for ENSO, the observed IPO pattern is very robust between different observed datasets, with SST pattern correlation exceeding 0.95 (black bars, Fig. 5.4h). Despite a westward shift of the location of maximum cooling relative to observations, both Class-I and Class-II models capture the PDO SST signature reasonably well over the north Pacific (Fig. 5.4bc). These models are also able to accurately simulate the location and spatial extent of the related SLP and wind signal over the north Pacific. There is however a large diversity in the ability of CMIP models to reproduce the pan-Pacific signature of the PDO, with SST pattern correlations between models and HadISST ranging from 0.4 to 0.82. There is also a clear tendency for Class-I model's pattern to agree more with observations than Class-II models (Fig. 5.4h), with averaged pattern correlation of 0.8 and 0.65 respectively.

As shown on Fig. 5.5a, there is indeed a 0.7 correlation between the ENSO/PDO maximum lag-correlation (i.e. the criterion used to classify the CMIP models) and the quality of the simulated IPO pattern. Fig. 5.4e, f indicate that a large part of the IPO-pattern difference between Class-I and Class-II models arises from the signal outside the north Pacific region: Class-I models have a larger equatorial and south Pacific SST and SLP signature compared to Class-II models, although still weaker than in observations. This relationship is further quantified in Fig. 5.5b: there is a 0.84 correlation between the quality of the model IPO pattern and the equatorial warming associated with the PDO. Similarly, the amplitude of the subtropical southern Pacific signal is also very clearly related to the amplitude of the equatorial warming (0.88 correlation; Fig. 5.5c), with an underestimated South Pacific cooling signal in Class-I models, and almost non-existent in Class-II models. Most differences in the Class-I and II models IPO patterns thus arise from the differences in the relative amplitude of

the SST signal associated with the PDO over the tropical and South Pacific regions.

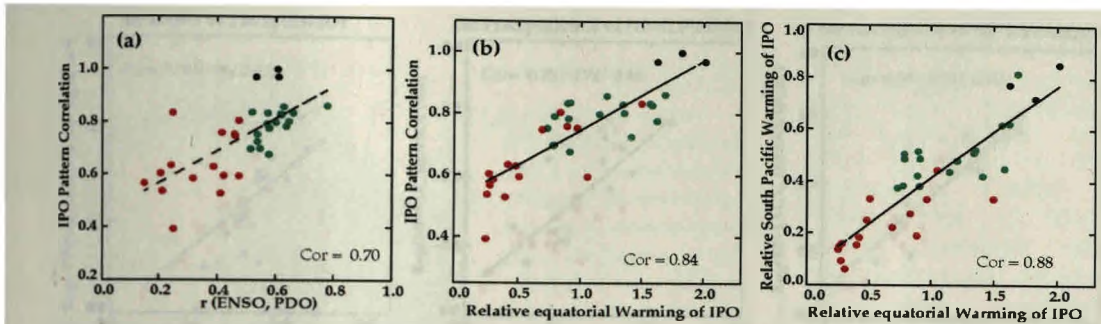


Fig. 5.5: (a) Scatterplot of the Pan-Pacific PDO pattern (IPO pattern) correlation of each dataset with HadISST shown in Fig. 5h against the maximum lag-correlation between the ENSO and the PDO time series shown in Fig. 2a for all CMIP (red for Class-II and green for Class-I models) and observational (black) datasets. (b) Same but between IPO pattern correlation and the relative amplitude of the PDO SST signature in the tropical Pacific. (c) Same but for the relative amplitude of PDO signature in South Pacific against relative amplitude of PDO signature in the tropical Pacific. The relative amplitude of the PDO SST signature in the tropical and South Pacific are computed by the spatial root mean square of re-projected SST pattern of the PDO in the tropical Pacific (120E-80W; 20N-20S) and South Pacific (120E-80W; 20S-50S).

In this section, I have described the relationship between ENSO and the PDO in CMIP models and its implications. The strength of ENSO/PDO relationship varies considerably amongst CMIP models: about half of the models (Class-I) exhibit a maximum ENSO/PDO lag-correlation comparable to observations, while the other half (Class-II) simulates a weaker ENSO influence on the PDO. The pan-Pacific signature of the PDO (i.e. the IPO pattern) differs markedly between these two classes of models, with a weaker equatorial and south Pacific SST signal in Class-II models with a weaker ENSO/PDO relationship. These results suggest that the coherent forcing of ENSO on the mid-latitudes of both hemispheres is the main cause for the inter-hemispheric signature of the IPO. I also show that, regardless of the strength of the ENSO/PDO relationship, the shape of the PDO spectrum can be explained in terms of a combination of ENSO forcing, stochastic forcing, and re-emergence of SST anomalies in 27 models out of 32. In the following section, I investigate the possible reasons explaining the diversity of the ENSO/PDO relationship in CMIP models.

5.4 Explaining the diversity of ENSO - PDO relationship

El Niño influences north Pacific SSTs through the atmospheric bridge: warm SST anomalies in the equatorial Pacific enhance rainfall and the associated diabatic heating, inducing upper-level tropospheric divergence over the central tropical Pacific. This heating forces Rossby waves that are channelled by the mean circulation toward the north Pacific (e.g. Trenberth et al. 1998), strengthening the Aleutian Low (e.g. Alexander et al. 2002), Fig. 5.4a). The mean surface winds being on average westerlies in the north Pacific and these geostrophically driven eastward anomalous flows are associated with an increased

latent heat uptake and Ekman transport (Alexander and Scott 2008), that causes the ENSO-related SST cooling in the north Pacific.

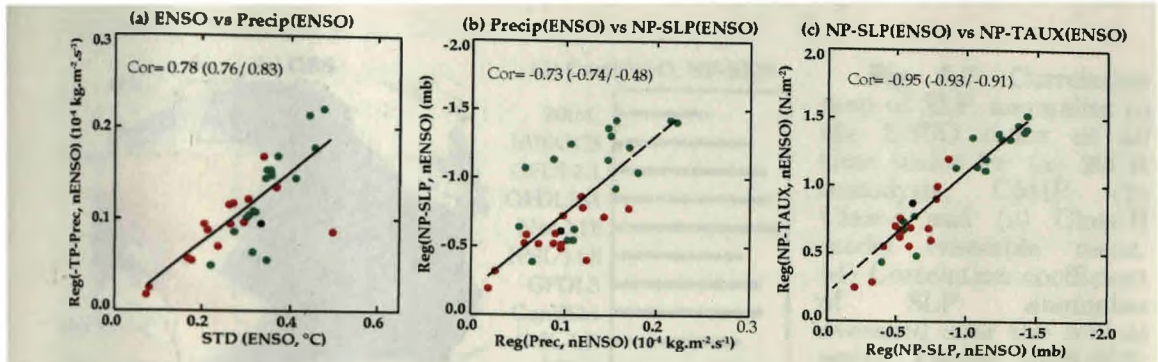


Fig. 5.6: Scatter plot of (a) the amplitude of ENSO against the ENSO-related precipitation amplitude in the equatorial Pacific [5N-5S; 130E-140W], (b) ENSO-related precipitation amplitude in the equatorial Pacific against ENSO-related mean sea-level pressure in the north Pacific [35N-55N; 160E-140W] and (c) ENSO-related mean sea-level pressure in the north Pacific against ENSO-related zonal wind stress in the north Pacific [30N-40N; 160E-150E] for CMIP models and HadISST/20CR datasets at all time scales. ENSO-related signals are derived by linear regression of variables onto the normalized ENSO index. Correlation coefficients corresponding to each scatter plot is also given on the upper left of each panel along with the same correlation respectively for interannual and decadal time scales in parenthesis.

Within the paradigm of this atmospheric bridge, a relationship between the amplitude of ENSO-related tropical Pacific SST/precipitation and north Pacific SLP/surface winds is expected. Fig. 5.6 assesses the strength of this relationship across the CMIP models. Fig. 5.6a demonstrates that the amplitude of equatorial Pacific ENSO-related precipitation (inferred from a regression of equatorial Pacific precipitation anomalies onto the normalized ENSO index) is indeed linked with the amplitude of ENSO-related SST signal across models (0.78 correlation). In turn, Fig. 5.6b illustrates that the amplitude of ENSO-related precipitation, a proxy for tropical diabatic heating, controls to a large extent the strength of the associated atmospheric planetary wave response channelled toward the north Pacific, and hence the amplitude of the mean SLP in the region of the Aleutian low across models (-0.73 correlation, see black dashed frame on Fig. 5.4a for the definition of the region over which the SLP anomaly is estimated). Finally, the amplitude of these SLP variations drive the amplitude of the surface wind response in the north Pacific region through geostrophic balance (-0.95 correlation, see grey dashed frame on Fig. 5.4a for the definition of the region over which the zonal wind stress anomaly is estimated). This analysis demonstrates that, across CMIP models, the amplitude of ENSO-related north Pacific SST signature is clearly connected to the amplitude of north Pacific SLP and surface wind signal through the amplitude of the ENSO-related tropical diabatic heating. This chain that connects the amplitude of ENSO to the ENSO-related surface signature in the north Pacific exists at both interannual and decadal time scales (correlations in parenthesis on each panel of Fig. 5.6), although the link between the amplitude of ENSO-related equatorial precipitation and the ENSO-related SLP variations in the north Pacific considerably weakens at decadal time scales (-0.48 correlation) compared to interannual one (-0.74

correlation). In the following, I consider the SLP variability averaged over the north Pacific to assess the strength of ENSO control on the atmospheric variability in the north Pacific.

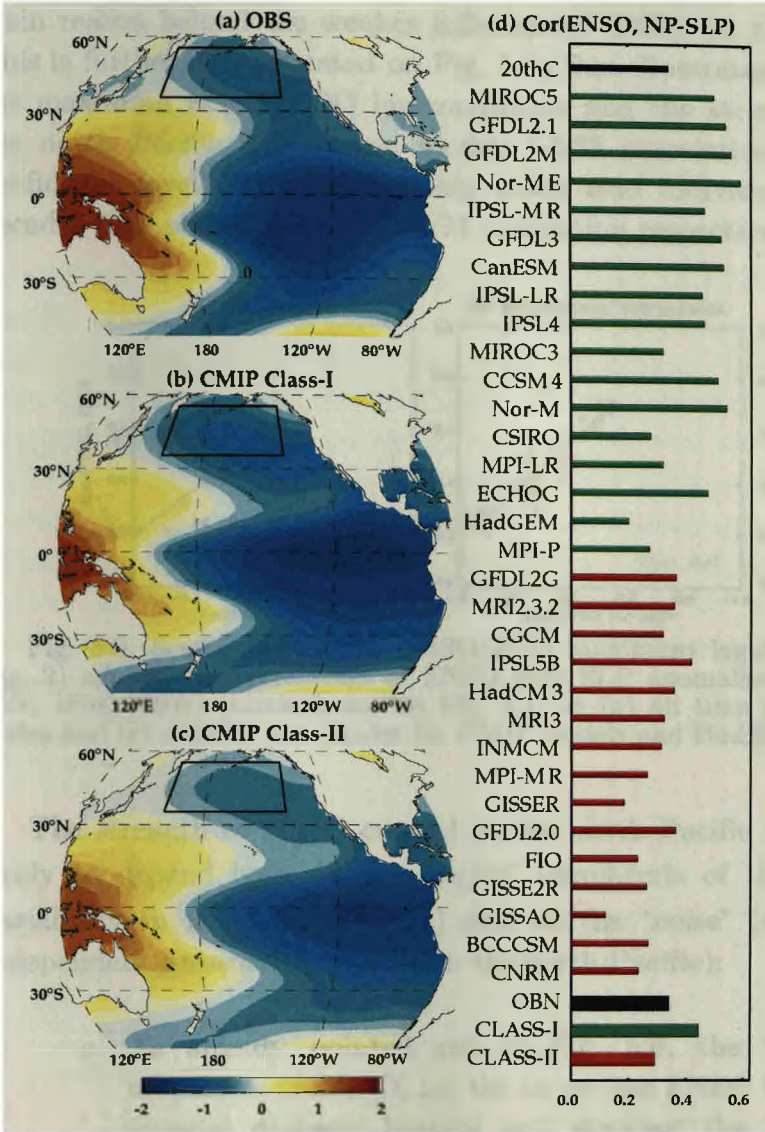


Fig. 5.7: Correlation map of SLP anomalies to the ENSO index at all time scales for (a) 20CR reanalysis, (b) CMIP Class-I and (c) Class-II model ensemble mean. (d) Correlation coefficient of SLP anomalies averaged over the central north Pacific [35N-55N; 160E-140W] (black frame on panels a-c) with ENSO index at all time scales.

Fig. 5.7 displays the spatial map of correlation of SLP anomalies onto ENSO index. The ENSO index is correlated with SLP over most of the Pacific in observations (Fig. 5.7a). Maximum correlations are found in the tropical Pacific, with positive correlations over the tropical western Pacific and Indonesian region (up to 0.7) and negative correlations in the central and eastern tropical Pacific (up to -0.8). Owing to the tropical-extratropical atmospheric bridge, the ENSO index also displays a ~ -0.37 correlation with SLP averaged over the central north Pacific region (framed on Fig. 5.4a and 5.7a,b,c). Class-I and Class-II models display correlation patterns similar to those in observations (Fig. 5.7b, c), but with varying strength. Class-I models do indeed display a stronger ENSO control on the north Pacific SLP than Class-II models (average correlation coefficients of -0.45 and -0.29 for Class-I and Class-II models respectively; Fig. 5.7d). The correlation between the ENSO index and SLP averaged over the central north

Pacific region shown on Fig. 5.7d for each model and observational data will be considered in the following as the *strength of ENSO control* on the north Pacific atmospheric variability. The weaker ENSO control on the north Pacific atmospheric variability in Class-II models shown in Fig. 5.7d is probably the main reason behind the weaker influence of ENSO on the PDO in those models. This is further demonstrated on Fig. 5.8a that illustrates the relationship between the maximum ENSO/PDO lag-correlation and the strength of ENSO control on the north Pacific SLP across models (-0.75 correlation, significant at the 99% confidence level). This relationship holds true individually for interannual and decadal time scales (-0.87 and -0.74 correlation respectively; see Fig. 5.8bc).

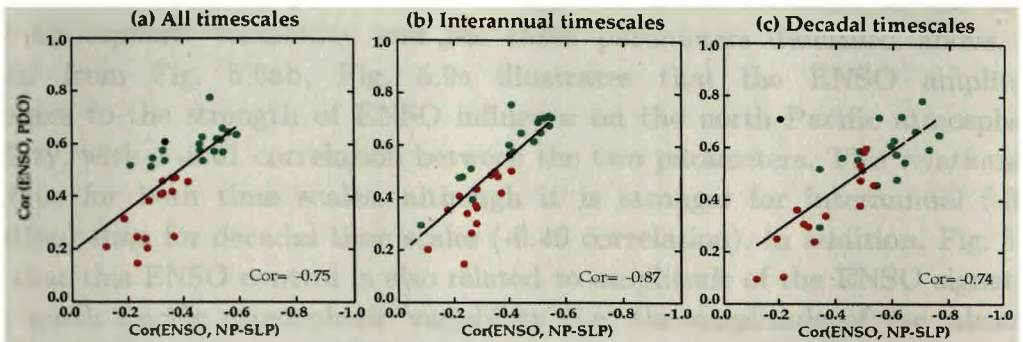


Fig. 5.8: Scatterplot of the ENSO/PDO maximum lag-correlation (as displayed on Fig. 2) against the correlation of ENSO with SLP anomalies in the north Pacific [35N-55N; 160E-140W] (black frame on Fig. 5.7) at (a) all time scales, (b) interannual time scales and (c) decadal time scales for CMIP models and HadISST/20CR datasets.

The strength of ENSO control on the north Pacific atmospheric variability is likely to depend both on the “signal” (amplitude of the ENSO-driven pressure variability in the north Pacific) and on the “noise” (amplitude of the ENSO-independent pressure variability in the north Pacific):

- As already pointed out in Fig. 5.6, the “signal” depends on the amplitude of ENSO, i.e. the larger the ENSO SST signal, the larger the tropical diabatic heating and stronger the ENSO signature on the north Pacific atmospheric variability is. In the following, the amplitude of ENSO is estimated as the standard deviation of the ENSO time series.
- The “signal” also depends on the strength of ENSO-driven atmospheric signature over the north Pacific. Although there is a clear relationship between the amplitude of the ENSO-related tropical rainfall and the SLP signature in the north Pacific across models, individual models are somewhat scattered around the regression line (see Fig. 5.6b). This scatter can be explained by the diversity in the location and amplitude of north Pacific SLP response to a given ENSO amplitude. The amplitude of ENSO-driven north Pacific atmospheric variability is estimated from the regression coefficient of the average central north Pacific SLP on the real-amplitude ENSO time-series.

- Finally, the amplitude of Aleutian low fluctuations, which is unrelated to ENSO forcing, referred as atmospheric “noise” in the following, could also impact the strength of ENSO control on the north Pacific atmospheric variability. If the atmospheric noise is large, the random-walk part of north Pacific variability will also be large relative to the ENSO-driven variability. We estimate the amplitude of this “noise” from the standard deviation of ENSO-independent SLP over the central north Pacific region (the ENSO contribution is removed using a linear regression).

Fig. 5.9 shows scatter plots of the strength of ENSO influence on the north Pacific atmospheric variability and the three parameters described above. As expected from Fig. 5.6ab, Fig. 5.9a illustrates that the ENSO amplitude contributes to the strength of ENSO influence on the north Pacific atmospheric variability, with a -0.61 correlation between the two parameters. This relationship holds true for both time scales, although it is stronger for interannual (-0.65 correlation) than for decadal time scales (-0.49 correlation). In addition, Fig. 5.9b shows that this ENSO control is also related to amplitude of the ENSO signature on the north Pacific atmospheric variability (i.e. the amplitude of the Aleutian low response to a given ENSO amplitude computed by a linear regression between the two), with a 0.60 correlation between these two parameters and similar relationship holds true at interannual and decadal time scales ($r=0.53$ and 0.61) also.

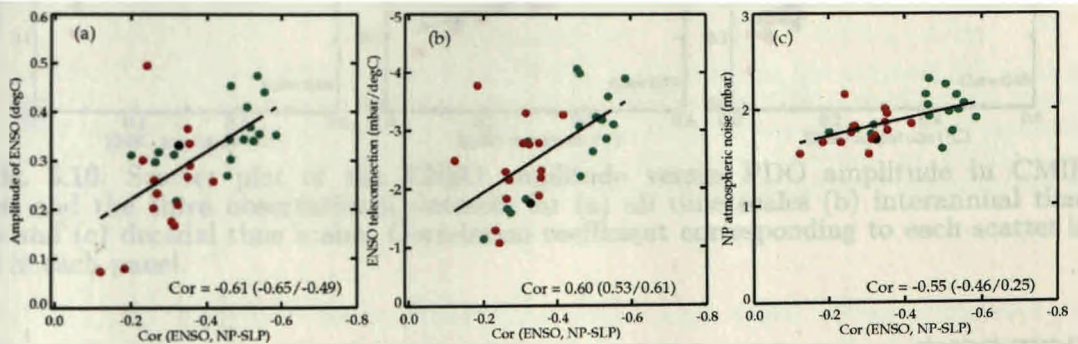


Fig. 5.9: Scatter of the strength of “ENSO-control” on the north Pacific atmospheric variability against (a) the ENSO amplitude, (b) the strength of ENSO teleconnection to north Pacific variability, and (c) atmospheric noise in the north Pacific for CMIP models and HadISST/20CR datasets at all time scales. Correlation coefficients corresponding to each scatter is given on the bottom right of each panel along with the same correlation individually for interannual and decadal time scales in parenthesis. See text for the definition of each of the metrics plotted.

In contrast, the amplitude of the north Pacific atmospheric noise does not seem to explain the diversity of this control. Although Fig. 5.9c indicates that the correlation between these two parameters is significant (-0.55), the sign of this relationship is opposite to what is expected: a larger noise in the north Pacific should indeed lead to a weaker correlation between ENSO and the north Pacific atmospheric variability, which is opposite to what depicts in Fig. 5.9c. This relationship between the amplitude of the noise and ENSO control on the north

Pacific SLP has an opposite sign between interannual (-0.46 correlation) and decadal time scales (0.25 correlation) suggesting that this relationship is not very stable indeed.

Fig. 5.10 provides another indication of the influence of ENSO amplitude on the PDO amplitude. There is a large range of simulated ENSO and PDO amplitude with some models underestimating the level of variability and others overestimating it. Across this range, there tends to be a linear relation (~ 0.66) between the ENSO amplitude and PDO amplitude amongst the different datasets (Fig. 5.10a). Although significant regardless of the time scale considered, this relationship is larger at interannual time scales (Fig. 5.10b; 0.75 correlation), compared to decadal time scales (Fig. 5.10c; 0.45 correlation). The strong relationship between the ENSO and PDO amplitudes at interannual time scales is in agreement with the earlier studies that identified ENSO as one of the major forcing of the PDO at this time scale (e.g. Alexander 1990; Lau and Nath 1994; Lau and Nath 1996; Alexander et al. 2002; Newman et al. 2003; Schneider and Cornuelle 2005).

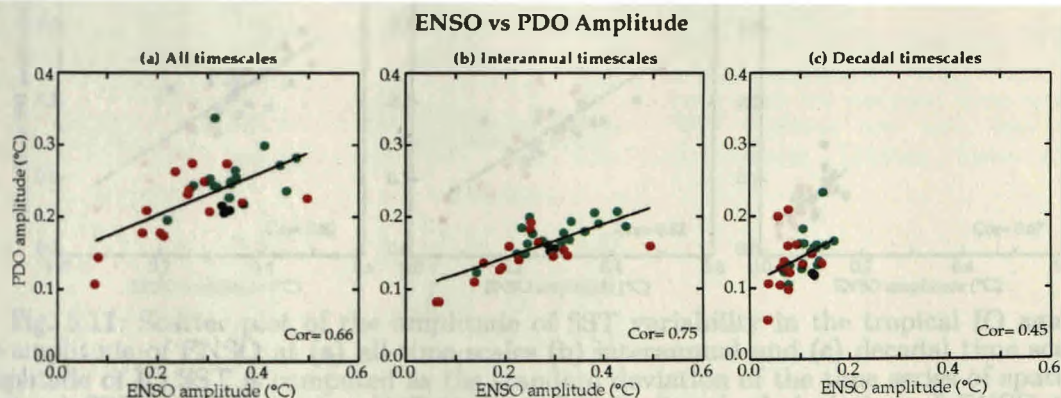


Fig. 5.10: Scatter plot of the ENSO amplitude versus PDO amplitude in CMIP models and the three observational datasets for (a) all time scales (b) interannual time scales and (c) decadal time scales. Correlation coefficient corresponding to each scatter is given in each panel.

The overall results demonstrate that the models with larger ENSO/PDO correlation exhibit a stronger ENSO-control on the north Pacific SLP and wind variability. In other words, the degree of ENSO-control on the north Pacific SLP/wind variability directly influences the ENSO-PDO relationship in CMIP models. The strength of this *ENSO-control* is shown to be related to both ENSO amplitude and the amplitude of ENSO imprint on the north Pacific SLP variability in CMIP models. Finally, the strong correlation between the ENSO and PDO amplitude amongst CMIP models points the influence of ENSO amplitude on the PDO.

5.5 ENSO teleconnection in Indian Ocean

In the previous sections we have seen how ENSO relates to the north Pacific variability in observations and CMIP models. In this section, we aim at assessing

the influence of ENSO variability on the IO SST variability in these datasets. ENSO is known to induce a homogenous SST signal in the IO at interannual time scales, generally referred to as the IOBM (see section 2). Fig. 5.11 shows that there is indeed a close relationship between ENSO amplitude and averaged IO SST in CMIP models, with a ~ 0.82 correlation across models (Fig. 5.11a). Performing this analysis separately for interannual and decadal time scales (Fig. 5.11bc) shows that although this link is stronger for interannual time scales (0.82 correlation), it is still significant at decadal time scales (0.67 correlation). This suggests ENSO influence on IO SST occurs also at decadal time scales. Fig. 5.11 also shows that Class-I and II models do not behave differently in terms of ENSO influence on IO SST. We will thus consider the two classes of models together for the rest of the analysis. In the following, we will focus on the spatial imprint of ENSO on IO SST at these two time scales in observations and CMIP models.

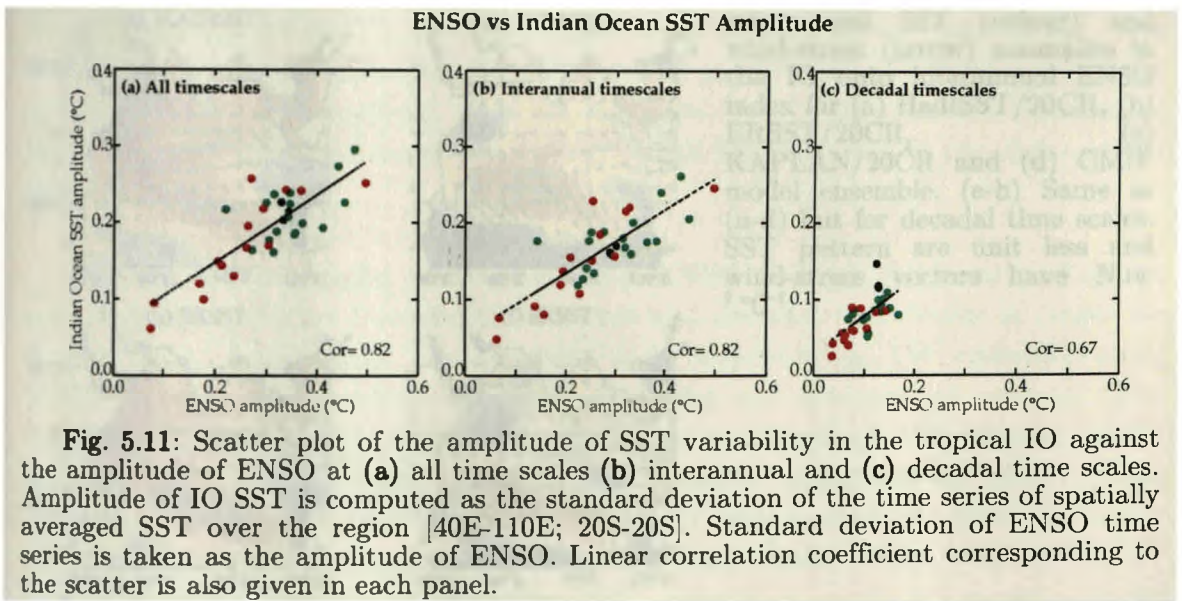


Fig. 5.12a-d provides the standardized SST and wind stress signature of ENSO in the IO at interannual time scales from observations (HadISST, ERSST and KAPLAN for SST, 20CR for wind) and the ensemble mean of CMIP models. Similar to Fig. 5.4, this pattern is derived by regressing the SST (color) and wind-stress anomalies (vectors) in the IO to the principal component (which is having the amplitude of ENSO for a given data) of the first tropical Pacific EOF (i.e. ENSO) at interannual time scales. The ability of individual CMIP models to reproduce the observed ENSO signature in the IO at interannual time scales is illustrated on Fig. 5.13a which displays the pattern correlation coefficient of each observed and model dataset with the one obtained from HadISST data. The ENSO interannual teleconnection to the IO exhibits a basin-wide warming pattern, with rather homogeneous positive SST anomalies spanning the entire 20N-20S band, except along the western Australian coast which exhibits a cooling signal (Fig. 5.12a). This warming has been extensively documented and attributed to increased downward surface shortwave fluxes over the tropical IO

related to the eastward shift of the Walker cell during El Niño events (Klein et al. 1999; Lau and Nath 2000). This SST pattern is associated with easterly wind anomalies at the equator and north-westerly anomalies in the southern IO, in agreement with previously published results (Yu et al. 2005; Rao and Behera 2005; Ohba and Ueda 2007). The other two observed SST datasets display a very consistent SST response in the IO (Fig. 5.12bc), with ~ 0.9 pattern correlation with HadISST (Fig. 5.13a). The CMIP ensemble mean pattern displays a reasonable agreement with observed SST and wind patterns (Fig. 5.12d). This is verified for most individual CMIP models, with a pattern correlation around 0.6 for two third of these models (Fig. 5.13a). Only a few models fail to reproduce the ENSO teleconnection pattern over the IO at interannual time scales (INMCM, GISS-AOM, GISS-E2R, MIROC3).

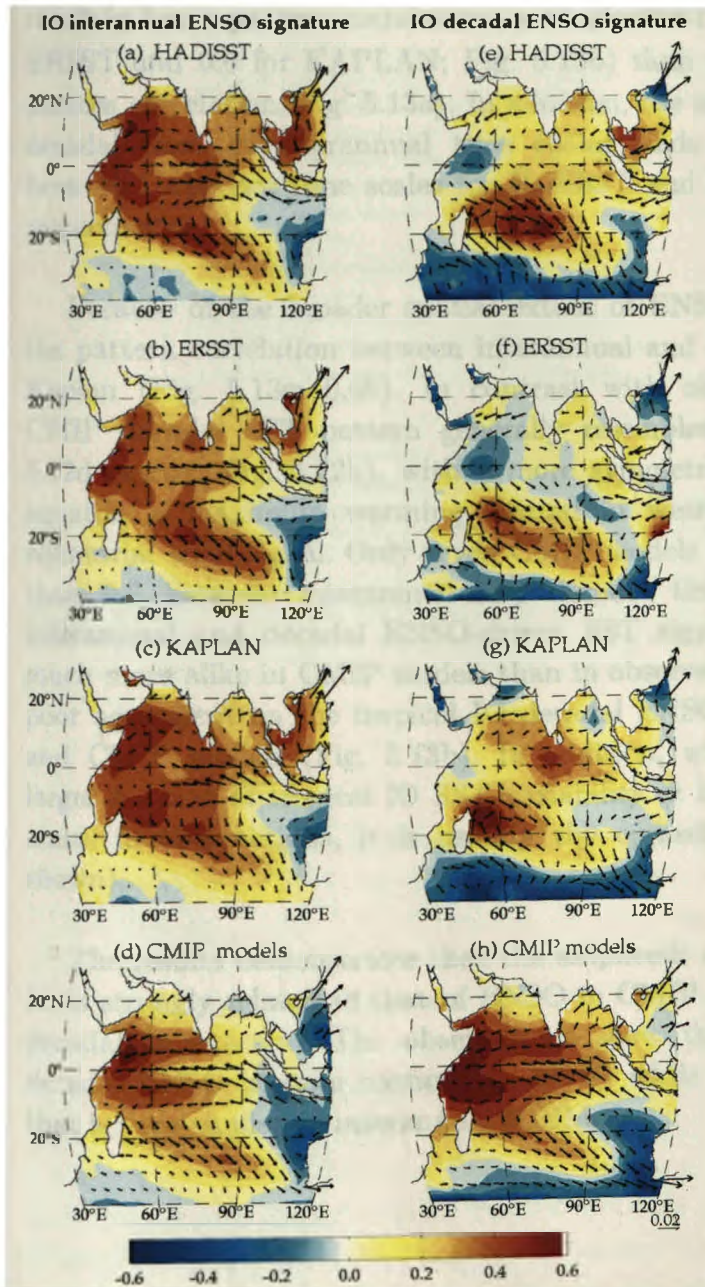


Fig. 5.12: Regression of interannual SST (colour) and wind-stress (arrow) anomalies in the IO onto interannual ENSO index for (a) HadISST/20CR, (b) ERSST/20CR, (c) KAPLAN/20CR and (d) CMIP model ensemble. (e-h) Same as (a-d) but for decadal time scales. SST pattern are unit less and wind-stress vectors have $N.m^{-2} \cdot ^\circ C^{-1}$.

Fig. 5.12e-h and 5.13b provide similar analyses to those of Fig. 5.12a-d and 5.13a but for decadal time scales. The decadal IO signal related to ENSO derived from HadISST considerably differs from that at interannual time scale (Fig. 5.12e and Fig. 5.12a): ENSO decadal signature consists of a localised warming over the SWIO, northeast of Madagascar, with considerably weaker signature elsewhere in the tropical IO. The associated decadal wind signal derived from 20CR also differs from that of interannual, with a cyclonic wind anomaly curling around the region of maximum warming. ERSST exhibits a qualitatively similar decadal IO ENSO signature to that derived from HadISST (Fig. 5.12ef), with a warming pattern confined to the southern tropical IO. However, this warming is located further south from the equator (around 20S; Fig. 5.12f) than in HadISST (around 15S; Fig. 5.12e), and the warming north of $\sim 10\text{N}$ is weaker. The Kaplan SST pattern also displays a similar warming in the south-western SWIO but also a central equatorial warming that is absent in other datasets. These mismatches result in lower pattern correlations with HadISST at decadal time scales (0.45 for ERSST and 0.6 for KAPLAN; Fig. 5.13b) than at interannual time scales (~ 0.9 pattern correlation; Fig. 5.13a). In addition, the more localised SWIO warming at decadal than at interannual time scales leads to a poor pattern correlation between these two time scales for HadISST and ERSST (Fig. 5.13c, 0.5 and 0.2 respectively).

Because of the broader spatial extent of ENSO decadal signature in Kaplan, the pattern correlation between interannual and decadal time scales is larger for Kaplan (Fig. 5.13c; 0.65). In contrast with observations, the ensemble-mean CMIP decadal SST pattern generally resembles the interannual pattern (Fig. 5.12d against Fig. 5.12h), with a more symmetric warming with respect to the equator, a maximum warming located in western equatorial IO and a large equatorial wind signal. Only seven CMIP models have a pattern correlation lower than 0.6 between interannual and decadal time scales (Fig. 5.13c), i.e. the interannual and decadal ENSO-driven SST signature in the IO appears to be much more alike in CMIP models than in observations. This results in a generally poor agreement on the tropical IO decadal ENSO signature between observation and CMIP models (Fig. 5.13b). In addition, while ENSO generally explains a larger fraction of tropical IO SST variability at interannual than at decadal time scales in observations, it is usually the opposite for most CMIP models (not shown).

The results demonstrates that the amplitude of SST variability in the tropical IO is strongly related to that of ENSO in CMIP models, at both interannual and decadal time scales. The observations show that the SST response of IO to decadal ENSO is more confined to SWIO while CMIP models exhibit a pattern that is very similar to interannual IOBM.

ENSO pattern agreement over IO

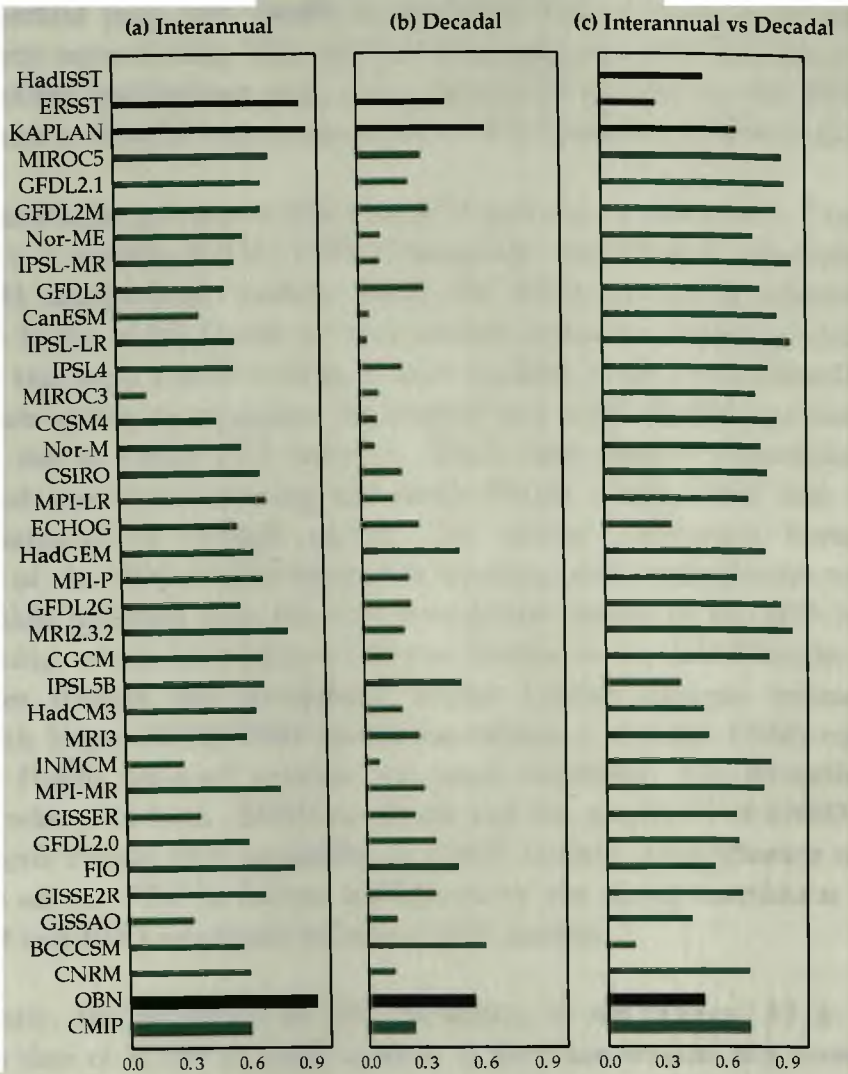


Fig. 5.13: Pattern correlation of HadISST ENSO signature in the IO region (40E-110E; 30N-30S) for HadISST with all models and other observed datasets (ERSST, KAPLAN) for (a) interannual and (b) decadal time scales. (c) Pattern correlation between interannual and decadal ENSO signature in the IO from all observations and CMIP models.

5.6 Summary

The ENSO/PDO relationship in CMIP models and observation is examined in this chapter. All CMIP models overestimate the time lag between ENSO and the PDO, this lag being 1 to 2 months in observation and 4 to 8 months in most CMIP models. Despite this caveat, about half of the 32 analysed CMIP models (Class-I) exhibit a maximum ENSO/PDO lag-correlation larger than 0.5, within the observed range. The other half (Class-II) underestimates this correlation (< 0.5). The autoregressive model of PDO Newman et al. (2003), which accounts for oceanic memory through re-emergence, ENSO and atmospheric white noise forcing, allows reproducing PDO time series with an average 0.7 correlation in observation and Class-I CMIP models but only an average correlation of 0.45 for Class-II models. This autoregressive model further captured the main PDO spectral characteristics in most CMIP models, regardless of the strength of their

ENSO/PDO correlation. Only 5 models out of 32 display a decadal (10-30yrs window) spectral peak that cannot be explained from a combination of ENSO and stochastic noise forcing. This analysis hence suggests that it is not necessary to invoke other mechanisms (e.g. ocean dynamics) to capture the PDO main spectral peaks at decadal time scales in most CMIP models and observations.

The pan-Pacific pattern of PDO (or IPO pattern) is different in Class-I (i.e. models with a realistic ENSO/PDO relationship) and Class-II (underestimated ENSO/PDO relationship) models. While the PDO pattern is relatively well reproduced in the north Pacific for most models (despite a westward shift in the position of the north Pacific cooling in most models), Class-I and Class-II models differ in their ability to reproduce the tropical and south Pacific signature of the PDO (i.e. the so called IPO pattern). While most models underestimate the PDO-related equatorial warming and south Pacific cooling, this bias is much more accentuated in Class-II models. The strong relationship between the amplitude of the PDO-related equatorial warming and south Pacific cooling in CMIP models indicates that the inter-hemispheric nature of the IPO is due to ENSO forcing, which introduces a coherent forcing to the mid-latitudes of both hemispheres through the atmospheric bridge. Further analysis indicates that models with larger ENSO/PDO correlation exhibit a stronger ENSO-control on the north Pacific sea-level pressure and wind variability. The strength of this control is related to both ENSO amplitude and the amplitude of ENSO imprint on the north Pacific SLP variability in CMIP models. The influence of ENSO amplitude on the PDO is further highlighted by the strong correlation between the ENSO and PDO amplitude amongst CMIP models.

Similarly, the amplitude of SST variability in the tropical IO is strongly related to that of ENSO in CMIP models, at both interannual and decadal time scales. Observational datasets point toward a different ENSO signature in the IO at interannual and decadal time scales. At interannual time scales, ENSO results in a rather homogeneous SST signal in the tropical IO (referred to as the IO Basin Mode (IOBM) in previous studies). At decadal time scales, the warming tends to be more localised in the SWIO, northeast of Madagascar, in observations. In contrast, CMIP models display very similar ENSO-related patterns of IO SSTs at interannual and decadal time scales, characterized by a basin wide signal.

5.7 Discussion

Half of the CMIP models analysed in the present study display an ENSO-PDO correlation comparable to that observed (~ 0.6). For the other half, the ENSO forcing on the PDO is underestimated either because of an underestimated ENSO amplitude or strength of ENSO teleconnection to north Pacific sea-level pressure and winds. The fact that half of the CMIP models accurately capture the strength of the ENSO influence on the PDO appears contradictory with previous studies on this topic (Furtado et al. 2011; Park et al. 2013). For instance, Furtado et al. (2011) concluded that the influence of ENSO on the PDO

is very weak or non-existent in most CMIP3 models, with only one third of CMIP3 models having a significant (but weak compared to observations) correlation between ENSO and the PDO. This discrepancy could be related to methodological aspects. Furtado et al. (2011) and Park et al. (2013) indeed derived their conclusions based on a simultaneous correlation between ENSO and PDO indices. While the relatively small lag of the PDO relative to ENSO (one to two months) justifies this approach in observations, using a simultaneous ENSO/PDO correlation may be more problematic for CMIP models, for which the PDO generally lags ENSO by 4 to 8 months. Not accounting for this lag will generally result in an underestimated ENSO influence on the PDO in most CMIP models. This is verified on Fig. 5.2b, which actually corresponds to the simultaneous correlation between yearly ENSO and PDO indices. Compared to Fig. 5.1a, it shows that not accounting for the lag weakly impacts the ENSO-PDO correlation in observations, but results in a systematic underestimation in CMIP models. This overestimated lag of the PDO relative to ENSO in CMIP models is a far more systematic bias (only one model does not overestimate it) than the underestimation of the ENSO influence on the PDO. Lienert et al. (2011) attributed this overestimated lag between ENSO and PDO to a deeper mixed layer and weaker air-sea feedback in the northern Pacific in winter and spring in CMIP models. As these biases may have important consequences on the forecast of the north Pacific variability from seasonal to decadal time scales (Lienert et al. 2011; Guemas et al. 2012), further studies are therefore required to understand the causes of these biases and ultimately to correct them.

This chapter also suggests that the underestimation of the ENSO influence on the PDO in half of the CMIP models can be track back to both underestimated ENSO amplitude and underestimated ENSO teleconnection to the north Pacific SLP and wind variability. The inability of some models to properly simulate the amplitude of ENSO signature in the central north Pacific may either arise from underestimated tropical-extratropical teleconnection or an erroneous location of ENSO signature in the north Pacific. Fig. 5.4 indicates that CMIP models generally capture the location of the north Pacific ENSO signature accurately. The analysis of Fig. 5.4b,c for individual models (not shown) indicates that it is the amplitude rather than the pattern of ENSO signature in mid-latitudes that is faulty in Class-II models. Whether this diversity can be related to mean state biases (such as the westward shift in tropical ENSO SST variability, strength/location of the upper level jet or of the Aleutian low) deserves further investigations.

The PDO spectra are consistent with the integration of ENSO and stochastic forcing by the oceanic mixed layer in most CMIP models. There is a PDO peak at decadal time scales (10-30 years window) that cannot be explained from ENSO and stochastic forcing in only 5 CMIP models out of 32. For these models other mechanisms such as ocean dynamics (gyre circulation, planetary waves) or other air-sea coupled processes need to be invoked to account for a statistically significant spectral peak relative to the red spectrum predicted by the Newman et

al. (2003) model. Ocean dynamics and local air-sea coupling may however still play a role in other models at multi-decadal and centennial time scales (Deser and Blackmon 1995; Nakamura et al. 1997; Schneider and Cornuelle 2005; Wu et al. 2003; Park et al. 2013).

The present work also underlines observational uncertainties for detecting patterns of IO decadal SST variability. While the Pacific IPO pattern is very consistent across observational products, it is not the case for IO decadal variability, which displays more marked differences across products. Two datasets (HadISST and ERSST) display rather similar decadal ENSO related pattern in the IO with a south-western tropical IO signature. On the other hand, apart from this south IO signature, Kaplan SST displays an equatorial signal. This is probably related to the relatively poor and inhomogeneous observational coverage in the IO before the satellite era (e.g. Izumo et al. 2013). These observational uncertainties make it difficult to ascertain ENSO signature in the IO at decadal time scales, or the potential existence of an independent IO decadal climate variability. The SWIO decadal SST signal is however likely to be real, as proxy-based studies revealed strong decadal ENSO teleconnections in this region (Cole 2000; Cobb and Charles 2001; Crueger et al. 2008; Grove et al. 2013). If the mismatch between interannual and decadal ENSO signatures in the IO is true, with a regionally strengthened variability in south-western tropical IO at decadal time scales, the reasons behind this time scale-dependent signature of ENSO would need to be understood. The reasons why CMIP models on the other hand produce similar patterns of ENSO-related interannual and decadal IO SST variability also need to be understood. Whether this discrepancy between observational products and CMIP models is due to unknown processes not captured by models and/or to measurement and sampling uncertainties in the historical SST observations remains an open question.

One of the strong motivations for this study was to evaluate Indo-Pacific decadal SST variability in CMIP models in view of prospects for decadal climate predictions. The main source of PDO predictability is the ENSO forcing. I have shown that the strength of the ENSO influence on the PDO was tightly related to both the amplitude of ENSO and the strength of ENSO signature in mid-latitudes. Those are hence important metrics to be monitored in models to be used for decadal forecasts. Understanding the causes of the biases that can affect the ENSO-teleconnection is also important. The depth of the winter mixed layer depth in the north Pacific is, for example as pointed by Lienert et al. (2011), a possible cause for the overestimated lag of the PDO response to ENSO in CMIP models. Identifying the biases that can lead to a misrepresentation of ENSO signature over the north Pacific (e.g. biases in ENSO-related tropical rainfall patterns, in the location of the Aleutian low and/or the jet that channels the equatorial signal towards higher latitudes) will hence also be important for the better establishment of decadal climate predictions over the Indo-Pacific region.

Natural decadal sea-level variability in the Indo-Pacific in CMIP models

In Chapter 4, I assessed the decadal sea-level variability in the tropical Indo-Pacific ocean derived from a large set of sea-level observations (tide gauge; satellite altimetry) and observationally-derived estimates (reanalyses and reconstructions). This analysis revealed that ENSO decadal modulation drives a large fraction of the decadal sea-level variability in the Pacific basin, with further contribution from Modoki decadal modulation. I also demonstrated that the Pacific decadal climate modes remotely influence the extra-tropical Pacific and the IO. While Pacific decadal sea-level variations are robust across sea-level products, the IO signatures of ENSO and Modoki decadal variations are not consistent across these products. Reconstructed sea-level products indeed suggest that ENSO has a significant impact on the IO sea level, with a broad sea-level seesaw that explains a large part of the IO decadal sea-level variations. In contrast, reanalyses and WOD thermosteric sea level suggest that, apart from signals along the WAC, decadal ENSO has little influence on IO sea-level variability. In this chapter, I investigate whether CMIP control runs exhibit consistent patterns of IO decadal sea-level variability, which may provide some guidance on real-world patterns of IO decadal sea-level variability.

A prerequisite before analysing decadal sea-level variations in CMIP models is to evaluate whether the known modes of Pacific decadal climate variability (e.g. the ENSO/PDO/IPO) are reasonably reproduced in CMIP models. This aspect has been discussed in detail in Chapter 5. I have shown that half of the analysed CMIP models accurately reproduce the influence of ENSO on the PDO and the spatial pattern related to the IPO. The analysis also highlights the key role of ENSO teleconnections in setting the inter-hemispheric pattern of the IPO and in influencing the decadal climate variations in the IO. There is indeed a strong

consensus among climate scientists that the tropical Pacific climate affects other oceanic regions (especially extra-tropical Pacific and IO) via atmospheric and oceanic teleconnections. This potential influence of tropical Pacific decadal climate variability on the IO low-frequency sea-level changes has been clearly illustrated in analyses presented in Chapters 3 and 4. However, very few studies did so far analyse the natural decadal sea-level variability simulated by CMIP models. This is particularly important for the IO, an under-sampled ocean basin, where existing observational products do not provide a consensus on the description of decadal sea-level variability (see Chapter 4). This motivated me to examine the CMIP models in the current chapter in order to address the following issues: (i) the control of Indo-Pacific sea-level variability by Pacific climate decadal variations and (ii) the possible existence of independent modes of decadal sea-level variability in the IO.

6.1 Data and Method

The details of the CMIP models analysed in the present thesis are described in the previous chapter (see Table 5.1, Chapter 5). The gridded sea-level products (WOD, reanalysis and reconstructions) discussed in Chapter 4 are also considered in this chapter as a baseline for comparison with CMIP outputs. Even though the Indo-Pacific decadal climate variability in 32 models is assessed in Chapter 5, I consider here 27 models amongst these 32 in the current chapter, based on the ability of the model to reproduce the observed SST pattern of decadal ENSO and decadal Modoki in the tropical Pacific region (see section 6.3). Hence, the ensemble mean maps of variables shown in this chapter include 27 models (Multi-Model Ensemble - MME) and 8 gridded products (Multi-Observational Ensemble - MOE). I analyse the first member of the these CMIP ensemble control simulations so that these simulations include the natural internal variability of the climate system and do not account for the signature of anthropogenic forcing (Meehl et al. 2007; Taylor et al. 2012). CMIP models provide sea surface height above the geoid. Observed SST from the Met Office Hadley Centre (HadISST; Reyner et al. 2003) and the wind and mean sea-level pressure data from 20CR are also considered in this study (for the 1960-2010 period, which is consistent with the period chosen for observational sea-level products in Chapter 4), for a comparison of ENSO and Modoki related SST and wind pattern in the Indo-Pacific Ocean.

All the analyses have been performed on a regular $2.5^\circ \times 2.5^\circ$ grid to facilitate comparison and focus on large-scale pattern. STL filtering method with a 7-year cut-off, as described in Chapter 3, is applied on these data to isolate the decadal variability. Similar to the analysis carried out in earlier chapters, SST and SLA relative to the global mean are analysed for both CMIP and observational data. A linear trend over the entire period of each dataset is also removed at each grid point to ensure that the results presented here are not affected by any long-term change or spurious model drift. An EOF analysis is used to define the tropical Pacific climate modes from decadal SST field (i.e. ENSO and Modoki) and to extract IO decadal sea-level modes, as detailed in Chapter 4. A linear regression

method onto these climate indices is used to re-project Indo-Pacific SST, sea-level and wind pattern associated with the tropical Pacific climate modes. The EOF spatial fields are normalized by their root mean square (RMS) value so that the amplitude of decadal ENSO and Modoki (defined in terms of tropical Pacific SST variability) is accounted for in the PCs. Besides that, the IOD variability for all models and HadISST data is represented by the Dipole Mode Index (DMI), defined as the difference between SST anomalies averaged over tropical western IO (50E-70E, 10S-10N) and tropical southeastern IO (90E-110E, 10S-0N) in order to examine the relationship between IO sea-level variability and the IOD at decadal timescales.

6.2 Amplitude of decadal sea-level variability

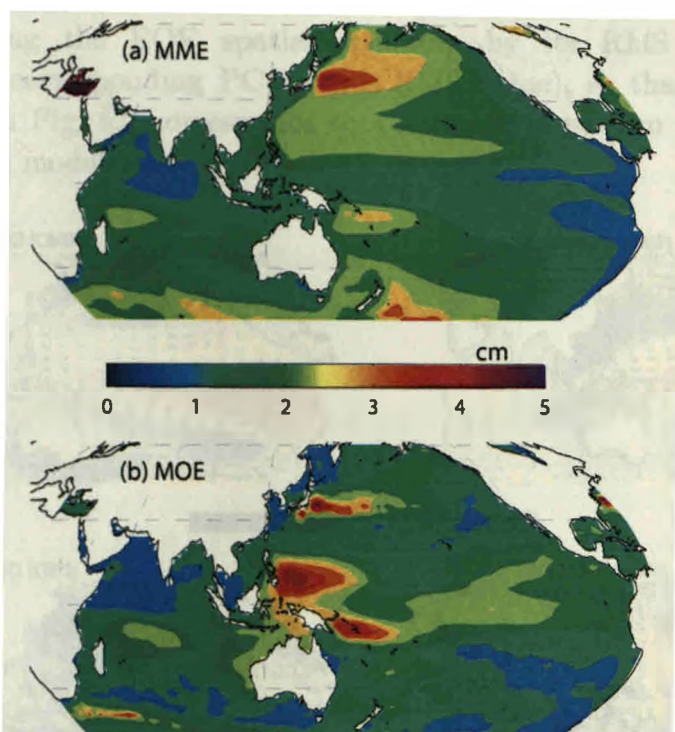


Fig. 6.1: Standard deviation of Indo-Pacific decadal SLA for (a) Multi-Model Ensemble (MME) and (b) Multi-Observational Ensemble (MOE).

Fig. 6.1 show the ensemble mean maps of the standard deviation of decadal sea-level variability from the 27 CMIP models (MME) and the eight observational products (MOE). Regions of maximum decadal variability in both CMIP and observations generally agree with those found in the NEMO OGCM and other observational products described in Chapters 3 and 4. In the tropical Indo-Pacific, the regions of strongest decadal sea-level variability are located in the western tropical Pacific and the southwest and southeast tropical IO with amplitude of about 2 to 3 cm. The large decadal sea-level variance in the northwest Pacific (30N-60N; off Japan with ~3-4 cm) in CMIP models is in agreement with observations and with the strong decadal variability seen in the Uchiura tide gauge record (see Chapter 4). Interestingly, the minimum variability

found in the central equatorial IO ($\pm 1\text{cm}$), extending to the Arabian Sea in observations is also captured by CMIP simulations. There are, however, a number of disagreements between model and observational pattern. The strong variability ($\sim 3\text{-}4\text{ cm}$) found in the northwest tropical Pacific (between $\sim 0\text{-}20\text{N}$) is considerably weaker in CMIP models. As a result, the variability along the WAC is underestimated in models compared to observations. In addition, observations exhibit a relative maximum of variability in the central equatorial Pacific, whereas this maximum is absent in CMIP models. The amplitude of the variability in the equatorial western Pacific is also significantly underestimated.

6.3 Decadal ENSO and Modoki in CMIP models

Decadal ENSO and Modoki indices are defined as described in section 3.2.3. However, as shown in Chapter 5, in order to obtain a standardised spatial map from each CMIP model and observation, I kept the amplitude of the EOFs in the PCs (by dividing the EOF spatial structure by its RMS value and then multiplying the corresponding PC by this RMS value), so that the spatial SST pattern shown in Fig. 6.2 corresponds to a normalized pattern of Pacific decadal variability for all models and observational datasets.

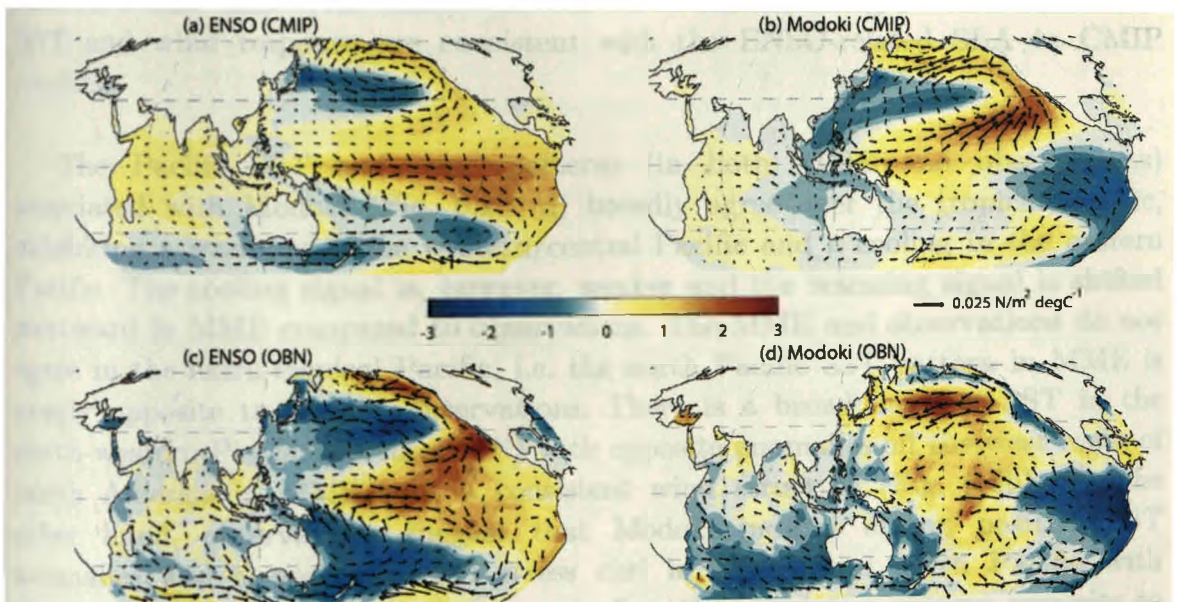


Fig. 6.2: Decadal ENSO-related Indo-Pacific SST and wind-stress signature for (a) MME and (c) OBN (HadISST & 20CR wind for the period 1960-2010). The Modoki pattern is shown on panels (b) and (d) for MME and OBN respectively. These climate modes are respectively obtained as the first and second EOFs of tropical Pacific decadal SST, as described in chapter 3. The spatial patterns shown in this figure are standardised (see text). For 27 models (out of the 32 discussed in the previous chapter), the tropical Pacific (20S-20N) SST pattern correlation with observation is above 0.5 for both ENSO and Modoki and those 27 models are considered in this analysis and all the following ones in this chapter (I discarded Nor-ME, Nor-M, MIROC3, MPI-LR and GISSAO based on this criterion).

Fig. 6.2a,c show the Indo-Pacific SST and wind signature of the decadal ENSO for MME mean and OBN (HadISST and 20CR winds) respectively. As already discussed in Chapter 5, the pan-Pacific ENSO pattern is generally well

represented in the MME mean, even though the positive SST anomalies in the eastern tropical Pacific are more centred towards the north of equator in observations (Fig. 6.2c) compared to the MME (Fig. 6.2a). In addition, the amplitude of SST variability in the central north and south Pacific is generally underestimated in CMIP models.

The wind patterns are rather similar in MME and observations, with westerlies in the equatorial Pacific and a large-scale positive (resp. negative) wind curl over the north (resp. south) Pacific Ocean. This large-scale wind pattern is typical of the ENSO atmospheric teleconnection to the mid-latitudes, which was the main focus of Chapter 5 (see fig. 5.3 also). However, the IO basin-wide SST pattern (similar to the IOBM at the interannual time scale) and the equatorial south-easterlies in the MME is not clearly seen in observations. This mismatch has already been discussed in Chapter 5: the SST response of IO to decadal ENSO differs in observations and CMIP models. There is however one consistent picture in the IO: both MME and OBN show a negative SSTA in the northwest coast of Australia and a cyclonic wind stress curl west of it. This SST and wind pattern in the southeastern IO is consistent with the ENSO-related atmospheric teleconnection described in chapter 4 based on several observed wind products (20CR, NCEP and WASWind). We will see in the following sections that these SST and wind response are consistent with the ENSO-related SLA in CMIP models.

The Pacific SST and wind patterns (in both MME and observations) associated with Modoki (Fig. 6.2b, d) broadly agree over the tropical Pacific, exhibiting a warming in the western/central Pacific and a cooling in the eastern Pacific. The cooling signal is, however, weaker and the warming signal is shifted westward in MME compared to observations. The MME and observations do not agree in the extra-tropical Pacific, i.e. the north Pacific SST pattern in MME is nearly opposite to that in observations. There is a broad negative SST in the north-western Pacific (north of 15N) with opposite anomalies off the west coast of north America in MME with a consistent wind structure (Fig. 6.2b). On the other hand, observations suggest that Modoki induces strong positive SST anomalies and a negative wind stress curl in the central north Pacific with negative anomalies along the west coast of north America; a pattern opposite to what is seen in CMIP models. The Modoki SST and wind signature in the IO (Fig. 6.2b) resembles that of ENSO (Fig. 6.2a) in CMIP models. Decadal Modoki is also associated with negative SST anomalies off the northwest coast of Australia in both MME and observations with an overlying cyclonic wind-stress pattern. This demonstrates that, even though ENSO and Modoki have distinct signatures over the Pacific, the response of IO to these climate modes is rather similar, i.e. the atmospheric teleconnection of ENSO and Modoki over the IO would be occurring in a rather similar way.

6.4 Sea-level fingerprint of Pacific climate modes

6.4.1 ENSO SLA fingerprint

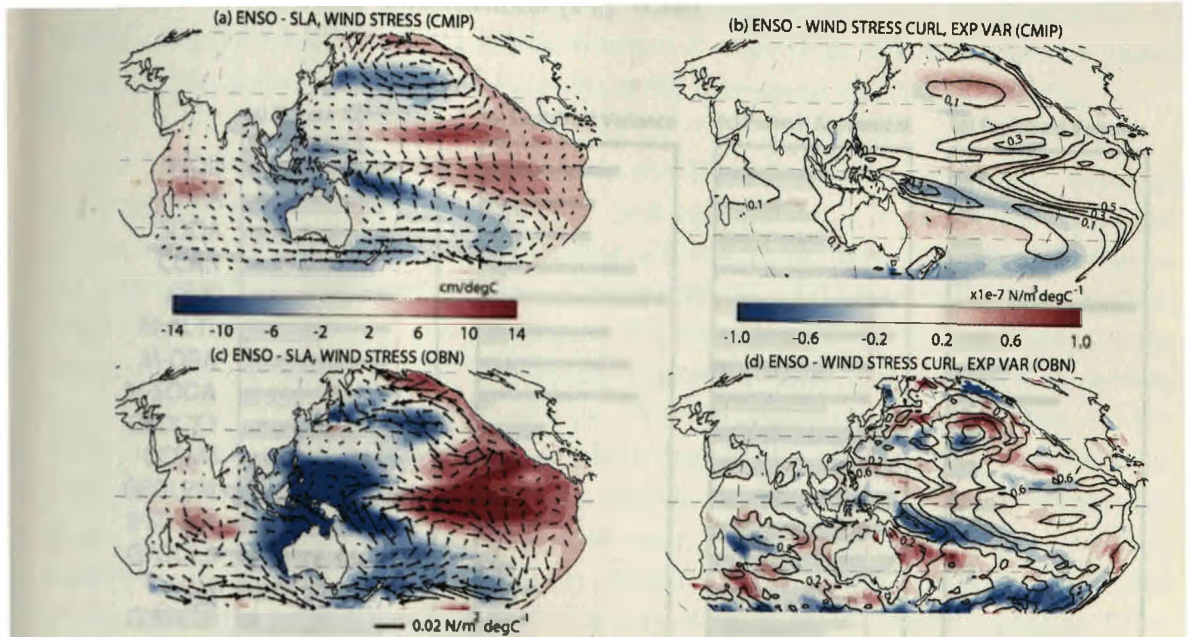


Fig. 6.3: Standardized regression pattern of decadal SLA (colour) and wind stress (vector) onto decadal ENSO for (a) MME and (c) MOE. Regression pattern of wind stress curl on ENSO (colour) and the percentage of sea-level variance (R-squared value) explained by ENSO (contour) for (b) MME and (d) MOE. Wind data from 20CR reanalysis is used in panels (c) and (d). Note that SLA pattern in panel (c) is the ensemble mean from the 8 gridded sea-level products discussed in chapter 4 (WOD, ORA, SODA, C&W, CCAR and 3 products from Meyssignac reconstruction (M-ORA, M-SODA and M-ALTI). See chapter 4 for more details.

Fig. 6.3 displays the Indo-Pacific sea-level and wind stress signature associated with decadal ENSO from MME and MOE (ensemble map from the 8 gridded products described in Chapter 4). In the Pacific, the IPO SLA agrees reasonably well between models and observations. They both exhibit negative SLA confined to the tropical western Pacific and broad positive SLA in the central tropical Pacific (Fig. 6.3a) that extend poleward along the west coast of north and south America. Large negative SLA are prominent in the central north and south Pacific, consistent with the strong wind stress curl signal found east of these anomalies (Fig. 6.3b,d; positive curl over north Pacific around 40N and negative curl over south Pacific south of 30S). There are however some discrepancies between IPO SLA pattern depicted by the MME and MOE. First, the amplitude of decadal ENSO-related SLA are generally underestimated in CMIP models. The strong negative sea-level signal equatorward of 20N in the NWP region is nearly absent in CMIP models. This is consistent with the underestimated sea-level amplitude in CMIP models in this region (Fig. 6.1). Besides, there is a narrow band of positive SLA found in CMIP in the north-equatorial Pacific (~10N) that extends into the western Pacific, which does not appear in the observational analysis. The reason for these mismatches between MME and MOE may be partly related to a misrepresentation of decadal wind variations related with

ENSO in CMIP models. For instance, the observations exhibit a positive curl west of the dateline between 0-15N that is consistent with the strong decadal variability in sea level observed further west of it (Fig. 6.3cd). However, this curl signal is nearly absent in CMIP (Fig. 6.3b), which may explain the weak sea-level signal in NWP in CMIP simulations (Fig. 6.3a).

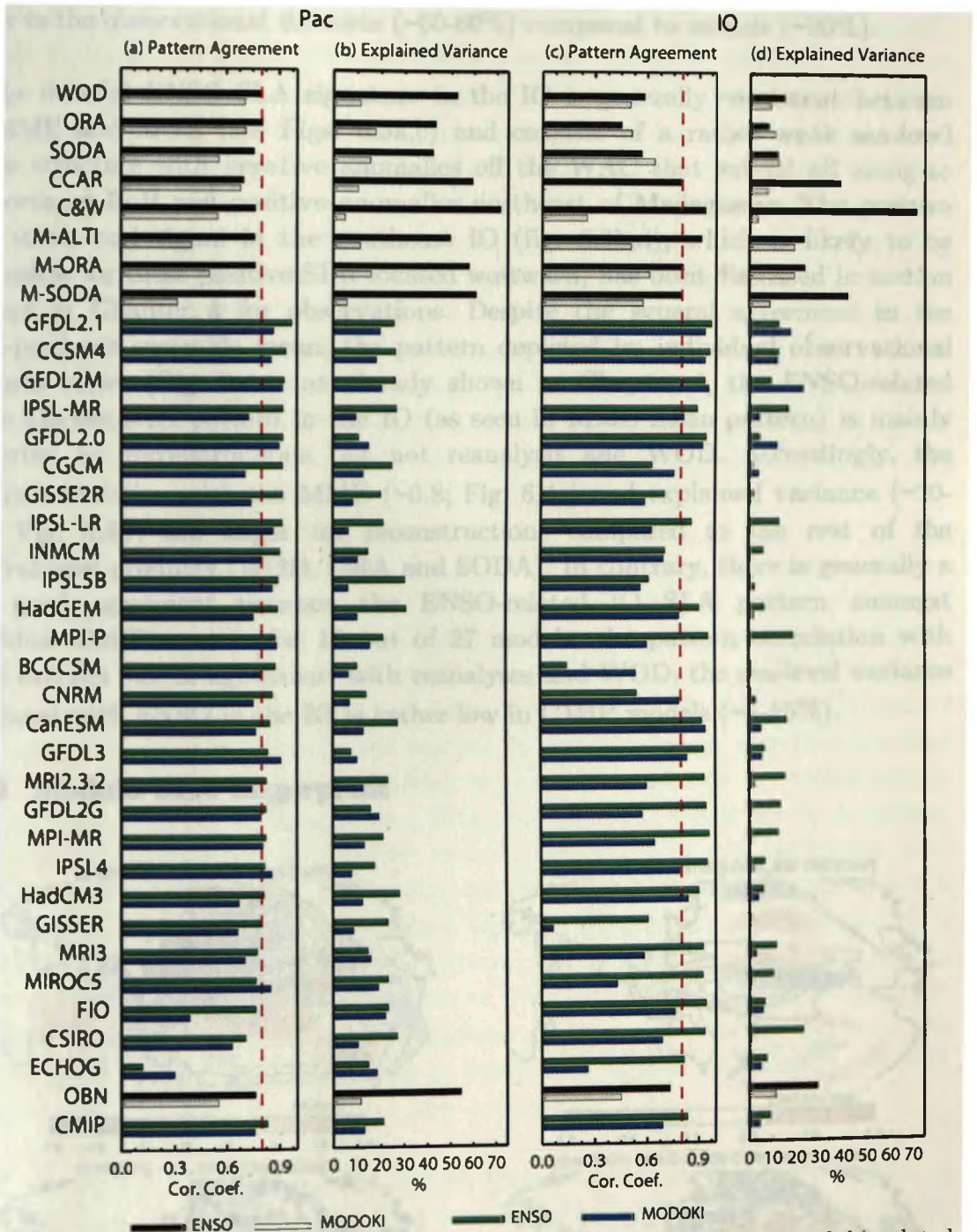


Fig. 6.4: Bar plot showing the (a) pattern correlation of ENSO and Modoki related SLA and (b) explained variance of sea level by these climate modes in the tropical Pacific (120E-290E, 20N-20S) for all models and observational datasets. Pattern correlation for each individual model and observation is computed against the MME shown in Fig. 6.3a. (c) Pattern correlation of ENSO and Modoki related SLA and (d) explained variance in tropical IO (40E-120E, 30N-30S) for all models and observational datasets. Pattern correlation for each individual model and observation is computed against the MME shown in Fig. 6.5a and 6.6a.

Fig. 6.4a provides a quantitative assessment of the agreement between the tropical Pacific decadal ENSO SLA patterns depicted by each observational product and model against the MME mean pattern shown in Fig. 6.3a. Despite the mismatches discussed above, the agreement is generally good for most of the datasets, with a pattern correlation generally exceeding 0.7. The decadal sea-level variance explained by the IPO in the tropical Pacific (Fig. 6.4b) is however much higher in the observational datasets (~50-60%) compared to models (~20%).

The decadal ENSO SLA signature in the IO is generally consistent between the MME and MOE (see Figs. 6.3a,c) and consists of a rather weak sea-level seesaw structure with negative anomalies off the WAC that extend all along to the northern BoB and positive anomalies northeast of Madagascar. The positive wind stress curl signal in the southeast IO (fig. 6.3b,d), which is likely to be responsible for these positive SLA located westward, has been discussed in section 6.3 and in Chapter 4 for observations. Despite the general agreement in the multi-products ensemble mean, the pattern depicted by individual observational products varies (Fig. 6.4c): as already shown in Chapter 4, the ENSO-related dipole like sea-level pattern in the IO (as seen in MME mean pattern) is mainly supported by reconstructions but not reanalysis and WOD. Accordingly, the pattern correlation with the MME (~0.8; Fig. 6.4c) and explained variance (~20-30%; Fig. 6.4d) are larger for reconstructions compared to the rest of the observational products (WOD, ORA and SODA). In contrary, there is generally a very good agreement between the ENSO-related IO SLA pattern amongst individual CMIP models: for 19 out of 27 models, the pattern correlation with MME exceeds 0.8. In agreement with reanalyses and WOD, the sea-level variance associated with ENSO in the IO is rather low in CMIP models (~5-15%).

6.4.2 Modoki SLA fingerprint

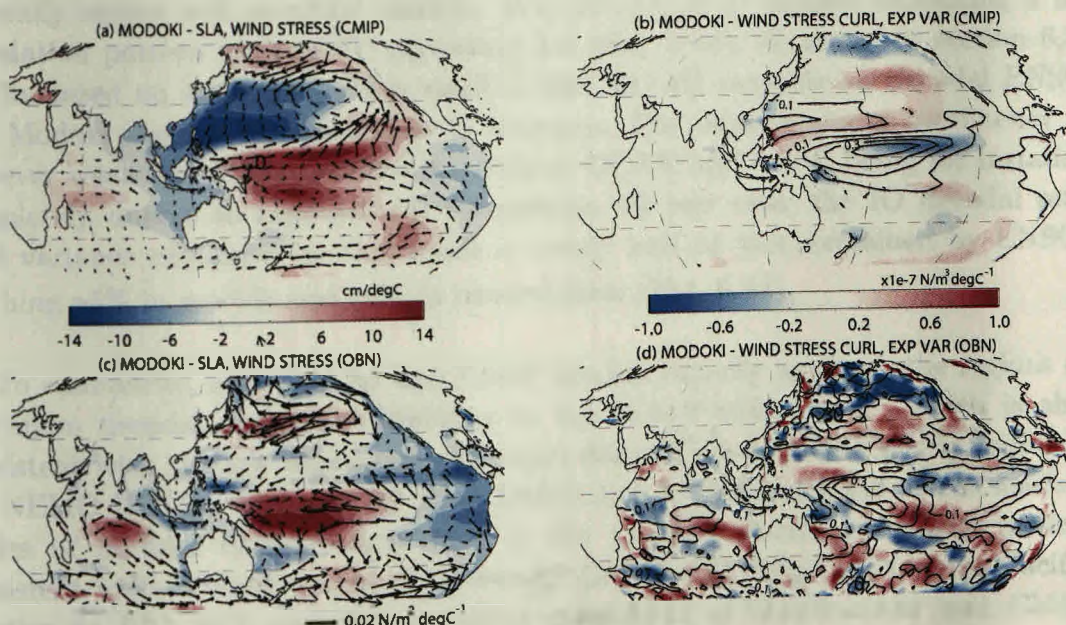


Fig. 6.5: Same as fig. 6.3 but for Modoki-related pattern.

Decadal Modoki-related sea-level and wind patterns are shown in Fig. 6.5. Both MOE and MME indicate that most of the decadal sea-level variance explained by this mode is located over the central equatorial Pacific near the dateline and is associated with a strong positive sea-level signal there. Models show that this mode is also associated with a broad negative SLA signal in the NWP extending from 10N to 45N. This negative sea-level signal is consistently associated with a large positive wind stress curl north of 10N in MME. This subtropical SLA pattern in the north Pacific is however absent in MOE. MOE rather suggest a positive SLA in the central north Pacific (~45N), with opposite signals along the eastern part of the north Pacific basin (Fig. 6.5c). This SLA mismatch between MOE and MME is somewhat similar to that of Modoki-related SST, discussed in section 6.3. Contrary to ENSO pattern, the discrepancies are larger for the Modoki SLA pattern between the different observational products (Fig. 6.4a). While reanalyses and WOD generally capture a SLA Modoki pattern similar to that depicted by the MME (~0.7 pattern correlation), the SLA pattern depicted by reconstructions differs from that of MME (especially for MESSIs products with 0.4 correlation). In contrast, the Modoki SLA pattern agrees fairly well among CMIP models, with a pattern correlation exceeding 0.6 for 25 out of 27 models. For both model and observational datasets, Modoki explains 5 to 15% of the decadal sea-level variance in the tropical Pacific.

The Modoki SLA signature in the IO exhibits a near basin-scale seesaw structure for both MME and MOE (Fig. 6.5a,c), which is very similar to that of the ENSO signature (Fig. 6.3a,c). The positive sea-level signal found in the central SIO is consistent with Modoki-related wind stress curl signal in this region in both models and observations (Fig. 6.5b,d), as already discussed in Chapter 4 for observations and in the previous section. In CMIP models, this positive SLA signal is however weaker and shifted westward compared to observations. Although less consistent than for the IPO, the Modoki related IO SLA pattern generally agrees well amongst models, with 22 out of 27 models exhibiting a IO correlation pattern with MME exceeding 0.6 (Fig. 6.4c). As noted in section 6.3, results based on sea level further confirm that the IO response to decadal ENSO and Modoki share a lot of features in common. The inter-products consistency is however weak for the observational datasets, CCAR and C&W being for instance completely unable to capture this IO pattern. In any case, the IO decadal sea-level variance explained by this mode is nearly half of that explained by ENSO, reaching ~5% in models and 10% in observations (Fig. 6.4d).

To summarise, observations and CMIP models broadly agree on the regions of maximum decadal sea-level variability in the Indo-Pacific Ocean; which is also consistent with the key regions of maximum decadal sea-level variability found in the NEMO OGCM (Chapter 3). Also, ENSO and Modoki emerged as the leading modes of decadal climate variability in the tropical Pacific in CMIP models consistent with in observations. The decadal ENSO SLA fingerprint in the Pacific (similar to IPO SST pattern) is rather consistent in observations and CMIP models, however the ENSO sea-level signature in the IO (a dipole pattern

including the WEP-WAC oceanic connection) seen in CMIP models agrees with reconstructions, but this pattern is absent in other observational products (reanalysis and WOD) as we have seen in Chapter 4. The sea-level fingerprint of decadal Modoki agrees fairly well in the tropical Pacific between observations and CMIP but strongly disagree in the north Pacific. While ENSO (Modoki) explains ~50% (~10%) of decadal sea-level variance in the tropical Pacific in observations, these numbers are roughly ~20% (10%) in CMIP models. Similarly, CMIP models indicate that the leading modes of tropical Pacific climate (ENSO and Modoki) explain less than 15% of the IO decadal sea-level variance together, but these numbers are considerably higher in reconstructions.

6.5 Main modes of IO decadal sea-level variability

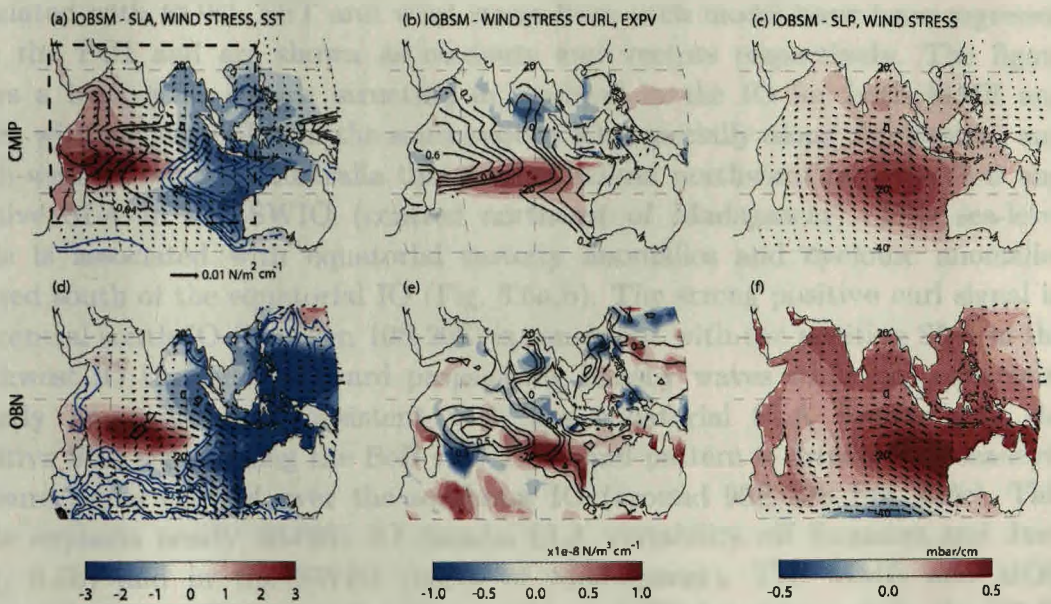


Fig. 6.6: (a) MME mean EOF1 pattern of IO decadal sea level (colour), associated wind stress (vector) and SST (contour) over the IO region. (b) MME mean regression pattern of wind stress curl (colour) onto PC1 and sea-level variance explained (R-squared value) by PC1 (contour). (c) MME mean regression pattern of SLP (colour) and wind stress (vector) on PC1. (d), (e) and (f) are same as (a), (b) and (c) but for MOE mean. The tropical IO region where the EOFs are computed is shown by a dashed rectangle on (a). The patterns are standardized as described in sections 6.1 and 6.2. The SLA pattern shown in panels (a) and (d) is referred to as “Indian Ocean Basin Scale Mode (IOBSM)” in the text.

Results from the previous section indicate that the Pacific decadal climate variability only controls a small amount of the tropical IO decadal SLA variations in CMIP models, reanalysis and WOD (~10-15% of IO explained variance for ENSO and Modoki together; see Fig. 6.4d). In chapter 4, an EOF analysis of the IO decadal SLA in observationally-derived products already revealed that one of the two leading modes (referred to as “Mode A” in chapter 4) of variability is an IOD-like basin-scale pattern, which is partly controlled by tropical Pacific climate variability. In some datasets, the other mode (“Mode B”) captures a large SLA variability in the SWIO region nearly independent of that in the tropical Pacific.

However, there is a considerable spread in the pattern of these modes amongst the different observational products as shown in Chapter 4. An independent EOF analysis of tropical IO SLA (40E-120E; 30S-30N) is hence performed for all CMIP models and the results are compared with those derived from observations in Chapter 4. As discussed in the following, this analysis reveals two modes of IO decadal SLA variability (depicted by the first two EOF patterns) that are generally consistent across CMIP models. One of this modes is a sea-level seesaw (Fig. 6.6) with basin scale features and is referred to as “IO Basin-Scale Mode (IOBSM)” hereafter. The other mode displays a strong variability in the SWIO region (~10S-30S), east the Madagascar (Fig. 6.8) and is referred to as “Southwest IO Mode (SWIOM)” hereafter¹.

Fig. 6.6a,d show the MME and MOE pattern of decadal SLA (shading) associated with EOF1. SST and wind stress from each model have been regressed onto the PC1 and are shown as contours and vectors respectively. The figure shows a basin-scale seesaw structure in sea-level in the IO for both MME and MOE, with negative SLA in the southeastern IO, especially along the western and north-western coast of Australia that further extend northward into the BoB and positive SLA in the SWIO (centred northeast of Madagascar). This sea-level mode is associated with equatorial easterly anomalies and cyclonic anomalies centred south of the equatorial IO (Fig. 6.6a,b). The strong positive curl signal in the central south IO (between 10S-20S) is consistent with the positive SLA in the southwest IO through westward propagating Rossby waves while the equatorial easterly anomalies are consistent with the equatorial SLA seesaw and the negative SLA signal along the BoB rim. This wind pattern is driven by a sea-level pressure signal centred over the southeast IO (around 90E;20S Fig. 6.6c). This mode explains nearly 40-60% IO decadal SLA variability off Sumatra and Java (Fig. 6.6b) and in the SWIO (north of Madagascar). The MME and MOE generally agree well except for the associated SST signature: while the MME exhibits opposite SST anomalies in the southeast and western IO (contours on Fig. 6.6a), the observed SST pattern exhibits a negative signal in the southeast IO but no opposite anomalies in the western part of the basin. The spatial sea-level structure of this IOBSM is very robust amongst all the CMIP models (pattern correlation with MME above 0.8 for all models except one) and relatively robust amongst the observational datasets (pattern correlation with MME around 0.6 for all datasets; Fig. 6.9c). The percentage of decadal SLA variance in the IO explained by this mode is large (35% on average in CMIP and 45% on average in observations) but strongly varies from one dataset to another, being particularly large in reconstructed SLA products (Fig. 6.9a).

¹ As mentioned in chapter 4 for observations, the IOBSM and SWIOM are shown up in CMIP models either as EOF1 or EOF2. The mode which shows variability in the SWIO is considered SWIOM and the dipole mode is considered as the IOBSM. However, 20 models out of 27 analyzed show IOBSM as the EOF1 suggesting that this mode is the leading mode of decadal sea-level variability in the IO. Hence as an easy way to present the results I use EOF1/PC1 to represent IOBSM and EOF2/PC2 for SWIOM in the discussion.

The IOBSM maximum SLA variance off Java and Sumatra and in the SWIO (between 10S-20S) and its dipolar structure suggests that this mode may be at least partly driven by decadal IOD modulations (see chapter 2, section 2.5.3 for a brief discussion on the IOD). Fig. 6.7, which shows the correlation coefficient between IOBSM time series (PC1) and decadal DMI further supports this hypothesis for CMIP simulations. While observations suggest a rather weak control of decadal IOD variability on this IOBSM mode (correlation lower than 0.6 for all observational datasets), most CMIP models exhibit a strong relationship between decadal IOD and the IOBSM, with 20 out of 27 models exhibiting correlation larger than 0.6. It must however be noticed that a few models (GISSER, IPSL5B, IPSL4, FIO, ECHOG) do not show any strong relationship between the two modes, as for the observational datasets.

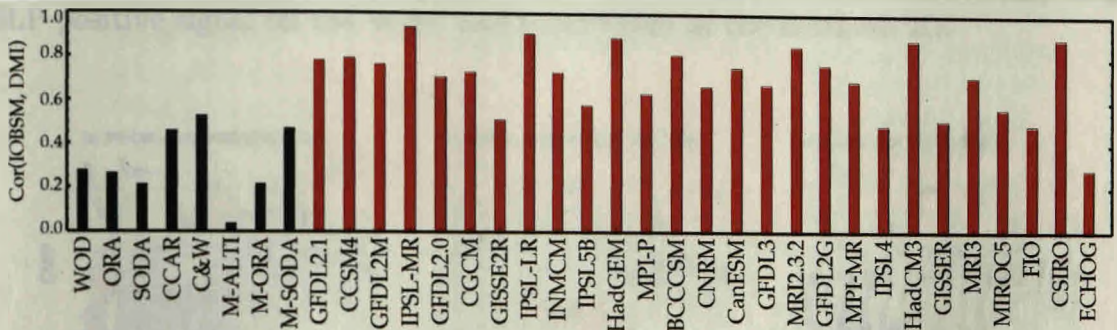


Fig. 6.7: Correlation between the IOBSM time series (PC1) and decadal DMI. Black bars are for the observational datasets and the red bars are for the CMIP models.

The second mode of IO decadal SLA variability (SWIOM) arises as a positive signal located in the SWIO (~40E-90E; 10S-30S) in CMIP models (Fig. 6.8a), explaining up to 40% of decadal sea-level variance there (Fig. 6.8b). This SLA pattern in CMIP models is consistent with the positive wind stress curl in the southeast IO and the positive SST anomalies associated with it (Fig. 6.8ab). In CMIP models, this mode is also related to stronger negative SLP signal over the southern IO (poleward of 30S) and a weaker positive SLP signal off the WAC (Fig. 6.8c), reminiscent of the typical SLP pattern related to the Mascarene high variability (Manatsa et al. 2013; Moriaka et al. 2015). The SWIOM mode explains an average of ~10-20% of total decadal sea-level variance in the IO (Fig. 6.9b) for CMIP models, with large deviations around this average number for some individual models (e.g. 45% in MIROC5). This SWIOM pattern is rather consistent amongst CMIP models, with 19 out of 27 models displaying a pattern correlation with the MME above 0.6.

The SWIOM is far less consistent across observational products as mentioned above, ORA and M-ORA (0.6 correlation) and to a certain extent WOD (0.5 correlation) being the only products that capture this mode reasonably well (Fig. 6.9c). All other products exhibit a very weak pattern correlation, highlighting the inability of these data sets to capture this mode. The readers may refer to Chapter 4 for a more in-depth discussion on this mode in observation. Even though not all observational sea-level products capture this SWIOM pattern, a

few of them (ORA, M-ORA and WOD to a certain extent) exhibit a strong variability in the SWIO and their signature dominates the MOE pattern shown on Fig. 6.8d. The MOE negative SLA found in the eastern side of the basin, especially along the Indonesian throughflow region, is a residual SLA signature from the reconstructed SLA products. Interestingly, both CMIP models and observations indicate a distinct SST variability in the SWIO associated with the SWIOM, suggesting mixed layer thermal variations in this region. Here, there is however an important inconsistency in the wind and SLP field between observations and CMIP. The strong negative wind stress curl over the SWIO in 20CR (Fig. 6.8e) is completely absent in CMIP (Fig. 6.8b). This negative curl could be a bias in the reanalysis wind or a forced atmospheric cyclonic winds response to the warming anomaly southeast of Madagascar. Similarly, the SLP pattern in observations is very different from the MME one, with a very large SLP positive signal off the WAC and everywhere in the northern IO.

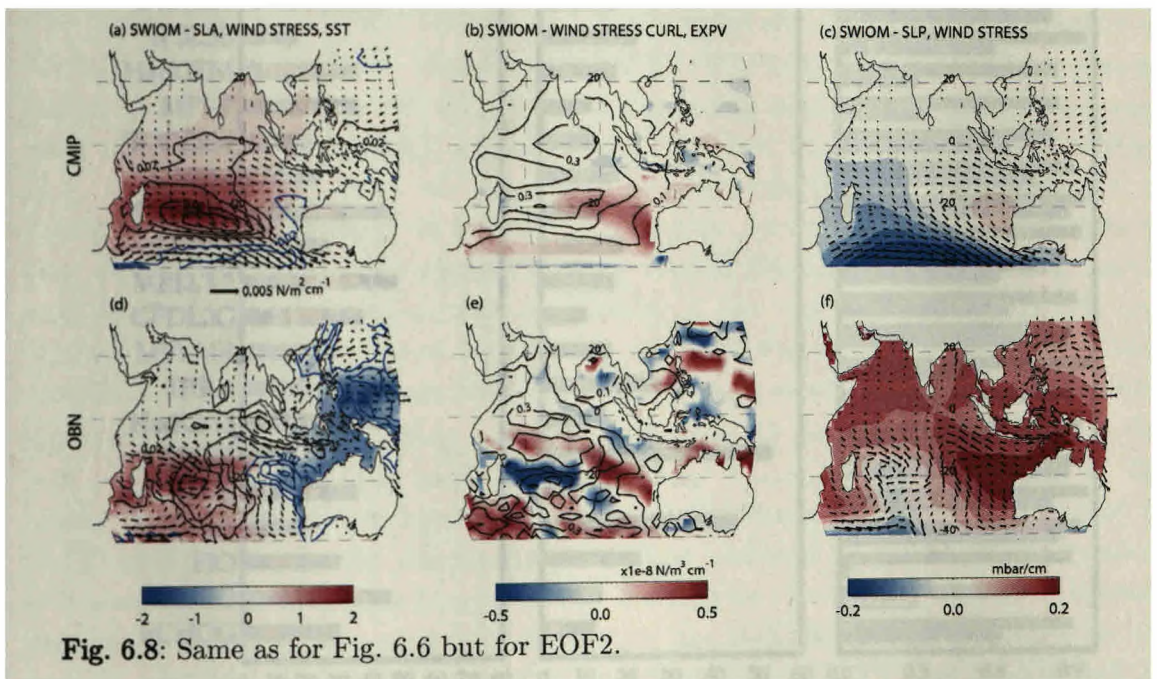


Fig. 6.8: Same as for Fig. 6.6 but for EOF2.

Finally, all models and observational datasets indicate that the SWIOM mode is largely independent from the tropical Pacific decadal variations, with a very weak percentage of variance explained by ENSO and Modoki respectively (Fig. 6.9b). The CMIP model analysis suggests that the IO decadal sea-level variability is largely independent from the Pacific climate variability. While the IOBSM is partly controlled by Pacific climate variability, SWIOM is largely independent. Given the observational uncertainties of these IO modes (discussed in detail in Chapter 4), results from CMIP models are encouraging as they reveal rather consistent modes of the decadal sea-level variability in the IO which are difficult to diagnose from observations.

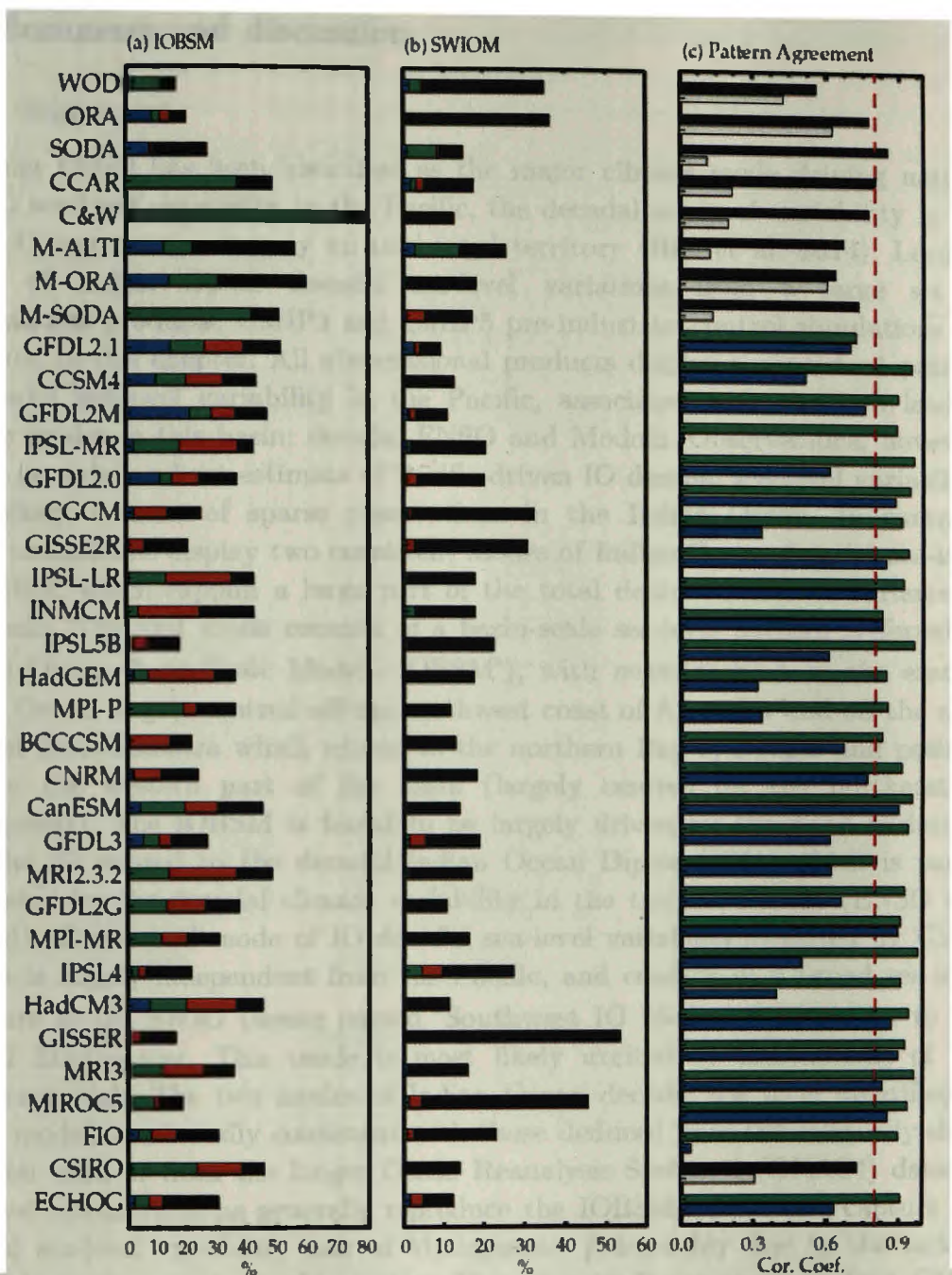


Fig. 6.9: Bar plot of percentage of IO decadal SLA variance explained by (a) EOF1 (IOBSM) and (b) EOF2 (SWIOM). The respective contribution of ENSO (green), Modoki (blue) and “independent DMI” (DMI index once ENSO and Modoki are removed through a linear regression; red) to the total explained variance is shown by colours on each bar. The black portion of the bar shows the variance that is independent of these climate modes (ENSO, Modoki and DMI). (c) pattern correlation for first (IOBSM; black bars for OBNs and green for models) and second (SWIOM; grey bars for observations and blue bars for models) decadal SLA EOFs over the tropical IO between all individual models and observational datasets against the multi-model ensemble mean (MME) shown in Fig. 6.6a and 6.8a.

6.6 Summary and discussion

6.6.1 Summary

While ENSO has been identified as the major climate mode driving natural decadal sea-level variability in the Pacific, the decadal sea-level variability in the Indian Ocean remains largely an uncharted territory (Han et al. 2014). Leading modes of Indian Ocean decadal sea-level variations from a large set of observational products, CMIP3 and CMIP5 pre-industrial control simulations are presented in this chapter. All observational products display a consistent pattern of decadal sea-level variability in the Pacific, associated with the two leading climate modes in this basin: decadal ENSO and Modoki. Observations, however, do not provide a robust estimate of Pacific-driven IO decadal sea-level variability, most likely because of sparse observations in the Indian Ocean. In contrast, CMIP simulations display two consistent modes of Indian Ocean decadal sea-level variability, which explain a large part of the total decadal sea-level variance in this basin. The first mode consists of a basin-scale sea-level pattern (referred as “Indian Ocean Basin-Scale Mode - IOBSM”), with negative SLA in the eastern Indian Ocean largely centred off the northwest coast of Australia and off the west coast of Java/Sumatra which extend to the northern Bay of Bengal and positive SLA in the western part of the basin (largely centred off the northeast of Madagascar). The IOBSM is found to be largely driven by the wind variations over the IO related to the decadal Indian Ocean Dipole (IOD) which is partly modulated by the decadal climate variability in the tropical Pacific (ENSO and Modoki). The second mode of IO decadal sea-level variability depicted by CMIP models is largely independent from the Pacific, and consists of a broad sea-level signature in the SWIO (hence named “Southwest IO Mode - SWIOM”) - to the east of Madagascar. This mode is most likely excited by fluctuations of the Mascarene high. The two modes of Indian Ocean decadal sea level identified in CMIP models are broadly consistent with those deduced from the relatively short altimeter data or from the longer Ocean Reanalysis System 4 (ORAS4) dataset. Sea-level reconstructions generally reproduce the IOBSM but do not capture the decadal sea-level variability east of Madagascar, presumably due to the lack of long tide-gauge records in this region. This chapter hence suggests that CMIP outputs can provide some guidance for identifying robust modes of decadal sea-level variability in regions that are not well sampled in observations.

6.6.2 Discussion

The spatial SLA signature of decadal ENSO in the Pacific is captured by most CMIP models reasonably well, except for the ENSO-related strong decadal variations observed in the northwest tropical Pacific. This bias in CMIP models could partly be related to an inaccurate representation of ENSO-related wind variability in this latitudinal band ($\sim 5\text{N}-20\text{N}$; Fig. 6.3a,c), that may be related to unrealistic westward extension of the equatorial cold tongue in these models (i.e. the well-known *cold tongue bias*, see Leloup et al. 2008, Yu and Kim 2010). Given the considerable uncertainties in the multi-decadal changes depicted by the

different observational wind products over the equatorial Pacific (e.g. Moon et al. 2013, Feng et al. 2011, Nidheesh et al. 2013), it is however not possible to confidently ascertain the decadal wind variations in this region. The equatorial Pacific sea-level signature of decadal Modoki is also reasonably captured in most CMIP models. However, these models generally also disagree with observational products in the NWP, where they exhibit a broad sea-level signature which is not seen in observations (Figure 6.5a,c). The most striking discrepancy between models and observational products lies on the sea-level variance explained by ENSO in the tropical Pacific. While observations indicate that 40 to 60% of the total decadal sea-level variance in the tropical Pacific is explained by the ENSO, CMIP models suggest an ENSO-related variance of about 20%.

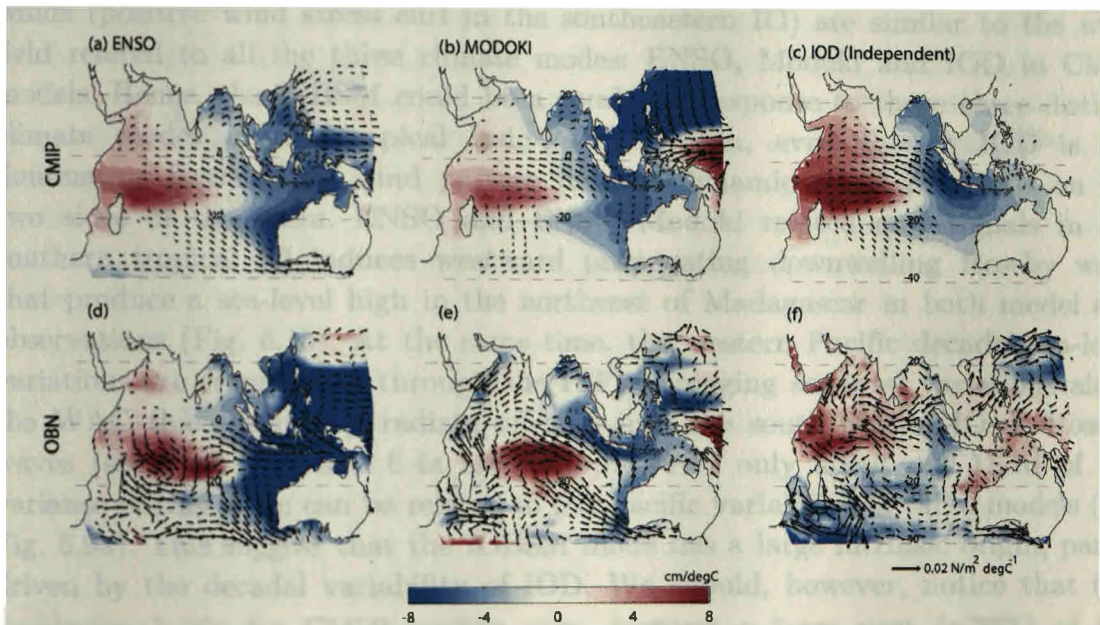


Fig. 6.10: (a) ENSO (b) Modoki and (c) DMI (ENSO and Modoki influence removed) patterns of decadal IO SLA (colour) and wind stress (vector) for MME. (d-f) Same as (a-c) but for MOE.

The IO sea-level response to ENSO and Modoki is similar in most CMIP models, with a dipolar SLA structure at the scale of the IO basin. The similarity between ENSO and Modoki sea-level signature in the IO in CMIP models is also consistent with the IO wind pattern associated with these climate modes, as shown in Figs. 6.3 and 6.5. The positive wind stress curl in the southeastern IO associated to both ENSO and Modoki represents a typical Matsuno-Gill type response to anomalous warming/cooling in the tropical IO. CMIP models indicate that Pacific climate modes (ENSO and Modoki) collectively explain only ~15% of the IO decadal sea-level variance. The observational SLA ensemble mean associated with ENSO and Modoki in the IO is also similar to that of most CMIP models. It is however not the case for each individual observational products. We have seen in chapter 4 that the IO response to ENSO in reanalyses strikingly differs from reconstructions and the possible reasons have been discussed there. It must be kept in mind that the dipole pattern seen in Fig. 6.3c (ENSO response in the IO) largely arises from reconstructions, not from reanalyses. As in CMIP

models, decadal ENSO explain ~15% of IO decadal SLA variance in reanalyses and WOD products, while reconstructions exhibit a much higher percentage of explained variance (40 to 70%), a mismatch that may be related to observational caveats (the lack of long tide gauges data in this basin) faced in reconstruction techniques (see Chapter 4 for a more detailed discussion on this).

Observational uncertainties in decadal sea-level estimates are larger in the IO than in the Pacific (see Chapter 4). Results from CMIP models are enlightening in this context. Figs. 6.7 and 6.9 show that the IOBSM is largely driven by decadal IOD fluctuations in CMIP models. The main tropical Pacific climate modes (ENSO and Modoki) also imprint their signatures on this mode (IOBSM), through their influence on decadal IOD. Fig. 6.10 shows that IOBSM related winds (positive wind stress curl in the southeastern IO) are similar to the wind field related to all the three climate modes: ENSO, Modoki and IOD in CMIP models. Hence, the IOBSM could be a combined response to these three distinct climate modes in the tropical Indo-Pacific Ocean, even though IOD is the dominating factor. This wind pattern induces dynamic ocean responses on the two sides of the basin. ENSO and ENSO Modoki related curl signals in the southern tropical IO induces westward propagating downwelling Rossby wave that produce a sea-level high in the northeast of Madagascar in both model and observations (Fig. 6.10). At the same time, the western Pacific decadal sea-level variations are transmitted through the ITF, impinging sea-level variations along the WAC that eventually radiate offshore into the south central IO as Rossby waves (see Figs. 6.3a and 6.4a as well). However only about one third of the variance of this mode can be related to the Pacific variability in these models (see Fig. 6.9a). This suggest that the IOBSM mode has a large intrinsic origin, partly driven by the decadal variability of IOD. We should, however, notice that this conclusion holds for CMIP models only, because a large part (~70%) of the variance of IOBSM is explained by Pacific variability in observational products. Fig. 6.10 indeed illustrates that, while CMIP models clearly show the role of IOD in shaping the IO decadal sea-level variability (Fig. 6.10c), the influence of independent decadal IOD variations on IOBSM is not so clear in gridded observational products (Fig. 6.10f). This discrepancy between models and observations may be either related to observational issues (too short records or data uncertainties) or to model caveats.

Apart from the IOBSM which is partly associated with Pacific climate variability, CMIP models also exhibit another mode of decadal SLA variability in the IO consisting of SLA variations in the southwest IO, east of Madagascar (SWIOM; fig. 6.8). These variations are largely independent from the Pacific climate variations and dynamically consistent with decadal wind curl variations in the southeast IO. The physical mechanisms driving this decadal SLA variability however have to be understood further. One of the initial studies that discussed the SLA variations in this region (SWIO) (Fukumori et al. 1998) showed that the seasonal steric variations in the mixed layer largely drive the SLA in the SWIO (especially southeast of Madagascar; their figure 7). The SST

variations found in the SWIO (slightly shifted southward to the maximum SLA signal; see fig. 6.8a) suggest that heat flux could play a role in inducing SLA in this region. Similarly, a recent study by Li and Han (2015; LH15 hereafter) based on an OGCM experiment provides a very detailed discussion on the decadal SLA variations in the SWIO and possible mechanisms. The region 'C' defined in LH15 has nearly the same extent as the SLA pattern seen in the SWIO related to SWIOM. LH15 stated that this sub-tropical sea-level variability is equally controlled by wind stress curl-driven ocean dynamics and wind speed-controlled turbulent heat flux. Fig. 6.8 a & b suggest that, even though the sea-level variability in the SWIO is dynamically consistent with the positive wind stress curl found in the southeast IO, the southern part of the SLA (south of 20S) could also be partly associated with the wind speed-controlled heat flux and related SST warming (SST and local wind maximum are observed south of 20S in fig. 6.8a), causing cooling/warming from surface to sub-surface (in the mixed layer) and induce thermosteric positive/negative SLA. In short, both wind stress-driven ocean dynamics and wind speed-controlled heat flux could be playing a role in shaping the decadal sea-level variations in SWIO as suggested by LH15. Further studies are however required to quantify these respective contributions (this is one of the main perspectives put forward by this thesis).

Summary and Perspective

7.1 Summary

The main findings of the present thesis can be summarised as follows.

7.1.1 Decadal sea-level variations in the Pacific

Largest amplitude Pacific decadal sea-level fluctuations occur in the western tropical Pacific (about 4-5 cm). Regions of largest decadal variations in this basin generally coincide with regions of strong interannual variability, with the noticeable exception of the eastern equatorial Pacific that displays a clear maximum of interannual variability linked to ENSO, but a weak decadal variability. The decadal sea-level variability in the tropical Pacific is dominated by the decadal modulation of ENSO and ENSO-Modoki. An intercomparison of various observationally derived sea-level products demonstrates that the Pacific sea-level pattern associated with decadal ENSO is very robust, similar to the one depicted by the short-period altimeter data, suggesting that any of these products can be used to describe ENSO-related Pacific decadal variability. The decadal ENSO related sea-level pattern in the Pacific is nearly basin-wide and resembles the IPO SST pattern, while the sea-level response to ENSO at interannual time scales is largely confined to the tropical Pacific. These decadal fluctuations of ENSO explains a large part of the decadal sea-level variance in the Pacific Ocean but this contribution considerably varies from one dataset to another (30 to 80%). The second leading mode of Pacific sea level at decadal time scales is related to decadal ENSO Modoki, which explains ~15-20% of the Pacific decadal sea-level variance. The sea-level response to ENSO Modoki is, however, mainly confined to the central equatorial Pacific near the dateline. Although not as consistent as decadal ENSO signature, there is a reasonable agreement in the sea-level imprint of decadal Modoki in the Pacific amongst various sea level products.

Overall, more than 50% of decadal sea-level variability in the Pacific is explained by the combined effect of decadal ENSO and Modoki.

7.1.2 Pacific influence on IO decadal sea level

Contrary to the Pacific, sea-level products do not display robust patterns of decadal sea-level variability in the IO. The most robust decadal sea-level variability in the IO across various sea-level products (also in tide gauge and altimeter sea level) is located along the WAC. These variations being largely driven by decadal wind fluctuations in the equatorial Pacific. The sea-level signals along the WAC radiate westward away from the coast as Rossby waves and induce sea-level changes in the SIO. Regarding the rest of the IO basin, the Pacific control on the IO decadal sea level indeed appears to be larger in reconstructed sea-level products (as compared to reanalyses), with a pattern that strongly resembles the IO signature of ENSO at interannual time scales (a dipole-like pattern reminiscent of the IOD sea-level signal). The strong control of the Pacific on the decadal IO sea-level in reconstruction sea level products may, however, be spurious and related to the reconstruction technique that rely on tide gauge records that are very sparse in the IO. In other sea-level products, the decadal ENSO signature is generally confined to the WAC as mentioned above, most likely because of a destructive interference of SLA generated by ENSO-driven oceanic and atmospheric teleconnection in the southern IO. The positive SLA in the southern IO triggered by the remotely driven wind stress curl by decadal ENSO opposes the negative SLAs induced by the ENSO-driven upwelling Rossby waves radiated from the WAC. In most of the datasets, decadal Modoki generally displays a strong signature over the south-central IO and a weaker opposite signature in the EEIO and along the rim of eastern BoB.

7.1.3 Independent IO decadal variability

The various sea-level products analysed show that IO decadal sea-level variability is to a large extent independent of the Pacific (this is contrary to interannual time scales, for which there is a tendency of IOD events to be triggered by ENSO). Equatorial wind stress decadal variations over the Indian and Pacific oceans are not significantly correlated, in all the wind products analysed. The percentage of the decadal IO sea-level variance independent from the Pacific, however, considerably varies amongst products, being larger in NEMO ocean simulation, reanalyses and WOD (~80%) than in reconstructions (from 65 to 20%). One of the two dominant modes of decadal IO sea-level variability exhibits a basin-wide dipole-like pattern, which is mostly decadal ENSO-driven in reconstructions but more independent in reanalyses. In reanalyses, IO decadal zonal wind stress variations at the equator induce sea-level fluctuations in the EEIO and BoB, through equatorial and coastal wave-guides. The second dominant mode of decadal sea-level variability in the IO is very diverse amongst the different sea-level products analyzed. Some products (including the short altimetry data), however, display a mode of decadal IO sea-

level variability in the south-western Indian Ocean (east of Madagascar) associated with wind stress curl fluctuations in the southern IO.

7.1.4 Representation of decadal ENSO variations in CMIP models

The disparity in the IO decadal sea-level variations depicted by various observational datasets does not allow to draw definitive conclusions on the dominant IO decadal sea-level patterns and their relationship with the Pacific. This difficulty led me to investigate whether CMIP control simulations exhibit any robust patterns of IO decadal sea-level variability, which may provide some guidance to better constrain IO decadal variability. A prerequisite before analysing decadal sea-level variations in CMIP models is to evaluate whether the known modes of Pacific decadal climate variability is reasonably reproduced in CMIP models. This is investigated by examining the signature of ENSO fluctuations at decadal time scales on the Indo-Pacific region and its relationship with the PDO in CMIP models. Results revealed that most of the CMIP models reproduce the influence of ENSO on the PDO and the spatial SST pattern related with the IPO reasonably well. These models generally exhibit larger PDO-related signals in the equatorial and south Pacific, highlighting the key role of ENSO teleconnections in setting the inter-hemispheric pattern of the PDO. The strength of the modelled ENSO/PDO relationship can be related to both ENSO amplitude and strength of ENSO teleconnection to the north Pacific atmospheric variability. The shape of the PDO spectrum is well explained by a combination of ENSO forcing, stochastic forcing and reemergence in most models. In the Indian Ocean, CMIP models display a more consistent spatially uniform signal compared to that in observation, similar to the IO's ENSO response at interannual time scales (IOBM). Finally, both Indian Ocean decadal variability and PDO amplitude are related to ENSO amplitude across CMIP models.

7.1.5 IO decadal sea-level variability in CMIP models

The ability of CMIP control experiments to simulate the Pacific decadal climate variability provided some confidence in analysing the Indo-Pacific decadal sea-level variations in these simulations. In contrary to the diverse behaviour found in observational products (inconsistency), CMIP simulations display two rather consistent modes of IO decadal sea-level variability, which explain a large part of the total decadal sea-level variance in this basin. The first mode consists of a basin-scale sea-level pattern (referred as "Indian Ocean Basin-Scale Mode - IOBSM"), with negative SLA in the eastern IO largely centred off the north-west coast of Australia and off the west coast of Java/Sumatra which extend to the northern BoB and positive SLA in the western part of the basin (largely centred in the northeast of Madagascar). The CMIP IOBSM pattern is similar to the first mode of decadal SLA variability found in most of the observational products. This IOBSM in CMIP simulations is found to be largely driven by the wind variations over the SIO related to the decadal Indian Ocean Dipole (IOD), which is partly modulated by the decadal climate variability in the tropical Pacific (ENSO and Modoki). IOBSM explains ~50% of decadal sea-level variability off

Sumatra and Java and in the southwest IO. The second dominant mode of IO decadal sea-level variability revealed by CMIP models is completely independent from Pacific variability and consists of a broad sea-level signature in the SWIO and is referred to as “Southwest Indian Ocean Mode (SWIOM)”. This mode is most likely excited by decadal wind variations in the subtropical Indian Ocean, probably driven by the Mascarene High variations. The two modes of IO decadal sea level identified in CMIP models are broadly consistent with those deduced from the relatively short altimeter data or from some observationally-derived sea-level products (ORA, WOD). Sea-level reconstructions generally reproduce the IOBSM (though excessively attributing this mode to decadal ENSO) but do not capture the SWIOM presumably due to the lack of long tide-gauge records in this region.

7.2 Perspectives

7.2.1 Improving the observational sea-level products

Results presented in the present thesis reveal that available sea-level products do not provide a consistent description of IO decadal sea-level variability. Sea-level reconstructions generally depict decadal IO sea-level variability that is largely controlled by decadal ENSO fluctuations in the Pacific with a sea-level pattern that resembles the IO sea-level signature at interannual time scales (a dipole-like pattern reminiscent of the IOD sea-level signal). This strong control of the Pacific on the decadal IO sea-level in these products may however be spurious, because of the sparse tide-gauge records in the IO. Reconstructions indeed rely on gridded sea-level data (generally altimeter) that are decomposed into EOFs that are further interpolated back in time using in-situ sea-level measurements from tide gauges. An insufficient tide gauge network in a given region or an incomplete description of the low-frequency sea-level patterns by the gridded dataset may hence result in an inappropriate description of sea-level evolution in reconstructed products. In contrast to the Pacific basin, long tide gauge records are rather sparse in the IO. This is particularly true for the southern IO, that possesses only one tide gauge (Fremantle) that holds data for more than at least 50 years. This century-long Fremantle tide gauge, located along the west coast of Australia is thus be the main source of information to reconstruct sea level in the SIO. Since Fremantle record largely mirrors western Pacific decadal variations through the oceanic bridge to this region, it may result in an overestimated influence of ENSO control on IO low-frequency sea-level variations in reconstructions. Besides, the longest tide gauge record located in the southwestern Indian ocean at Port Louis spans less than 40 years and is hence generally not accounted for when building sea-level reconstructions. It may hence be useful to include this tide gauge data in the next generation of reconstructed sea-level products. In any case, maintaining the existing tide gauge network in the IO is crucial for better describing the low-frequency sea-level variations in this region. Apart from tide gauge records, reconstructed products also use gridded altimetry data that provides near-global high resolution which allows to accurately depict sea-level variations since 1992. This ~25 years data are,

however, not sufficient to provide an accurate description of the full range of decadal IO sea-level fluctuations. The strong influence of basis functions used to reconstruct basin-scale sea level from tide-gauges is illustrated by discrepancies between the different products provided by Meyssignac, which use the same technique and same tide gauge network but different basis spatial functions. Another twenty to thirty years of sea-level data may thus be required to provide a robust description of Indian Ocean decadal variations, as a minimum of fifty years of data is usually required to confidently isolate natural low-frequency climate variability from observational data.

Another way to improve reconstruction sea-level data would be to improve ocean reanalyses. The different reanalyses products analysed generally do not agree with the decadal sea-level variations depicted by reconstructed products. During the early period of the record, most of these variations are wind-driven since there are not many data to constrain the re-analyses. The realism of decadal sea-level variations in these products thus largely relies on the realism of the decadal wind variability. However, I have shown that decadal wind variations over the IO varies considerably depending on the wind product. Improving decadal sea-level variations in reanalyses would hence requires an improvement of the decadal wind data which is used to force the ocean models. Reanalysis sea-level products also assimilate a number of observed oceanic variables (including sea level, e.g. ORA-S4 use along-track sea level from altimeter since 1993). Hence, poor sampling of the IO may also result in unrealistic sea-level variability in reanalysis data. The vision proposed by the *Argo Steering Team* (Freelan et al. 2010, Riser et al. 2016) for an enhancement of world ocean monitoring by Argo, especially over turbulent oceanic regions (e.g. oceanic western boundaries) and climatically important regions (equatorial oceans where active air-sea coupling controls local as well as global climate variations) is promising in this context.

7.2.2 Improve understanding of IO decadal sea-level variability

Despite the large observational discrepancies in the IO, CMIP models and a few observational products suggest that the IO is home to two distinct modes of decadal sea-level variability (see chapter 6) that collectively explain more than 50% of the total decadal sea-level variance in the IO. This thesis provides some preliminary insights on the characteristics of these sea-level modes. An exhaustive description and understanding of these modes will require further analyses of both CMIP control simulations and observations.

The first mode (referred as “Indian Ocean Basin-Scale Mode - IOBSM”) is strongly related to wind variations related to the decadal Indian Ocean Dipole (IOD), which is partly modulated by the decadal climate variability in the tropical Pacific (ENSO and Modoki). It is, however, not the case in some models and further analyses are required to understand the climate variability driving the IOBSM unrelated to the IOD. It would be interesting, in particular, to compare simulations of a classical CMIP model historical run, with experiments that artificially suppress SST variations in other oceans. This would allow to describe

the part of the IO decadal sea level (and SST) variations which are intrinsic to the Indian Ocean.

The other mode of IO decadal sea-level variability depicted by CMIP models is largely independent of the Pacific decadal climate, and consists of a broad sea-level signature in the SWIO (hence named “Southwest IO Mode - SWIOM”), to the east of Madagascar. The preliminary assessments based on CMIP models suggest that the wind stress curl west of Australia is consistent with this SLA, but that heat flux can also contribute to SLA variations in the southern part of this pattern. Further study are hence needed to precisely quantify the respective contributions of these two processes in driving this variability. A way to quantify these contributions would be to run sensitivity experiments with decadal variability applied in only specific regions, as done in Trenary and Han (2013). Experiments using only decadal wind-stress variability and neglecting the freshwater and heat flux forcing decadal variations would also allow ascertaining the dominance of the dynamic forcing mechanism, over forcing by buoyancy fluxes. Finally, because of the large uncertainties in decadal and longer steric sea-level variations, it would be interesting to run a series of experiments forced with various existing forcing products. The analyses also suggest that the SWIOM is related to strong SLP fluctuations in the subtropical SIO, a pattern reminiscent of the typical SLP variations related to the Mascarene high. To ascertain this relationship, it is a must to calculate an index of the Mascarene high variability (by performing an EOF on the SLP in the subtropical IO as done in Moriaka et al. 2015) and investigate how much this index correlate with the time series of the decadal SWIOM. I will perform this analysis in a near future.

These two modes of IO decadal sea level identified in CMIP models are broadly consistent with those deduced from some observational datasets (e.g. the relatively short altimeter data or the longer ORAS4, M-ORA datasets). Sea-level reconstructions generally reproduce the IOBSM but do not capture the decadal sea-level variability east of Madagascar. As the Port Louis tide gauge may be considered as a reasonable index for the observed SWIOM variations, it could be interesting to try to relate these variations with decadal variations of neighbouring surface pressure measurements to further characterize this mode in observations.

7.2.3 Accounting for natural decadal variability in the estimation of mean sea-level change induced by climate change

Global mean sea-level has risen at a rate of 3.2 mm/yr during the last two decades (Masters et al. 2012). However, the sea-level rise is far from being uniform over the world oceans. For instance, the sea-level rise trends are much higher in the western tropical Pacific whereas sea level falls in some regions. This spatial heterogeneity in the sea-level trends has been shown to be intimately related to the natural decadal/multi-decadal variability in the Pacific (e.g. Hamilton et al. 2014). Mean sea-level changes in a given oceanic region are indeed embedded within natural low-frequency variability and the estimation of secular

trend will systematically be aliased by this natural variability. A better understanding of natural decadal sea-level variability and its driving mechanisms is crucial for the detection of secular sea-level change in any oceanic basin. One of the latest practices in sea-level research to separate natural low-frequency sea-level variability and anthropogenically induced long-term sea-level change is to use known climate indices (e.g. indices of ENSO, PDO, IOD, NPGO etc) as “explanatory variables” (e.g. Meyssignac et al. 2012a, McGregor et al. 2012, Merrifield et al. 2012, Zhang and Church 2012, Frankcombe et al. 2014, England et al. 2014). The IPO being the main mode of decadal variability in the Pacific Ocean, Zhang and Church (2012) removed the IPO related signals from the altimeter sea-level data before estimating the anthropogenic long-term sea-level trend in the Pacific. The trends derived from this method are very different from those directly derived from a simple linear regression in time (see fig. 2.24 in chapter 2).

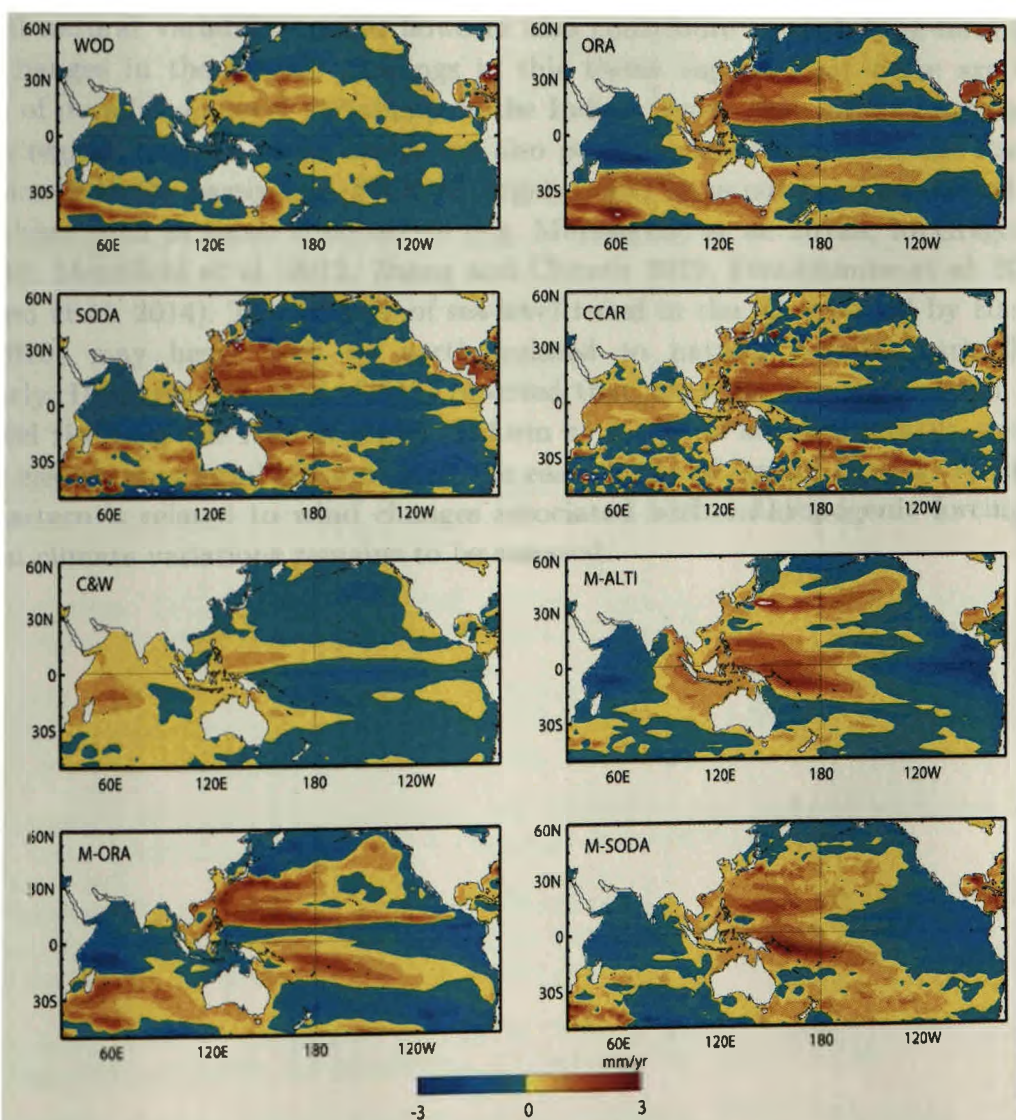


Fig. 7.1: Spatial map of sea-level trend from the eight different products discussed in Chapter 4 for the 1960-2010 period. Figure shows the regional sea-level trends as the global mean sea-level time series is removed from each grid point prior to trend estimation.

Fig. 0.1 shows the sea-level trends over the 1960-2010 period for each of the gridded product discussed in Chapter 4. The sea-level trend patterns derived from these products are nearly consistent in the Pacific. They all show to a certain extent an accelerated sea-level rise in the western tropical Pacific and a sea-level fall in the equatorial central/eastern Pacific. Because it is now well established that decadal ENSO (and to a certain extent decadal Modoki) largely drive the natural decadal sea-level variations in the Pacific, it would be interesting to investigate how much of these trends can be explained by natural decadal variations and how much of them can be explained by the trade wind variations induced by climate change over the last 50 years!

Except for CCAR and C&W datasets, Fig. 7.1 suggest that the IO is experiencing a sea-level fall northeast of Madagascar and over most of the AS. Han et al. (2010) attributed this pattern to surface wind changes in response to anthropogenically-driven ocean variability. Intrinsic modes of IO decadal/multi-decadal natural variability could however also contribute to such long-term sea-level changes in the SWIO. Findings in this thesis suggest that there are two modes of decadal sea-level variability in the Indian Ocean that influence sea-level in this region. Both of these modes are also partly independent from the Pacific influence (IOBSM partly and SWIOM largely), and have not been accounted for in analyses such as those cited above (e.g. Meyssignac et al. 2012a, McGregor et al. 2012, Merrifield et al. 2012, Zhang and Church 2012, Frankcombe et al. 2014, England et al. 2014). The pattern of sea-level trend in the IO reported by Han et al. (2010) may hence well be partly related to natural decadal variability. Similarly, Unnikrishnan et al. (2015) reported that, over the altimetry period, the sea-level rise over the NIO is rather uniform at a rate of about 3 mm/yr, except in the eastern equatorial IO and along the eastern rim of Bay of Bengal. Whether this pattern is related to wind changes associated with anthropogenic forcing or natural climate variations remains to be assessed.

Bibliography

Achuta Rao K. M., Sperber K. R. (2006). ENSO Simulation in Coupled Ocean-Atmosphere Models: Are the Current Models Better?. *Clim. Dyn.*, Vol. 27: 1-15.

Alexander MA (1990). Simulation of the response of the North Pacific Ocean to the anomalous atmospheric circulation associated with El Niño. *Clim. Dyn.*, 5:53-65.

Alexander MA, Blade I, Newman M, et al. (2002). The Atmospheric Bridge: The Influence of ENSO Teleconnections on Air-Sea Interaction over the Global Oceans. *J Climate* 15:2205-2231.

Alexander MA, Deser C (1995). A mechanism for the recurrence of wintertime midlatitude SST anomalies. *J. Phys. Oceanogr.*, 25, 122-137.

Alexander MA, Scott JD (2008). The Role of Ekman Ocean Heat Transport in the Northern Hemisphere Response to ENSO. *J. Climate*, 21, 5688-5707.

Alexander MA. (2010). Extratropical air-sea interaction, SST variability and the Pacific Decadal Oscillation. In *Climate Dynamics: Why Does Climate Vary?*, ed. D Sun, F Bryan. Washington, DC: *Am. Geophys. Union*.

Alory G, Delcroix T (2002). Interannual sea-level changes and associated mass transports in the tropical Pacific from TOPEX/Poseidon data and linear model results (1964-1999). *J Geophys Res* 107.

Alory GS, Wijffels and Meyers G (2007). Observed temperature trends in the Indian Ocean over 1960-1999 and associated mechanisms. *Geophys. Res. Lett.* 34 (2):L02606.

Anderson, D.L.T. and A.E. Gill (1975). Spin-up of a stratified ocean, with applications to upwelling, *Deep Sea Research.* 22, 583-596.

Annamalai, H., R. Murtugudde, J. Potemra, S. P. Xie, P. Liu, and B. Wang (2003). Coupled dynamics over the Indian Ocean: Spring initiation of the zonal mode, *Deep Sea Res.*, Part II, 50 (12-13), 2305-23.

Antonov JI, Levitus S and Boyer TP (2002). Steric sea-level variations during 1957-1994: Importance of salinity. *J. Geophys. Res.* 107(C12):8013.

Aparna, S. G., McCreary, J. P., Shankar, D. and Vinayachandran, P. N., Signatures of Indian Ocean Dipole and El Niño-Southern Oscillation events in sea level variations in the Bay of Bengal. *J. Geophys. Res. C*, 2012, 117, C10012, 13.

Ashok, K., S. K. Behera, S. A. Rao, H. Weng, and T. Yamagata, 2007 : El Niño Modoki and its possible teleconnection. *J. Geophys. Res.*, 112, C11007.

AVISO (1996) AVISO User Handbook: Merged TOPEX/Poseidon Products. Toulouse France.

Balmaseda, M. A., Mogensen, K., and Weaver, A. T. (2013). Evaluation of the ECMWF ocean reanalysis system ORAS4, *Q. J. Roy. Meteorol. Soc.*, 139, 1132-1161.

Barnett, T. P., D. W. Pierce, and R. Schnur (2001). Detection of anthropogenic climate change in the world's oceans, *Science*, 292, 270–273.

Barnett, T. P., D. W. Pierce, K. M. AchutaRao, P. J. Gleckler, B. D. Santer, J. M. Gregory, and W. M. Washington (2005). Penetration of human-induced warming into the world's oceans, *Science*, 309, 284–287.

Barnier B, Madec G, Penduff T, Molines JM, Treguier AM, Le Sommer J, Beckmann A, Biastoch A, Boning C, Dengg J, Derval C, Durand E, Gulev S, Remy E, Talandier C, Theetten S, Maltrud M, McClean J, De Cuevas B (2006). Impact of partial steps and momentum advection schemes in a global ocean circulation model at eddy permitting resolution. *Ocean Dynamics* 56:543-567.

Behera, S. K., and T. Yamagata, (2010). Imprint of the El Niño Modoki on decadal sea level changes. *Geophys. Res. Lett.*, 37, L23702.

Bindoff NL, Willebrand J, Artale V, Cazenave A, Gregory J, Gulev S, Hanawa K, Quere C, Levitus S, Nojiri Y, Shum C, Talley L and Unnikrishnan A (2007). Climate Change 2007: The Physical Science Basis. Contribution of Working Group I to the Fourth Assessment Report of the Intergovernmental Panel on Climate Change, chapter 5. Cambridge University press, Cambridge pp 385-432.

Biondi, F., A. Gershunov, and D. R. Cayan (2001). North Pacific decadal climate variability since 1661, *J. Clim.*, 14, 5–10.

Bjerknes J. (1969). Atmospheric teleconnections from the equatorial Pacific. *Mon. Weather Rev.* 97:163–72.

Blanke B and Delecluse P (1993). Variability of the tropical Atlantic ocean simulated by a general circulation model with two different mixed layer physics. *J. Phys. Oceanography*. 23:1363-1388.

Bouttes, N., J. M. Gregory, T. Kuhlbrodt, and R. S. Smith, (2014). The drivers of projected North Atlantic sea level change. *Climate Dyn.*, 43, 1531–1544.

Boyer, T. P., et al. (2009), World Ocean Database (2009). vol. 1, Introduction, NOAA Atlas NESDIS, vol. 66, edited by S. Levitus, 219 pp., NOAA, Silver Spring, Md.

Bretherton CS, Windmann M, Dymnikov VP, Wallace JM, Blade I (1999). The effective number of spatial degrees of freedom of a time-varying field. *J. Clim* 12:1990–2009.

Brodeau L, Barnier B, Treguier A, Penduff T and Gulev S (2010). An ERA40-based atmospheric forcing for global ocean circulation models. *Ocean Modell.* 31:88-104.

Bromirski, P. D., A. J. Miller, R. E. Flick, and G. Auad (2011). Dynamical suppression of sea level rise along the Pacific Coast of North America: Indications for imminent acceleration, *J. Geophys. Res.*, 116, C07005.

Cai W, Cowan T, Dix M, Rotstayn L, Ribbe J, Shi G and Wijffels G (2007). Anthropogenic aerosol forcing and the structure of temperature trends in the southern Indian Ocean. *Geophys. Res. Lett.* 34:L14611.

Cai W, Hendon HH and Meyers G (2005b). An Indian Ocean dipole in the CSIRO coupled climate model. *J. Clim.* 18:1449-1468.

Cai W, Meyers G and Shi G (2005a). Transmission of ENSO signal to the Indian Ocean. *Geophys. Res. Lett.* 32:L05616.

Cai W, Sullivan A and Cowan T (2008). Shoaling of the off-equatorial south Indian Ocean thermocline: Is it driven by anthropogenic forcing?. *Geophys. Res. Lett.* 35:L12711.

Cai, W., and T. Cowan, (2013). Why is the amplitude of the Indian Ocean dipole overly large in CMIP3 and CMIP5 climate models? *Geophys. Res. Lett.*, 40, 1200–1205.

Capotondi A, Wittenberg AT, Newman M, Di Lorenzo E, Yu J-Y, Braconnot P, Cole J, Dewitte B, Giese B, Guilyardi E, Jin FF, Karnauskas K, Kirtman B, Lee T, Schneider N, Xue Y, Yeh SW. (2015). Understanding ENSO diversity. *Bull. Am. Meteorol. Soc.* 96(6): 921–938.

Carson M., Cohl A., Stammer D. (2015). The impact of regional multi-decadal and century-scale internal climate variability on sea level trends in CMIP5 models. *Journal of Climate.*

Carton JA, Giese BS, Grodsky SA (2005). Sea level rise and the warming of the oceans in the Simple Ocean Data Assimilation (SODA) ocean reanalysis. *J. Geophys. Res.* 110:C09006.

Carton, J., Giese, B., (2008). A reanalysis of ocean climate using Simple Ocean Data Assimilation (SODA). *Monthly Weather Rev.* 136, 2999–3017.

Cazenave A and Nerem RS (2004). Present-day sea level change: observations and causes. *Rev. Geophys.* 42:RG3001.

Chambers D, Merrifield M, Nerem R (2012). Is there a 60-year oscillation in global mean sea level? *Geophys Res Lett* 39:L18607 (6 pp).

Chelton DB, and Schlax MG (1996). Global observations of oceanic Rossby waves. *Science* 272: 234-238.

Chelton, D. B., R. A. deSzoeki, M. G. Schlax, K. El Naggar and N. Siwertz, (1998). Geographical variability of the first-baroclinic Rossby radius of deformation. *J. Phys. Oceanogr.*, 28, 433-460.

Chen D, Zebiak SE, Busalacchi AJ, Cane MA (1995). An improved procedure for El Niño forecasting. *Science* 269:1699–1702.

Cheng X, Qi Y, Zhou W (2008). Trends of sea level variations in the Indo-Pacific warm pool. *Global and Planetary Change*, 63:57-66.

Church JA, Godfrey JS, Jackett D R, and McDougall TJ (1991). A model of sea level rise caused by ocean thermal expansion. *J. Clim.* 4:438-444.

Church, J. A., and N. J. White, (2011). Sea-level rise from the late 19th to the early 21st century. *Surv. Geophys.*, 32, 585–602.

Church, J.A., P.U. Clark, A. Cazenave, J.M. Gregory, S. Jevrejeva, A. Levermann, M.A. Merrifield, G.A. Milne, R.S. Nerem, P.D. Nunn, A.J. Payne, W.T. Pfeffer, D. Stammer and A.S. Unnikrishnan, (2013). Sea Level Change. In: Climate Change 2013: The Physical Science Basis. Contribution of Working Group I to the Fifth Assessment Report of the Intergovernmental Panel on Climate Change [Stocker, T.F., D. Qin, G.-K. Plattner, M. Tignor, S.K. Allen, J. Boschung, A. Nauels, Y. Xia, V. Bex and P.M. Midgley (eds.)]. Cambridge University Press, Cambridge, United Kingdom and New York, NY, USA.

Clarke AJ (1991). On the reflection and transmission of low-frequency energy at the irregular western Pacific Ocean boundary. *J. Geophys. Res.* 96:3289-3305.

Clarke AJ and Liu X (1993). Observations and dynamics of semi-annual and annual sea levels. *Journal of Physical Oceanography* 23:386-399.

Clarke AJ, Liu X (1994). Interannual sea level in the northern and eastern Indian Ocean. *J. Geophys. Res.* 99:1224-1235.

Clarke, A.J., van Gorder, S., Colantuono, G., (2007). Wind stress curl and ENSO discharge/recharge in the equatorial Pacific. *Journal of Physical Oceanography*. 37 (4), 1077.

Cleveland RB, Cleveland WS, McRae JE and Terpenning I (1990). STL: A Seasonal-Trend Decomposition Procedure Based on Loess. *Journal of Official Statistics* 6:3-73.

Cobb KM, Charles CD (2001). A central tropical Pacific coral demonstrates Pacific, Indian, and Atlantic decadal climate connections. *Geophysical Research letters*, VOL. 28, No. 11, 2209-2212

Cole, J. E., R. B. Dunbar, T. R. McClanahan, and N. A. Muthiga, (2000). Tropical Pacific forcing of decadal SST variability in the western Indian Ocean over the past two centuries. *Science*, 287, 617-619.

Compo GP and co-authors (2011). The Twentieth Century Reanalysis Project. *Quarterly J. Roy. Meteorol. Soc.* 137:1-28.

Cravatte S, G. Madec, T. Izumo, C. Menkes, and A. Bozec (2007). Progress in the 3-D circulation of the eastern equatorial Pacific in a climate ocean model. *Ocean modelling*. 17:28-48.

Cravatte S, Picaut J and Eldin G (2003). Second and first Kelvin modes in the equatorial Pacific at intraseasonal timescales. *J. Geophys. Res.* 108:

Cravatte, S., T. Delcroix, D. Zhang, M. McPhaden, and J. Leloup, (2009). Observed freshening and warming of the western Pacific Warm Pool. *Climate Dyn.*, 33, 565-589.

Crueger T, Zinke J, Pfeiffer M (2008). Patterns of Pacific decadal variability recorded by Indian Ocean corals. *Int J Earth Sci (Geol Rundsch)* 98:41-52. doi: 10.1007/s00531-008-0324-1

Deser C, Alexander MA, Timlin MS (2003). Understanding the Persistence of Sea Surface Temperature Anomalies in Midlatitudes. *J. Climate*, 16, 57-72.

Deser C, Blackmon ML (1995). On the relationship between tropical and North Pacific sea surface temperature variations. *J. Climate*, 8,1677-1680.

Deser C, Phillips AS, Hurrell JW. (2004). Pacific interdecadal climate variability: linkages between the tropics and the North Pacific during boreal winter since 1900. *J. Climate* 17:3109-24.

Deser C, Phillips AS, Tomas RA, et al (2012). ENSO and Pacific Decadal Variability in the Community Climate System Model Version 4. *J Climate* 25:2622-2651.

Deser C, Wallace JM. (1990). Large-scale atmospheric circulation features of warm and cold episodes in the tropical Pacific. *J. Climate* 3:1254-81.

Deser et al. (2010). Sea surface temperature variability: Patterns and mechanisms. *Annu. Rev. Mar. Sci.* 2:115-43.

Di Lorenzo, E., et al. (2008). North Pacific Gyre Oscillation links ocean climate and ecosystem change, *Geophys. Res. Lett.*, 35, L08607.

Di Lorenzo, E., K. M. Cobb, J. C. Furtado, N. Schneider, B. T. Anderson, A. Bracco, M. A. Alexander and D. J. Vimont, (2010). Central Pacific El Niño and decadal climate change in the North Pacific Ocean. *Nature Geoscience*, 3(11) 762-765.

Dong et al. (2016). The footprint of the Inter-decadal Pacific Oscillation in Indian Ocean sea surface temperatures. *Nature (Scientific Reports)*, 6, 21251.

Douglas et al. (2001). Sea Level Rise : History and Consequences. (Academic press) IGS; volume 75.

Durand F, Shankar D, Birol F, and Shenoi SSC (2009). Spatio-temporal structure of the East India Coastal Current from satellite altimetry. *J. Geophys. Res.* 114:C02013.

Easterling DR, Wehner MF (2009). Is the climate warming or cooling? *Geophys Res Lett* 36:L08706.

England MH, Huang F (2005). On the interannual variability of the Indonesian Throughflow and its linkage with ENSO. *J Climate* 18:1435–1444.

England MH, McGregor S, Spence P, et al (2014). Recent intensification of wind-driven circulation in the Pacific and the ongoing warming hiatus. *Nature Climate change* 4:222–227.

Feng M, Biastoch A, Boning C, Caputi N and Meyers G (2008). Seasonal and interannual variations of upper ocean heat balance off the west coast of Australia. *J. Geophys. Res.* 113: C12025.

Feng M, Li Y and Meyers G (2004). Multi-decadal variations of Fremantle sea level: Footprint of climate variability in the tropical Pacific. *Geophys. Res. Lett.* 31:L16302.

Feng M, McPhaden M J and Lee T (2010). Decadal variability of the Pacific subtropical cells and their influence on the southeast Indian Ocean. *Geophys. Res. Lett.* 37:L09606.

Feng M, Meyers G and Wijffels S (2001). Interannual upper ocean variability in the tropical Indian Ocean. *Geophys. Res. Lett.* 28:4151– 4154.

Feng M, Meyers G, Pearce A and Wijffels S (2003). Annual and interannual variations of the Leeuwin Current at 32S. *J. Geophys. Res.* 108(C11):3355

Feng M, Wijffels S, Godfrey S and Meyers G. (2005). Do eddies play a role in the momentum balance of the Leeuwin Current?, *Journal of Physical Oceanography* 35:964-975.

Folland CK (2002). Relative influences of the Interdecadal Pacific Oscillation and ENSO on the South Pacific Convergence Zone. *Geophys Res Lett* 29:1643.

Frankcombe, L.M. and Dijkstra, H.A., (2009). Coherent multidecadal variability in North Atlantic sea level. *Geophysical Research Letters*, 36, L15604.

Frankcombe, L.M., McGregor, S. & England, M.H. (2015). Robustness of the Modes of Indo-Pacific Sea-level variability. *Clim Dyn* (2015) 45: 1281.

Frankignoul, C., and K. Hasselmann (1977). Stochastic climate models. Part 2. Application to sea-surface temperature variability and thermocline variability, *Tellus*, 29, 284–305.

Freeland, H. et al. (2010). Argo-a decade of progress. In *Proc. Ocean Obs'09* Vol. 2, WPP-306 10.5270/OceanObs09.cwp.32 (ESA, 2010).

- Fukumori, I., R. Raghunath, and L.-L. Fu (1998). Nature of global large-scale sea level variability in relation to atmospheric forcing: A modeling study, *J. Geophys. Res.*, 103(C3), 5493–5512.
- Furtado JC, Di Lorenzo E, Schneider N (2011). North Pacific Decadal Variability and Climate Change in the IPCC AR4 Models. *J Climate* 24:3049–3067.
- Gadgil S, Joseph PV, Joshi NV. (1984). Ocean-atmosphere coupling over monsoon regions. *Nature* 312:141–43.
- Garreaud R, Battisti DS (1999). Interannual (ENSO) and Interdecadal (ENSO-like) Variability in the Southern Hemisphere Tropospheric Circulation*. *J Climate* 12:2113–2123.
- Gedalof, Z., N. J. Mantua, and D. L. Peterson (2002). A multicentury perspective of variability in the Pacific Decadal Oscillation: New insights from tree rings and coral, *Geophys. Res. Lett.*, 29(24), 2204.
- Gill, A. E. (1980). Some simple solutions for heat-induced tropical circulation, *Q. J. Roy. Meteor. Soc.*, 106, 447–462.
- Graham F., Brown G., Wittenberg A., Holbrook N., (2015). Reassessing conceptual models of ENSO. *J. of Climate*, DOI: <http://dx.doi.org/10.1175/JCLI-D-14-00812.1>.
- Graham NE, Barnett TP. (1987). Sea surface temperature, surface wind divergence, and convection over tropical oceans. *Science* 238:657–59.
- Graham, N. E., et al. (1994). On the roles of tropical and midlatitude SSTs in forcing interannual to interdecadal variability in the winter Northern Hemisphere circulation, *J. Clim.*, 7, 1416–1441.
- Greatbatch RJ (1994). A note on the representation of steric sea level in models that conserve volume rather than mass. *J. Geophys. Res.* 99:12,767–12,771.
- Gregory JM (1993). Sea level changes under increasing atmospheric CO₂ in a transient coupled ocean-atmosphere GCM experiment. *J. Clim.* 6(12):2247–2262.
- Gregory, J. M., H. T. Banks, P. A. Stott, J. A. Lowe, and M. D. Palmer, (2004). Simulated and observed decadal variability in ocean heat content. *Geophys. Res. Lett.*, 31, L15312.
- Grove CA, Zinke J, Peeters F, et al (2013). Madagascar corals reveal a multi-decadal signature of rainfall and river runoff since 1708. *Clim Past* 9:641–656.
- Guemas V, Doblas Reyes FJ, Lienert F, et al (2012). Identifying the causes of the poor decadal climate prediction skill over the North Pacific. *J Geophys Res.* doi: 10.1029/2012JD018004
- Hamlington B D, Leben R R, Nerem R S, Han W, Kim K-Y. (2011). Reconstruction sea level using cyclostationary empirical orthogonal functions. *J. Geophys. Res.*, 116: C12015.
- Hamlington B D, Leben R R, Strassburg M W, Nerem R S, Kim K-Y. (2013). Contribution of the Pacific Decadal Oscillation to global mean sea level trends. *Geophys. Res. Lett.*, 40: 5 171–5 175.
- Hamlington, B. D., M. W. Strassburg, R. R. Leben, W. Han, R. S. Nerem, and K.-Y. Kim (2014). Uncovering an anthropogenic sea-level rise signal in the Pacific Ocean, *Nat. Clim. Change*, 4, 782–785.

- Hamlington, B.D., Leben, R., Nerem, S., Han, W., Kim, K.Y., (2011). Reconstructing sea level using cyclostationary empirical orthogonal functions. *J. Geophys. Res.* 116, C12015.
- Han W (2005). Origins and dynamics of the 90-day and 30–60-day variations in the equatorial Indian Ocean. *J. Phys. Oceanogr.* 35:708-728.
- Han W, Lawrence DM, and Webster PJ (2001). Dynamical response of equatorial Indian Ocean to intra-seasonal winds: Zonal flow. *Geophys. Res. Lett.* 28:4215–4218.
- Han W, Meehl GA, Rajagopalan B, Fasullo JT, Hu A, Lin J, Large WG, Wang J, Quan XW, Trenary LL, Wallcraft A, Shinoda T, Yeager S (2010). Patterns of Indian Ocean sea level change in a warming climate. *Nature Geoscience* 3:546–550.
- Han W, Vialard J, McPhaden MJ, et al (2014). Indian Ocean Decadal Variability: A Review. *Bull. Amer. Meteor. Soc.*, 95, 1679–1703.
- Harrison DE and Larkin NK (1998). El Niño-Southern Oscillation sea surface temperature and wind anomalies 1946-1993. *Rev. Geophys.* 36(3):353–399.
- Holgate, S. J. (2007). On the decadal rates of sea level change during the twentieth century, *Geophys. Res. Lett.*, 34, L01602.
- Horii T, Ueki I, Ando K, Mizuno K (2013). Eastern Indian Ocean warming associated with the negative Indian Ocean dipole: a case study of the 2010 event. *J Geophys Res Oceans* 118:536–549.
- Houston, J. R. & Dean, R. G., (2013). Effects of sea-level decadal variability on acceleration and trend difference. *J. Coastal Res.* 29, 1062–1072.
- Hu, A., and C. Deser, (2013). Uncertainty in future regional sea level rise due to internal climate variability. *Geophys. Res. Lett.*, 40, 2768–2772.
- IPCC, 2013: Summary for Policymakers. In: Climate Change (2013). The Physical Science Basis. Contribution of Working Group I to the Fifth Assessment Report of the Intergovernmental Panel on Climate Change, Stocker, T.F., D. Qin, G.-K. Plattner, M. Tignor, S.K. Allen, J. Boschung, A. Nauels, Y. Xia, V. Bex and P.M. Midgley (eds.)). Cambridge University Press, Cambridge, United Kingdom and New York, NY, USA.
- Ishii, M., and M. Kimoto, (2009). Reevaluation of historical ocean heat content variations with time-varying XBT and MBT depth bias corrections. *J. Oceanogr.*, 65, 287–299.
- Izumo T, Lengaigne M, Vialard J, et al (2013). Influence of Indian Ocean Dipole and Pacific recharge on following year's El Niño: interdecadal robustness. *Clim Dyn* 42:291–310.
- Izumo, T., Vialard, J., Dayan, H. et al. (2016). A simple estimation of Equatorial Pacific response from windstress to untangle Indian Ocean Dipole and basin influences on El Niño. *Clim Dyn* 46: 2247.
- Jackett DR and McDougall TJ (1995). Minimal adjustment of hydrographic profiles to achieve static stability. *J. Atmos. Ocean. Technol.* 12(4):381-389.
- Jacobs, G. A., H. E. Hurlburt, J. C. Kindle, E. J. Metzger, J. L. Mitchell, and A. J. Wallcraft (1994). Decade-scale trans-Pacific propagation and warming effects of an El Niño anomaly, *Nature*, 370, 360–363.

Jevrejeva, S., A. Grinsted, and J. C. Moore, (2009). Anthropogenic forcing dominates sea level rise since 1850. *Geophys. Res. Lett.*, 36, L20706

Jin FF (1997). An equatorial ocean recharge paradigm for ENSO. Part I: conceptual model. *J. Atmosph. Sci.* 54:811-829.

Jin, F.-F. (1997b). An equatorial recharge paradigm for ENSO. II: A stripped-down coupled model, *J. Atmos. Sci.*, 54, 830–8847.

Jourdain N, M. Lengaigne, J. Vialard, T. Izumo, A. Sen Gupta, (2016). Delayed IOD-ENSO relationship in the observations and CMIP5 models : physical mechanisms and statistical artefacts, *Journal of Climate*, 29, 637-658.

Jourdain NC, Lengaigne M, Vialard J, et al (2015). Further insights on the influence of the Indian Ocean Dipole on the following year's ENSO from observations and CMIP5 models.

Jourdain, N. C., A. Sen Gupta, A. S. Taschetto, C. C. Ummenhofer, A. F. Moise, and K. Ashok, (2013). The Indo-Australian monsoon and its relationship to ENSO and IOD in reanalysis data and the CMIP3/CMIP5 simulations. *Climate Dyn.*, 41, 3073–3102.

Kalnay E and co-authors (1996). The NCEP/NCAR 40-Year Reanalysis Project. *Bulletin of the American Meteorological Society* 77(3): 437–471.

Kao, H.-Y. & Yu, J.-Y. (2009). Contrasting eastern Pacific and central-Pacific types of ENSO. *J. Clim.* 22, 615–632.

Kaplan A, Cane MA, Kushnir Y, Clement AC (1998). Analyses of global sea surface temperature 1856-1991. *J. Geophys. Res.*, 103, 18 567–18 589.

Kashino Y, Espana N, Syamsudin F, Richards KJ, Jensen T, Dutrieux P and Ishida A (2009). Observations of the north equatorial current, Mindanao current and the Kuroshio current system during the 2006/07 El Niño and 2007/08 La Nina. *J. Oceanogr.* 65:325–333.

Keerthi MG, Lengaigne M, Vialard J, Montegut CB, Muraleedharan PM (2013). Interannual variability of the tropical Indian Ocean mixed layer depth. *Clim Dyn.* 40-3, pp 743–759.

Klein SA, Soden BJ, Lao NC (1999). Remote sea surface temperature variations during ENSO: Evidence for a tropical atmospheric bridge. *J. Climate*, 12, 917–932, doi:10.1175/1520-0442(1999)0122.0.CO;2

Knapp KR, Kruk MC, Levinson DH, Diamond HJ, Neumann CJ (2010). The International Best Track Archive for Climate Stewardship (IBTrACS): Unifying tropical cyclone best track data. *Bull. Amer. Meteorol. Soc.* 91:363–376.

Köhl, A., and D. Stammer, (2008) Decadal sea level changes in the 50-year GECCO ocean synthesis. *J. Climate*, 21, 1876–1890.

Kosaka Y, Xie SP (2013). Recent global-warming hiatus tied to equatorial Pacific surface cooling. *Nature* 501, 403–407

Krishnan R, Sugi M (2003). Pacific decadal oscillation and variability of the Indian summer monsoon rainfall. *Clim Dyn* 21:233–242.

Kug, J.-S., Jin, F.-F. & An, S.-I. (2009). Two Types of El Niño Events: Cold Tongue El Niño and Warm Pool El Niño *J. Clim.* 22, 1499–1515.

Kwon M, Yeh S-W, Park Y-G, Lee Y-K (2012). Changes in the linear relationship of ENSO-PDO under the global warming. *Int J Climatol* 33:1121–1128.

Landerer FW, Jungclaus JH and Marotzke J (2008). El Niño–Southern Oscillation signals in sea level, surface mass redistribution, and degree-two geoid coefficients. *J. Geophys. Res.* 113: C08014.

Latif, M., and T. P. Barnett (1994). Causes of decadal climate variability over the North Pacific and North America, *Science*, 266, 634–637.

Lau NC, Nath MJ (1994). A modelling study of the relative roles of tropical and extra-tropical SST anomalies in the variability of the global atmosphere-ocean system. *J. Climate*, 7, 1184-1207

Lau NC, Nath MJ (1996). The Role of the “Atmospheric Bridge” in Linking Tropical Pacific ENSO Events to Extratropical SST Anomalies. *J. Climate*, 9, 2036–2057.

Lau NC, Nath MJ (2000). Impact of ENSO on the variability of the Asian-Australian monsoons as simulated in GCM experiments. *J Climate* 13:4287–4309.

Lee S-K, Park W, Baringer MO, et al (2015). Pacific origin of the abrupt increase in Indian Ocean heat content during the warming hiatus. *Nature Geoscience* 8:445–449. doi: 10.1038/ngeo2438.

Lee T (2004). Decadal weakening of the shallow overturning circulation in the South Indian Ocean. *Geophys. Res. Lett.* 31:L18305.

Lee T and McPhaden MJ (2008). Decadal phase change in large-scale sea level and winds in the Indo-Pacific region at the end of the 20th century. *Geophys. Res. Lett.* 35:L01605.

Leith, C. E., (1973). The standard error of time-averaged estimates of climatic means. *J. Appl. Meteor.*, 12, 1066–1069.

Leloup, J., M. Lengaigne, and JP. Boulanger, (2008). Twentieth century ENSO characteristics in the IPCC database. *Clim. Dyn.*, 30, 277–291.

Lengaigne M and Vecchi GA (2009). Contrasting the termination of moderate and extreme El Niño events in Coupled General Circulation Models. *Clim. Dyn.* 35:299-313.

Lengaigne M, Boulanger JP, Menkes C, Spencer H (2006). Influence of the seasonal cycle on the termination of El Niño events in a coupled general circulation model. *J Clim* 19:1850–1868.

Lengaigne M, Haussman U, Madec G, Menkes C and Vialard J and Molines JM (2012). Mechanisms controlling warm water volume interannual variations in the equatorial Pacific: Diabatic versus adiabatic processes. *Clim. Dyn.* 38:1031-1046.

Lengaigne M, Madec G, Menkes C and Alory G (2003). Impact of isopycnal mixing on the tropical ocean circulation. *J. Geophys. Res.* 108(C11):0148-0227.

Levitus S, Antonov AJI, Boyer TP and Stephens C (2000). Warming of the world ocean. *Science* 287:2225–2229.

Levitus S, Boyer TP, Conkright ME, O'Brien T, Antonov J, Stephens C, Stathopoulos L, Johnson D, Gelfeld R (1998). NOAA Atlas NESDIS 18 and World Ocean Database. U.S. Gov. Printing Office Washington DC vol:1.

Levitus, S., et al. (2012). World ocean heat content and thermosteric sea level change (0–2000 m), 1955–2010, *Geophys. Res. Lett.*, 39, L10603.

Levitus, S., J. Antonov, and T. Boyer (2005a). Warming of the world ocean, 1955–2003, *Geophys. Res. Lett.*, 32, L02604.

Li, Y., and W. Han (2015). Decadal sea level variations in the Indian Ocean investigated with HYCOM: Roles of climate modes, ocean internal variability, and stochastic wind forcing, *J. Clim.*, 28, 9143–9165.

Lienert F, Fyfe JC, Merryfield WJ (2011). Do Climate Models Capture the Tropical Influences on North Pacific Sea Surface Temperature Variability? *J Climate* 24:6203–6209.

Lighthill, M. J. (1969). Dynamic response of the Indian Ocean to the onset of the southwest monsoon. *Philosophical Transactions of the Royal Meteorological Society, A*, A265, 45–92.

Liu Z (2012). Dynamics of Interdecadal Climate Variability: A Historical Perspective*. *J Climate* 25:1963–1995.

Llovel W, Guinehut S, Cazenave A (2010b). Regional and interannual variability in sea level over 2002–2009 based on satellite altimetry, Argo float data and GRACE ocean mass. *Ocean Dyn.* 60: 1193–1204.

Madec G (2008). "NEMO ocean engine". Note du Pole de modélisation, Institut Pierre-Simon Laplace (IPSL), France, No 27:1288-1619.

Mantua NJ, Hare SR, Zhang Y, et al (1997). A Pacific Interdecadal Climate Oscillation with Impacts on Salmon Production. *Bull. Amer. Meteor. Soc.*, 78, 1069–1079.

Mark A. Merrifield, Philip R. Thompson, Mark Lander. (2012). Multidecadal sea level anomalies and trends in the western tropical Pacific. *Geophysical Research Letters* 39:13.

Masters, D., R. S. Nerem, R.S., Choe, C., Leuliette, E., Beckley, B., White, N. and Ablain, M., (2012). Comparison of global mean sea level time series from TOPEX/Poseidon, Jason-1 and Jason-2. *Marine Geodesy*, 35, 20–41.

Masumoto Y and Meyers G (1998). Forced Rossby waves in the southern tropical Indian Ocean. *J. Geophys. Res.*, 103:27,589–27,602.

Matsuno, T. (1966). Quasi-geostrophic motions in the equatorial area, *J. Meteorol. Soc. Japan*, 44, 25–43.

McCreary JP, Han W, Shankar D and Shetye SR (1996b). Dynamics of the east India coastal current 2. Numerical solutions. *J. Geophys. Res.* 101:13993–14010.

McCreary JP, Kundu PK, and Molinari RL (1993). A numerical investigation of dynamics, thermodynamics and mixed layer processes in the Indian Ocean. *Prog. Oceanogr.* 31:181–244.

McCreary JP, Miyama T, Furue R, Jensen T, Kang H-W, Bang B, Qu T (2007). Interactions between the Indonesian Throughflow and circulations in the Indian and Pacific Oceans. *Prog Oceanogr* 75(1):70–114.

McCreary, J. P. (1981). A linear stratified ocean model of the coastal undercurrent. *Philosophical Transactions of the Royal Society of London*, 298, 603–635.

McCreary, J.P., (1983). A model of tropical ocean-atmosphere interaction, *Mon. Weather Rev.*, 111, 370-387.

McCreary, J.P., Modelling wind-driven ocean circulation, (1980). Tech. Rep. HIG-80-3, 64 pp., Hawaii Inst. of Geophys., Honolulu.

McPhaden MJ (1999). Genesis and evolution of the 1997–1998 El Niño. *Science* 283:950–954.

McPhaden MJ and Zhang D (2004). Pacific Ocean circulation rebounds. *Geophysical Research Letters* 31(18):0094-8276.

McPhaden MJ, and Zhang DX (2002). Slowdown of the meridional overturning circulation in the upper Pacific Ocean. *Nature* 415:603– 608.

McPhaden MJ, Zebiak SE, Glantz MH (2006). ENSO as an integrating concept in earth science. *Science* 314:1740.

McPhaden, M. J., and J. Picaut, (1990). El Niño-Southern Oscillation displacement of the western equatorial Pacific warm pool, *Science*, 250, 1385-1388.

Meehl GA and co-authors (2009). Decadal prediction: Can it be skillful?. *Bull. Am. Meteorol. Soc.* 90:1467–1485.

Meehl GA, Aixue H and Benjamin DS (2009). The Mid-1970s Climate Shift in the Pacific and the relative roles of forced versus Inherent decadal variability. *J. Clim.* 22(3):780.

Meehl GA, Arblaster JM, Fasullo JT, et al (2011). Model-based evidence of deep-ocean heat uptake during surface-temperature hiatus periods. *Nature Climate change* 1:360–364. doi: 10.1038/nclimate1229.

Meehl GA, Covey C, Delworth T, Latif M, McAvaney B, Mitchell JFB, Stouffer RJ and Taylor KE (2007). The WCRP CMIP3 multi-model dataset: a new era in climate change research. *Bull. Am. Meteorol. Soc.* 88(9):1383-1394

Meehl GA, Goddard L, Boer G, et al (2014) Decadal Climate Prediction: An Update from the Trenches. *Bull. Amer. Meteor. Soc.*, 95:243–267.

Meehl, G. A., et al., (2007): Global climate projections. In: *Climate Change 2007: The Physical Science Basis. Contribution of Working Group I to the Fourth Assessment Report of the Intergovernmental Panel on Climate Change* [Solomon, S., D. Qin, M. Manning, Z. Chen, M. Marquis, K. B. Averyt, M. Tignor and H. L. Miller (eds.)]. Cambridge University Press, Cambridge, United Kingdom and New York, NY, USA, pp. 755–828.

Meinen CS and McPhaden MJ (2000). Observations of warm water volume changes in the equatorial Pacific and their relationship to El Niño and La Niña. *J. Clim.* 13:3551-3559.

Merrifield, M., (2011). A shift in western tropical Pacific sea level trends during the 1990s. *J. Climate*, 24, 4126–4138.

Meyers G (1996). Variation of the Indonesian throughflow and the El Niño Southern Oscillation. *J. Geophys. Res.* 101:12,255–12,263.

Meyers, G., (1979). On the annual Rossby wave in the tropical North Pacific Ocean. *J. Phys. Oceanogr.*, 9, 663–674.

Meyssignac B., Becker M., Llovel W., Cazenave A. (2012). An assessment of two-dimensional past sea level reconstructions over 1950-2009 based on tide gauge data and different input sea level grids. *Survey in Geophysics*, 33, 5:945-972.

Meyssignac, B., D. Salas y Melia, M. Becker, W. Llovel, and A. Cazenave, (2012). Tropical Pacific spatial trend patterns in observed sea level: Internal variability and/or anthropogenic signature? *Climate Past*, 8, 787-802.

Millero FJ and Poisson A (1981). International one-atmosphere equation of state of seawater. *Deep-Sea Res.* 28:625-629.

Minobe S. (1999). Resonance in bidecadal and pentadecadal climate oscillations over the North Pacific: role in climatic regime shifts. *Geophys. Res. Lett.* 26:855-58.

Mitas CM and Clement A (2005). Has the Hadley cell been strengthening in recent decades? *Geophys. Res. Lett.* 32: L03809.

Monselesan, D. P., T. J. O'Kane, J. S. Risbey, and J. A. Church, (2015). Internal climate memory in observations and models. *Geophys. Res. Lett.*, 42, 1232-1242.

Moon, J.-H., Y. T. Song, P. D. Bromirski, and A. J. Miller (2013). Multi-decadal regional sea level shifts in the Pacific over 1958-2008, *J. Geophys. Res. Oceans*, 118, 7024-7035.

Morioka, Y., T. Tozuka, and T. Yamagata, (2013). How is the Indian Ocean subtropical dipole excited? *Climate Dyn.*, 41, 1955-1968.

Murtugudde, R., McCreary, J. P., & Busalacchi, A. J. (2000). Oceanic processes associated with anomalous events in the Indian Ocean with relevance to 1997-1998. *Journal of Geophysical Research*, 105, 3295-3306.

Namias J, Born RM (1974). Further studies of temporal coherence in North Pacific Sea surface temperatures. *Journal of Geophysical Research: Oceans* (1978-2012) 79:797-798.

Neelin, D (1991). The Slow Sea Surface Temperature Mode and the Fast-Wave Limit: Analytic Theory for Tropical Interannual Oscillations and Experiments in an Hybrid Coupled Model. *J. Atm. Sci.*, 48, 584-606.

Neelin, J. D., Battisti, D. S., Hirst, A. C., Jin, F.-F., Wakata, Y., Yamagata, T., and Zebiak, S. E. (1998). ENSO Theory, *J. Geophys. Res.*, 103, 14 261-14 290.

Newman M (2007). Interannual to Decadal Predictability of Tropical and North Pacific Sea Surface Temperatures. *J Climate* 20:2333-2356.

Newman M (2013). An Empirical Benchmark for Decadal Forecasts of Global Surface Temperature Anomalies. *J Climate* 26:5260-5269.

Newman M, Compo GP, Alexander MA (2003). ENSO-forced variability of the Pacific decadal oscillation. *J Climate*, vol. 16, No. 23.

Newman, M., M. Alexander, T. R. Ault, K. M. Cobb, C. Deser, E. Di Lorenzo, and e. al. (2016). The Pacific decadal oscillation, revisited, *J. Clim.*, in press.

Nidheesh, A. G., M. Lengaigne, J. Vialard, A. S. Unnikrishnan, and H. Dayan, (2013). Decadal and long-term sea level variability in the tropical Indo-Pacific Ocean. *Climate Dyn.*, 41, 381-402.

Ohba M, Ueda H (2007). An impact of SST anomalies in the Indian Ocean in acceleration of the El Niño to La Niña transition. *Journal of Meteorological Society of Japan*, Vol 85, No.3, pp. 335-348.

Ohba, M., and H. Ueda, (2006). A role of zonal gradient of SST between the Indian Ocean and the western Pacific in localized convection around the Philippines. *SOLA*, 2, 176–179.

Oliver ECJ and Thompson KR (2010). Madden-Julian Oscillation and sea level: Local and remote forcing. *J. Geophys. Res.* 115:C01003.

Oshima K, Tanimoto Y (2009). An Evaluation of Reproducibility of the Pacific Decadal Oscillation in the CMIP3 Simulations. *JMSJ* 87:755–770.

Park J-H, An SI, Yeh S-W, Schneider N (2013). Quantitative assessment of the climate components driving the pacific decadal oscillation in climate models. *Theor Appl Climatol* 112:431–445.

Pattullo J, Munk W, Revelle R and Strong E (1955). The seasonal oscillation in sea level. *J. Mar. Res.* 14:88–156.

Paulson CA and Simpson JJ (1977). Irradiance measurements in the upper ocean. *J. Phys. Oceanogr.* 7:952-956.

Philander SGH. (1990). *El Niño, La Nina, and the Southern Oscillation*. San Diego, CA: Academic.293 pp.

Philander, S. et al. (1996). Why the ITCZ is mostly north of the equator. *J. Clim.* 9, 2958–2972.

Pierce DW, Barnett TP, Latif M (2000). Connections between the Pacific Ocean Tropics and Midlatitudes on Decadal Timescales. *J Climate* 13:1173–1194.

Pierce, D. W. (2001). Distinguishing coupled ocean-atmosphere interactions from background noise in the North Pacific, *Prog. Oceanogr.*, 49, 331–352.

Potemra JT (2001). Contribution of equatorial Pacific winds to southern tropical Indian Ocean Rossby waves. *J. Geophys. Res.* 106:2407–2422.

Potemra JT, Hautala SL, Sprintall J and Pandoe W (2002). Interaction between the Indonesian seas and the Indian Ocean in observations and numerical models. *J. Phys. Oceanogr.* 32:1838–1854.

Power S, Tseitkin F, Mehta V, Lavery B (1999). Decadal climate variability in Australia during the twentieth century. *Int. Jour. of Climatology* vol. 19, 2, 169-184.

Qiu B and Chen S (2006). Decadal variability in the large-scale sea surface height field of the south Pacific Ocean: Observations and causes. *J. Phys. Oceanogr.* 36:1751-1762

Qiu B, Schneider N, Chen S (2007). Coupled Decadal Variability in the North Pacific: An Observationally Constrained Idealized Model*. *J Climate* 20:3602–3620.

Qiu, B., and S. Chen, (2012). Multidecadal sea level and gyre circulation variability in the northwestern tropical Pacific Ocean. *J. Phys. Oceanogr.*, 42, 193–206.

Qu, X. & Huang, G. (2015). The decadal variability of the tropical Indian Ocean SST - the South Asian High relation: CMIP5 model study. *Clim Dyn* (2015) 45: 273.

Rao AS, Behera SK (2005). Subsurface influence on SST in the tropical Indian Ocean: Structure and interannual variability. *Dynamics of Atmospheres and Oceans* 39:103–135.

Rao RR, Girish Kumar MS, Ravichandran M, Rao AR, Gopalakrishna VV, Thadathil P (2010). Interannual variability of Kelvin wave propagation in the wave guides of the equatorial Indian Ocean, the coastal Bay of Bengal and the Southeastern Arabian Sea during 1993-2006. *Deep-Sea Res I* 57:1-13.

Rao, S. A., S. K. Behera, Y. Masumoto, and T. Yamagata (2002). Interannual subsurface variability in the tropical Indian Ocean with a special emphasis on the Indian Ocean Dipole. *Deep Sea Research* 49, 7-8, 1549-1572.

Rayner NA, Parker DE, Horton EB, et al (2003). Global analyses of sea surface temperature, sea ice, and night marine air temperature since the late nineteenth century. *Journal of Geophysical Research, Oceans* (1978–2012) 108:4407.

Reason CJC, Allan RJ, Lindesay JA, and Ansell TJ (2000). ENSO and climatic signals across the Indian Ocean basin in the global context: Part I, interannual composite patterns. *Int. J. Clim.* 20:1285–1327.

Reverdin, G., Cadet, D., & Gutzler, D. (1986). Interannual displacements of convection and surface circulation over the equatorial Indian Ocean. *Quarterly Journal of the Royal Meteorological Society*, 112, 43–67.

Riser, S., and Coauthors, (2016). Fifteen years of ocean observations with the global Argo array. *Nat. Climate Change*, 6, 145–153.

Roulet G and Madec G (2000). Salt conservation, free surface, and varying levels: a new formulation for ocean general circulation models. *J. Geophys. Res.* 105(C10):23927–23942.

Saji NH, Goswami BN, Vinayachandran PN and Yamagata T (1999). A dipole mode in the tropical Indian Ocean. *Nature* 401:360-363.

Saji NH, Xie SP and Yamagata T (2006). Tropical Indian Ocean variability in the IPCC twentieth-century climate simulations. *J. Clim.* 19:4397–4417.

Schneider N, Cornuelle BD (2005). The Forcing of the Pacific Decadal Oscillation *J. Climate*, 18, 4355–4357.

Schneider T, Bischoff T, Haug GH (2014). Migrations and dynamics of the intertropical convergence zone. *Nature* 513, 45–53.

Schott FA, Xie SP and McCreary JP (2009). Indian Ocean circulation and climate variability. *Rev Geophys.* 47:RG1002.

Schott, F. A., and J. P. McCreary, (2001). The monsoon circulation of the Indian Ocean. *Prog. Oceanogr.*, 51, 1–123.

Schwarzkopf FU, and Böning CW (2011). Contribution of Pacific wind stress to multi-decadal variations in upper ocean heat content and sea level in the tropical south Indian Ocean, *Geophys. Res. Lett.*, 38, L12602.

Sengupta DR, Senan, Goswami BN and Vialard J (2007). Intraseasonal variability of equatorial Indian Ocean zonal currents. *J. Clim.* 20:3036–3055.

Shakun JD, Shaman J (2009). Tropical origins of North and South Pacific decadal variability. *Geophys Res Lett* 36:L19711.

Shankar D, Shetye SR (1999). Are interdecadal sea level changes along the Indian coast influenced by variability of monsoon rainfall?. *J. Geophys. Res.* 104:26031–26042.

Shankar D, Vinayachandran PN, Unnikrishnan AS. (2002). The monsoon currents in the north Indian ocean. *Prog. Oceanogr.* 52:63–120.

Shankar, D., (2000). Seasonal cycle of sea level and currents along the coast of India. *Current Science* 78, 279–288.

Shankar D., (1998). Low-frequency variability of sea level along the coast of India. Ph.D. Thesis, Goa University - National Institute of Oceanography, Goa, India.

Shi G, Ribbe J, Cai W and Cowan T (2007). Multidecadal variability in the transmission of ENSO signals to the Indian Ocean. *Geophys. Res. Lett.* 34:L09706.

Si, Z. & Xu, Y. Chin. (2014). Influence of the Pacific decadal oscillation on regional sea level rise in the Pacific Ocean from 1993 to 2012. *J. Ocean. Limnol.* 32: 1414.

Slangen, A. B. A., C. A. Katsman, R. S. W. van de Wal, L. L. A. Vermeersen, and R. E. M. Riva, (2012). Towards regional projections of twenty-first century sea-level change based on IPCC SRES scenarios. *Climate Dyn.*, 38, 1191–1209.

Slangen, A. B. A., M. Carson, C. A. Katsman, R. S. W. van de Wal, A. Köhl, L. L. A. Vermeersen, and D. Stammer, (2014). Projecting twenty-first century regional sea-level changes. *Climatic Change*, 124, 317–332.

Smith TM, Reynolds RW, Peterson TC, Lawrimore J (2008). Improvements to NOAA's Historical Merged Land–Ocean Surface Temperature Analysis (1880–2006). *J Climate* 21:2283–2296.

Storch HV, Zwiers FW (1999). Statistical Analysis in Climate Research. Cambridge University Press, Cambridge.

Suarez, M. J., and P.S. Schopf, (1988). A delayed action oscillator for ENSO, *J. Atmos. Sci.*, 45, 3283–3287.

Sverdrup HU (1947). Wind driven currents in a baroclinic ocean, with application to the equatorial currents of the eastern Pacific, *Proc. Natl. Acad. Sci. U.S.A.*, 33, 318–326.

Takahashi, K., A. Montecinos, K. Goubanova, and B. Dewitte (2011). ENSO regimes: Reinterpreting the canonical and Modoki El Niño, *Geophys. Res. Lett.*, 38.

Taylor KE, Stouffer RJ, Meehl GA (2012). An Overview of CMIP5 and the Experiment Design. *Bull. Amer. Meteor. Soc.* 93:485–498.

Timmermann A, McGregor S and Jin FF (2010). Wind effects on past and future regional sea level trends in the southern Indo-Pacific. *J. Climate* 23:4429–4437.

Tokinaga H and Xie SP (2011). Wave and Anemometer-based Sea surface Wind (WASWind) for climate change analysis. *J. Climate* 24:267–285.

Tokinaga H, Hiroki, Xie SP, Timmermann A, McGregor S, Ogata T, Kubota H, Okumura YM (2012). Regional patterns of tropical Indo-Pacific climate change: Evidence of the walker circulation weakening. *J. Climate* 25:1689–1710.

Tozuka T, Yokoi T, Yamagata T (2010). A modelling study of interannual variations of the Seychelles dome. *J. Geophys. Res.* 115:C04005.

- Trenary, L., and W. Han, (2008). Causes of decadal subsurface cooling in the tropical Indian Ocean during 1961–2000. *Geophys. Res. Lett.*, 35, L17602.
- Trenary, L., and W. Han, (2013). Remote and local forcing of decadal sea level and thermocline depth variability in the south Indian Ocean. *J. Geophys. Res.*, 118, 381–398.
- Trenberth KE, Branstator GW, Karoly D, et al (1998). Progress during TOGA in understanding and modeling global teleconnections associated with tropical sea surface temperatures. *Journal of Geophysical Research: Oceans* (1978–2012) 103:14291–14324.
- Trenberth, K. E. & Stepaniak, D. P. (2001). Indices of El Niño evolution. *J. Clim.* 14, 1697–1701.
- Trenberth, K. E., and J. W. Hurrell (1994). Decadal atmosphere-ocean variations in the Pacific, *Clim. Dyn.*, 9, 303–319.
- Unnikrishnan AS and Shankar D (2007). Are sea level-rise trends along the coasts of north Indian Ocean consistent with global estimates?. *Global and Planetary Change* 57:301-307.
- Unnikrishnan, A.S.; Nidheesh, A.G.; Lengaigne, M (2015). Sea-level-rise trends off the Indian coasts during the last two decades, *Current Science*, 108, 966-971.
- Uppala and co-authors (2005). The ERA-40 re-analysis. *Q. J. R. Meteorol. Soc.* 131:2961-3012.
- Vecchi G A and Soden BJ (2007). Global warming and the weakening of the tropical circulation. *J. Climate* 20:4316–4340.
- Vecchi, GA, Soden BJ, Wittenberg AT, Held IM, Leetmaa A and Harrison MJ (2006). Weakening of tropical Pacific atmospheric circulation due to anthropogenic forcing. *Nature* 441:73–76.
- Vialard J, Menkes C, Boulanger JP, Delecluse P, Guilyardi E and McPhaden M (2001). A model study of the oceanic mechanisms affecting the equatorial SST during the 1997–98 El Niño. *J. Phys. Oceanogr.* 31:1649–1675.
- Vialard J, Shenoi SSC, McCreary JP, Shankar D, Durand F, Fernando V and Shetye SR (2009). Intraseasonal response of northern Indian Ocean coastal waveguide to the Madden-Julian Oscillation. *Geophys. Res. Lett.* 36: L14606.
- Vialard J. (2015). Ocean Science: Hiatus heat in the Indian Ocean. *Nature Geoscience* 8, 423–424.
- Vimont DJ (2005). The contribution of the interannual ENSO cycle to the spatial structure of decadal ENSO-like variability. *J. Climate* 18:2080–2092.
- Vinayachandran, P. N., S. Lizuka, and T. Yamagata (2002). Indian Ocean dipole mode events in an ocean general circulation model, *Deep Sea Res., Part II*, 49 (7–8), 1573–1596.
- Wainwright L, Meyers G, Wijffels S and Pigot L (2008). Change in the Indonesian Throughflow with the climatic shift of 1976/77. *Geophys. Res. Lett.* 35: L03604
- Waliser, D. E. & Gautier, C. A (1993). satellite-derived climatology of the ITCZ. *J. Clim.* 6, 2162–2174.

- Walker, G.T. and Bliss, E.W., (1932). World Weather V, Memoirs of the Royal Meteorological Society, 4, (36) , 53-84.
- Wang, C., (2001). A unified oscillator model for the El Niño-Southern oscillation. *Journal of Climate* 14, 98–115.
- Webster PJ, Moore AM, Loschnigg JP and Leben RR (1999). Coupled oceanic-atmospheric dynamics in the Indian Ocean during 1997-98. *Nature* 401:356-360.
- Widlansky M, Timmermann A, Cai W (2105). Future extreme sea level seesaws in the tropical Pacific. *Science* Vol. 1 No.8. DOI: 10.1126/sciadv.1500560.
- Wijffels S and Meyers G (2004). An intersection of oceanic wave guides: Variability in the Indonesian throughflow region. *J. Phys. Oceanogr.* 34:1232–1253.
- Wijffels, S. E., J. Willis, C. M. Domingues, P. Barker, N. J. White, A. Gronell, K. Ridgway, and J. A. Church (2008). Changing expendable bathythermograph fall rates and their impact on estimates of thermosteric sea level rise, *J. Clim.*, 21, 5657–5672.
- Wirth A, Willebrand J and Schott F (2002). Variability of the Great Whirl from observations and models. *Deep-Sea Res. II* 49:1279–1295.
- Woodruff SD, Worley SJ, Lubker SJ, Ji Z, Freeman JE, Berry DI, Brohan P, Kent EC, Reynolds RW, Smith SR and Wilkinson C (2011) ICOADS release 2.5: Extensions and enhancements to the surface marine meteorological archive. *Int. J. Climatol.* 31:951–967
- Woodworth PL and Player R (2003). The Permanent Service for Mean Sea Level: an update to the 21st century. *Journal of Coastal Research* 19:287-295.
- Wu L, Liu Z, Gallimore R, et al (2003). Pacific decadal variability: The tropical Pacific mode and the North Pacific mode. *J Climate*, Vol. 16, No.8.
- Wyrtki, K. (1973). An equatorial jet in the Indian Ocean, *Science*, 181, 262–264.
- Xie S-P, Hu K, Hafner J, et al (2009). Indian Ocean Capacitor Effect on Indo-Western Pacific Climate during the Summer following El Niño. *J Climate* 22:730–747.
- Xie, S-P., H. Annamalai, F. A. Schott, and J. P. McCreary, (2002). Structure and mechanisms of South Indian Ocean climate variability. *J. Climate*, 15, 864–878.
- Yim BY, Kwon M, Min HS, Kug J-S (2014). Pacific Decadal Oscillation and its relation to the extratropical atmospheric variation in CMIP5. *Clim Dyn* 44:1521–1540.
- Yin X, Gleason BE, Compo GP, Matsui N (2008). The International Surface Pressure Databank (ISPD) land component version 2.2., National Climatic Data Center, Asheville, NC, pp.1-12, 2008.
- Yu B and Zwiers FW (2010). Changes in equatorial atmospheric zonal circulations in recent decades. *Geophys. Res. Lett.* 37:L05701.
- Yu J-Y and Kim S T (2010). Identification of Central-Pacific and Eastern-Pacific types of ENSO in CMIP3 models. *Geophys. Res. Lett.* 37 L15705.
- Yu W, Xiang B, Liu L and Liu N (2005). Understanding the origins of interannual thermocline variations in the tropical Indian Ocean. *Geophys. Res. Lett.* 32:L24706.

Yu, X. and M.J. McPhaden, (1999). Dynamical analysis of seasonal and interannual variability in the equatorial Pacific. *J. Phys. Oceanogr.*, 29, 2350–2369.

Zhang D and McPhaden MJ (2006). Decadal variability of the shallow Pacific meridional overturning circulation: Relation to tropical sea surface temperatures in observations and climate change models. *Ocean Modell.* 15:250–273.

Zhang X, Lu Y, Thompson KR (2009). Sea level variations in the tropical Pacific ocean and the Madden–Julian Oscillation. *J. Phys. Oceanogr.* 39:1984–1992.

Zhang Y, Rossow WB, Lacis AA, Oinas V, Mishchenko MI (2004). Calculation of radiative fluxes from the surface to top of atmosphere based on ISCCP and other global data sets: refinements of the radiative transfer model and the input data. *J. Geophys. Res.* 109:1-27.

Zhang Y, Wallace JM, Battisti DS (1997). ENSO-like interdecadal variability: 1900-93. *J Climate* 10:1004–1020.

Zhang, X., and J. A. Church (2012). Sea level trends, interannual and decadal variability in the Pacific Ocean, *Geophys. Res. Lett.*, 39, L21701.

Zhuang, W., M. Feng, Y. Du, A. Schiller, and D. Wang, (2013). Low-frequency sea level variability in the southern Indian Ocean and its impacts on the oceanic meridional transports. *J. Geophys. Res.*, 118, 1302–1315.

T- 780